

Fracture and Fatigue of Adhesively-Bonded Fiber-Reinforced Polymer Structural Joints

THÈSE N° 4662 (2010)

PRÉSENTÉE LE 20 AVRIL 2010

À LA FACULTÉ ENVIRONNEMENT NATUREL, ARCHITECTURAL ET CONSTRUIT
LABORATOIRE DE CONSTRUCTION EN COMPOSITES
PROGRAMME DOCTORAL EN STRUCTURES

ÉCOLE POLYTECHNIQUE FÉDÉRALE DE LAUSANNE

POUR L'OBTENTION DU GRADE DE DOCTEUR ÈS SCIENCES

PAR

Ye ZHANG

acceptée sur proposition du jury:

Prof. I. Smith, président du jury
Prof. T. Keller, Dr A. Vasilopoulos, directeurs de thèse
Dr A. Brunner, rapporteur
Prof. E. Brühwiler, rapporteur
Prof. G. Sedlacek, rapporteur



ÉCOLE POLYTECHNIQUE
FÉDÉRALE DE LAUSANNE

Suisse
2010

CONTENTS

PREFACE	V
ABSTRACT	VII
RÉSUMÉ	IX
ACKNOWLEDGEMENTS	XI
1 INTRODUCTION	1
1.1 Motivation	1
1.2 Objectives	6
1.3 Methodology	7
1.4 Composition of the work	9
2 PUBLICATIONS	15
2.1 Mechanical and fracture behavior of fracture joints under quasi-static loading	15
2.2 Mechanical and fracture behavior of structural joints under quasi-static loading	48
2.3 Modeling of mechanical and fracture behavior under quasi-static loading	74
2.4 Environmental effects under quasi-static loading	103
2.5 Mechanical behavior under fatigue loading	130
2.6 Fracture behavior under fatigue loading	149
2.7 Environmental effects under fatigue loading	174
3 SUMMARY	195
3.1 Summary of results	195
3.2 Original contributions	197
3.3 Further investigations and future prospects	201
CURRICULUM VITAE	205
APPENDICES ON CD-ROM	

CONTENTS OF APPENDICES

A	Material Properties of GFRP Laminates	2
A.1	Burn-off experiments and fiber volume fraction	2
A.2	Determination of tensile strength and modulus of elasticity	5
A.2.1	Experimental program and instrumentation	5
A.2.2	Summary of experimental results	5
A.2.3	Experimental results for individual specimens	7
A.3	Determination of flexural modulus	10
A.3.1	Experimental program and instrumentation	10
A.3.2	Summary of experimental results	11
B	Material Properties of Epoxy Adhesive (Sikadur 330)	12
B.1	Effects of loading rate on tensile modulus of elasticity	12
B.1.1	Experimental program and instrumentation	12
B.1.2	Summary of experimental results	15
B.1.3	Experimental results for individual specimens	18
B.2	Determination of shear properties	27
B.2.1	Experimental program and instrumentation	27
B.2.2	Summary of experimental results	27
B.3	Dynamic Mechanical Analysis (DMA)	30
C	Experimental Investigations of Fracture Joints under Quasi-Static Loading	31
C.1	Mode I fracture experiments	31
C.1.1	Experimental program and instrumentation	31
C.1.2	Summary of experimental results	31
C.1.3	Experimental results for individual specimens	35
C.2	Mode II fracture experiments	41
C.2.1	Experimental program and instrumentation	41
C.2.2	Summary of experimental results	41
C.2.3	Experimental results for individual specimens	45
C.3	Preliminary Mode II fracture experiments	54

C.3.1 Experimental program and instrumentation	54
C.3.2 Summary of experimental results	55
C.3.3 Experimental results for individual specimens	61
D Experimental Investigations of Structural Joints under Quasi-Static Loading	67
D.1 Double-lap joint experiments	67
D.1.1 At 23°C	67
D.1.2 At -35°C	94
D.1.3 At temperatures of 40°C and higher	107
D.1.4 At 40°C + 90%RH	125
D.1.5 Preconditioned double-lap joint experiments	137
D.2 Stepped-lap joint experiments	140
D.2.1 At 23°C	140
D.2.2 At -35°C	154
D.2.3 At 40°C	161
E Experimental Investigations of Structural Joints under Fatigue Loading	168
E.1 Double-lap joint experiments	168
E.1.1 At 23°C + 50%RH	168
E.1.2 At -35°C	200
E.1.3 At 40°C + 50%RH	235
E.1.4 At 40°C + 90%RH	270
E.2 Stepped-lap joint experiments at 23°C + 50%RH	305
E.2.1 Experimental program and instrumentation	305
E.2.2 Summary of experimental results	305
E.2.3 Experimental results for individual specimens	308
E.3 Preliminary fatigue experiments at a frequency of 2 Hz	337
E.3.1 Experimental program and instrumentation	337
E.3.2 Summary of experimental results	338
E.3.3 Experimental results for individual specimens	342

F	Numerical Model Source Code (for ANSYS 10.0)	358
F.1	Application of Virtual Crack Closure Technique (VCCT)	358
F.1.1	Source code for Double-Cantilever-Beam model (3D)	358
F.1.2	Source code for End-Loaded-Split (3D)	363
F.1.3	Source code for double-lap joint model (2D)	373
F.1.4	Source code for stepped-lap joint model (2D)	385
F.2	Temperature-dependent joint stiffness	407

PREFACE

Fiber-reinforced polymer (FRP) composites are increasingly used in engineering structures thanks to their advantageous material properties such as high specific strength, high insensitivity to frost and de-icing salts, and short installation times with minimum traffic interference in the case of bridge construction. Advances in pultrusion technology allow the production of large-scale structural profiles at acceptable costs for civil infrastructure applications. However, structural FRP components are still difficult to connect due to the brittle fibrous and anisotropic nature of the materials. The current practice of bolting leads, in most cases, to an oversizing of components. Adhesive bonding is much more appropriate for FRP composites since adhesive joints exhibit higher joint efficiencies and are much stiffer compared to bolted joints. This is significant with regard to the stiffness-governed design of structures using glass fibers (GFRP).

Since GFRP bridges are very light in weight compared to their live loads, the repetitive loading to which they are subjected raises the question of the fatigue behavior of such structures and, in particular, their connections. Research concerning the fatigue behavior of adhesive connections has been done mainly in areas other than civil engineering (aircraft and vehicle construction). In these areas, mainly traditional laminated FRP materials are used and the adhesive layers are very thin, well below 1 mm. The internal material structure of pultruded FRP components is, however, very different and much larger tolerances in the connections of civil engineering structures require much thicker adhesive layers. It is thus almost impossible to directly compare and transfer research results between these very different areas and modes of application.

In the field of adhesive connections of pultruded profiles, very little research has been done to date. The aim of this thesis is therefore to contribute to a better understanding of the fracture and fatigue behavior of adhesively-bonded structural joints composed of pultruded GFRP adherends.

I would like to acknowledge the support provided for this research project by the Swiss National Science Foundation, Fiberline Composites A/S, Denmark (pultruded laminate supplier), and Sika AG, Zurich (adhesive supplier).

Prof. Dr. Thomas Keller

CCLab Director/Thesis Director

ABSTRACT

Being good structural replacement for other conventional material, the pultruded glass fiber reinforced polymer (GFRP) profiles are being increasingly used in civil engineering structures. The connection between components is considered the most suspect area for failure initiation. The adhesive bonding is preferred for FRP composite structures, rather than the mechanical fastening, due to the brittle failure nature of composite materials. During past decades, many efforts have been made by researchers to better understand the mechanism of adhesive bonding, to analyze the stress distributions and to improve the strength of composite structural joints. However there is still no commonly accepted design code/standard existing for adhesively-bonded joints in civil engineering infrastructures since several important knowledge gaps are to be filled.

Besides the joint strength at failure, the characterization and modeling of the progressive failure process, in particular involving the so-called crack initiation and propagation phases, is also an important concern. By employing the strain energy release rate (SERR) as the fracture parameter, the linear-elastic fracture mechanics (LEFM) approach is considered an efficient method to model the fracture behavior of structural joints. However, due to the uncontrollable crack initiation and the complex geometric configurations, the crack measurement techniques and the calculation method for the SERR are to be validated. In fracture mechanics, the fracture of a material or component can be described by a single mode or the combinations of the following three basic modes: opening mode (Mode I), shearing mode (Mode II), and tearing mode (Mode III). During the fracture of a structural joint, crack initiation and propagation are driven by combined through-thickness tensile (peeling), and shear stresses, thus resulting in a mixed mode fracture. In order to use the fracture results of structural joints to form the mixed fracture criterion for a specific composite material, a feasible analytical or numerical method are to be developed to determine the Mode I and II components of the SERR during fracture.

Although many efforts have been made to better understand the short-term behavior of structural joint under quasi-static loading, the long-term performance under fatigue loading and different environmental conditions is a more demanding task when adhesively-bonded joints are applied in a real structure. Most of structural failures occur due to mechanisms that are driven by fatigue loading and for composite structures, the fatigue produced by the repeated application of live load is more critical due to its lighter self-weight, in other words the lower dead load. Besides the fatigue loading, a structure in practice may also experience the combined environmental effects of two basic factors: temperature and humidity. These environmental conditions may directly affect properties of structural

joints, including the failure mechanism, the stiffness and strength, the crack initiation and propagation and etc.. Thus, the missing knowledge and confidences in the long-term behavior under cyclic loading and the durability under different environmental conditions are the main obstacles to the further development of FRP composites in civil engineering infrastructures.

In this research, the mechanical and fracture behavior of adhesively-bonded double-lap and stepped-lap joints (DLJs and SLJs) composed of pultruded GFRP laminates and an epoxy adhesive were experimentally and numerically investigated under both quasi-static and fatigue loadings. The crack measurement techniques and the calculation methods for the SERR were validated for DLJs and SLJs. The LEFM approach was successfully applied to characterize and model the progressive failure process of structural joints. The Mode I and II components of the SERR of DLJs and SLJs were determined using the Virtual Crack Closure Technique in finite element analysis. Combining with the results of pure Mode I and II experiments, a mixed mode fracture criterion for pultruded GFRP composite was formed. Under fatigue loading, the fatigue behavior of structural joints was successfully modeled by using the stiffness-based and fracture mechanics approaches, besides the $F-N$ curves. Based on the stiffness degradation, a linear and a sigmoid non-linear model were established and the fatigue live corresponding to the failure and allowable stiffness degradation can be predicted. Concerning fracture mechanics approach, the Fatigue Crack Growth (FCG) curves were formed for DLJs and SLJs and the corresponding fracture parameters were obtained. Similarly to stiffness-based approach, fatigue lives corresponding to the failure and allowable crack length can be predicted. The environmental effects on both short- and long-term performances of structural joints were experimentally evaluated and numerically modeled based on experimental results. The temperature-dependent joint stiffness can be predicted using the finite element analysis based on the thermomechanical properties of constituent materials. A relationship between the equivalent quasi-static joint strength under different environmental conditions and the cyclic stresses and the fatigue life was established.

Keywords

Adhesively-bonded joints; pultruded GFRP; fracture; fatigue; crack initiation; crack propagation; stiffness degradation; environmental effects

RÉSUMÉ

Les matériaux composites pultrudés à base de polymères renforcés par des fibres de verre (GFRP) sont de plus en plus utilisés dans les structures de génie civil puisqu'ils peuvent remplacer les matériaux traditionnels tout en apportant de nouveaux avantages aux constructions. La liaison entre les composants est considérée comme étant le point critique pour l'initiation de la rupture. Les assemblages collés sont préférés aux assemblages mécaniques en raison du comportement fragile des matériaux FRP. Au cours des dernières décennies de nombreuses recherches ont été menées visant à améliorer les connaissances du mécanisme de collage, analyser la distribution des contraintes et améliorer la résistance des joints structuraux. Cependant, il n'existe toujours pas de norme unanimement acceptée pour le dimensionnement de joints collés dans les infrastructures de génie civil puisque plusieurs lacunes restent encore à combler.

Outre la résistance des joints à la rupture, la caractérisation et la modélisation du processus progressif de ruine, en particulier l'amorçage et la propagation des fissures, sont également des préoccupations importantes. La mécanique de la rupture linéaire élastique (LEFM) est considérée comme une méthode efficace pour la modélisation du comportement de la rupture des joints structuraux en utilisant le taux de restitution d'énergie (SERR) comme paramètre de rupture. Cependant, en raison de l'amorçage incontrôlable des fissures et des configurations géométriques complexes, les techniques de mesure des fissures et les méthodes de calcul de SERR doivent encore être validées. En mécanique de la rupture, la rupture d'un matériau ou d'un composant peut être décrite par un seul mode ou par la combinaison des trois modes de base : le mode d'ouverture (Mode I), le mode de glissement dans le plan (Mode II) et le mode de glissement antiplan (Mode III). Lors de la rupture d'un joint structural, l'amorçage et la propagation des fissures sont dictés par l'action combinée de contraintes dans le sens de l'épaisseur et de contraintes de cisaillement, ce qui entraîne une rupture en mode mixte. Afin d'utiliser les résultats de la rupture de joints structuraux pour le développement du critère de rupture mixte d'un matériau composite spécifique, une méthode analytique ou numérique devrait être développée permettant de déterminer les modes I and II constitutifs du SERR.

Bien que de nombreuses études aient été réalisées pour mieux comprendre le comportement à court terme des joints structuraux sous les charges statiques, la recherche de la résistance à long terme sous les charges de fatigue et sous diverses conditions environnementales reste une tâche d'autant plus ardue que les joints collés sont utilisés dans des structures réelles. Une majorité des ruptures a lieu en raison de mécanismes provoqués par des sollicitations cycliques. Ceci affecte d'autant plus les structures en matériaux composites en raison de leur faible poids propre. Outre les charges de fatigue,

une structure peut aussi être soumise à des sollicitations environnementales combinées de température et humidité. Ces conditions environnementales affectent les propriétés des joints structuraux y compris le mécanisme de rupture, la rigidité, la charge ultime, l'amorçage et la propagation des fissures. Ainsi le manque de connaissances et de confiance dans le comportement à long terme sous des charges cycliques et dans la durabilité sous différentes conditions environnementales sont les principaux obstacles au développement futur des FRPs dans les infrastructures de génie civil.

Dans cette recherche, le comportement mécanique et la résistance de joints collés à double recouvrement (DLJs) et de joints de type escalier simple (SLJs), constitués de profilés en GFRP pultrudés et d'un adhésif époxyde, ont été testés et modélisés sous des charges statiques et de fatigue. Les techniques de mesure des fissures et les méthodes de calcul pour la SERR ont été validées pour les joints DLJs et SLJs. L'approche LEFM a été appliquée pour la caractérisation et la modélisation du processus progressif de ruine des joints structuraux. Les composants Mode I and II de la SERR de joints DLJs et SLJs ont été déterminés en utilisant le Virtual Crack Closure Technique (VCCT) dans l'analyse d'éléments finis. Un critère de rupture en mode mixte, combinant les résultats des essais du Mode I et du Mode II, a été établi pour les joints à base de GFRP pultrudés. Le comportement des joints structuraux a été modélisé sous des charges de fatigue à l'aide d'approches de rigidité et de mécanique de la rupture, en plus des courbes F-N. Un modèle linéaire puis un modèle sigmoïde non-linéaire fonction de la dégradation de la rigidité ont permis de prédire la durée de vie à la fatigue correspondante à la rupture et à la dégradation de la rigidité admissible. En ce qui concerne l'approche mécanique de la rupture, des courbes de progression de fissure de fatigue (FCG) ont été établies pour les joints DLJs et SLJs ; les paramètres correspondants ont été définis. De manière analogue à l'approche fondée sur la rigidité, la durée de vie à la fatigue et la longueur de la fissure admissible peuvent être prédites. L'effet des actions environnementales sur les performances à court et à long terme des joints structuraux a été évalué expérimentalement puis modélisé à partir de résultats expérimentaux. La rigidité des joints structuraux en fonction de la température peut être prédite par un modèle d'éléments finis basé sur les propriétés thermomécaniques des matériaux constitutifs. Une relation d'équivalence a été établie entre la résistance des joints sous des charges statiques et différentes conditions environnementales et la durée de vie sous des contraintes cycliques.

Mots-clés

Joints collés, GFRP pultrudés ; rupture ; fatigue ; amorçage de la fissure ; propagation de la fissure ; dégradation de la rigidité ; effets environnementaux

ACKNOWLEDGEMENTS

This work would not have been achieved without the help of many people to whom I would like to express my deepest gratitude. It is hard to list in one small place all the people who directly or indirectly supported me during the course of my PhD research, but I am going to try.

First of all, I would like to express my most sincere gratitude to Prof. Dr. Keller, who offered me the opportunity to work on this research project. I am also grateful for his constant guidance, support and confidence throughout these years, especially during the most difficult times when I was losing sight of the light at the end of the tunnel. I would like to thank my thesis co-director, Dr. Anastasios Vasilopoulos, who supervised my thesis during the last three years, and with whom I eventually published five papers, despite a certain amount of conflict!

I would also like to express my gratitude to the following exceptional sources of support:

- The Swiss National Science foundation for providing the funding for the research (Grant No. 200020-111702/1);
- Fiberline composites A/S (pultruded laminate supplier), Denmark and Sika AG (adhesive supplier), Zurich for their generous donation of the experimental materials;
- My thesis defense committee for their patience and efforts in reading and evaluating this thesis and for their expert suggestions: Prof. Eugen Brühwiler, Structural Maintenance and Safety Laboratory (MCS), EPFL, Switzerland; Dr. Andreas Brunner, Mechanical Systems Engineering, EMPA, Switzerland; and Prof. Gerhard Sedlacek, Lehrstuhl für Stahl- und Leichtmetallbau, RWTH Aachen University, Germany;
- Dr. Andreas Brunner for the fruitful discussions and valuable advice concerning fracture mechanics, which however is definitely an unfamiliar field for a civil engineer like me;
- Prof. Dr. Till Vallée, the supervisor of my Master thesis, for leading me into the wonderful world of the adhesively-bonded joint, and for his sympathetic encouragement;
- Prof. Dr. Aixi Zhou for directing my thesis during the first two years;
- The whole team of technicians at IS-EPFL for their steadfast support: Sylvain Demierre for

always providing intelligent and practical solutions for experimental testing and measuring problems; Gilles Guignet for proposing the awesome “video extensometer” technique for my fracture experiments; Patrice Gallay for manufacturing mechanical elements of “Swiss Made” quality and his incredible patience in listening to requests in my poor French; and Ronland Gysler, François Perrin, Gérald Rouge and Hansjakob Reist;

- My colleagues at CCLab-EPFL: Dr. Julia de Castro for the expert suggestions concerning adhesively-bonded joints; Dr. Yu Bai with whom I shared an office for almost the entire period of my PhD studies; Behzad Dehghan for his valuable advice on finite element analysis; Omar Moussa for his passion and expertise in helping me complete the adhesive experiments; all the former and current CCLab members, Dr. Erika Schaumann, Dr. Florian Riebel, Roohollah Sarfaraz, Moslem Shahverdi and Ping Zhu, for their friendship and for creating a multicultural but harmonious atmosphere; Magdalena Schauenberg and Marlène Sommer for their enthusiastic and efficient administrative support;
- Those who helped me to prepare the thesis document: Prof. Keller and Dr. Anastasios Vasilopoulos for their careful reading and valuable comments; Margaret Howett for her efforts in converting my without-article-English into proper English; Dr. Julia de Castro for correcting and improving the résumé.

And last but not least, I would like to thank my family – my mother Ying Wang and my father Guoliang Zhang for their uninterrupted unfailing understanding and support, especially during the hardest time of my thesis; my gratitude also goes to Kewei Zhu for his translation of the abstract into French, but more worthy of mention, for his patience in listening to my endless complaining when things had gone wrong - and of course also for the wonderful time we shared together in Switzerland.

1 INTRODUCTION

1.1 Motivation

As a structural replacement for other conventional materials, fiber-reinforced polymer (FRP) composites provide excellent material properties for civil engineering applications. The combination of the high-stiffness/strength fibers with lightweight polymers results in composite materials with a high stiffness/strength-to-weight ratio. Besides the good mechanical properties, FRP composites also offer excellent resistance to environmental effects, e.g. corrosion resistance and low thermal expansion. Other advantages of FRP composites include good fatigue performance, non-magnetic properties, ease of transportation and construction and tailorability according to the loading conditions. In view of the product consistency and economy, the pultrusion technique is the most popular solution for manufacturing constant cross-sectioned FRP composite structural shapes for civil engineering applications. The successful use of FRP composites, however, depends much upon the integrity and reliability of the joint, which is considered the most likely area for failure initiation. The advantages of FRP composites might be eliminated if the characteristics of the associated joints are not properly understood and the structural joints not properly designed. Generally speaking, the key methods used for joining FRP composites are mechanical fastening (such as bolting and riveting) and adhesive bonding (Zhou and Keller, 2005). The combination of fastening and bonding can be used to take advantage of both methods. Each method has its advantages and disadvantages in application, but the brittle nature of FRP composites limits the efficiency of mechanical fastening and favors adhesive bonding. Since no cutouts for bolts or rivets are required in an adhesively-bonded joint, the reinforcing fibers remain continuous and local stress concentrations (except at the edge of the overlap) are reduced, thus ensuring a potentially better fatigue and durability performance of the joint. Furthermore, when connecting two or more components, an adhesively-bonded connection

weighs less than a mechanically-fastened joint, emphasizing the advantageous light weight of composite structures. Although adhesive bonding offers obvious advantages for composite joints, several knowledge gaps still remain to be filled, e.g. the fatigue performance and durability in different environments, and furthermore, no widely accepted design code/standard exists.

Over the last few decades, considerable experience has been accumulated to better understand the mechanism of adhesive bonding. A large number of results have been published aiming to characterize the stress distribution along the overlap length, optimize the geometric configurations and improve joint strength (Völkersen, 1938; Goland and Reissner, 1944; Hart-Smith, 1973a, 1973b; Tsai et al., 1998). Some valuable reviews (Kinloch, 1980, 1982; Baldan, 2004) focusing on the above topics were presented to provide a summary of previous works and suggestions for further study. Besides the strength of joints at ultimate failure, the characterizing and modeling of the failure process is also a topic worthy of discussion. During the loading of a structural joint, a crack or cracks initiate and propagate along the weakest path within the joint. When the crack develops sufficiently, the joints can sustain no further loading and then final collapse occurs. Fracture mechanics is considered an efficient approach to characterize and then model the progressive failure process, in particular the fracture process of joints. The concept of fracture mechanics was originated by Griffith for linear elastic solids in (Griffith, 1921), which concluded that for a specimen with a crack the maximum stress was not an appropriate strength criterion and an alternative theory was needed. A fundamental contribution to the development of fracture mechanics was made by Irwin in the 1950s. Based on the energy balance theory, the stress intensity factor (SIF), K , and the strain energy release rate (SERR), G , were proposed in (Irwin, 1957), instead of the stress at the crack tip, to describe the fracture behavior. More details of the historic developments in fracture mechanics can be found in (Erdogan, 2000). Due to the brittle fracture nature of GFRP composites, linear-elastic fracture mechanics (LEFM) is applicable and the strain energy release rate, defined as the necessary energy for unit crack propagation during fracture, is the most readily accessible fracture parameter.

The fracture mechanics approach has been used by many researchers to investigate the performance of fracture joints based on existing standards (ASTM D5528-01, 2007; ISO 15024:2000(E), 2000; ESIS(TC4), 2006). While only a few attempts have been made to use this approach for structural joints, and furthermore, most of them have focused on

aerospace/automotive applications. The aforementioned fracture and structural joints are two major categories of joints based on their function, which nevertheless exhibit several essential differences during the failure process. Fracture joints are particularly intended for fracture study and therefore an initial crack is predefined to produce stable crack propagation. When fracture joints are made of pultruded GFRP profiles, the materials which are commonly used in civil engineering structures, significant deviations from the standardized conditions (ASTM D5528-01, 2007; ISO 15024:2000(E), 2000; ESIS(TC4), 2006) are probably imposed by the large component dimensions on the full-scale level, the complex material architecture and the asymmetric geometry caused by the un-centered crack propagation path. Therefore, the existing standardized calculation methods for the strain energy release rate have to be validated. As for the failure process, in contrast to pre-cracked fracture joints, cracks in structural joints initiate naturally from small material defects (voids, microcracks or inhomogeneities) in an uncontrollable way. Following crack initiation, the crack propagation phase can be non-stable. The limited knowledge concerning the fracture behavior of structural joints can be attributed to the difficulties of crack measurement and the lacking or un-validated methods for calculating the strain energy release rate. The uncontrollable crack initiation and rapid propagation can hardly be detected and recorded by visual observation or other techniques used for fracture joints. Due to the complex geometric configuration, a commonly accepted analytical solution for strain energy release rate is missing, and the experimental and numerical methods need to be validated moreover.

In fracture mechanics, the fracture of a material or component can be described by a single mode or combinations of the following three basic modes: opening mode (Mode I), shearing mode (Mode II), and tearing mode (Mode III). During the fracture of a structural joint, crack initiation and propagation are driven by combined through-thickness tensile (peeling) and shear stresses. A loading combination leads to the mixed mode fracture (dominated by Mode I and II), which is characteristic of lap joints. The fracture mode mixity, defined as the ratio of strain energy release rates between Mode I and II, is mainly determined by the geometric configuration and loading condition of joints. Contrary to fracture joints, the mode mixity in structural joints is not predefined and it also changes with crack development. In order to use the results obtained for structural joints for establishing a mixed mode fracture criterion, it is necessary to quantify the fracture mode mixity. Very little work has been carried out however due to the lack of either an analytical or numerical calculation method.

Thanks to the experience accumulated from previous works, the short-term performance of structural joints under quasi-static loading is well understood. With regard to the practical demands made upon structural joints, a more significant concern, however, is how to ensure long-term performance under fatigue loading and various environmental conditions. In fact, most structural failures occur due to mechanisms driven by fatigue loading, whereas purely static failure is rarely observed. The repeated application of live loads may lead to failure of the material even when the load level is lower than for the ultimate limit states. For composite structures, fatigue caused by the live load is a more crucial consideration due to the low dead load, resulting from the low self-weight of composite materials. Although the fatigue of composite structural joints was initially investigated for aerospace/automotive applications, there are fundamental differences between aerospace/automotive and civil engineering applications concerning the manufacturing process, material architecture, component dimensions and operational conditions. Despite the fact that the modeling and prediction of fatigue behavior is a demanding task, there is no commonly accepted design code/standard for adhesively-bonded structural joints in civil engineering infrastructures.

A general review of the study of the fatigue behavior of adhesively-bonded composite joints was presented in (de Goeij et al., 1999), concerning different joint types and investigative approaches. As indicated, different categories of approaches can be adopted according to the damage metric that is selected to describe the fatigue life of joints. The first approach is based on the establishment of the $S-N$ curve for the examined material or component under specified loading and environmental conditions. The $S-N$ curves, and more often, the load- N ($F-N$) curves, are usually obtained from fatigue tests on structural joints. The second category includes the strength or stiffness degradation fatigue theories, those that assume residual strength or residual stiffness as the damage metric. Theories based on stiffness degradation measurements during fatigue life exhibit their non-destructive characteristic and can be used for on-line damage monitoring and continuous life assessment. In the third category, fatigue lifetime is linked with crack growth based upon linear-elastic fracture mechanics (LEFM). Using the so-called "Paris Law", the crack growth rate can be approximated as a function of the strain energy release rate, thus forming the Fatigue Crack Growth curves. This approach has been widely applied to pre-cracked fracture joints, which always exhibit stable crack propagation; its applicability to structural joints exhibiting uncontrollable crack initiation and rapid propagation needs to be validated however.

In addition to the behavior under cyclic loading, the long-term performance of adhesively-bonded joints under different environmental conditions is another major concern when they are used in real structures. In practice, a structure may experience the combined effect of the applied fatigue loads together with the following environments: thermal effects (including low/high temperatures and freeze-thaw effect), moisture, solutions with special chemical composition (sodium hydroxide and hydrochloric acid solution, alkaline environment etc.), and ultraviolet etc. Most research on the effects of environmental conditions has focused on investigating two basic factors: temperature and humidity. These two factors have several direct effects on the mechanical and fracture behavior of FRP composites and the polymer adhesives: 1) the change in the failure mechanism, 2) the degradation of the elastic modulus and ultimate strength, and 3) the acceleration/deceleration of crack initiation and propagation. Many efforts have been made to evaluate environmental effects on the long-term performance of aerospace/automotive applications (John et al., 1991; Harris and Fay, 1992). There is far less knowledge concerning structural joints in civil engineering infrastructures, which must sustain a longer service life, however.

Concerning the aforementioned considerations for adhesively-bonded joints when used in civil engineering structures, the investigations of this PhD thesis were organized as illustrated in Fig. 1. The investigated adhesively-bonded joints were composed of pultruded GFRP laminates and a two-component epoxy adhesive. Double-lap and stepped-lap joints (DLJs and SLJs) were selected as representative structural joints while Double-Cantilever-Beam (DCB) and End-Loaded-Split (ELS) specimens were selected as representative fracture joints.

Under both quasi-static and fatigue loading, the mechanical behavior of structural joints (Task 1.1-1.3 and 3.1-3.4 in Fig. 1) and fracture joints (Task 1.2-1.3 in Fig. 1) was investigated in terms of the strength, stiffness/stiffness degradation, failure mode, fatigue life, etc. With regard to the fracture mechanics approach, the applicability of LEFM was validated firstly for fracture joints and then extended to structural joints. The fracture behavior was characterized and modeled taking crack initiation and propagation into account (Task 2.1-2.6 and 4.1-4.4 in Fig. 1). In addition, the environmental effects on both the short- and long-term performance of structural joints were evaluated (Task 1.4, 2.7, 3.5 and 4.5 in Fig. 1).

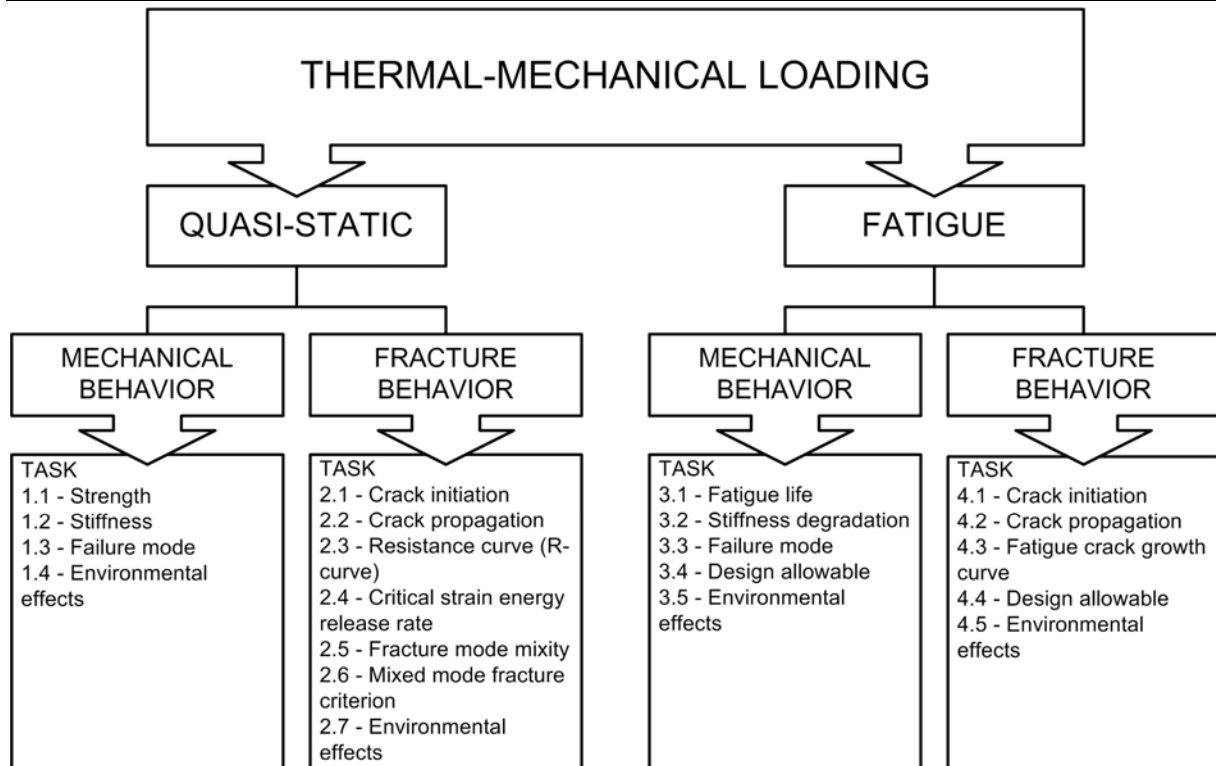


Figure 1. Scheme of the research.

1.2 Objectives

This PhD thesis focuses on the mechanical and fracture behavior of adhesively-bonded pultruded joints under quasi-static and fatigue loading, also considering environmental effects. Based on the above analysis, the objectives can be defined as characterizing and modeling the performance of adhesively-bonded joints in terms of:

1. Mechanical behavior under quasi-static loading;
2. Fracture behavior under quasi-static loading;
3. Mechanical behavior under fatigue loading;
4. Fracture behavior under fatigue loading;
5. Environmental effects on mechanical and fracture behavior under quasi-static and fatigue loading;

1.3 Methodology

In accordance with the objectives listed in Section 1.2 and the investigated joint types, the methodologies used are explained in Section 1.3.1-1.3.4.

1.3.1 Mechanical behavior under quasi-static loading

In order to characterize and model the mechanical behavior of fracture and structural joints under quasi-static loading, the following methodologies were employed corresponding to Task 1.1-1.4 listed in Fig. 1:

1. The mechanical behavior of fracture (DCBs and ELSs) and structural joints (DLJs and SLJs) under quasi-static tensile loading was experimentally investigated with regard to joint strength, joint stiffness and failure mode (Task 1.1-1.3);
2. The temperature effects on the mechanical behavior of structural joints (DLJs) under quasi-static tensile loading were experimentally characterized with regard to joint strength, joint stiffness and failure mode; the thermomechanical behavior of joints, in particular the temperature-dependent joint stiffness, was modeled using two empirical models and the finite element method (FEM) (Task 1.4).

1.3.2 Fracture behavior under quasi-static loading

In order to characterize and model the fracture behavior of structural and fracture joints under quasi-static loading, the following methodologies were employed corresponding to Task 2.1-2.7 listed in Fig. 1:

1. The fracture behavior of fracture joints (DCBs and ELSs) and structural joints (DLJs and SLJs) under quasi-static loading was experimentally investigated; three experimental techniques were used for the crack measurement: video extensometer (only for fracture joints), crack propagation gages and back-face strain gages (only for structural joints); all three techniques were employed to identify crack initiation and the former two were employed to monitor crack propagation (Task 2.1 and 2.2);
2. Based on linear-elastic fracture mechanics (LEFM), the strain energy release rate (SERR)

of fracture joints was calculated using different methods, including the analytical solutions based on beam theory, the experimental compliance method and the Virtual Crack Closure Technique (VCCT) in finite element analysis (FEA); the SERR of structural joints was calculated using ECM and VCCT; the Resistance curves (R-curves) were formed to describe the fracture behavior and the critical strain energy release rate, G_c , for Mode I, II and mixed mode fracture was determined, corresponding to crack initiation and propagation respectively (Task 2.3 and 2.4);

3. By using VCCT in FEA, the fracture mode mixities of structural joints (DLJs and SLJs) were determined and a mixed mode fracture criterion was established (Task 2.5 and 2.6);

4. In the temperature range where LEFM is still applicable, the temperature effects on the fracture behavior of structural joints (DLJs) were evaluated in terms of R-curves and the critical strain energy release rate (Task 2.7).

1.3.3 Mechanical behavior under fatigue loading

In order to characterize and model the mechanical behavior of structural joints under fatigue loading, the following methodologies were employed corresponding to Task 3.1-3.5 listed in Fig. 1:

1. The mechanical behavior of structural joints (DLJs and SLJs) under fatigue loading was experimentally investigated with regard to fatigue life, joint stiffness degradation during fatigue and failure mode (Task 3.1-3.3);

2. The stiffness degradation during fatigue was modeled by a linear and a non-linear sigmoid stiffness degradation model; these models were then used for the fatigue life predictions corresponding to failure and the allowable stiffness degradation (Task 3.4);

3. The temperature and humidity effects on the mechanical behavior of structural joints (DLJs) under fatigue loading were experimentally characterized with regard to fatigue life, joint stiffness degradation and failure mode; a relationship between the equivalent static strengths of joints (DLJs) under different environmental conditions and cyclic loads and fatigue life was established (Task 3.5) using an empirical wear-out model.

1.3.4 Fracture behavior under fatigue loading

In order to characterize and model the fracture behavior of structural joints under fatigue loading, the following methodologies were employed corresponding to Task 4.1-4.5 listed in Fig. 1:

1. The fracture behavior of structural joints (DLJs and SLJs) under fatigue loading was experimentally investigated; the crack initiation and propagation during fatigue were identified and monitored using crack propagation gages; based on LEFM, the SERR was calculated using ECM; the crack propagation rate was calculated using the 5-point incremental polynomial method (Task 4.1 and 4.2);

2. The fatigue behavior of structural joints was modeled using Fatigue Crack Growth (FCG) curves; the obtained empirical fracture parameters were then used for the fatigue life predictions corresponding to failure and the allowable crack length (Task 4.3 and 4.4);

3. The temperature and humidity effects on the fracture behavior of structural joints (DLJs) under fatigue loading were experimentally characterized with regard to the cycles for crack initiation and propagation, failure crack length and crack propagation rate (Task 4.5).

1.4 Composition of the work

Corresponding to objectives 1-5 listed in Section 1.2, six research papers have been published and one paper is currently under review. This PhD thesis is constructed on the basis of these papers, which are presented in Chapter 2.

Chapter 2 presents the publications:

1. Section 2.1 presents an experimental investigation of the mechanical and fracture behavior of fracture joints (DCBs and ELSs) to validate the applicability of the LEFM approach; the proposal of a new crack measurement technique and the comparison of methods for calculating the SERR are presented; it also involves the modeling of fracture behavior using the FEM;

2. Section 2.2 presents an experimental investigation of the mechanical and fracture behavior of structural joints (DLJs and SLJs); it covers the validation of the applicability of the LEFM approach with regard to crack measurement techniques and methods for calculating

the SERR;

3. Section 2.3 presents the modeling of fracture behavior and the determination of the fracture mode mixity of structural joints (DLJs and SLJs) using FEM; incorporating the modeling of the fracture behavior of fracture joints in Section 2.1, this section also covers the development of a mixed mode fracture criterion for pultruded GFRP composites;

4. Section 2.4 presents an experimental investigation of temperature effects on the mechanical and fracture behavior of structural joints (DLJs) under quasi-static loading; it also comprises the modeling of the temperature-dependent joint stiffness;

5. Section 2.5 presents the modeling of the mechanical behavior of structural joints (DLJs and SLJs) under fatigue loading by employing stiffness degradation models; it also comprises the fatigue life predictions corresponding to failure and allowable stiffness degradation;

6. Section 2.6 presents the modeling of the fracture behavior of structural joints (DLJs and SLJs) under fatigue loading by employing FCG curves; it also comprises the fatigue life predictions corresponding to failure and allowable crack length;

7. Section 2.7 presents an experimental investigation of environmental effects on the mechanical and fracture behavior of structural joints (DLJs) under fatigue loading; it also comprises the modeling of environmental effects on fatigue life;

The relationship between the objectives, methodology and the resultant publications are shown in Table 1. The investigated joint types are also indicated in Table 1.

Table 1. Relationship between objectives and methodology (in Chapter 1) and publications (in Chapter 2)

Objectives (Section 1.2)	Methodology (Section 1.3)	Publications (Section 1.4)	Joint type
1. Mechanical behavior under quasi-static loading	- Experimental investigation - Linear-elastic fracture mechanics	Section 2.1	DCB ELS
2. Fracture behavior under quasi-static loading	- Finite element method (VCCT)		
1. Mechanical behavior under quasi-static loading	- Experimental investigation - Linear-elastic fracture mechanics	Section 2.2	DLJ SLJ
2. Fracture behavior under quasi-static loading			
2. Fracture behavior under quasi-static loading	- Experimental investigation - Linear-elastic fracture mechanics - Finite element method (VCCT)	Section 2.3	DCB ELS DLJ SLJ
5. Environmental effects under quasi-static loading	- Experimental investigation - Linear-elastic fracture mechanics - Empirical thermomechanical model - Finite element method	Section 2.4	DLJ
3. Mechanical behavior under fatigue loading	- Experimental investigation - Stiffness degradation model	Section 2.5	DLJ SLJ
4. Fracture behavior under fatigue loading	- Experimental investigations - Fatigue Crack Growth (FCG) curve (based on linear-elastic fracture mechanics)	Section 2.6	DLJ SLJ
3. Mechanical behavior under fatigue loading	- Experimental investigation - Empirical wear-out model	Section 2.7	DLJ
4. Fracture behavior under fatigue loading			
5. Environmental effects under fatigue loading			

References

- ASTM D5528-01, 2007. Standard Test Method for Mode I Interlaminar Fracture Toughness of Unidirectional Fiber-Reinforced Polymer Matrix Composites. Annual book of ASTM standards: adhesive section 15.03.
- Baldan, A., 2004. Adhesively-bonded joints in metallic alloys, polymers and composite materials: Mechanical and environmental durability performance. *Journal of Materials Science* 39(15), 1573-4803.
- Erdogan, F., 2000. Fracture mechanics. *International Journal of Solids and Structures* 37, 171-183.
- ESIS(TC4), 2006. Determination of the Mode II Delamination Resistance (Critical Energy Release Rate G_{IIC}) of Unidirectional Fiber-Reinforced Polymer Laminates Using the End-Loaded-Split Specimen (ELS). ESIS(TC4) Protocol, 2006.
- de Goeij, W.C., van Tooren, M.J.L., Beukers, A., 1999. Composite adhesive joints under cyclic loading. *Materials & Design* 20, 213-221.
- Goland, M., Reissner, E., 1944. The stresses in cemented joints. *Journal of Applied Mechanics* 1, A17-A27.
- Griffith, A.A., 1921. The phenomena of rupture and flow in solids. *Philosophical Transactions, Roy. Soc. London* A221, 163±198.
- Harris, J.A., Fay, P.A., 1992. Fatigue life evaluation of structural adhesives for automotive applications. *International journal of adhesion and adhesives* 12(1), 9-18.
- Hart-Smith, L.J., 1973. Adhesive-bonded double-lap joints. NASA, CR-112235.
- Hart-Smith, L.J., 1973. Adhesive-bonded single-lap joints. NASA, CR-112236.
- Irwin, G.R., 1957. Analysis of stresses and strains near the end of a crack traversing a plate. *Journal of Applied Mechanics* 24, 361–364.
- ISO 15024:2000(E), 2000. Standard test method for the mode I interlaminar fracture toughness, G_{IIC} , of unidirectional fibre-reinforced polymer matrix composites.
- John, S.J., Kinloch, A.J., and Matthews, F.L., 1991. Measuring and predicting the durability of bonded carbon fibre/epoxy composite joints. *Composites* 22(2), 121-127.
- Kinloch, A.J., 1980. The science of adhesion part 1 surface and interfacial aspects. *Journal of Material Science* 15, 2141-2166.
- Kinloch, A.J., 1982. The science of adhesion part 2 mechanics and mechanisms of failure.

Journal of Material Science 17, 617-651.

Tsai, M.Y., Oplinger, D.W., and Matthews, F.L., 1998. Improved theoretical solutions for adhesive lap joints. *International Journal of Solids and Structures* 35(12), 1163-1185.

Volkersen, O., 1938. Rivet strength distribution in tensile-stressed rivet joints with constant cross section. *Luftfahrtforsch* 15, 41-47.

Zhou, A.X., Keller, T., 2005. Joining techniques for fiber reinforced polymer composite bridge deck systems. *Composite structures* 69(3), 336-345.

2 PUBLICATIONS

This chapter presents a compilation of the publications resulting from this thesis. Each paper is preceded by an introductory summary and reference details.

2.1 Mechanical and fracture behavior of fracture joints under quasi-static loading

Summary

The linear-elastic fracture mechanics (LEFM) approach has been widely applied to fracture behavior modeling for fracture joints, which have the pure Mode I, II fracture and the combination of both with known fracture mode mixity. The crack length measurement techniques and the calculation methods of strain energy release rate have been standardized and included in testing standards and protocols. Nevertheless, fracture joints composed of pultruded GFRP laminates have large component dimensions on the full-scale structural level and asymmetric crack propagation in the laminates, thus imposing deviations from standardized conditions. The applicability of LEFM first needs to be validated for fracture joints before being applied to structural joints. Besides fracture behavior modeling, the critical strain energy release rates for pure Mode I and II fracture are calculated and can then be used for establishing the mixed mode fracture criterion (Section 2.3).

In this paper, an experimental investigation was performed to characterize and model the mechanical (Tasks 1.2-1.3 in Fig. 1) and fracture behavior (Task 2.1-2.4 in Fig. 1) of adhesively-bonded fracture joints composed of pultruded GFRP laminates (Task 2.1-2.4 in Fig. 1). Double-Cantilever-Beam (DCB) and End-Loaded-Split (ELS) specimens were employed for Mode I and II experiments respectively and the testing procedure was carried out in accordance with existing standards and protocols. In addition to visual observation, an

alternative crack length measurement technique, the video extensometer, was proposed. It provided accurate results especially for Mode II fracture, in which it is difficult to identify the crack tip. The values of the SERR were calculated using standardized analytical methods based on beam theory, the standardized experimental compliance method as well as 3D finite element models. Similar values were obtained from all of these methods, with the exception of Simple Beam Theory (SBT). The applicability of the existing standardized testing procedure and the fracture data interpretations based on LEFM was validated for pultruded GFRP fracture joints.

Reference details

This paper, "Mode I and II fracture behavior of adhesively-bonded pultruded composite joints" by Ye Zhang, Anastasios P. Vassilopoulos and Thomas Keller, was published in Engineering Fracture Mechanics 2009, in Press.

[doi:10.1016/j.engfracmech.2009.09.015](https://doi.org/10.1016/j.engfracmech.2009.09.015)

MODE I AND II FRACTURE BEHAVIOR OF ADHESIVELY-BONDED PULTRUDED COMPOSITE JOINTS

Ye Zhang, Anastasios P. Vassilopoulos and Thomas Keller

Composite Construction Laboratory (CCLab),
Ecole Polytechnique Fédérale de Lausanne, (EPFL),
Station 16, Bâtiment BP, CH-1015 Lausanne, Switzerland

ABSTRACT

The Mode I and II fracture behaviors of adhesively-bonded joints composed of pultruded glass fiber-reinforced polymer (GFRP) laminates were experimentally investigated using Double-Cantilever-Beam (DCB) and End-Loaded-Split (ELS) specimens. The large specimen dimensions on the full-scale level and asymmetric crack propagation in the laminates imposed deviations from the standardized specimens. For crack length measurement, in addition to visual observation, a video extensometer was used. Similar strain energy release rate values were obtained from all standardized methods as well as from 3D finite element models, with the exception of simple beam theory. The applicability of existing standards for interpretation of the fracture data for the fracture mechanics joints used was proved.

KEYWORDS

Polymer matrix composites, Fracture mechanics, Crack growth, Civil engineering structures, Bonded joints.

Nomenclature

a	crack length
a_0	initial crack length
a_c	corrected crack length
B	specimen width
C	specimen compliance
C_0	specimen compliance before crack initiation
D	distance between dots marked on ELS specimens
E_s	tensile modulus or flexural modulus of adherend
E_f	back-calculated tensile modulus or flexural modulus of adherend
F	correction factor for large displacement
F_x, F_y	nodal force at crack tip
G	strain energy release rate
G_c	critical strain energy release rate
G_I	strain energy release rate for Mode I
G_{II}	strain energy release rate for Mode II
G_{Ic}	critical strain energy release rate for Mode I
G_{IIc}	critical strain energy release rate for Mode II
h	half specimen thickness
L	free length
m	slope of a plot $(BC)^{1/3}$ vs. $a/2h$ (determined from Mode I experiment)
m	slope of a plot C vs. a^3 (determined from Mode II experiment)
m^*	slope of a plot C vs. a^3 (determined from Mode II experiment)
N	correction factor for loading blocks
n	power fitting parameter of C versus a
P	applied load
P_{max}	maximum applied load
u_x, u_y	nodal displacement adjacent to crack tip
Δa	crack increment in finite element analysis
Δ_{clamp}	correction for clamp length (determined from Mode II experiment)
ΔI	crack length correction (determined from Mode I experiment)
ΔII	crack length correction (determined from Mode II experiment)
δ	displacement of the cross-head of testing machine
4ENF	4-Point End-Notched-Flexure
C105	onset of 5%-compliance increase
CBT	Corrected Beam Theory
CBTE	Corrected Beam Theory with Effective crack length
CCM	Compliance Calibration Method
CFRP	Carbon Fiber-Reinforced Polymer
DCB	Double-Cantilever-Beam
ECM	Experimental Compliance Method
ELS	End-Loaded-Split
FEA	Finite Element Analysis
GFRP	Glass Fiber-Reinforced Polymer

MAX	onset of maximum load on the load-displacement curve
MCC	Modified Compliance Calibration
MMB	Mixed-Mode-Bending
NL	onset of the derivation from linear load-displacement response
SERR	Strain Energy Release Rate
SBT	Simply Beam Theory
TDCB	Tapered Double-Cantilever-Beam
VCCT	Virtual Crack Closure Technique
VIS	onset of the visual observation of crack initiation

1 INTRODUCTION

Only a limited number of standards and testing protocols exist for the fracture mechanics testing of composite materials and joints [1-6]. They concern either the fracture of the adhesives in joints [1-2], or determination of the interlaminar fracture toughness of unidirectional composite laminates in the case of Mode I, Mode II or mixed-mode fracture [3-6], see Table 1. Depending on the examined fracture mode, different specimen types are proposed, and different methods are adopted for calculation of the strain energy release rate (SERR), see Table 1. For Mode I, Double-Cantilever-Beam (DCB) and Tapered-DCB (TDCB) specimens are employed, Mixed-Mode-Bending (MMB) specimens are proposed for mixed-mode fracture [5], while End-Loaded-Split (ELS) or 4-Point End-Notched-Flexure (4ENF) specimens are used for Mode II fracture [6]. The use of a traveling microscope is suggested for Mode II [6], since it is difficult to measure crack length purely on the basis of visual observation.

Basically four methods are used for calculation of the Mode I and II SERR: the Simple Beam Theory (SBT), the Corrected Beam Theory (CBT), the Experimental Compliance Method (ECM) and the Modified Compliance Calibration (MCC), see Table 1. For 4ENF specimens (Mode II), the Compliance Calibration Method (CCM) is proposed instead of the aforementioned methods. Irrespective of the calculation method used, SERR values are usually plotted against the corresponding crack lengths to form a resistance curve (R-curve). The ideal R-curve presents an initially increasing SERR before reaching a plateau, although its shape is strongly dependent on the material and joint configuration [7]. If large-scale fiber bridging occurs as mentioned in [8], that is, if the bridging length is comparable to or exceeds a specimen dimension, the R-curve behavior may depend on specimen dimensions. Since the use of materials other than standardized laminates may cause doubt regarding the applicability of data reduction schemes based on linear-elastic fracture mechanics, an objectives of several studies was the validation of standard procedures for calculation of the Mode I [9-16] and Mode II [17-21] SERR for specific non-standardized materials and joints, as summarized in Tables 2 and 3.

Independent of fracture mode, the SERRs for crack initiation and crack propagation are defined on the basis of the load-displacement curve and resulting R-curve. Three different SERR values can be assigned to crack initiation: a) the non-linear (NL) value, corresponding to the critical load and displacement associated with the deviation from linear response, b) the

visual (VIS) value derived from visual observation of crack initiation and c) the maximum (MAX) value or 5%-compliance increase (C105) value, corresponding to the maximum load reached or the load that causes a 5% increase in compliance, whichever occurs first. In reality, however, it is not always possible to determine all these values, see Tables 2 and 3. The derivation of all three values for crack initiation was not possible in [9-11, 13, 14, 17-19]. The VIS value was therefore attributed to the first measurable crack length in [11, 13, 18] and assumed as being the critical SERR, G_c , for initiation.

The determination of the critical SERR for crack propagation is based on the R-curve and is more difficult since an ideal plateau region is often not observed. Depending on the form of the R-curve, different values were selected to represent the critical SERR for crack propagation, see Tables 2 and 3. The mean value of the plateau-like region [9-12, 14, 15, 19, 20], or the mean value of all data points corresponding to crack propagation [17, 18, 21] were selected.

Table 1. Standards and protocols for Mode I, Mode II and mixed-mode fracture.

Standards and protocols	Fracture	Specimen type	G calculation method	Fitting range
ASTM D3433 – 99 (2005) [1]	Mode I	Joint: DCB, TDCB	SBT	—
ESIS TC4 Protocol (2000) [2]	Mode I	Joint: DCB, TDCB	SBT, CBT, ECM	Only propagation
ASTM D5528 – 01 (2007) [3]	Mode I	Laminate: DCB	CBT, ECM, MCC	VIS + propagation
ISO 15024:2000(E) [4]	Mode I	Laminate: DCB	CBT, MCC	VIS + propagation
ASTM D6671/D6671M-06 (2006) [5]	Mixed	Laminate: MMB	SBT	—
ESIS TC4 Protocol (2006) [6]	Mode II	Laminate: ELS, NF	CBT, ECM, CCM	VIS + propagation or only propagation

Table 2. Determination of G for crack initiation and propagation for Mode I fracture.

Reference	Specimen	Material (adhesive)	Method	Choice of G_{IC} for initiation	Choice of G_{IC} for propagation
[9]	Joint: DCB	CFRP (epoxy)	SBT	—	Mean of visually determined plateau
[10]	Joint: DCB	CFRP (epoxy)	SBT, CBT	—	Mean of visually determined plateau
[11]	Laminate: DCB	E-glass/vinylester	CBT (designated MBT), ECM (designated CC)	VIS	Mean of visually determined plateau (> 20 -mm crack length)
[12]	Joint: DCB, TDCB	Metal (epoxy)	SBT, CBT, ECM	NL, VIS, MAX/5%	Mean of visually determined plateau
[13]	Laminate: DCB	E-glass/polyester	SBT, ECM	VIS	—
[14]	Laminate: DCB	Twintex	CBT	—	Mean of visually determined plateau (but no value provided)
[15]	Laminate: DCB	E-glass/polyester	CBT (designated MBT), ECM (designated CC), MCC	NL, VIS, MAX/5%	Mean of visually determined plateau
[16]	Laminate: DCB	CFRP, GFRP	CBT	VIS, MAX/5%	—

Table 3. Determination of G for crack initiation and propagation for Mode II fracture.

Reference	Specimen	Material (adhesive)	Method	Choice of G_{IIc} for initiation	Choice of G_{IIc} for propagation
[17]	Laminate: 3ENF	Graphite/epoxy	SBT	—	Mean of all points corresponding to propagation
[18]	Joint: 4ENF	CFRP (epoxy)	SBT, FEA	VIS	Mean of all points corresponding to propagation
[19]	Laminate: ELS SLB (single-leg bending)	GFRP/polyester	SBT, CBT, FEA	—	Mean of visually determined plateau
[20]	Joint: ELS	CFRP (epoxy)	SBT, CBT, ECM	NL, VIS, MAX / C105	Mean of visually determined plateau (75-100-mm crack length)
[21]	Joint: ELS	CFRP (epoxy)	SBT, CBT, ECM	NL, VIS, MAX / C105	Mean of all points corresponding to propagation

Previous studies conducted for the aerospace or automotive industries mainly focused on the delamination resistance of carbon fiber-reinforced polymer (CFRP) laminates and/or the fracture behavior of joints according to available standards. However, in civil engineering structures, joint dimensions are significantly larger mainly due to the pultruded structural glass fiber-reinforced polymer (GFRP) adherends of thicknesses above 5 mm and adhesive layer thicknesses of between 1-3 mm to compensate for tolerances. Furthermore, fiber-tear failure, which is the most common failure mode for these joints, occurs in the GFRP adherends in a plane away from the joint symmetry axis [22]. Such asymmetry was found to introduce a Mode II component in Mode I fracture in [7]. Due to these deviations from standardized specimens, validation of the steps involved in the calculation of the SERR for the material and joint configuration examined here is necessary before fracture mechanics is applied in this field of engineering.

In the present work, adhesively-bonded pultruded GFRP fracture mechanics joints (DCB and ELS) were examined to obtain fracture mechanics data. Specimen configuration, experimental setup and procedures for calculation of the SERR were chosen to correspond with existing standards as far as possible. An alternative video extensometer method was used for the measurement of crack length. The SERR was calculated based on all the available standard methods. Additionally, 3D finite element models were developed for the numerical derivation of the Mode I and Mode II SERR. The theoretical results were compared to the corresponding experimental data to evaluate the applicability of the available methods to the new fracture mechanics joints.

2 THEORETICAL BACKGROUND

The methods and equations used in the present work for the analysis of the fracture mechanics data from the investigated DCB and ELS specimens are summarized in this section. In linear elastic fracture mechanics (LEFM), the SERR is directly derived from Eq.(1):

$$G = \frac{P^2}{2B} \frac{dC}{da} \quad (1)$$

where B is the specimen width, a the crack length obtained with the applied load P and corresponding displacement δ , and C the specimen compliance. Standard methods for the SERR calculation are based on this equation, the difference between them basically being the

way in which the derivative dC/da is obtained.

SBT was developed based on the shear-corrected beam analysis as presented in [23] and incorporated into ASTM D3433 [1]. The closed-form solution of the compliance is expressed as:

$$C = \frac{8a}{E_s B h^2} (a^2 + h^2) \quad (2)$$

where $2h$ is the thickness of the joint specimen, and E_s is the axial tensile Young's modulus or flexural modulus of the adherend. Since the pultruded GFRP adherends used are non-homogeneous and their flexural modulus differs significantly from the tensile modulus (14.2 GPa derived from 4-point bending vs. 31.4 GPa derived from tensile tests), the flexural modulus was used. By substituting the derivative, dC/da , in Eq.(1), the Mode I fracture energy, G_I , is calculated as:

$$G_I = \frac{4P^2}{E_s B^2} \left(\frac{3a^2}{h^3} + \frac{1}{h} \right) \quad (3)$$

As experimental efforts have demonstrated that SBT may lead to erroneous results, CBT was introduced [24]. In CBT, three correction factors take the following effects into account in the calculation of the SERR: the root rotation (factor Δ_I), the stiffening of the loading blocks (factor N), and the moments resulting from large displacements (factor F) [24]. The procedures for the estimation of these factors according to [2, 3] were applied and the compliance and Mode I SERR were calculated based on:

$$C = \frac{8}{E_s B h^2} (a + |\Delta_I|)^3 \quad (4)$$

$$G_I = \frac{3P\delta}{2B(a + |\Delta_I|)} \frac{F}{N} \quad (5)$$

The stiffness of the adherends was cross-checked (back-calculated) as follows [12]:

$$E_f = \frac{8(a + |\Delta_I|)^3}{(C/N) B h^3} \quad (6)$$

Experimental results showed that the back-calculated value of E_f is slightly higher than the measured value [12, 16]. However, large deviations may indicate erroneous results.

In ECM, the measured compliance ($C=\delta/P$) is usually fitted to the measured crack length by a power-law equation of the form: $C=k a^n$, and the SERR is calculated as:

$$G_I = \frac{nP\delta}{2Ba} \quad (7)$$

Correction factors F and N , which can be applied (as in Eq. (5)), were not used.

The MCC method differs from ECM only in the fitting of the compliance against the crack length, which is normalized by the specimen thickness ($2h$) in this case to exclude its effect on the SERR [4, 7]:

$$G_I = \frac{3m}{2(2h)} \left(\frac{P}{B}\right)^2 \left(\frac{BC}{N}\right)^{2/3} F \quad (8)$$

where m is the slope of the straight line calculated after fitting $(BC)^{1/3}$ against $a/2h$.

SBT and CBT are based on an analytical calculation of the compliance (Eqs. (2, 4)), while results from ECM and MCC depend on the quality of the fitting of the measured compliance (Eqs. (7, 8)). However, similar results are expected from CBT and MCC since the correction factor Δ_I in CBT (Eq. (5)) and the exponent m in MCC (Eq. (8)) are obtained by fitting $(C)^{1/3}$ against the crack lengths, a and $a/2h$ respectively. MCC is therefore not considered in [2] for Mode I fracture. In the present work, however, both methods were applied.

The SBT, CBT and ECM procedures were also used for calculation of the Mode II fracture energy, G_{II} . For an ELS specimen, the compliance based on the SBT is calculated as:

$$C = \frac{3a^3 + L^3}{2Bh^3E_s} \quad (9)$$

and the derived equation for the SERR is then:

$$G_{II} = \frac{9P^2a^2}{4B^2h^3E_s} \quad (10)$$

where L is the free length.

Similarly to Mode I, more accurate results are obtained from CBT with a corrected crack length being calculated as $a_c = a + \Delta_{II}$. If Δ_I is available (which is the case here), the correction factor Δ_{II} can be assumed as being equal to $0.42\Delta_I$ [25] and the compliance is calculated as:

$$C = \frac{3(a + \Delta_{II})^3 + (L + 2\Delta_I)^3}{2Bh^3E_s} \quad (11)$$

By incorporating dC/da into Eq. (1), G_{II} is calculated as:

$$G_{II} = \frac{9P^2a_c^2}{4B^2h^3E_s} = \frac{9P^2(a + \Delta_{II})^2}{4B^2h^3E_s} \quad (12)$$

If no information is available concerning Δ_I , an alternative process for calculation of the

corrected crack length can be used [26]. The pre-cracked part of the ELS specimen is clamped and a load applied to the free end. The compliance of the specimen is measured for different free lengths and its cubic root, $(C)^{1/3}$, is fitted against the free length, L , by a straight line. The intersection of this line with the abscissa (x-axis) is designated Δ_{clamp} . The corrected crack length can then be calculated as:

$$a_c = a + \Delta_{II} = \left(\frac{1}{3} \left(\frac{2Bh^3 E_s C}{N} - (L + \Delta_{clamp})^3 \right) \right)^{1/3} \quad (13)$$

CBT of this type is referred to as Corrected Beam Theory with Effective crack length (CBTE) [26] and is independent of crack length, which is often difficult to measure. According to CBTE, the compliance can be calculated using Eq. (11) if parameter Δ_I is replaced by $\Delta_{clamp}/2$.

ECM can be applied for either the measured or the corrected crack length. It is assumed that the compliance of the specimen is a linear function of a^3 or a_c^3 [20]:

$$C = C_0 + ma^3, \text{ or } C = C_0 + m^* a_c^3 \quad (14)$$

where C_0 is the compliance of the specimen before crack initiation and m and m^* are the slopes of the lines that fit the measured compliance against the measured and corrected crack lengths respectively. This approach leads to:

$$G_{II} = \frac{3P^2 ma^2}{2B} \text{ or } G_{II} = \frac{3P^2 m^* a_c^2}{2B} \quad (15)$$

Fitting C against a^3 makes ECM equivalent to MCC for Mode II. Therefore, MCC is not referred to in any standards or protocols for Mode II and was not applied here.

Finite element analysis has also been used to calculate the SERR [27, 28]. The virtual crack closure technique (VCCT) applied here relies on the accurate numerical calculation of the nodal forces at the crack tip (F_{xi} and F_{yi}) and the displacements of the adjacent nodes j and k , as shown in Fig. 1 for a 2-dimensional (2D) model. G_I and G_{II} are then calculated as:

$$G_I = \frac{1}{2\Delta a} [F_{yi}(u_{yj} - u_{yk})] \quad (16)$$

$$G_{II} = \frac{1}{2\Delta a} [F_{xi}(u_{xj} - u_{xk})] \quad (17)$$

where Δa is the increment of the crack which is equal to the element size at the crack tip. In the case of a 3D model, the calculated G_I and G_{II} over the nodes through the width of the specimen are summed to calculate the SERR for the crack opening.

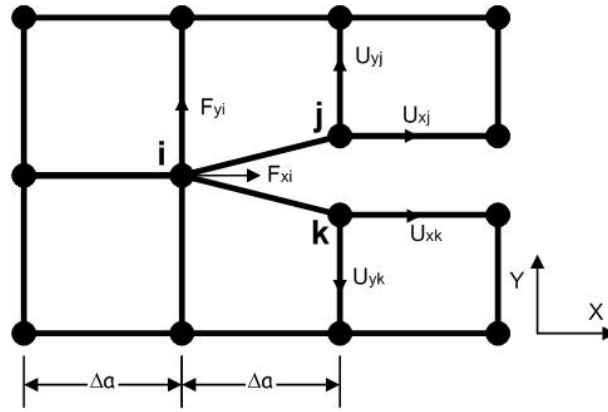


Figure 1. Nodes at crack tip for VCCT in 2D finite element model.

3D finite element models were established for the DCB and ELS specimens using the software ANSYS (v. 10). In order to allow crack propagation inside the adherends (as observed during the experiments), the GFRP laminate was modeled as a layered solid, considering the roving, mat and veil layers of each laminate (see Section 3 for laminate composition). The mechanical properties of each layer were calculated based on the fiber volume fraction and estimated layer thickness. A typical crack, as schematically illustrated in Fig. 1, was introduced in the FEA models between the outer layers of the adherend where crack propagation was observed. The element type SOLID45 was used and, based on a parametric study, a mesh size of 5 mm for the crack increment (Δa) was selected for both joint types. In order to avoid the mutual penetration of the adherends in Mode II fracture, the correlated contact (CONTA174) and target (TARGE170) elements were employed for the two crack surfaces. The DCB model comprised 3250 elements and the ELS model 5520 elements. The boundary conditions of the testing configuration were simulated. A line load across the width was applied on the top of the upper adherend of both joint types. Experimental load values corresponding to arbitrarily selected crack lengths were used as input for calculation of the corresponding nodal displacements and forces.

3 EXPERIMENTAL SETUP

DCB and ELS specimens composed of pultruded GFRP laminates bonded by an epoxy adhesive system were manufactured. The pultruded GFRP laminates (supplied by Fiberline A/S, Denmark) consisted of E-glass fibers embedded in an isophthalic polyester resin and had a width of 50 mm and thickness of 6 mm. The GFRP laminate comprised a roving layer in the

middle with mat layers on each side, which consisted of a chopped strand mat (CSM) and a $0^\circ/90^\circ$ woven mat stitched together. Below the surface, a polyester veil (40 g/m²) had been added to protect against an aggressive environment. The fiber content was 48.5 vol.-% or 69.4 weight-%. The mean tensile strength of the laminates was 283 MPa, the Young's modulus 31.4 GPa, and the flexural modulus 14.2 GPa. The mean tensile strength of the epoxy adhesive (SikaDur 330, Sika AG Switzerland) was 38.1 MPa, and the Young's modulus 4.6 GPa.

The total lengths of the DCB and ELS specimens were 250 mm and 400 mm respectively, see Figs. 2 and 3. All bonded surfaces were mechanically abraded with sandpaper (grit class P80) using a grinder and then chemically degreased using acetone. A special aluminum frame was designed to ensure a constant adhesive thickness of 2 mm and good alignment of the laminates. All specimens, 5 DCBs and 5 ELSs, were cured under ambient laboratory conditions (approx. 23°C and 50% RH) for ten days.

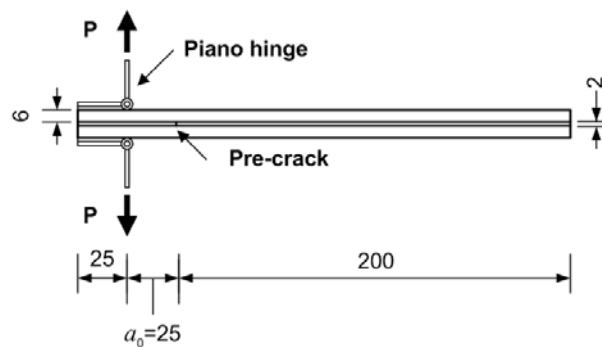


Figure 2. Geometrical configuration for DCB (dimensions in [mm]).

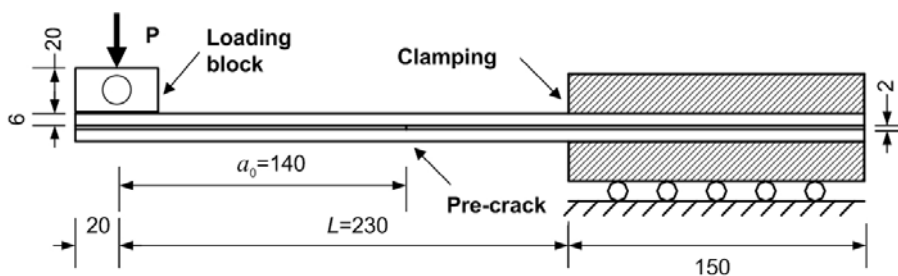


Figure 3. Geometrical configuration for ELS (dimensions in [mm]).

A pair of steel piano-hinged loading blocks was bonded to the DCB specimens with a 0.5-mm-thick layer of the same adhesive as that used for the specimens, see Figs. 2 and 4. A 25-mm pre-crack, a_0 , as measured from the loading axis, was created during specimen

fabrication by inserting a 50-mm-long Teflon film of 0.05-mm thickness between the lower GFRP laminate and the adhesive layer. Mode I tests were performed on a 5-kN testing rig under displacement control at a constant rate of 1 mm/min. Load, displacement and crack length were recorded.

The experimental setup for Mode II is shown in Figs. 3 and 5. The 150-mm-long end part of the ELS specimens was clamped, allowing horizontal movement of the system during loading. A 40-mm-long loading block was bonded onto the upper surface by means of a 0.5-mm-thick adhesive layer. The free length, from the clamping edge to the loading axis, was 230 mm. A pre-crack of 140 mm length (designated a_0 in Fig.3) was created during specimen fabrication by inserting a 160-mm-long Teflon layer between the lower laminate and the adhesive. The experiments were carried out under displacement control at a loading rate of 1 mm/min. Load, displacement and crack length were recorded.

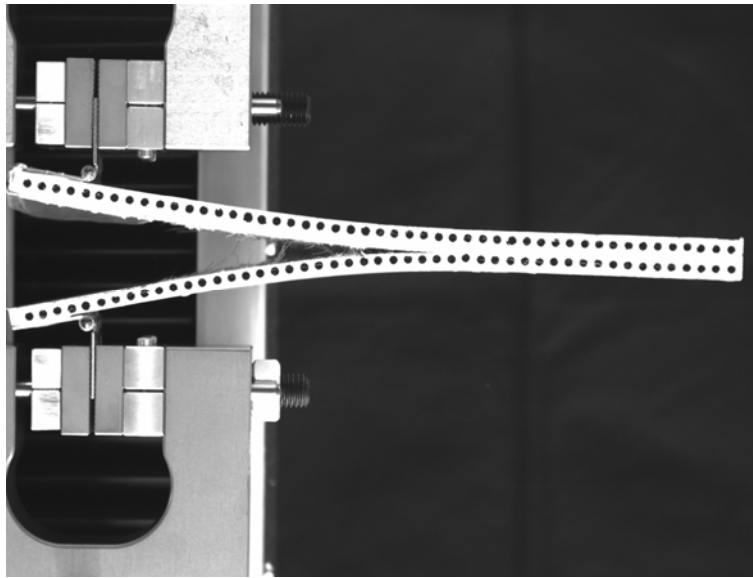


Figure 4. Experimental setup for Mode I fracture (DCB03).

Two methods were used to measure the crack length: visual observation and a video extensometer. For the former, vertical lines were drawn at 5-mm intervals on the lateral surface of the specimen, which were intersected by the propagating crack and, thus allowing the crack length to be recorded. For the video extensometer method, pairs of black dots were marked at equal intervals on the lateral surface of the specimen, see Fig 4. The displacement of these dots was recorded with a frequency of 1 Hz by a camera. Simple processing of the

recorded data provided the estimation of the crack length as a function of load and displacement. The video extensometer was employed for three DCB (DCB03-05) and three ELS (ELS03-05) joints while visual observation was used for the remaining two DCB (DCB01-02) and all ELS (ELS01-05) specimens. For technical reasons, it was not possible to use both methods together for the DCB specimens.

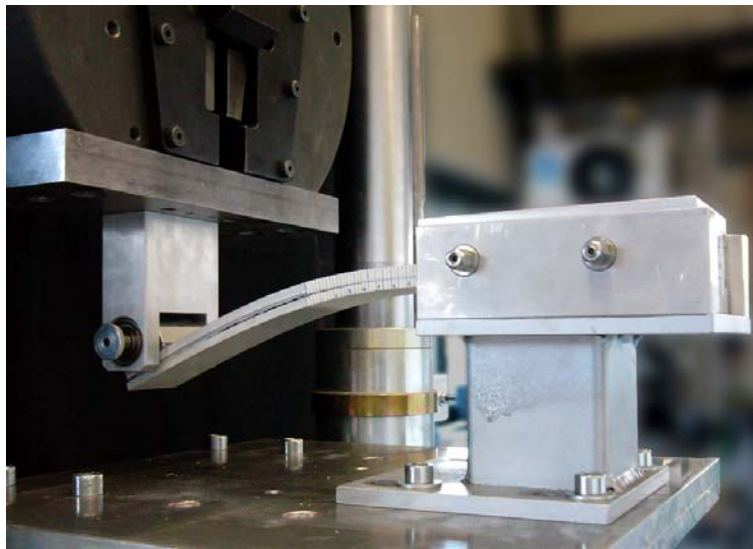


Figure 5. Experimental setup for Mode II fracture (ELS03).

4 EXPERIMENTAL RESULTS

4.1 Failure modes

In Mode I fracture, the dominant failure was a fiber-tear failure in the mat layer of the GFRP laminates, as shown in Fig. 6. According to results presented in [29], fiber-tear failure in pultruded GFRP profiles occurs because the through-thickness tensile strength of the laminate is lower than that of the adhesive-laminate interface. As a result, the crack-bridging fibers of the woven or random chopped mat layer were pulled out of the polyester matrix.

The same failure mode was observed in most of the Mode II tests (ELS02, ELS03 and ELS05), see Fig. 7. The crack initiated and propagated in the mat layer of the GFRP laminate almost up to the clamping region. In specimens ELS01 and ELS04, however, the crack, after initiating in the mat layer, propagated deeper into the roving layer, as shown in Fig. 8. In view of this different failure mode, the results of these specimens were taken into account only for crack initiation.

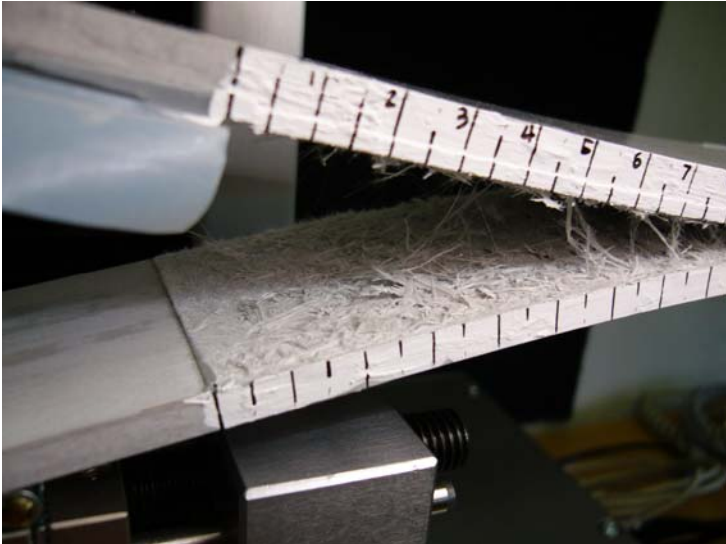


Figure 6. Failure mode of DCB01.

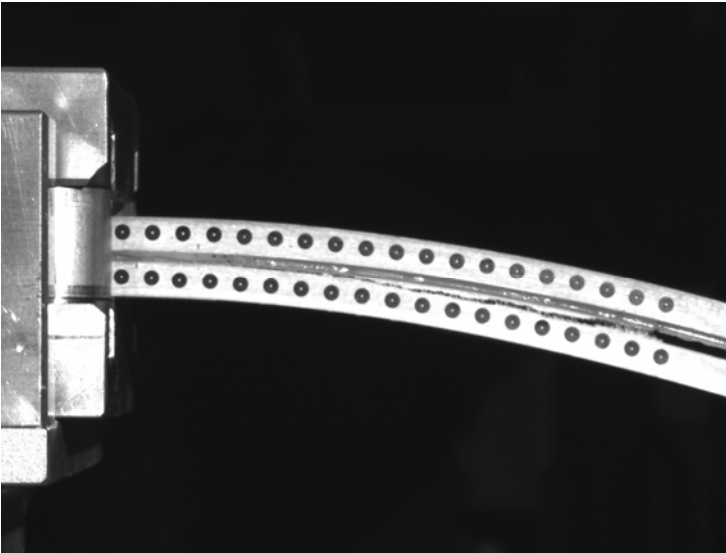


Figure 7. Failure mode of ELS03 (crack in mat layer).



Figure 8. Failure mode of ELS01 (crack in roving layer).

4.2 Load-displacement response

The load-displacement response of the DCB specimens is shown in Fig. 9. The loading was manually stopped when the crack length reached 150 mm. All curves followed a linearly increasing trend up to the maximum load and then decreased. The effect of fiber-bridging was expressed by a saw pattern of the descending branch. The alternating increasing and decreasing segments of this pattern corresponded to alternating phases of crack initiation and crack arrest. There was one exception (DCB04) where a sudden drop in load occurred when the displacement reached approximately 13 mm, after which the crack propagated through the adhesive layer. Measurements for DCB04 after this 13-mm displacement were not taken into account in the subsequent calculations.

The load-displacement response of the ELS specimens is shown in Fig. 10. For specimens ELS02/03/05, where the crack path remained in the mat layer, the response exhibited an almost linearly increasing trend until the maximum load was reached. During crack propagation, the load fluctuated around 550 N and then increased again for displacements of more than 55-60 mm because the crack tip approached the fixed end. Specimens ELS01/04 followed the same load-displacement trend as long as the crack was short and not propagating in the roving layer (up to a displacement of approximately 30 mm). During crack propagation in the roving layer, the load increased again.

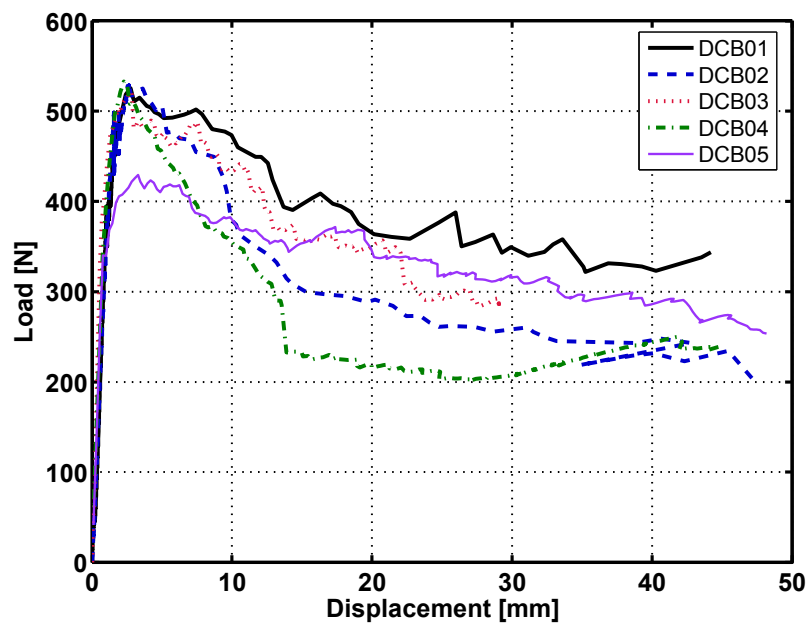


Figure 9. Load-displacement response of DCB specimens.

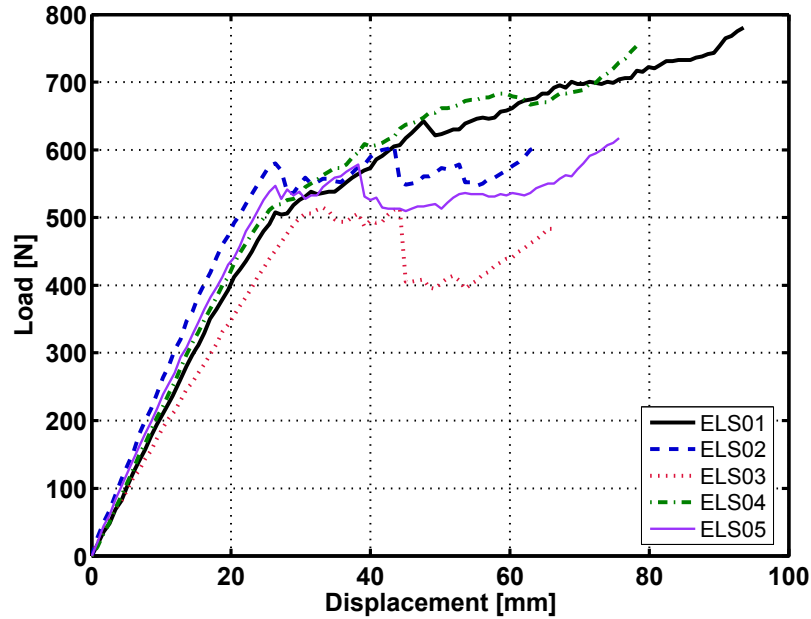


Figure 10. Load-displacement response of ELS specimens.

4.3 Crack length measurements

The crack length measurements obtained from visual observation and the video extensometer could be directly compared on ELS specimens ELS03-05. Almost identical results were obtained from both methods, as shown in Fig. 11 for ELS04. The DCB specimens also exhibited similar crack length vs. displacement curves, although the methods were applied separately during different tests. These results proved that the video extensometer technique and visual observation can be used with equal accuracy for Mode I and Mode II testing.

For Mode II fracture, a corrected crack length was obtained from Eq.(13). Inversed ELS tests were performed for ten different free lengths, ranging from 60 mm to 185 mm. The values obtained for Δ_{clamp} are summarized in Table 4. The mean value of five specimens was 35.1 mm with a standard deviation of 15%. Typical corrected crack measurements are shown in Fig. 11 for specimen ELS04 and demonstrate that CBTE is appropriate for the modeling of crack propagation only for the type of specimen used here. A correction of the measured crack length of between 5 and 20 mm was estimated. Concerning crack initiation, in most cases crack lengths less than that of the pre-crack (140 mm) were obtained. In the crack initiation range, the value of the corrected crack length, a_c in Eq.(13), was found to be very sensitive to the specimen half-thickness, h , where the crack propagates in standard specimens. In the

present case, however, specimen separation was asymmetric, exhibiting ratios of 0.65-0.75 between the remaining thicknesses of the two separated beams

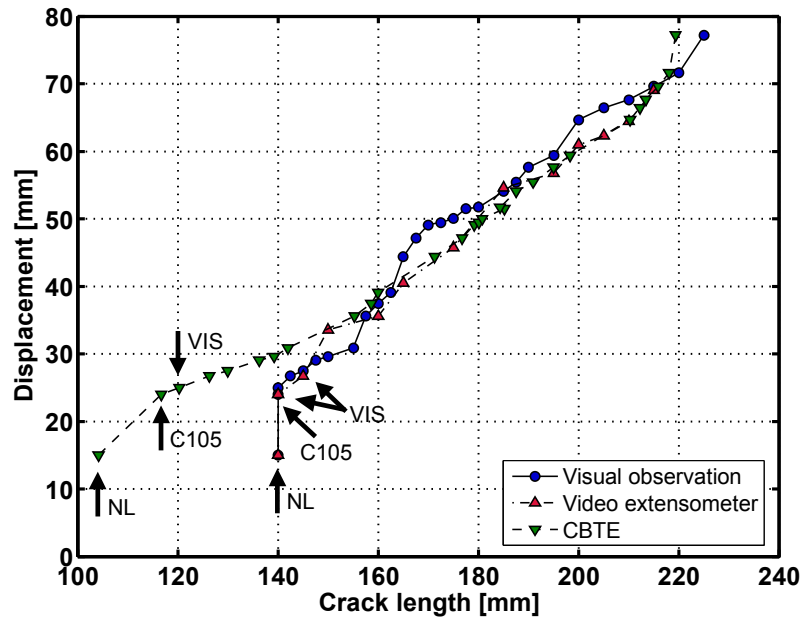


Figure 11. Comparison of crack length obtained from different methods for ELS04.

Table 4. Values of correction factors Δl and Δl_{clamp} and back-calculated flexural modulus E_f .

Specimen number	DCB		ELS
	Δl [mm]	E_f [GPa]	Δl_{clamp} [mm]
	Eqs. (4-6)	Eq.(6)	Eq. (13)
1	25.7	23.2	29.3
2	15.2	14.3	43.3
3	19.8	16.2	32.3
4	10.9	12.4	37.3
5	15.6	14.2	33.5
Mean	17.4 ± 5.6	16.1 ± 4.2	35.1 ± 5.4

4.4 Effect of specimen asymmetry on fracture mode

The crack location was approximately 1.5 mm below the symmetry axis of the 14-mm-thick specimen (0.5 mm inside the adherend). The effect of this asymmetry on the fracture modes was qualitatively and quantitatively examined by using the video extensometer and FEA

results for both failure modes.

The through-thickness relative displacement between the two beams of the joint is related to crack opening, i.e. to the Mode I fracture component, while the in-plane relative displacement or sliding is related to the Mode II fracture component. As shown in Fig. 12 for a representative DCB specimen, the change in the relative in-plane displacement (up to 0.5 mm) was much smaller than the displacement increase in the through-thickness direction (up to 40 mm). Therefore, the Mode II fracture component can be considered negligible for DCB specimens.

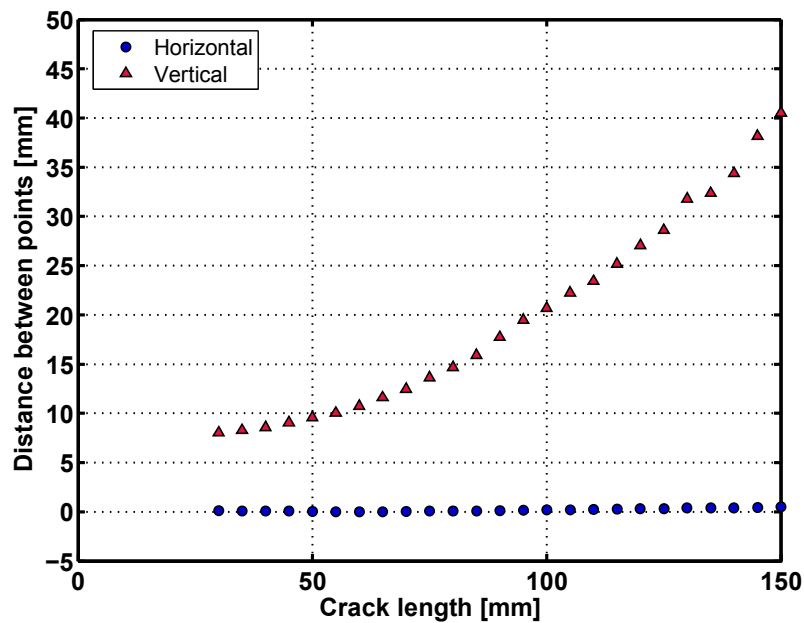


Figure 12. Fracture mode components of DCB03 from video extensometer.

Concerning Mode II, distances d_1 and d_2 between two adjacent pairs of dots were measured, see Fig. 13. Their difference ($d_1 - d_2$) remained constant during crack propagation, indicating that no relative through-thickness displacement occurred between the two adjacent dots. The increase of the absolute distances d_1 and d_2 results from the sliding component. Accordingly, the Mode I fracture component can be disregarded for ELS specimens. FEA results based on Eqs. (16) and (17) confirmed these results. The G_{II} component for the DCB specimens and the G_I component for the ELS specimens were found to be less than 1%. This result, however, is in contradiction to the results in [7] for the delamination of thin glass/epoxy laminates. For a thickness ratio of 0.78 of the two beams of an asymmetric DCB specimen, the G_{II} component,

estimated from FEA analysis, was approximately 8% of G_I . However, as pointed out in [7], the results are strongly dependent on the examined material.

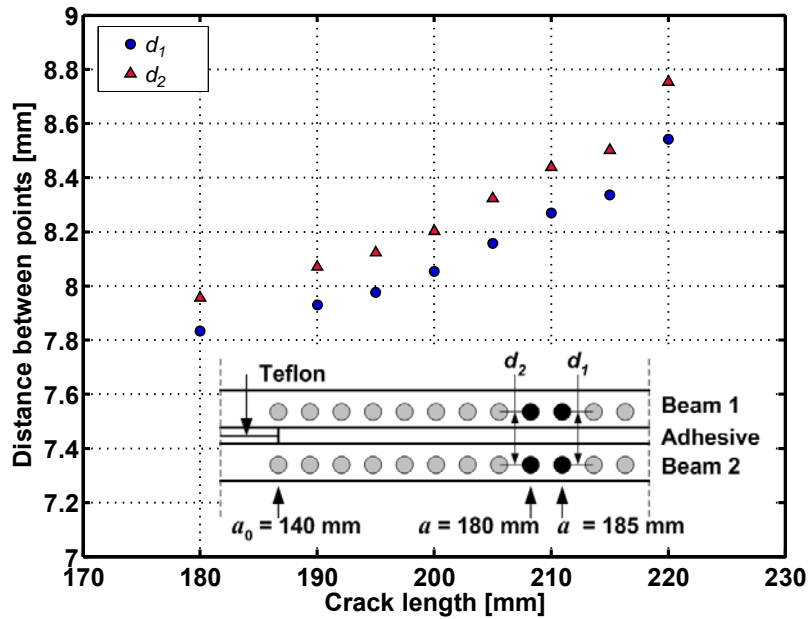


Figure 13. Fracture mode components of ELS03 from video extensometer.

5 EXPERIMENTAL DATA REDUCTION

5.1 Identification of crack initiation and propagation

Typical load displacement curves for DCB and ELS specimens are shown in Fig. 14. The loads corresponding to crack initiation (NL, VIS, C105 and Max) are shown in Table 5. The NL and C105 values were directly derived from the load-displacement response, which was linear up to approximately 60% of the maximum load P_{max} . The C105 value was obtained at approximately 65% of P_{max} for Mode I and 90% of P_{max} for Mode II. C105 values were always lower than P_{max} and were therefore used for the calculation of G_c . VIS values, corresponding to the first measurable crack length (either by visual observation or video extensometer), were always higher than NL and C105 values and reached approximately 95% of P_{max} for both fracture modes. These results indicate that even very short and visually undetectable cracks can affect specimen stiffness. Values higher than the VIS values were attributed to crack propagation. For both Mode I and Mode II fractures, good correlation between the results for all specimens was observed with the highest standard deviation being of the order of 15%.

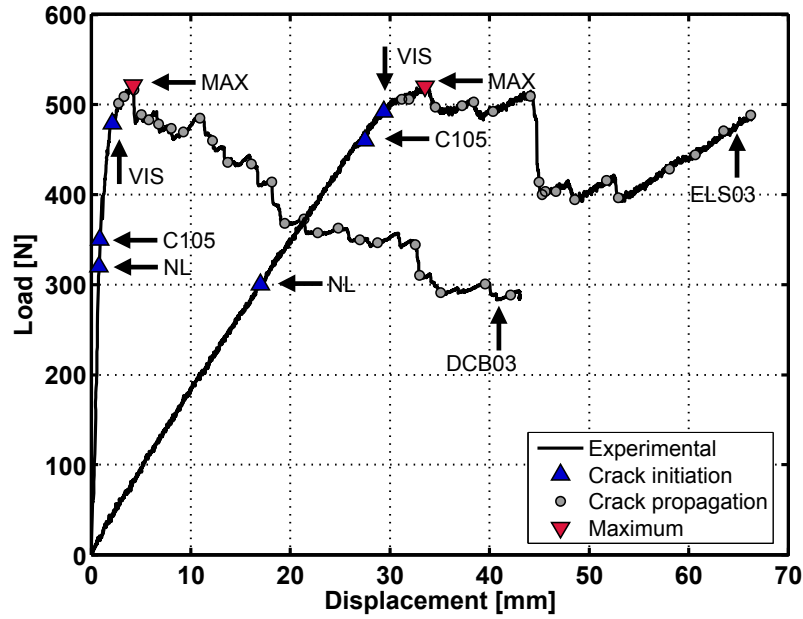


Figure 14. Load-displacement response of DCB03/ELS03 with indicated crack initiation (from different methods) and propagation.

Table 5. Comparison of mean loads corresponding to NL, C105, VIS and MAX for DCB and ELS tests (mean values and standard deviation for five specimens).

Load [N] at	DCB	ELS
NL	327.0 ± 36.2	354.0 ± 57.6
C105	405.0 ± 60.0	493.0 ± 24.1
VIS	501.0 ± 33.9^1	523.1 ± 34.5^1
	462.4 ± 65.0^2	511.8 ± 17.8^2
MAX	505.1 ± 42.9	559.7 ± 34.2^3

¹ visual observation

² video extensometer

³ based on specimens (ELS02, 03, 05)

5.2 Calculation of compliance

The analytically and numerically calculated values for compliance from Eqs (2, 4, 9, 11, 14) were compared to the experimentally derived values for both Mode I and Mode II experiments. Typical results are shown in Figs. 15-16 for Mode I and II respectively. Compliance increases with increasing crack length. However, a different trend is exhibited in

the two fracture modes. During Mode I fracture, the compliance increase accelerates with crack opening, whereas in Mode II the trend is linear up to failure. A comparison of the applied theoretical methods shows that ECM and MCC always provided the most accurate results, since these methods are based on the experimentally derived compliance. SBT always underestimated the measured values owing to the deficiencies of this method referred to above. The 3D FEA results were accurate for Mode I fracture, but underestimated the results for Mode II, especially short crack lengths. For Mode II fracture (see Fig. 16), the values obtained from CBTE did not compare well to the experimental results because of the inaccurate crack length calculation by CBTE.

For Mode I fracture, Δ_l values for correction of the measured crack length and the back-calculated stiffness E_f are summarized in Table 4. In accordance with [12, 16], a slightly higher value of E_f was observed when compared to the independently measured bending stiffness, E_s , (16.1 vs. 14.2 GPa). Furthermore, higher values of Δ_l were estimated for stiffer specimens. Table 4 further shows that $\Delta_{clamp} \approx 2\Delta_l$ (for mean values over five specimens). Although CBTE is based on this relationship, it was not always attained due to the different clamping conditions used for DCB and ELS specimens [19]. The correction factor for the measured crack length in CBT, $\Delta_{II} = 0.42\Delta_l$, was calculated using the mean value of Δ_l in Table 4.

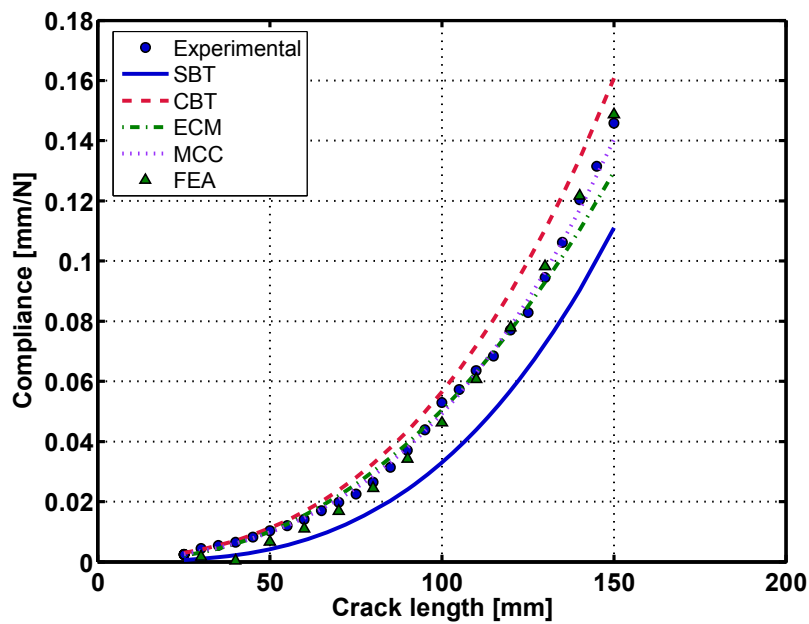


Figure 15. Comparison between calculated compliance (from different methods) and experimental values for DCB03.

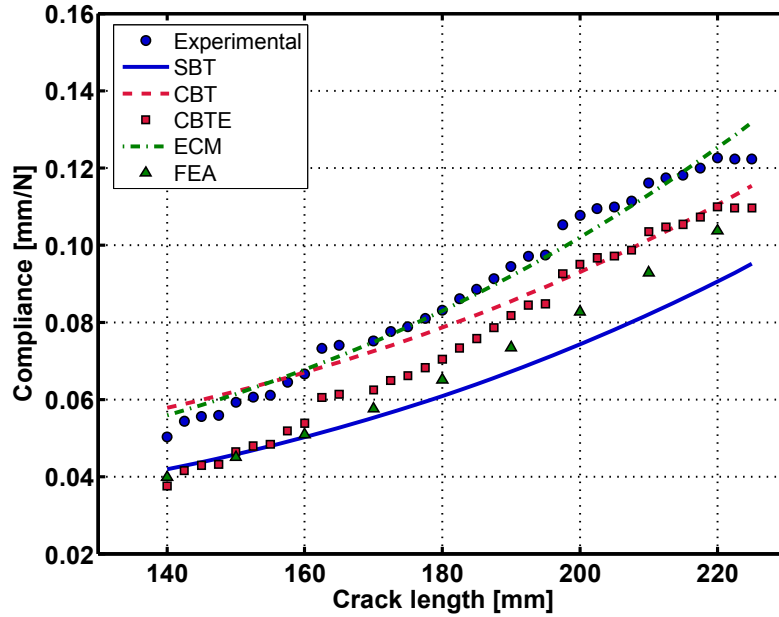


Figure 16. Comparison between calculated compliance (from different methods) and experimental values

5.3 Estimation of G_I and G_{IC}

The SERR values for Mode I fracture, G_I , were calculated using Eqs. (3, 5, 7, 8, 16). A typical R-curve, obtained for DCB03, is shown in Fig. 17. G_I increased with an increasing crack length of up to approximately 100 mm and then approached a plateau for longer crack lengths. A critical SERR for propagation, G_{IC} , was attributed to this plateau region. The resulting values of G_{IC} for crack initiation and propagation are listed in Table 6. Similar values were obtained from CBT, ECM and MCC methods, while SBT showed significantly lower values as expected. The FEA results were situated between the first group and SBT for crack initiation, but overestimated crack propagation values, mainly because the large displacements were not taken into account in the FEA results.

Summarizing the results obtained from the five methods, the G_{IC} values for crack initiation were between 70 J/m² and 250 J/m² at NL, while two to three times higher values were obtained at C105 and VIS. Starting from VIS, G_I values during crack propagation increased from approximately 230 J/m² to 1980 J/m². The values corresponding to the plateau-like region (crack lengths between 100 and 150 mm), were approximately 1670±460 J/m² (mean and standard deviation calculated by all methods).

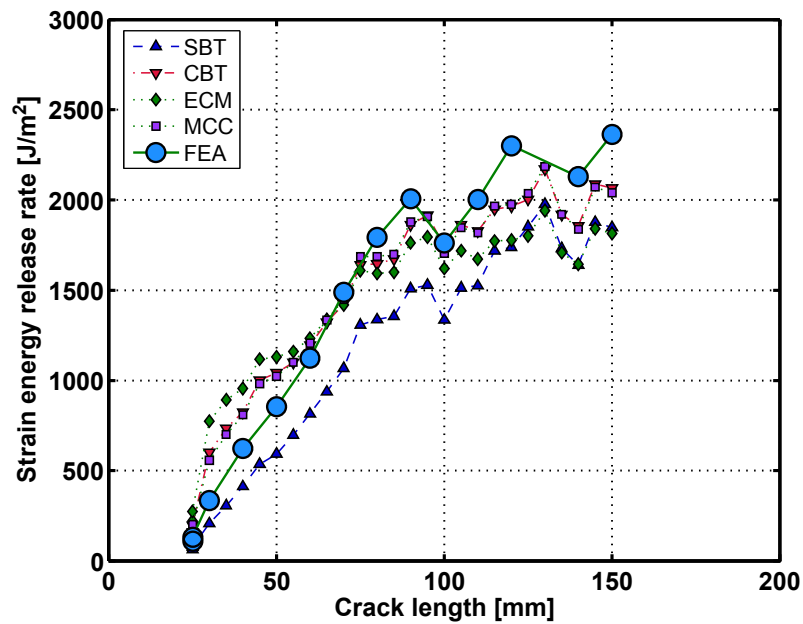


Figure 17. Comparison of strain energy release rates obtained from different methods for DCB03.

Table 6. G_{IC} for crack initiation (NL, C105 and VIS) and propagation using SBT, CBT, ECM, MCC and FEA (mean values and standard deviation for five DCB specimens).

G_{IC} [J/m ²] at	SBT	CBT	ECM	MCC	FEA
	Eq. (3)	Eq. (5)	Eq. (7)	Eq. (8)	Eq. (16)
NL	68.2 ± 14.9	189.9 ± 60.2	250.7 ± 60.4	181.0 ± 46.6	116.1 ± 25.3
C105	105.5 ± 32.4	333.3 ± 156.1	441.8 ± 190.4	303.7 ± 122.9	179.4 ± 55.0
VIS ¹	227.2 ± 30.7	684.7 ± 324.8	870.5 ± 340.5	602.4 ± 225.7	367.2 ± 49.6
VIS ²	195.6 ± 53.0	575.3 ± 159.4	702.0 ± 178.0	517.8 ± 134.7	316.1 ± 85.7
propagation	1537.1 ± 535.7	1674.1 ± 372.2	1505.9 ± 330.1	1667.0 ± 375.2	1982.7 ± 688.6

¹ visual observation

² video extensometer

5.4 Estimation of G_{II} and G_{IIC}

The SERR values for Mode II fracture, G_{II} , were estimated from Eqs (10, 12, 15, 17). Fig. 18 shows a typical R-curve, obtained for ELS02, which shows an increasing trend up to a crack length of approximately 185 mm and then seems to approach a plateau. Crack lengths of up to 210 mm (of specimens ELS02/03/05, see Section 4.1) were considered, which were assumed

as not yet being affected by the clamp region. G_{IC} values for crack initiation and values obtained for the plateau-like region of the R-curve are listed in Table 7. Similar values were obtained from CBT and ECM. Although FEA produced lower values in terms of compliance (see Fig. 16), it provided the highest SERR values of all the methods due to the sharper slope of the compliance vs. crack length curve. SERR results obtained from CBTE were inaccurate for crack initiation, being much lower than those derived from all other methods due to the erroneous crack length estimation. The crack propagation values were in the same range as all the other results however.

The G_{IC} values for crack initiation at NL values were in the range between 470 J/m² and 600 J/m² (see Table 7, excluding CBTE). Values approximately two times higher were obtained at C105 and VIS, whichever method was used. The value of G_{IC} for propagation was 2000±500 J/m² (mean and standard deviation calculated by all methods).

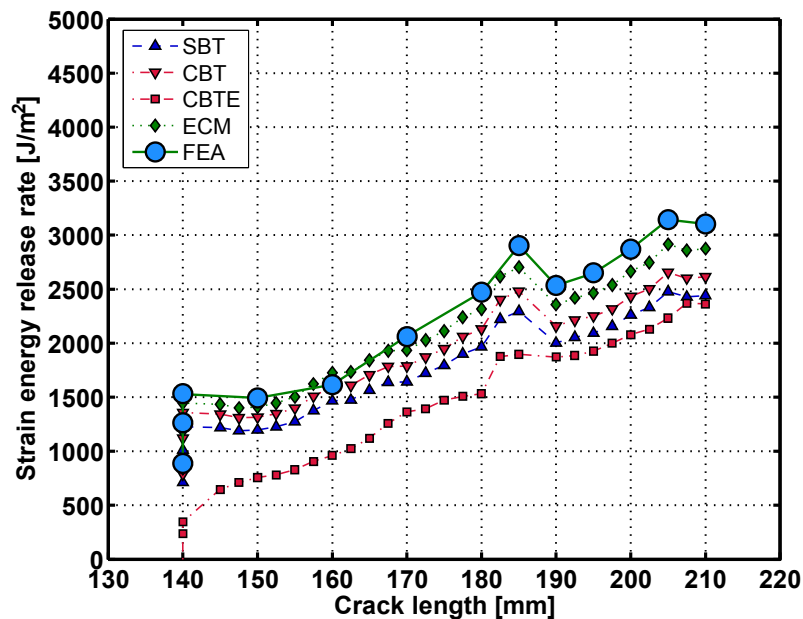


Figure 18. Comparison of strain energy release rates obtained from different methods for ELS02.

5.5 Comparison of G_{IC} , G_{IIC} and results in literature

The comparison of Mode I and Mode II fracture energies shows that G_{IIC} is always higher than G_{IC} . For crack initiation, the ratio between the two values is between 2 and 3, while for crack propagation the ratio is approximately 1.2. To the authors' knowledge, no other similar results

(concerning the fracture of pultruded GFRP joints) exist in the literature. However, there are a number of studies on the fracture behavior of GFRP laminates and/or joints comprising GFRP adherends. Existing results also show that G_{IIC} is higher than G_{IC} regardless of the material examined or method used for calculation [30]. In [16], a Mode I CBT-based VIS value for glass fiber polymethyl methacrylate adherends of 360 J/m^2 was obtained, which is in the range of the values given in Table 6. For Mode II fracture and especially delamination of a unidirectional GFRP laminate, G_{IIC} was estimated as being 1750 J/m^2 in [31]. Although it is not specified whether this value corresponds to crack initiation or propagation, it compares well to the G_{IIC} values obtained in the present work.

Analyzing Figs. 17 and 18, the bridging length was certainly at least as long as the specimen thickness (14 mm) and large-scale bridging may therefore have governed the R-curve. The obtained R-curve shape may therefore depend on the specimen geometry.

Table 7. G_{IIC} for crack initiation (NL, C105 and VIS) and propagation using SBT, CBT, CBTE, ECM and FEA (mean values and standard deviation for five ELS specimens).

$G_{IIC} [\text{J/m}^2]$ at	SBT Eq. (10)	CBT Eq. (12)	CBTE Eq. (12)	ECM Eq. (15)	FEA Eq. (17)
NL	469.7 ± 157.0	520.0 ± 173.8	309.8 ± 131.7	602.1 ± 176.3	586.1 ± 195.4
C105	892.1 ± 87.7	987.7 ± 97.1	670.0 ± 298.0	1153.4 ± 125.3	1113.9 ± 108.5
VIS ¹	1004.3 ± 136.3	1111.9 ± 150.8	806.6 ± 307.6	1300.9 ± 195.9	1255.4 ± 168.8
VIS ²	982.1 ± 87.9	1085.9 ± 95.8	904.2 ± 145.0	1337.1 ± 204.3	1199.6 ± 82.6
propagation ³	1722.4 ± 536.3	1855.3 ± 573.6	1957.1 ± 240.4	2292.8 ± 479.2	2177.9 ± 692.2

¹ visual observation

² video extensometer

³ based on specimens (ELS02, 03, 05)

6 CONCLUSIONS

The Mode I and II fracture behaviors of adhesively-bonded joints composed of pultruded GFRP laminates were investigated using DCB and ELS specimens. The pultruded material, which is commonly used in civil engineering applications, imposed minor deviations from standardized specimens. The following conclusions were drawn:

1. An alternative method to visual observation, a video extensometer, was used for measurement of the crack length. The method provided accurate results especially for Mode II fracture in which it is difficult to identify the crack tip.
2. For both Mode I and Mode II fracture, the values of G_c for crack initiation at NL, C105 and VIS points were estimated based on the load-displacement curves. An almost ideal R-curve was derived for Mode I fracture, while a similar trend was observed for Mode II fracture. For both fracture modes, the mean value of the plateau of the R-curves was considered as being G_c for crack propagation.
3. The values of G_I and G_{II} were calculated using SBT, CBT, ECM and FEA. In addition, MCC was used for Mode I and CBTE for Mode II fracture. For both Mode I and Mode II fracture, similar results were obtained from CBT, ECM and FEA. SBT always underestimated the values of G due to the well-known deficiencies of this method. Similar results were obtained from MCC and CBT, which are based on the same fitting of compliance against crack length. Less accurate results were obtained from CBTE for crack initiation due to the geometrical characteristics and asymmetric fracture process of the joint.
4. Calculated using the same method, the values of G_{IIC} for crack initiation and propagation were always higher than the values of G_{IC} . The values of G_{IC} and G_{IIC} were in agreement with similar results obtained in previous studies for comparable materials.
5. The asymmetry of the cracked specimens did not affect the results, except for the calculation of the corrected crack length and the subsequent G_{II} calculations based on the CBTE in the crack initiation range. Less than 1% of Mode II fracture component was found in DCB specimens and the same proportion of Mode I fracture component was found in ELS specimens.
6. Based on the aforementioned results, the applicability of existing standard methods and protocols for interpretation of the fracture mechanics data obtained from the fracture joints used in these experiments was validated. Due to large-scale bridging, however, the obtained R-curve shape may depend on specimen geometry.

ACKNOWLEDGEMENTS

The authors would like to thank the Swiss National Science Foundation (Grant No 200020-111702/1), Sika AG, Zurich (adhesive supplier) and Fiberline Composites A/S, Denmark (pultruded laminate supplier) for their support of this research.

REFERENCES

- [1] ASTM D3433-99(2005): Standard test method for fracture strength in cleavage of adhesives in bonded metal joints, in Annual book of ASTM standards: adhesive section 15.06.
- [2] Blackman BRK, Kinloch AJ. Determination of the Mode I adhesive fracture energy, G_{IC} , of structural adhesives using the double cantilever beam (DCB) and the tapered double cantilever beam (TDCB) specimens. Version 00-06.ESIS(TC4) Protocol, 2000.
- [3] ASTM D5528-01(2007): Standard Test Method for Mode I Interlaminar Fracture Toughness of Unidirectional Fiber-Reinforced Polymer Matrix Composites, in Annual book of ASTM standards: adhesive section 15.03.
- [4] ISO 15024:2000(E): Standard test method for the mode I Interlaminar fracture toughness, G_{IIC} , of unidirectional fibre-reinforced polymer matrix composites.
- [5] ASTM, ASTM D6671/D6671M-06: Standard test method for mixed mode I-mode II interlaminar fracture toughness of unidirectional fiber reinforced polymer matrix composites, in Annual book of ASTM standards: adhesive section 15.03.
- [6] ESIS Protocol: Determination of the Mode II Delamination Resistance (Critical Energy Release Rate G_{IIC}) of Unidirectional Fiber-Reinforced Polymer Laminates Using the End-Loaded-Split Specimen (ELS). ESIS(TC4) Protocol, 2006.
- [7] Ducept F, Gamby D, Davies P. A mixed-mode failure criterion derived from tests on symmetric and asymmetric specimens. Compos. Sci. Technol. 1999;59(11):609-619.
- [8] Sorensen BF, Jacobsen TK. Large-scale bridging in composites: R-curves and bridging laws. Compos., Part A 1998;29(11):1443-1451.
- [9] Kinloch AJ, Osiyemi SO. Predicting the fatigue life of adhesively-bonded joints. J. Adhesion. 1993;43(1-2):79-90.
- [10] Ashcroft IA, Hughes DJ, Shaw SJ. Mode I fracture of epoxy bonded composite joints: 1. Quasi-static loading. Int. J. Adhes. Adhes. 2001;21(2):87-99.

-
- [11] Suppakul P, Bandyopadhyay S. The effect of weave pattern on the mode-I Interlaminar fracture energy of E-glass/vinyl ester composites. *Compos. Sci. Technol.* 2002;62(5):709-717.
- [12] Blackman BRK, Kinloch AJ, Paraschi M, Teo WS. Measuring the mode I adhesive fracture energy, G_{IC} , of structural adhesive joints: the results of an international round-robin. *Int. J. Adhes. Adhes.* 2003;23(4):293-305.
- [13] Hodzic A, Kim JK, Lowe AE, Stachurski ZH. The effects of water aging on the interphase region and Interlaminar fracture toughness in polymer-glass composites. *Compos. Sci. Technol.* 2004;64(13-14):2185-2195.
- [14] Ferreira JM, Silva H, Costa JD, Richardson M. Stress analysis of lap joints involving natural fibre reinforced interface layers. *Compos., Part B* 2005;36(1):1-7.
- [15] Thanomsilp C, Hogg PJ. Interlaminar fracture toughness of hybrid composites based on commingled yarn fabrics. *Compos. Sci. Technol.* 2005;65(10):1547-1563.
- [16] Brunner AJ, Blackman BRK, Williams JG. Calculation a damage parameter and bridging stress from G_{IC} delaminating tests on fibre composite. *Compos. Sci. Technol.* 2006;66(6):785-795.
- [17] Mall S. Characterization of debond growth mechanism in adhesively-bonded composites under mode II static and fatigue loadings. *Eng. Fract. Mech.* 1988;31(5):747-758.
- [18] Martin RH, Davidson BD. Mode II fracture toughness evaluation using four point bend, end notched flexure test. *Plast. Rubber. Compos.* 1999;28(8):401-406.
- [19] Szekrenyes A, Uj J. Beam and finite element analysis of quasi-unidirectional composite SLB and ELS specimens. *Compos. Sci. Technol.* 2004;64(15):2393-2406.
- [20] Blackman BRK, Kinloch AJ, Paraschi M. The determination of the mode II adhesive fracture resistance, G_{IIC} , of structural adhesive joints: an effective crack length approach. *Eng. Fract. Mech.* 2005;72(6):877-897.
- [21] Blackman BRK, Brunner AJ, Williams JG. Mode II fracture testing of composites: a new look at an old problem. *Eng. Fract. Mech.* 2006;73(16):2443-2455.
- [22] Keller T. Recent all-composite and hybrid fiber reinforced polymer bridges and buildings. *Prog Struct Eng Mater* 2001;3(2):132-40.
- [23] Mostovoy S, Crosley PB, Ripling EJ. Use of crack-line loaded specimens for measuring plane-strain fracture toughness. *J. Mater.* 1967;2(3):661-81.

-
- [24] Williams JG. End corrections for orthotropic DCB specimens. *Compos. Sci. Technol.* 1989;35(3):367-376.
- [25] Wang Y, Williams JG. Correction for mode II fracture toughness specimens of composite materials. *Compos. Sci. Technol.* 1992;43(3):251-256.
- [26] Blackman BRK, Kinloch AJ, Paraschi M. The determination of the mode II adhesive fracture resistance, G_{IIC} , of structural adhesive joints: an effective crack length approach. *Eng. Fract. Mech.* 2005; 72(6):877-897.
- [27] Rybicki FE, Kaninen MF. A finite element calculation of stress intensity factor by a modified crack closure integral. *Eng. Fract. Mech.* 1977;9(4):931-938.
- [28] Dakshina Moorthy CM, Reddy JN. Modelling of laminates using a layerwise element with enhanced strains. *Int. J. Numer. Meth. Engng.*, 1998;43(4):755-779.
- [29] Keller, T, and Vallée, T. Adhesively bonded lap joints from pultruded GFRP profiles, Part I: Stress-strain analysis and failure modes. *Compos., Part B*, 2005;36(4): 331-340.
- [30] Hashemi S, Kinloch AJ, Williams JG. The analysis of interlaminar fracture in uniaxial fibre-polymer composites. *Proc. R. Soc. Lond. A*, 1990 :427(1872):173-199.
- [31] Matsubara G, Ono H, Tanaka K. Mode II fatigue crack growth from delamination in unidirectional tape and satin-woven fabric laminates of high strength GFRP. *Int. J. Fatigue* 2006;28(10):1177-1186.

2.2 Mechanical and fracture behavior of structural joints under quasi-static loading

Summary

The LEFM approach is considered an efficient method to characterize the progressive failure process of adhesively-bonded joints and its applicability has been validated for fracture joints composed of pultruded GFRP laminates in Section 2.1. This paper attempts to extend this applicability validation to structural joints made of the same constituent materials. During the axial tensile loading of a structural joint, a crack or cracks initiate within the composite adherends due to a material defect and propagate in the same location until the final collapse occurs. In contrast to pre-cracked fracture joints, crack initiation in structural joints occurs in an uncontrollable way and the subsequent crack propagation is probably unstable. Since crack development cannot be visually recorded, an alternative technique needs to be proposed for crack length measurement. Due to the complex geometric configuration of structural joints, an accurate analytical solution for the SERR is usually lacking and the experimental and numerical methods remain to be validated.

An experimental investigation was performed for adhesively-bonded DLJs and SLJs composed of pultruded GFRP laminates. For both joint types, the stiffness and quasi-static strength of joints were obtained and the dominant failure mode was found to be a fiber-tear failure that occurred within the mat layers of the GFRP laminates. In addition to discussions concerning the mechanical behavior of structural joints (Task 1.1-1.3 in Fig. 1), this paper also covers the characterization of the fracture behavior (Task 2.1-2.4 in Fig. 1). Two crack measurement techniques were proposed: crack propagation and back-face strain gages. Their applicability for identifying crack initiation and describing crack propagation was validated, although the failure mechanism was always sudden and brittle. The SERR values were calculated using ECM, in which the compliance was fitted against the total crack length using a Berry method. The R-curves were established for both joint types, though no ideal form with a remarkable plateau was observed. Different values of the critical strain energy release rate (G_c) were obtained for DLJs and SLJs due to different combinations (Mode I and II) of fracture modes.

Reference details

This paper, "Progressive failure process of adhesively bonded joints composed of pultruded GFRP" by Ye Zhang and Thomas Keller, was published in Composite Science and Technology 2007, volume 68, pages 461-470.

[doi:10.1016/j.compscitech.2007.06.011](https://doi.org/10.1016/j.compscitech.2007.06.011)

PROGRESSIVE FAILURE PROCESS OF ADHESIVELY BONDED JOINTS COMPOSED OF PULTRUDED GFRP

Ye Zhang and Thomas Keller

Composite Construction Laboratory (CCLab),
Ecole Polytechnique Fédérale de Lausanne (EPFL),
Station 16, Bâtiment BP, CH-1015 Lausanne, Switzerland

ABSTRACT

Adhesively bonded joints are being used increasingly in civil engineering, especially for joints comprising pultruded glass-fiber reinforced polymer (GFRP) laminates. The layered material architecture, however, leads to a complex delamination failure within the pultruded material, thus necessitating understanding of the progressive failure mechanism of such joints under axial tensile loading. In this work, adhesively bonded joints composed of pultruded GFRP laminates, including double and stepped lap joints, were experimentally investigated. The static strengths of joints were obtained and the failure mechanism was understood. Crack propagation and back face strain gages were successfully employed to identify crack initiation and describe crack propagation, even though the failure mechanism was always sudden and brittle. The dominant failure mode for both types of joints was a fiber-tear-off failure that occurred in the mat layers of the GFRP laminates. The critical strain energy release rate was calculated. Different values were obtained for the two joint types due to different combinations of fracture modes.

KEYWORDS

Adhesive joints; Strength; Crack; Pultrusion

1 INTRODUCTION

Adhesively bonded joints are being used increasingly in civil engineering, especially joints composed of pultruded GFRP laminates. Due to the complicated material architecture of pultruded composites, it is important to understand the failure mechanism of the joints under both static and cyclic loading, as well as the progressive failure process considering crack initiation and propagation.

Considerable experience on the mechanical behavior of adhesively bonded FRP joints under static and fatigue loads has already been gathered for aerospace and automotive structures. However, when these applications are compared with adhesively bonded FRP joints in civil infrastructure, there are essential differences in the manufacturing process, the material architecture, the dimensions of the components and the application environments. It is therefore urgent to fill the gap of knowledge regarding the fracture behavior of adhesively bonded joints for the civil engineering sector.

Two categories of joints can be differentiated based on their function: validation (or structural) and fracture mechanics joints. In contrast to fracture mechanics joints where the joint is pre-cracked in order to produce more stable crack propagation, the crack in validation joints initiates naturally during the failure process. Single lap and double lap joints are considered as two main types of validation joints that are representative for typical joints found in many structural applications [1]. Due to the stress singularity at end of the overlap of these joints, however, the failure is almost always brittle and hard to catch. This characteristic often prevents the use of fracture mechanics to describe their behavior. Hence, to understand the fracture behavior of adhesively bonded joints, fracture mechanics joints, which are designed to generate fracture mechanics design data for pure mode I or II fracture, are often preferred [2-7].

Little documented work has been done on the fracture behavior of validation joints. Giare [8] attempted to introduce initial cracks in double lap joints with two different geometric configurations. The pre-defined cracks proved to have a significant influence on the critical strain energy release rate G_{crit} . Giare reported that the crack propagation was quite fast and that global failure occurred instantaneously once the maximum load was reached. A recent contribution by Keller and Vallée [9, 10] showed that the static strength of adhesively bonded GFRP joints, including single and double lap joints, can be successfully predicted

using a quadratic failure criterion. Experimental investigations on the fatigue behavior of similar double lap joints were performed by Keller and Tirelli [11]. In these tests, a fatigue limit was observed that is far above the fatigue stress amplitudes observed in bonded connections of typical GFRP bridge structures. However, due to the sudden and brittle failure of the adhesively bonded pultruded GFRP joints, it was still not possible to identify the initiation of the crack and to qualify its propagation.

Several solutions have been proposed to decrease the stress singularity occurring at the tips of the overlap of lap joints [12]. The scarf joint was found to be an efficient alternative to produce lower stress peaks. It can be considered as a joint with many steps, hence the stepped lap joints act as another alternative to reduce the stress concentration. The single stepped lap joint is a special type of stepped joint with only one step. This type of detail is often observed in engineering structures, for example, in the bridge deck shown in Fig. 1. Kim et al. [13] evaluated the static tensile strength of stepped lap joints manufactured by different methods. Later, Kim et al. [14] performed a fatigue study for stepped lap joints with various geometric configurations and they showed that changing the step length and the edge angle of adherends leads to an increased fatigue life and strength. There is, nevertheless, still a lack of knowledge about the fracture behavior of stepped lap joints and more research effort is necessary.

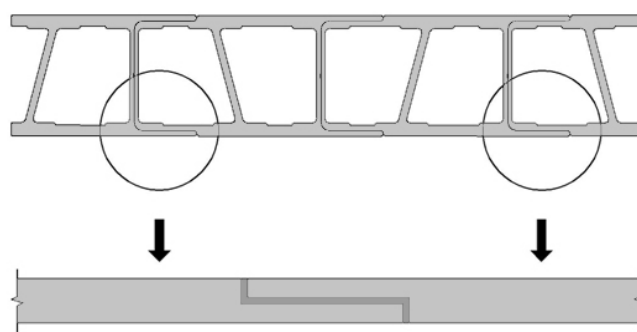


Figure 1. DuraSpan bridge deck with stepped lap joint.

In the present work, the quasi-static and fatigue behavior of structural (validation) joints, that is, adhesively bonded double and stepped lap joints from pultruded GFRP laminates and an epoxy adhesive, are investigated. These types of joints are widely used in existing civil

engineering structures. Axial tensile experiments have been performed and numerical modeling has been used to predict the strength and stiffness behavior. This paper focuses on the experimental results from the quasi-static loading. Crack initiation has been determined by crack gage and back face strain gage measurements. The crack propagation could be described by the changing compliance and back face strain, and the critical strain energy release rate could be calculated.

2 EXPERIMENTAL PROGRAM

2.1 Specimen description

Two types of specimens were investigated: balanced double lap joints (DLJ) and stepped lap joints (SLJ), both composed of pultruded GFRP laminates of 50 mm width and 6 or 12 mm thickness. The adhesive layer thickness was 2 mm. The dimensions of the specimens are shown in Fig. 2. All specimens were manufactured in ambient laboratory conditions. Before manufacture, all surfaces subjected to bonding were mechanically abraded with sandblasting paper using a grinder and then chemically degreased using acetone. To ensure a constant thickness of the adhesive and good alignment of the GFRP laminates, a special aluminum laying frame was designed and employed for each type of joint. After their manufacture, all specimens were cured in ambient laboratory conditions for 10 days.

2.2 Material properties

The pultruded GFRP laminates (delivered by Fiberline A/S, Denmark) consisted of E-glass fibers embedded in an isophthalic polyester resin. The fiber contents, resulting from burn-off tests according to ASTM D3171-99, are summarized in Table 1. A glass fiber density of 2.56g/cm^3 was assumed, as specified by the manufacturer. The fiber architecture was investigated using a microscope. Fig. 3 shows the fiber architecture of the two laminates, which was built up from outer mats and rovings in the core region. The 12 mm thick laminate comprised two mat layers on each side, while the 6 mm thick laminate showed only one mat layer on each side. A mat layer consisted of a chopped strand mat (CSM) and a woven mat $0^\circ/90^\circ$, both stitched together. Based on experimental results given in [10], it was assumed that the different number of outer mat layers would not affect the joint behavior. The combined through-thickness tensile and shear strength is only slightly influenced by the number of

outer mat layers. The thickness of each of the fiber layers was estimated and is shown in Fig. 3. On the outside, a polyester surface veil (40 g/m²) has been added to protect against environmental actions (not visible in Fig. 3).

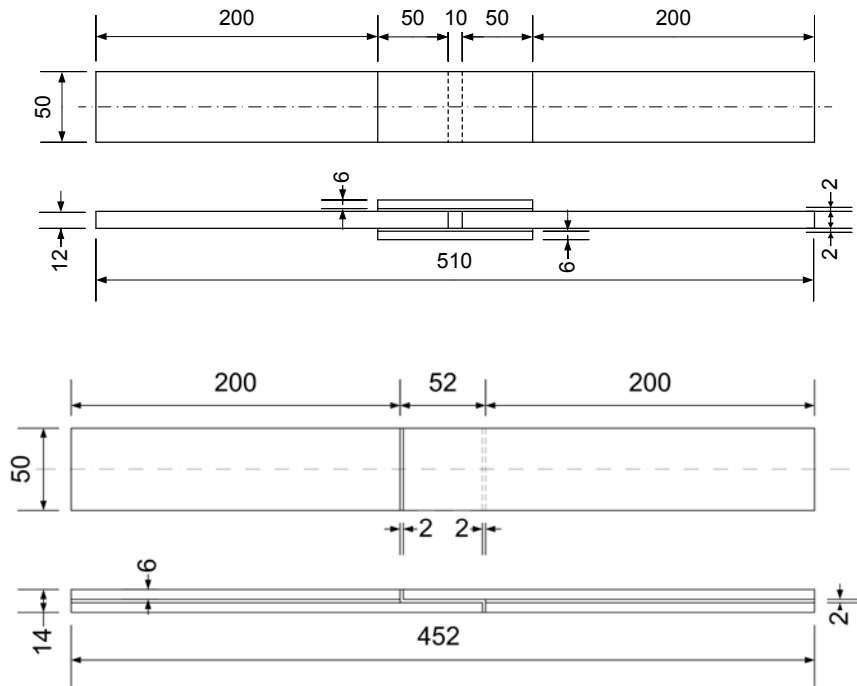


Figure 2. Double lap (above) and stepped lap (below) joints (DLJ and SLJ) from GFRP laminates.

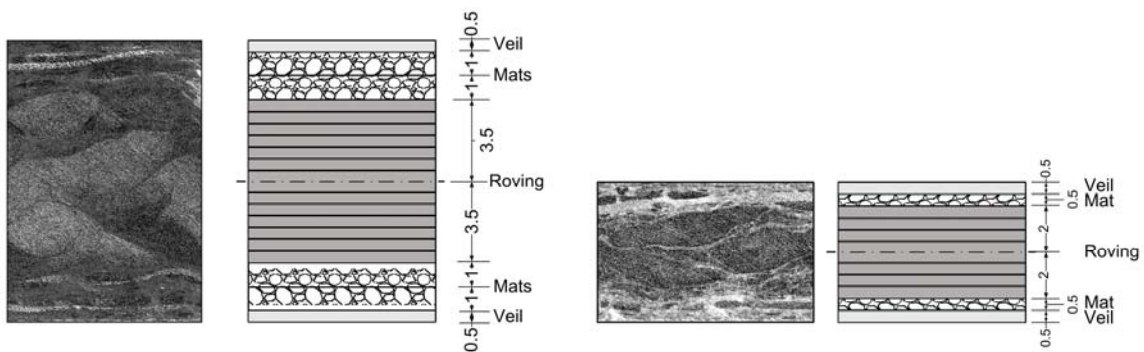


Figure 3. Microscopic view and model of fiber architecture of 12 mm (left) and 6 mm (right) laminates.

Table 1. Fiber volume and weight fractions of GFRP laminates.

Sample	Material	Volume fraction [%]	Weight fraction [%]
6 mm laminate	Fiber	43.6	64.3
	Matrix	56.4	35.7
12 mm laminate	Fiber	48.5	69.4
	Matrix	51.5	30.6

Table 2. Strength and stiffness of GFRP laminates and adhesive.

Properties	GFRP laminates		Epoxy adhesive
	6 mm	12 mm	
Young's modulus [GPa]	31.4±1.6	34.4±2.3	4.55±0.14
Tensile strength [MPa]	283±7	355±15	38.1±2.1

The load-elongation responses were almost linear-elastic up to brittle failure. The final collapse occurred in the glass fibers in a very sudden manner, without any visible cracks on the specimen surfaces. The strength of the 12 mm laminates with higher fiber fractions was approximately 25% higher than that of the 6 mm laminates.

A two-component epoxy was used for the specimens (SikaDur 330 from Sika). Axial tensile tests according to EN ISO 527-1 were performed to characterize the epoxy [15]. The specimens were made of bulk adhesives and prepared according to the supplier's specifications. The epoxy showed an almost elastic behavior and a brittle failure. The resulting material properties are also given in Table 2.

2.3 Instrumentation and set-up

Four crack propagation gages (HBM/RSD20) were used to detect the crack initiation and propagation in three specimens of each joint type, as shown in Fig. 4 (labeled C) and Table 3. The crack propagation gages consisted of 20 wires spaced at 1.15 mm intervals perpendicular to the adhesive layer, and covered almost half of the overlap length. The gages covered the part of the overlap length where stable crack propagation was expected to occur. As the crack propagates, the wires are broken progressively and thereby increase the electrical resistance of the gage. Two measurement frequencies were employed: 800 Hz for the double lap joints

and 200 Hz for the stepped lap joints.

In each specimen, two back face strain gages (D) were placed above the locations, where crack initiation was expected to influence the strain response and two more strain gages (A) were used to measure the axial strains outside the joint where the stresses were expected to remain uniformly distributed. Furthermore, two displacement transducers (B) were employed to measure the elongation of the joint over the gage lengths indicated in Fig. 4.

An Instron Universal 8800 hydraulic machine was used to apply the axial force with a displacement rate of 0.5 mm/min for the SLJs and of 1 mm/min for the DLJs. The lengths of the specimens between the grips were 460 mm for the DLJs and 402 mm for the SLJs. The specimens were loaded up to failure. An HBM/Spider8 was used to gather the data.

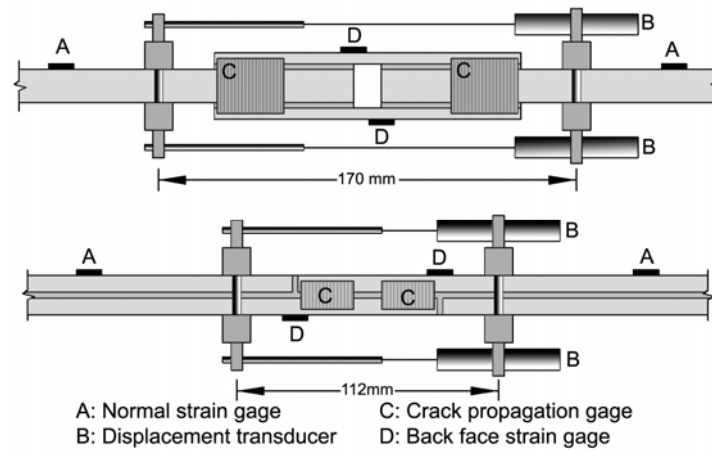


Figure 4. Experimental instrumentation for DLJ (above) and SLJ (below).

3 EXPERIMENTAL RESULTS

3.1 Load-elongation responses and ultimate loads

The double lap joints had an almost linear load-elongation response up to a very brittle failure, as shown in Fig. 5. In contrast, the stepped lap joints exhibited a discontinuous two stage behavior, although the final failure was also brittle. For the SLJs, when the load reached 7.0 kN on average, a failure in the adhesive in the two small gaps perpendicular to the longitudinal adhesive layer occurred, which was followed by a steep decrease of the load. After this first failure, however, the joints continued to sustain an increase in load, although the crack initiation and propagation led to a decrease in overall stiffness. The crack initiation in the two gaps occurred almost simultaneously. Only in one specimen the cracks occurred

one after the other (two local peaks in Fig. 5). One SLJ specimen was subjected to three loading cycles. Fig. 6 shows that a small amount of inelastic energy was dissipated through the initial cracking and, therefore, the joint showed a pseudo-ductile behavior as defined by De Castro and Keller [15].

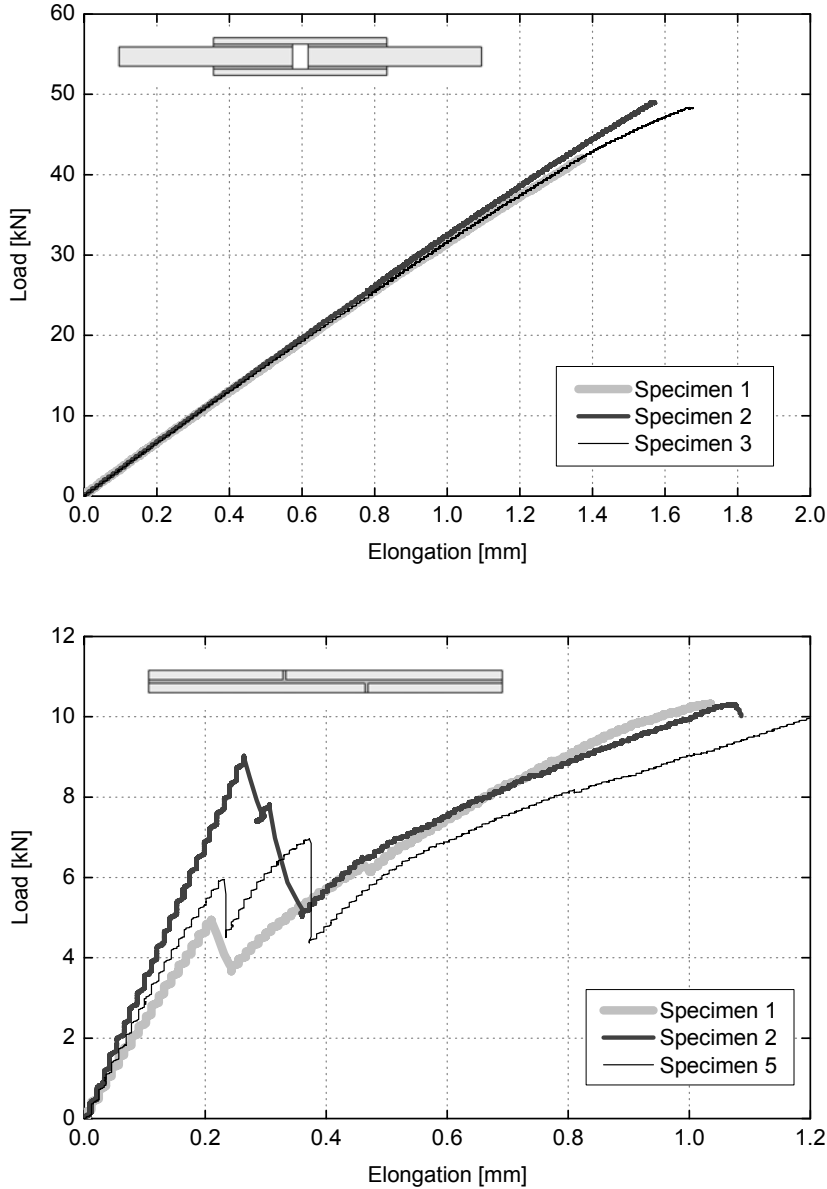


Figure 5. Selected load-elongation curves of DLJ (above) and SLJ (below).

The average static ultimate loads of the double lap and stepped lap joints were 45.6 kN and 10.5 kN, respectively (see Table 3). The scatter in the ultimate loads of both joint types was found less than 4.8%, which seemed to indicate that the manufacturing quality and curing

time only slightly influenced the static strength of the joints. However, the scatter in the gap adhesive failure loads for SLJs was greater at 27.1%. This load level depended mainly on the strength of the adhesive in the small gaps, which seemed to be more sensitive to the manufacturing process and environmental conditions during curing.

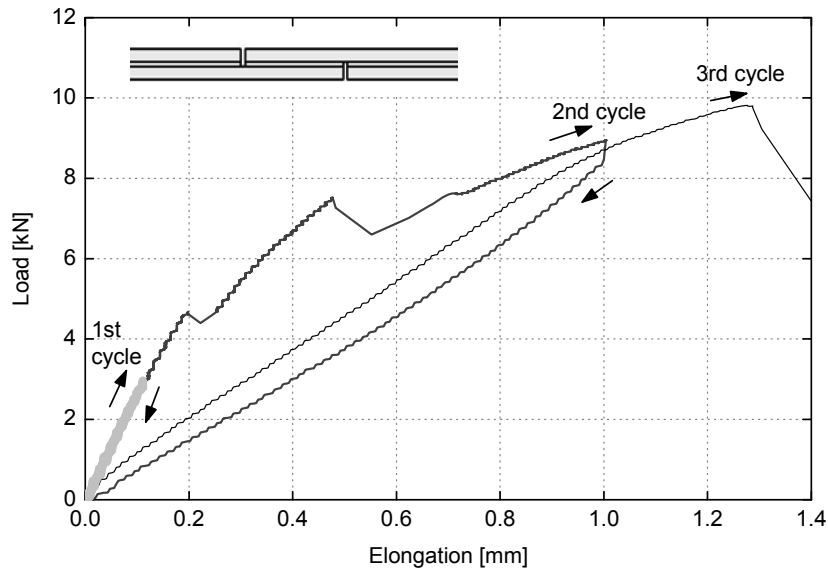


Figure 6. Pseudo-ductile behavior of SLJ.

Table 3. Ultimate loads of double and stepped lap joints (DLJs and SLJs, * with crack propagation gages).

Specimen	DLJ		SLJ
	Ultimate load [kN]	Adhesive failure [kN]	Ultimate load [kN]
1 *	42.1	4.9	10.3
2 *	49.0	9.0	10.3
3 *	47.5	8.9	11.1
4	45.1	7.0	10.2
5	45.9	7.0	10.0
6	43.7	5.1	10.9
Average	45.6±2.0	7.0±1.9	10.5±0.5

3.2 Failure modes

The typical failure modes of the DLJs and SLJs are shown in Fig. 7. For both types of joints, the dominant failure mode was a fiber-tear-off failure in the GFRP laminates. Failure initiation occurred in the outer mat layers of the 12 mm laminates below the ends of the outer 6 mm laminates in the DLJs, and in the 6 mm laminates below the (already cracked) small gaps in the SLJs. Failure propagation then occurred in the same mat layers up to final joint failure. In some cases, cracks were observed even below the mat layers in the roving layer. Failures were brittle and sudden and their initiation and propagation were normally not observable by the naked eye, with the exception of some SLJs, where approximately the first 20 mm of crack growth could be observed, see Fig. 7 (below).

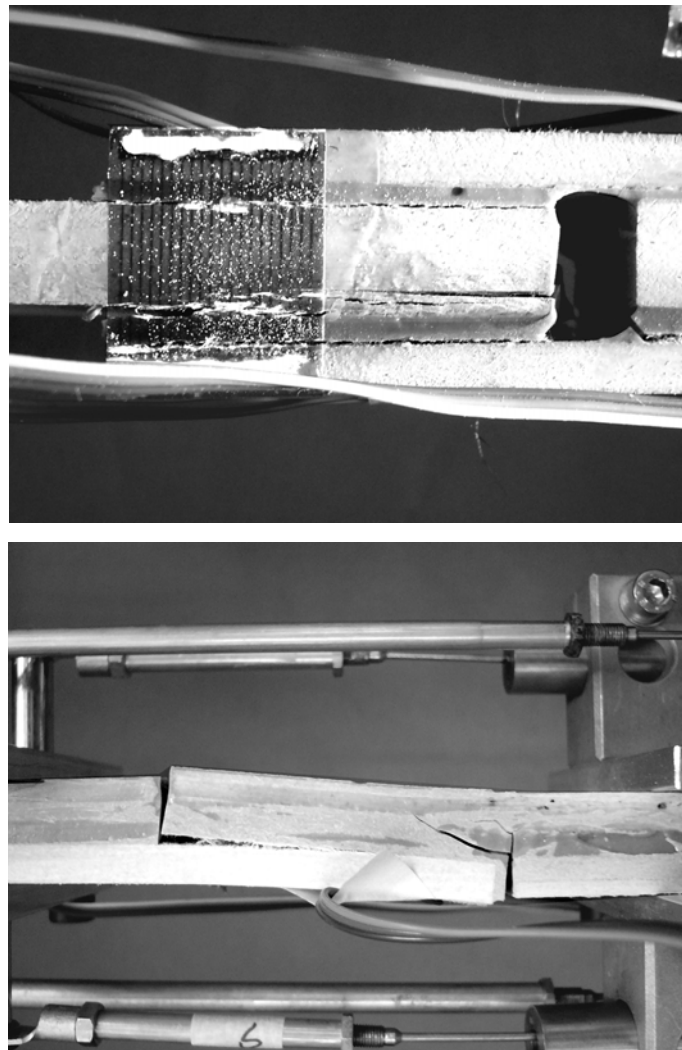


Figure 7. Failure modes of DLJ (above) and SLJ (below) under quasi-static axial tensile loading (DLJ with broken crack gage, primary failure of SLJ on the left side).

3.3 Results from crack gages

Fig. 8 shows typical measured crack gage resistances with increasing load for the DLJs and SLJs. The resistance increased if one of the twenty wires of one gage was cut; the corresponding crack length was 1.15mm (distance of two wires). The results from three of the gages on one of the DLJs are shown on the above. The crack initiated simultaneously on both sides of one joint end at a load of 26.9 kN (locations 1 and 2 in Fig. 8, left). The crack then did not grow up to approximately 41 kN. Subsequently, it propagated rapidly and cut the remaining gage wires up to final failure. On the other joint edge, crack initiation also occurred at 26.9 kN, but only at one side (3 in Fig. 8). Subsequently, only one more point was caught. The cutting of the remaining wires could not be recorded due to the too rapid crack propagation, even at a measurement frequency of 800 Hz. No crack developed at the fourth gage location (4 in Fig. 8).

For the SLJs, crack initiation in the laminates occurred on each of the four potential locations at a different load (between 4.7 and 6.3 kN). The cracks then propagated at different rates up to the ultimate load. Table 4 gives the measured average loads of failure initiation, which corresponded to approximately 59.0% of the ultimate load for the DLJ and 42.8% for the SLJ.

3.4 Results from back face strain gages

Fig. 9 shows typical measured back face strains with increasing load for a DLJ and SLJ. For comparison, the strain responses obtained from the normal strain gages outside of the joint are added. While the normal strains in the DLJ remained almost linear up to ultimate load, the back face strains showed an offset at 30 kN for this specific joint. The back face strains for the SLJ were first influenced by the adhesive failure in the small joint gaps. The strains changed from tension to compression, and then followed the shape of the global load-deformation curve shown in Fig. 5. The normal strains in the SLJ also followed the shape of the global curve, but remained on the tension side. When the load started increasing again after the first crack, similar but smaller offsets than observed for the DLJ became visible between 6.2 and 7.3 kN. Table 4 gives the measured average load at failure initiation in the laminates deduced from back face strains. The value for the SLJ was taken from the re-increasing part of the curve.

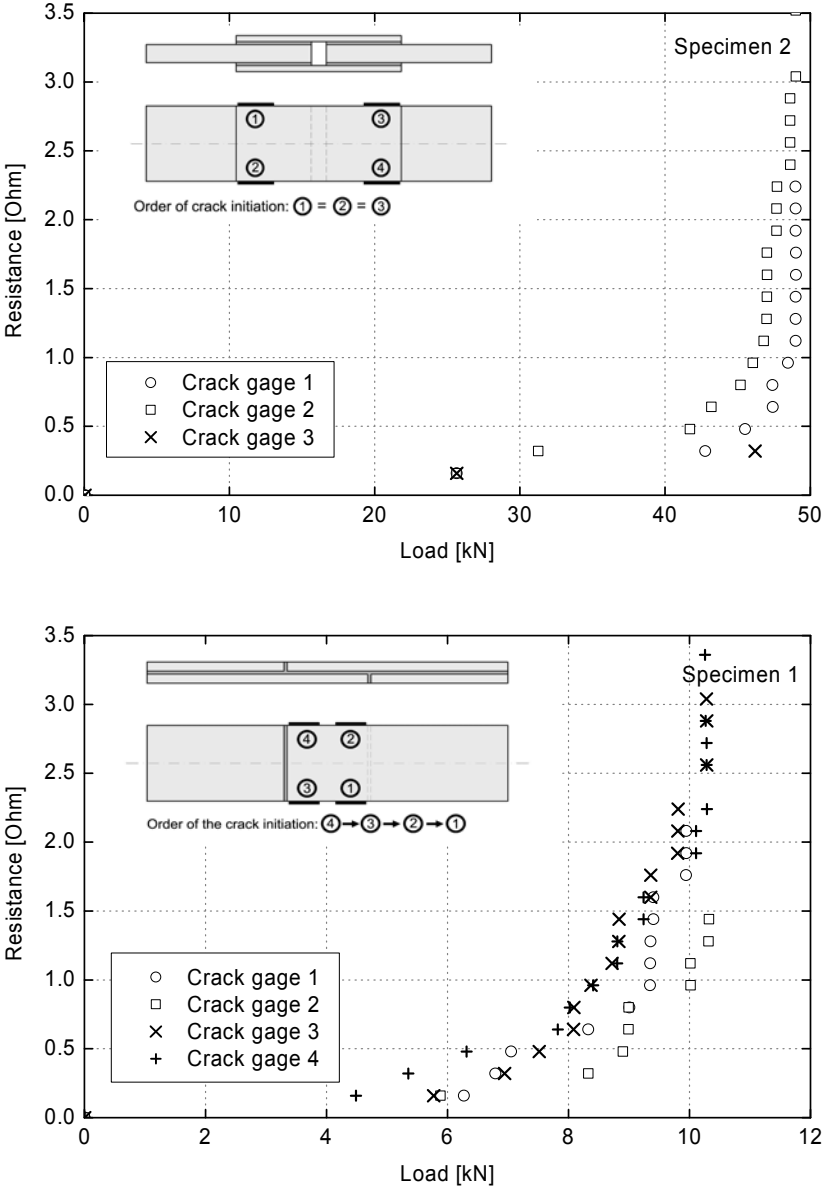


Figure 8. Measured crack propagation gage resistance versus load of typical DLJ (above) and SLJ (below).

Table 4. Comparison of load at crack initiation in laminates from crack propagation and back face strain gages.

	Load [kN] from crack gage method	Load [kN] from back face gage method
DLJ	26.9±2.9	26.8±3.0
SLJ	4.5±0.2	4.7±0.3

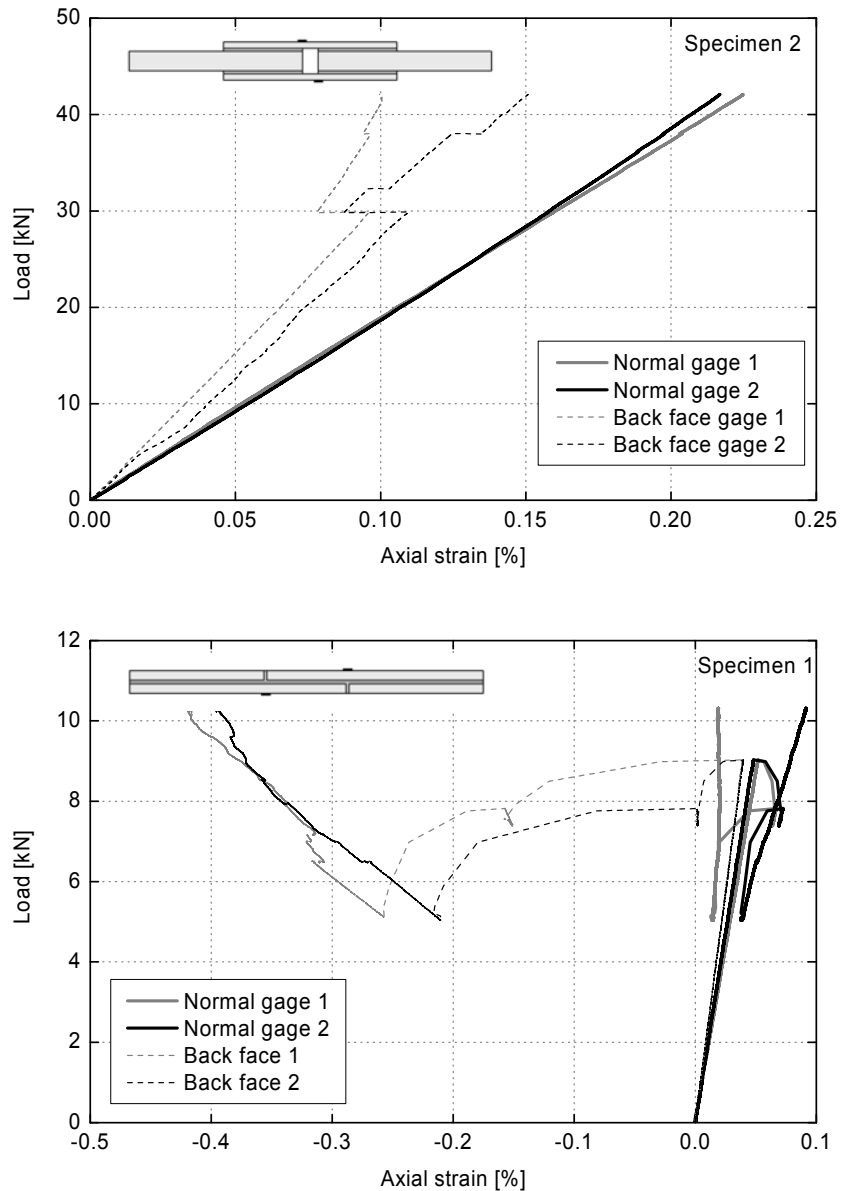


Figure 9. Measured back face strain versus load of typical DLJ (above) and SLJ (below).

4 DISCUSSION

4.1 Comparison of failure mechanisms

In fracture mechanics, a progressive failure process is described in three stages: crack initiation, crack propagation and final failure. Table 5 summarizes qualitatively the results from the GFRP laminates, double lap and stepped lap joints in this respect.

The load-elongation response of the laminates was almost linear up to the brittle failure. Crack initiation and propagation were not detectable. The behavior of the double lap joints was similar. After crack initiation in the inner laminate, the initial crack length remained

almost constant for a short period only (see Fig. 8). Subsequently, the cracks propagated suddenly and very quickly in an unstable manner up to brittle final failure.

Table 5. Comparison of failure mechanism between GFRP laminates, DLJ and SLJ.

	Laminates	Double lap joints	Stepped lap joints
Behavior	Almost linear and brittle	Almost linear and brittle	Two stages and pseudo-ductile
Crack initiation	Not detectable	In mat layer of 12 mm laminate	In the adhesive of the gap
Crack propagation	Not detectable	In mat layer of 12 mm laminate; very fast and difficult to catch	In mat layer of 6 mm laminate; stable and easy to catch
Final collapse	Failure of glass fibers	In mat layer (fiber-tear-off)	In mat layer (fiber-tear-off)

The load-elongation response of the stepped lap joints was similar to that of the DLJs until adhesive gap failure. In this phase, the behavior was almost symmetrical, as shown by the similar response of normal and back face strain gages in Fig. 9 (below). The effect of the small adhesive-filled gaps of lower stiffness on the symmetry of the joint configuration was therefore negligible. The joint behavior, however, differed from that of the laminates and DLJs after adhesive failure in the joint gaps. This failure led to a pronounced drop in stiffness due to a system change from a stepped lap (almost symmetric) to single lap (non-symmetric) configuration. The cracks entered then into the 6 mm laminate and turned by 90°. Subsequently, they propagated in the layer of the mats in a stable manner for a short period and then became unstable and grew rapidly up to final joint failure.

The dominant failure mode was the same fiber-tear-off failure in the mat layers of the laminates for both joint types. Comparing the ultimate loads of both joint types, the average DLJ ultimate load was more than two times higher than the double of that of the SLJ (the double has to be taken to equalize the shear surface). This much higher performance of DLJs was mainly due to the upkeep of a symmetric joint configuration. The change from stepped to single lap joint configuration during the failure process in the SLJs is a major drawback of this

joint type.

4.2 Detection of crack initiation in the laminates

The crack initiation in the laminate could be caught by employing both crack propagation gages and back face strain gages. As shown in Fig. 8, the first cracks initiated when the resistance of the crack propagation gages began to increase. A sudden decrease of the back face strains occurred due to stress redistribution after crack initiation (see Fig. 9). After adhesive failure in the small gaps of the SLJs, the much higher eccentricity of the axial load in the new single lap joint configuration provoked bending moments that changed the sign of the back face strains from tension to compression. Subsequently, small offsets in the again increasing strain curves were measured, the first offset evidently being caused by the stress redistribution due to crack initiation in the laminate. Table 4 compares the measured average loads at which crack initiation in the laminates occurred according to crack propagation and back face gage measurements. The loads compare very well.

The result from the crack propagation gages also showed clearly that crack initiation occurs at different locations and at different times. Hence, the assumption of plane strains in a two dimensional numerical analysis of such joints should be considered only as an approximation. Moreover, in experimental studies, a fully equipped instrumentation is always recommended, that is, in order to identify crack initiation, sufficient crack gages to monitor all positions where cracks may initiate are recommended.

4.3 Tracing of crack propagation in the laminates

A key question within the progressive failure process is how the crack propagates: in a stable or unstable manner. Several parameters can be used to describe crack propagation, such as the joint stiffness or the joint compliance. The first normally decreases, while the second increases with increasing crack length. The compliance, C , is defined according to [2]:

$$C = \frac{\delta}{P} \quad (1)$$

where δ is the elongation and P the applied load. The Berry method uses a plot of compliance, C , against crack length, a , on a log-log chart [2]. A straight line is obtained in this chart from:

$$C = A(a)^B \quad (2)$$

where A and B are obtained from poly-fitting of the experimental data. The experimentally found values for the two joint types are given in Table 6 for the local and global compliance. The local compliance corresponds to the compliance of the joint part (elongations from transducers, see Fig. 4), while the global compliance considers the whole specimen (elongations from machine).

In contrast to double cantilever beams, which are normally used to obtain the fracture properties, structural joints always develop more than one crack (see Fig. 7). In the stepped lap joints, two cracks initiated and propagated from both side of the overlap. In the double lap joints, moreover, four possible locations existed at the edges of the overlaps for cracks to initiate and propagate. All new surfaces produced by these cracks contributed to the change of the system potential energy. Therefore, the total crack length, measured with the four crack gages, was taken into account to describe the crack propagation, instead of the crack length of one single crack. Accordingly, only half of the specimen width was attributed to each crack. Fig. 10 shows the relationship of the compliance versus the total crack length from representative joints of both joint types. The global and local compliances had similar trends for each type of joint and were not sensitive to the beginning of the unstable crack propagation.

The strain of back face strain gages is another parameter that may be sensitive to an increase in crack length. Fig. 11 shows the back face strain against the total crack length for representative joints of both joint types. The back face strains showed a high sensitivity to the initial stage of crack propagation up to approximately 30 mm total crack length. Subsequently, the curves leveled off and approached an almost constant value when the crack started to propagate unstably.

Table 6. Fitted A and B values for compliance calculation.

	Depending on global compliance		Depending on local compliance	
	A	B	A	B
DLJ	0.028±0.003	0.038±0.024	0.016±0.002	0.066±0.036
SLJ	0.038±0.007	0.211±0.048	0.030±0.007	0.024±0.067

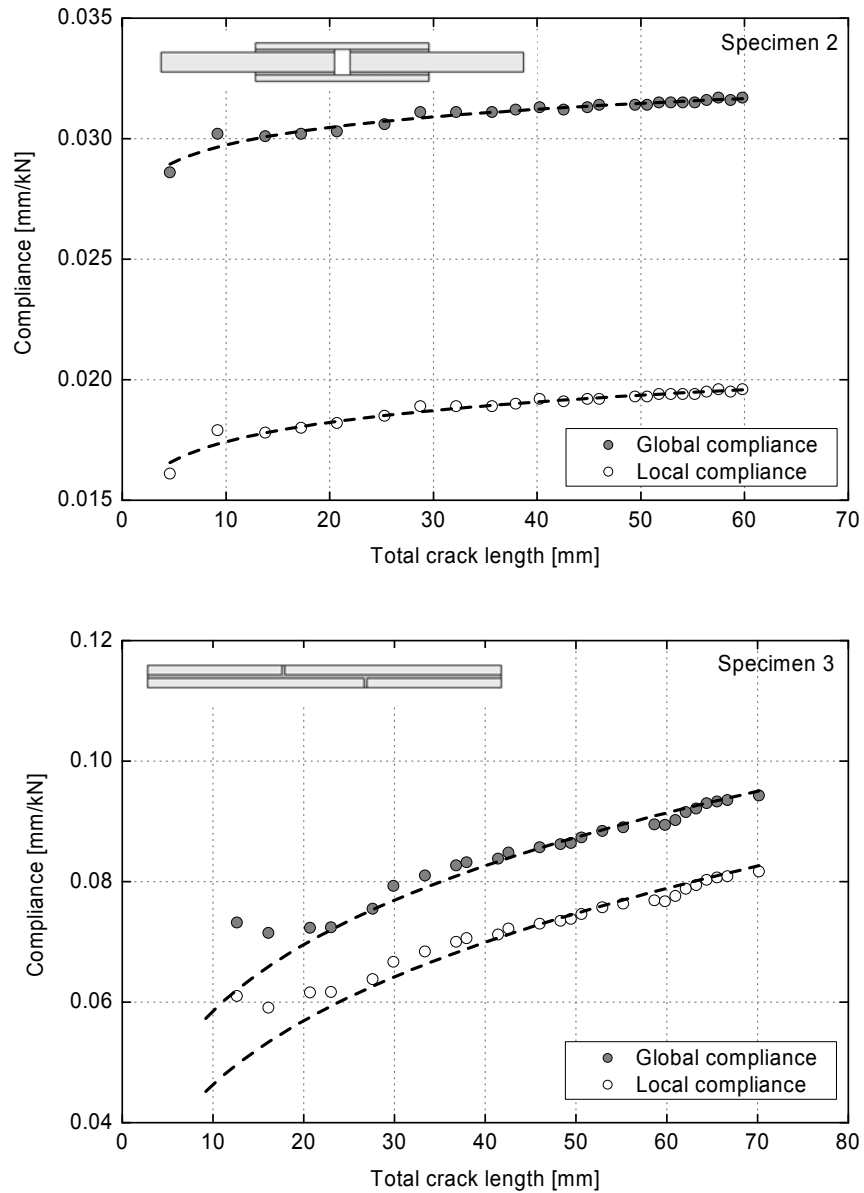


Figure 10. Compliance versus total crack length of typical DLJ (above) and SLJ (below) (from measurements and fitted).

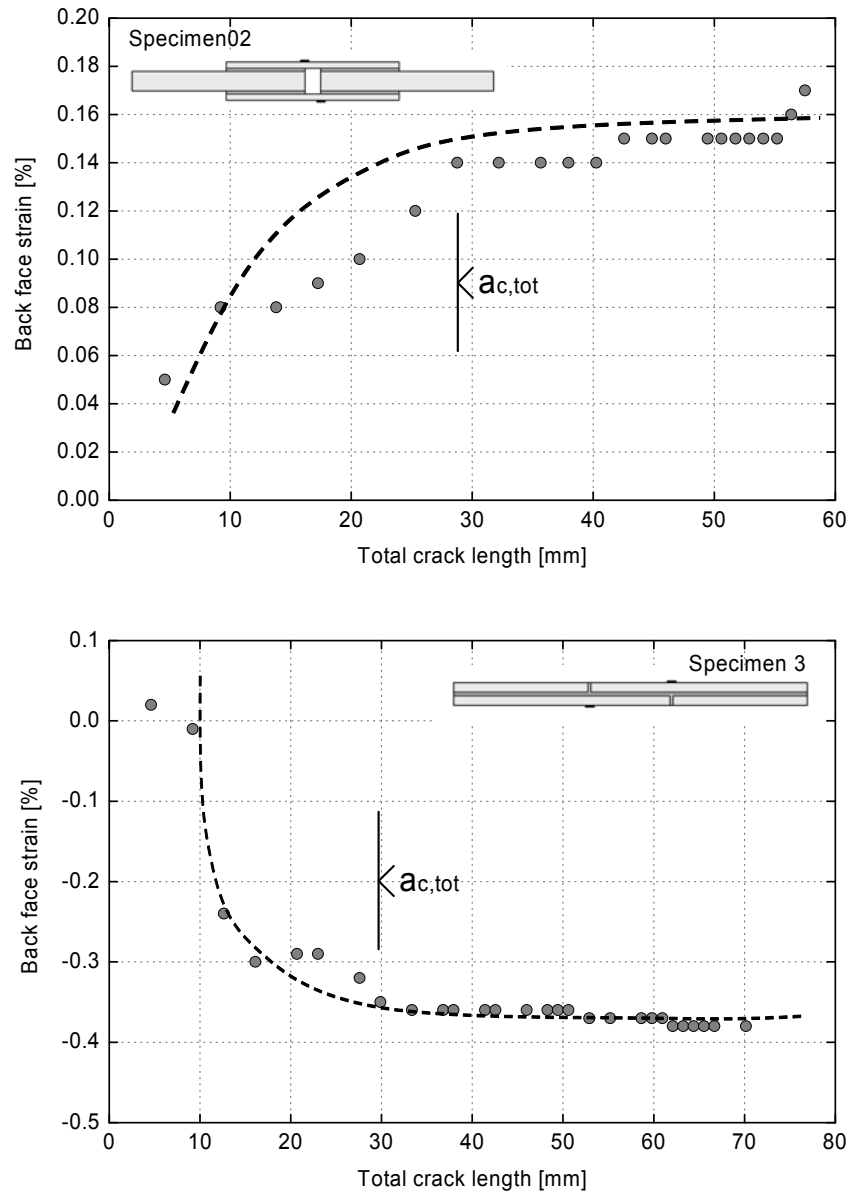


Figure 11. Back face strain versus total crack length of typical DLJ (above) and SLJ (below) (from measurements and fitted).

4.4 Comparison of crack propagation rate

Time-total crack length curves were used to compare the crack propagation rate in the laminates of DLJs and SLJs, as shown in Fig. 12. The crack propagation rate corresponds to the slope of the curves. Because of the different loading rates used (0.5 and 1.0 mm/min for SLJs and DLJs, respectively), the time was normalized by the loading rate to facilitate comparison. SLJs showed a higher propagation rate from crack initiation up to the unstable crack growth than double lap joints. The propagation rate of DLJs was much smaller in the first stage and then increased abruptly.

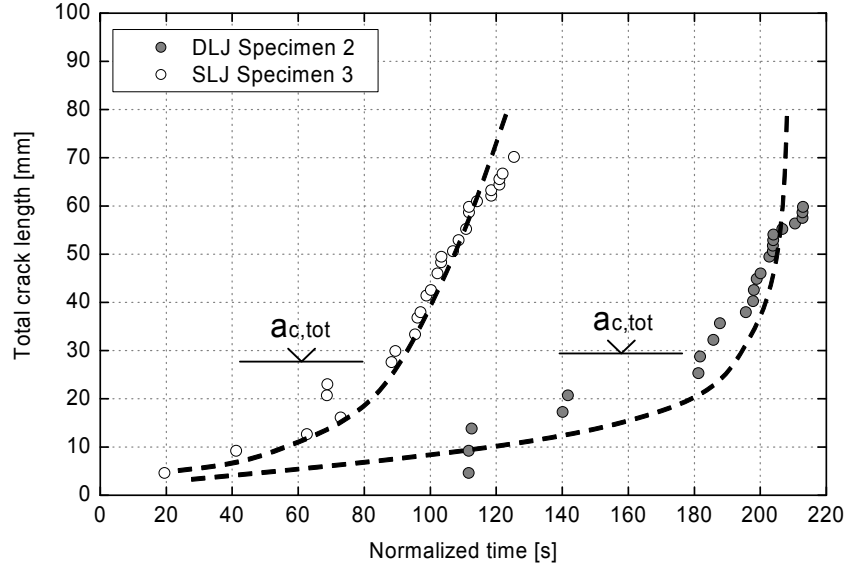


Figure 12. Comparison of crack propagation rate of typical DLJ and SLJ (from measurements and fitted).

4.5 Critical strain energy release rate

The critical strain energy release rate, G_c , in a plate with a through-thickness crack, assuming linear elastic behavior, is calculated according to [2]:

$$G_c = \frac{P_c^2}{2b} \frac{dC}{da} \quad (3)$$

where, P_c is the applied load at failure, b the specimen width, a the crack length and C the compliance, which is defined according to Eqs. (1) and (2).

Combining Eqs. (2) and (3) gives Eq. (4) for the estimation of the critical strain energy release rate:

$$G_c = \frac{BP_c \delta}{2ba_c} \quad (4)$$

Fig. 13 shows the resulting G calculated from the specimen and joint elongation (global and local compliance), as a function of the total crack length for both joint types. In an ideal model, after an increasing curve, a plateau is reached, which refers to the stable crack propagation and its value is defined as the critical strain energy release rate, G_c . The crack length at the end of this plateau, before the curve starts decreasing (unstable propagation), is the critical crack length, a_c . As shown in Fig. 13, the increasing part of the curve could not be captured by the measurements. The DLJs measurements, however, showed a clear peak in the

curve with only a short plateau, while this peak was not so obvious for SLJs. Hence, the peak values of G were taken as the critical strain energy release rate and the corresponding total crack length as the critical total crack length, $a_{c,tot}$. The corresponding results are summarized in Table 7. The G values for the local and global compliance compared well, as shown in Fig. 13. Hence, similar values of G_c were obtained based on global and local compliance. This proved that G_c is not dependent on the system whose energy change is considered.

Table 7. Critical strain energy release rate (G_c) and total critical crack length ($a_{c,tot}$) for DLJs and SLJs.

	G_c [mm/J ²] based on global compliance	G_c [mm/J ²] based on local compliance	G_c [mm/J ²] average	$a_{c,tot}$ [mm] average
DLJ				
Specimen 1	999.8	1212.5	1106.2	17.3
Specimen 2	1419.8	1583.1	1501.5	28.8
Specimen 3	1680.8	1720.9	1700.9	38.0
Average			1436.1±302.7	28.0±10.4
SLJ				
Specimen 1	577.0	520.4	548.7	12.7
Specimen 2	723.5	697.0	710.3	25.3
Specimen 3	913.1	863.9	888.5	29.9
Average			714.2±172.4	22.6±8.9

The resulting average G_c from SLJs (714.2 J/m²) was 49.7% of the value from DLJs (1436.1 J/m²). This difference is supported by theory, which states that G_c depends on the material properties and fracture mode ratio. Neither DLJs nor SLJs have pure mode fracture; the calculated G_c is the critical strain energy release rate for mixed mode fracture with a certain fracture mode ratio. In DLJs, mode II fracture, driven by shear stresses, is dominant in contrast to SLJs, where mode I fracture, driven by peeling stresses, is dominant. As G_c for mode II fracture is always higher than G_c for mode I fracture [16], a higher value of G_c was obtained for DLJs than for SLJs.

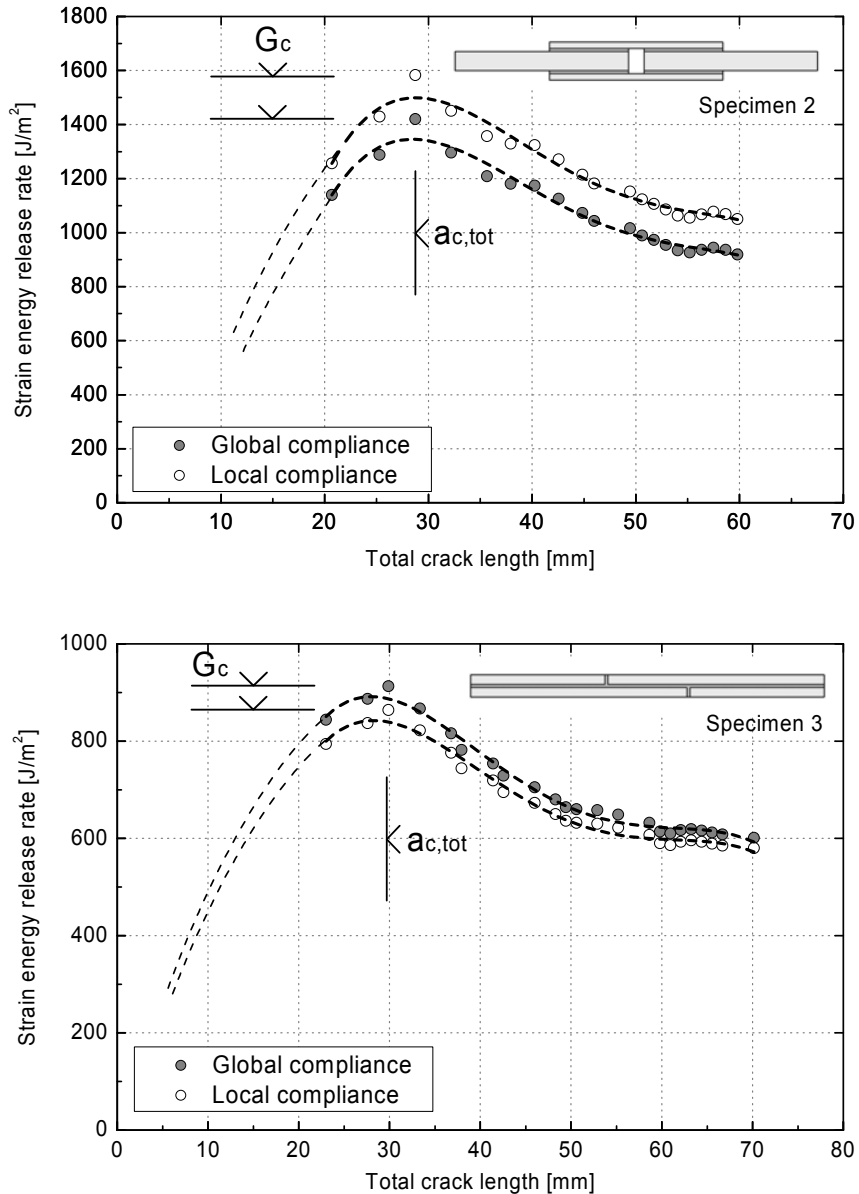


Figure 13. Strain energy release rate versus total crack length of typical DLJ (above) and SLJ (below) (from measurements and fitted).

For both joint types, the average critical crack length, which is one fourth of the total critical crack length (see Section 4.3), was much shorter than half of over lap length (25 mm), which is an upper bound of the critical crack length according to [3, 4]. The total critical crack length, given in Table 7, can also be identified in Figs. 11 and 12. The back face strain curves (in Fig. 11) started to level off when the total critical crack length was reached. Similarly, the crack propagation rate (in Fig. 12) exhibited a sudden increase, particularly for DLJs, and unstable crack growth occurred when the total critical crack length was reached.

5 CONCLUSIONS

Adhesively bonded double and stepped lap joints composed of pultruded GFRP laminates and epoxy adhesives were experimentally investigated under quasi-static axial tensile loading. The following conclusions were drawn:

1. Double lap joints showed a typical, almost linear behavior under axial tensile stresses, up to sudden and brittle failure. Stepped lap joint showed two stages of failure: adhesive failure in the small joint gap perpendicular to loading and failure of the whole joint. The gap failure changed the joint configuration from stepped lap (symmetric configuration) to single lap (non-symmetric configuration) with a corresponding decrease in joint stiffness. The adhesive-filled gaps did not significantly affect the symmetric joint behavior before adhesive failure in the gap. The dominant failure mode for both types of joints was a fiber-tear-off failure, which occurred in the outer mat layers of the GFRP laminates.
2. Though the dominant failure mode of both types of joints was considered as very brittle and sudden, it was still possible to catch the crack initiation using both crack propagation gages and back face strain gages. The crack initiation phase was short for both joint types. Unstable crack propagation occurred at crack lengths smaller than 20% of the overlap length.
3. The joint compliance calculated from measured joint elongation as well as the back face strains proved to be sensitive to describe the crack propagation.
4. The critical strain energy release rate, G_c , was calculated. A higher value of the critical strain energy release rate was obtained for DLJs than for SLJs due to different dominant fracture modes (mode II for DLJ, mode I for SLJ).

ACKNOWLEDGEMENT

The authors would like to thank the Swiss National Science Foundation (Grant No 200021-103866/1), Sika AG, Zurich (supplier of the adhesives) and Fiberline Composites A/S, Denmark (supplier of the pultruded laminates) for the support of this research.

REFERENCES

- [1] Abdel-Wahab MM, Ashcroft IA, Crocombe AD, Smith PA. Finite element prediction of fatigue crack propagation lifetime in composite bonded joints. *Composite Part A* 2004; 35: 213-222.
- [2] Ashcroft AI, Hughes DJ, Shaw SJ. Mode I fracture of epoxy bonded composite joints: 1. Quasi-static loading. *International Journal of Adhesion & Adhesives* 2001; 21: 87-99.
- [3] Hadavinia H, Kinloch AJ, Little MSG, Taylor AC. The prediction of crack growth in bonded joints under cyclic-fatigue loading. I. Experimental studies. *International Journal of Adhesion & Adhesives* 2003; 23: 449-461.
- [4] Hadavinia H, Kinloch AJ, Little MSG, Taylor AC. The prediction of crack growth in bonded joints under cyclic-fatigue loading. II. Analytical and finite element studies. *International Journal of Adhesion & Adhesives* 2003; 23: 463-471.
- [5] Blackman BRK, Hadavinia H, Kinloch AJ, Paraschi M, Williams JG. The calculation of adhesive fracture energies in mode I: revisiting the tapered double cantilever beam (TDCB) test. *Engineering Fracture Mechanics* 2003; 70: 233-248.
- [6] Blackman BRK, Kinloch AJ, Paraschi M. The determination of the mode II adhesive fracture resistance, G_{IIc} , of structural adhesive joints: an effective crack length approach. *Engineering Fracture Mechanics* 2005 ; 72: 877-897.
- [7] Cheuk PT, Tong L, Wang CH, Baker A, Chalkley P. Fatigue crack growth in adhesively bonded composite-metal double-lap joints. *Composite structures* 2002; 57: 109-115.
- [8] Giare GS, Mulholland DJ, Felton RF. Experimental investigation of the effect of geometry on the efficiency of double lap joint using fracture mechanics technique in shear mode (mode II). *Engineering Fracture Mechanics* 1992; 41: 487-497.
- [9] Keller T, Vallée T. Adhesively bonded lap joints from pultruded GFRP profiles. Part I: stress-strain analysis and failure modes. *Composites: Part B* 2005; 36: 331-340.
- [10] Keller T, Vallée T. Adhesively bonded lap joints from pultruded GFRP profiles. Part II: Joint strength prediction. *Composites: Part B* 2005; 36: 341-350.
- [11] Keller T, Tirelli T. Fatigue behavior of adhesively connected pultruded GFRP profiles. *Composite Structures* 2004; 65: 55-64.
- [12] Vallée T, Keller T. Adhesively bonded lap joints from pultruded GFRP profiles. Part III: Effects of chamfers. *Composites Part B* 2006; 37(4-5): 328-336.

-
- [13] Kim HS, Lee SJ, Lee DG. Development of a strength model for the cocured stepped lap joints under tensile loading. *Composite structures* 1995; 32: 593-600.
- [14] Kim JH, Park BJ, Han YW. Evaluation of fatigue characteristics for adhesively-bonded composite stepped lap joint. *Composite structures* 2004; 66: 69-75.
- [15] De Castro J, Keller T. Ductile double-lap joints from brittle GFRP laminates and ductile adhesives. Part I: Experimental investigation. *Composites Part B*, in review.
- [16] Dowling, Norman E. *Mechanical behavior of materials: engineering methods for deformation fracture and fatigue*. Upper Saddle River, N.J.: Pearson Prentice-Hall, 2007.

2.3 Modeling of mechanical and fracture behavior under quasi-static loading

Summary

For complex structural joints, fracture behavior can be predicted by evaluating whether the critical strain energy release rate, G_c , is reached under mixed mode loading conditions. Since the values of critical strain energy release rate can be different for various mixed modes, the prediction of fracture for a structural joint requires the establishment of a mixed mode fracture criterion. In practice, a mixed mode fracture criterion for a certain composite material, corresponding to crack initiation and propagation respectively, can be established based on the experimentally obtained values of G_c for Mode I and II fracture together with values obtained from mixed mode fracture specimens in which the mode mixity is known.

In Section 2.1, the applicability of LEFM was validated for fracture joints, and values of G_{IC} and G_{IIC} for Mode I and II fracture were obtained using DCB and ELS specimens. Similarly in Section 2.2, LEFM was applied to structural joints (DLJs and SLJs) and the critical strain energy release rate was calculated using ECM. During the fracture of DLJs and SLJs, crack initiation and propagation were driven by combined through-thickness tensile (peeling) and shear stresses. A loading combination resulted in a mixed mode fracture and the obtained critical strain energy release rate was therefore the total strain energy release rate ($G_{C,tot}$), which designates the sum of strain energy release rate components for Mode I and II and their ratio is designated as the fracture mode mixity. The fracture mode mixity for DLJs and SLJs, however, was unknown in Section 2.2 because the experimental compliance method used considered only the global behavior.

This paper attempts to cover Task 2.3-2.6 in Fig. 1: to compare and further validate methods for calculating the SERR, to determine the fracture mode mixity using VCCT and then to establish a mixed mode fracture criterion. The fracture behavior of adhesively-bonded DLJs and SLJs composed of pultruded GFRP laminates subjected to quasi-static tensile loading was numerically modeled using finite element analysis. The sensitivity of VCCT to major FEA parameters was checked in terms of the model dimension, element size and shape, crack length ratio for DLJs and crack propagation paths. The values of G_{tot} , obtained from the

experimental compliance method (SLJs in Section 2.2 and DLJs in Section 2.4) and VCCT that was validated for DCBs and ELSs in Section 2.1 were compared. Good agreement was found for SLJs while deviations were observed for DLJs due to small stiffness changes. The fracture mode mixities were determined using VCCT for both structural joint types and a non-convex mixed mode fracture criterion for crack initiation and propagation was established.

Reference details

This paper, “Mixed-mode fracture of adhesively-bonded pultruded composite lap joints” by Ye Zhang, Anastasios P. Vassilopoulos and Thomas Keller, was submitted to Engineering Fracture Mechanics on December 15th, 2009.

MIXED-MODE FRACTURE OF ADHESIVELY-BONDED PULTRUDED COMPOSITE LAP JOINTS

Ye Zhang, Anastasios P. Vassilopoulos and Thomas Keller

Composite Construction Laboratory (CCLab),
Ecole Polytechnique Fédérale de Lausanne (EPFL),
Station 16, Bâtiment BP, CH-1015 Lausanne, Switzerland

ABSTRACT

The fracture behavior of adhesively-bonded double- and stepped-lap joints (DLJs and SLJs) composed of pultruded glass fiber-reinforced polymer composite laminates and subjected to axial tension was experimentally investigated and numerically modeled. Two methods were used for the calculation of the strain energy release rate: the experimental compliance method (ECM) and the virtual crack closure technique (VCCT). Their results showed good agreement for SLJs while significant deviations were observed for DLJs due to small stiffness changes. The ECM results were sensitive to these small changes and VCCT accuracy was affected by the inability of the FEA to accurately model behavior before visual crack initiation. The dominant fracture mode changed from Mode I to Mode II in the case of SLJs, while an almost constant mode ratio was retained for the DLJs in the applied loading range. A non-convex mixed mode fracture criterion was established for crack initiation and propagation based on the VCCT results. ECM and VCCT proved applicable for the interpretation of the fracture mechanics data of the structural joints examined, provided that stiffness degradation can be accurately described.

KEYWORDS

Pultruded composites; fracture mechanics; fracture criterion; crack growth; civil engineering structures; adhesively-bonded joints

1 INTRODUCTION

Being well adapted to the nature of fiber-reinforced polymer (FRP) composites, the use of adhesive bonding in a lap joint configuration is an advantageous connection method for structural FRP components. Contrary to what occurs in pre-cracked fracture joints, cracks in structural joints initiate naturally from small material defects (voids, microcracks or inhomogeneities) in an uncontrollable way. Crack initiation and propagation are caused by combined through-thickness tensile (peeling) and shear stresses, a loading combination which is characteristic of lap joints [1]. As a result of the complex fracture behavior of adhesively-bonded composite structural joints, much research has been performed to investigate the fracture mechanisms and develop appropriate modeling techniques [2-7].

To describe the fracture behavior of this type of joint, linear-elastic fracture mechanics theory, where the strain energy release rate, G , is considered as the fracture parameter, is normally used, e.g. [2-11]. The authors sought to find accurate analytical solutions for the strain energy release rate during the fracture of composite single-lap joints (SLJs) [5], or even metal-to-metal double-lap joints (DLJs) under static [9] or fatigue loading [10]. Although good agreement was found in some cases when compared to numerical results, the analytical solutions present significant drawbacks since they are limited to the examined joint configuration. Furthermore, the fracture modes (I and II) can be differentiated only if the proportion between the shear and normal stresses is known. The experimental compliance method (ECM) successfully used for Mode I and II fracture analysis appears to be a very practical alternative for the calculation of G . However, it has seldom been used for structural joints and, to the authors' knowledge, no comparison to other methods is available. Moreover, this method cannot estimate the mode mixity, which changes with crack propagation.

An alternative to the above-mentioned methods is the numerical solution using finite element analysis (FEA). Based on Irwin's virtual crack closure method (CCT) [12] and the assumption of very small crack increments, Δa , the virtual crack closure technique (VCCT) was developed [13] and, thanks to its excellent adaptability to complex structural joint configurations and ability to describe fracture mode mixity, has been widely used, e.g. for adhesively-bonded composite and metal/composite hybrid DLJs and SLJs [2-5, 7-10] and T-joints [6]. The sensitivity of the method to the selection of several parameters has been numerically investigated in the past, e.g. the effects of the element size [4, 11, 14], or element

shape [11, 14]. Element sizes of between $1/32$ and $1/4$ of crack length or between $1/16$ and $1/2$ of specimen thickness and the use of square elements were recommended. However, to the authors' knowledge, numerical results obtained using VCCT have never been compared to ECM results.

Knowledge of the mode mixity allows the formulation of a fracture initiation or propagation criterion, which, according to the literature, e.g. [15], can be expressed in terms of the Mode I and II strain energy release rate components by a canonical elliptic equation. A wide range of composite materials fulfill the fracture criteria of a convex form (with the exponents of the ellipse equation ranging between 1 and 3), as for instance reported for graphite/epoxy [15], glass/epoxy [16] and carbon/PES [17] materials. Nevertheless, non-convex forms have also been reported, e.g. for glass/PMMA [18], carbon/epoxy [19] and carbon/PEEK [19] materials. Although the aforementioned fracture loci are limited by the critical values of Mode I and Mode II components, this is not the rule as can be seen in [20] for glass/epoxy, glass/vinyl ester and glass/polyester composite laminates.

Most of the above investigations consider mainly joints used in the aeronautics and/or automotive industries and only a small number of investigations can be found in the field of civil engineering applications. In civil engineering structures, pultruded profiles are used in most of these cases, whose fiber architecture often significantly differs from that of laminated components and adhesive layer thicknesses are in the range of 1 to 3 mm to compensate for tolerances. The fracture behavior of double-cantilever-beam (DCB) and end-loaded-split (ELS) joints, both composed of adhesively-bonded pultruded laminates, was investigated in [21], and it was demonstrated that current G calculation methods, including the ECM and VCCT, are applicable to these materials and joint configurations. An experimental study on the fracture behavior of structural DLJs and SLJs under quasi-static loads was performed in [22]. The ECM was used to determine the total strain energy release rates for both joint types. However, the applicability of the VCCT to structural joints for civil engineering applications has not yet been validated and or compared to experimental results.

The present work addresses this problem. Results obtained using the ECM and VCCT, based on the quasi-static investigation of adhesively-bonded pultruded DLJs and SLJs, are compared. Experimental results from previous publications of the authors were used: SLJ results presented in [22] and DLJ results reported in [23]. The sensitivity of the VCCT to

modeling parameters such as element size and shape and model dimension (2D or 3D) was evaluated. Based on obtained stiffness (compliance) variation and strain energy release rate values, a mixed-mode fracture criterion was formulated to describe the fracture behavior of structural joints.

2 EXPERIMENTAL INVESTIGATIONS

2.1 Joint configurations and materials

Balanced double-lap and stepped-lap joints composed of pultruded glass fiber-reinforced polymer (GFRP) laminates and a two-component epoxy adhesive were used. The laminate's width was 50 mm and the thicknesses 12 and 6 mm. The overlap length was 50 mm and the adhesive thickness 2 mm for both joint types. The geometric configurations are shown in Fig. 1.

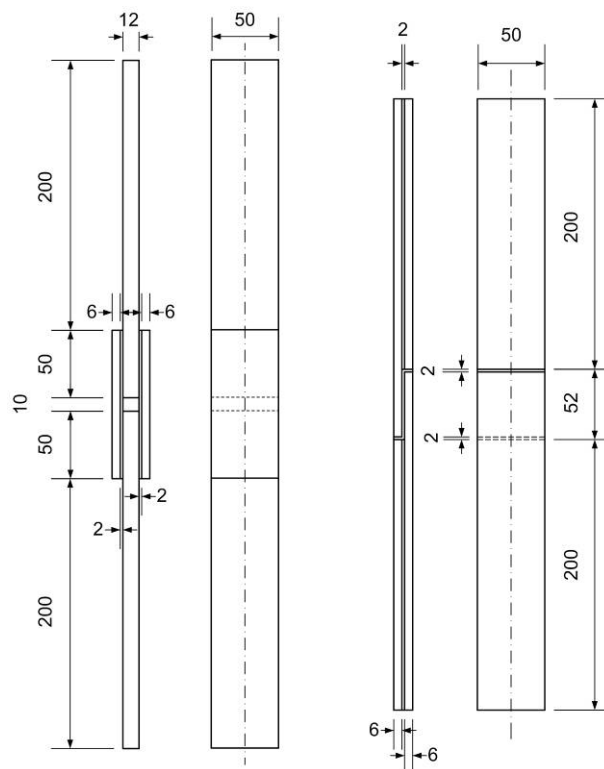


Figure 1. Geometric configurations of DLJs and SLJs.

The laminates (supplied by Fiberline A/S, Denmark) consisted of E-glass fibers and isophthalic polyester and were both composed of mat layers on the outside and rovings in the core. A mat layer consisted of a chopped strand mat (CSM) and a woven mat $0^{\circ}/90^{\circ}$

stitched together. The 12-mm-thick laminate comprised two mat layers, while the 6-mm-thick laminate comprised only one mat layer on each side. All laminates were covered by a polyester surface veil of 40 g/m².

Burn-off tests were performed to determine the fiber layer weights, while the layer thicknesses were estimated using an optical microscope; the resulting fiber volume fractions and mean thicknesses of each layer are given in Table 1. The material properties of all layers were subsequently estimated by using the rule of mixture or derived experimentally, see Table 1. In the case of the mat layers, only 35% of the fiber volume fraction was considered as being effective in the axial direction. This value was estimated by the comparison of the experimental and FE results obtained for the laminates under axial tensile and bending loading. The mean tensile strength and Young's modulus of the thick laminates were 355 MPa and 34.4 GPa respectively, and 283 MPa and 31.4 GPa for the thin ones [22]. A two-component epoxy resin (SikaDur 330 from Sika AG) was used for the bonding. The measured mean tensile strength of this adhesive was 38.1 MPa, the Young's modulus 4.6 GPa, and the strain to failure 1.0% [22]. All specimens were manufactured under ambient laboratory conditions. Before manufacturing, the surfaces of the bonding region were mechanically abraded with sandpaper and then chemically degreased using acetone. To ensure a constant thickness of the adhesive and good alignment of the GFRP laminates, a special aluminum frame was designed and employed for the production of the joints. After manufacture, all specimens were cured under ambient laboratory conditions for ten days.

2.2 Set-up and instrumentation

For each joint type, five specimens were examined under ambient laboratory conditions. Axial tensile loads were applied using an INSTRON testing rig of 100-kN capacity. All specimens were loaded up to failure at a displacement rate of 1 mm/min for DLJs and 0.5 mm/min for SLJs. An HBM/Spider8 was used to record the measured experimental data, including load, axial displacement and crack length at a frequency of 800 Hz. Load and displacement were directly recorded by the machine's transducers. Total specimen elongation was recorded since the effect of the laminates outside of the joint on joint behavior was small.

Table 1. Fiber volume fractions and properties used for FE modeling (* experimentally determined property)

Joint and material data	6-mm GFRP		12-mm GFRP		Veil	Adhesive
	Roving	Mat	Roving	Mat/Mat		
Layer thickness [mm]	3.0	1.0	8.0	0.5/1.0	0.5	2.0
Fiber vol. fraction [%]	57.8	45.7	52.7	46.9	-	-
E_{11} [GPa]	42.9	18.9	39.5	19.3	3.2	4.6*
E_{22} [GPa]	3.5*	18.9	3.5*	19.3	3.2	4.6*
E_{33} [GPa]	3.5*	3.5*	3.5*	3.5*	3.2	4.6*
G_{12} [GPa]	2.7	7.4	2.4	7.1	1.2	1.7
G_{23} [GPa]	1.4	1.5	1.4	1.5	1.2	1.7
G_{31} [GPa]	2.7	1.5	2.4	1.5	1.2	1.7
ν_{12}	0.32	0.27*	0.33	0.27*	0.38	0.37
ν_{23}	0.27*	0.36	0.27*	0.36	0.38	0.37
ν_{31}	0.03	0.36	0.03	0.36	0.38	0.37

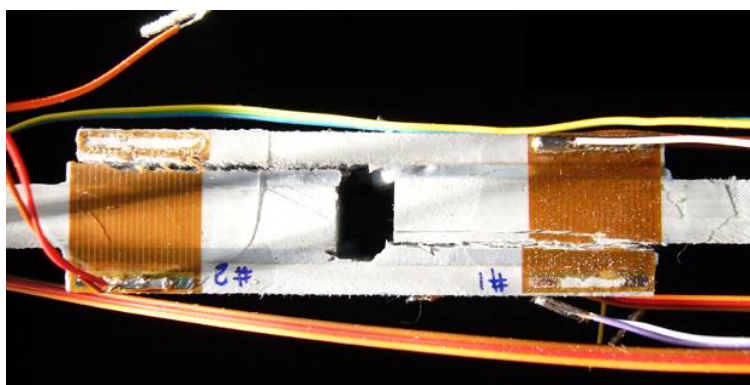


Figure 2. Typical failure mode of DLJs (also showing crack gages).

Crack propagation gages (type HBM/RSD20) consisting of 20 wires spaced at 1.15-mm intervals perpendicular to the adhesive layer were employed to measure crack length of three of the five specimens, see Table 2. Each crack gage covered half of the overlap length where crack propagation was expected to occur. As the crack propagated, the wires were

progressively broken (see Fig. 2), thereby increasing the electrical resistance of the gages. Experiments showed that each crack gage was crossed by one crack and the sum of the four individually measured crack lengths (designated total crack length, a_{tot}) was therefore taken into account to describe crack propagation.

2.3 Experimental results

The measured ultimate loads and specimen elongations at failure for both joint types are given in Table 2. The crack initiation was identified using crack gages and the corresponding loads and elongations are also included in Table 2. DLJs exhibited an almost linear load-elongation response up to the ultimate load of 43.5 ± 2.3 kN, as shown in Fig. 3. Joint stiffness started to decrease at approximately 20 kN, well below the crack initiation load indicated by the crack gages (approx. 35.9 ± 2.5 kN). However, stiffness degradation up to ultimate failure remained very low, approximately 2-3%. As shown in Fig. 2, fiber-tear failure occurred at ultimate load in a sudden way without prior visible cracking. Post-failure inspection showed that a crack initiated at one joint end in the adhesive-adherend interface. The crack then penetrated into the 12-mm laminate and generally propagated between the two mat layers. In some cases, the crack also penetrated the roving layer. Subsequently (as concluded from the crack gage measurements), another shorter crack started developing from the opposite joint end. The ratio between the short and long crack lengths was between 0.2 and 0.7, with a mean value of around 0.5. The cracks propagated until the load transfer area was too small to sustain the applied load and ultimate failure occurred.

SLJs exhibited a double-peak load-elongation response, see Fig. 4. Adhesive failure occurred first in the small transverse gaps. The stepped-lap configuration was changed to a single-lap configuration, which subsequently exhibited lower stiffness. At both gap locations, the cracks then penetrated into the adherend and propagated between the veil and mat layer from both sides towards the joint center, always having approximately the same length. Figs. 5 and 6 show that two different locations of the propagation paths could be observed: a same-side crack pattern (SLJ-1/-3/-4/-5, both cracks in the same adherend) and an opposite-side crack pattern (SLJ-2, one crack in each adherend). During crack propagation, the load could be increased while the joint stiffness steadily decreased up to the ultimate load of 10.4 ± 0.4 kN, at which fiber-tear failure again occurred. The non-linear response

therefore resulted from the progressive change in joint configuration and not from material non-linearity.

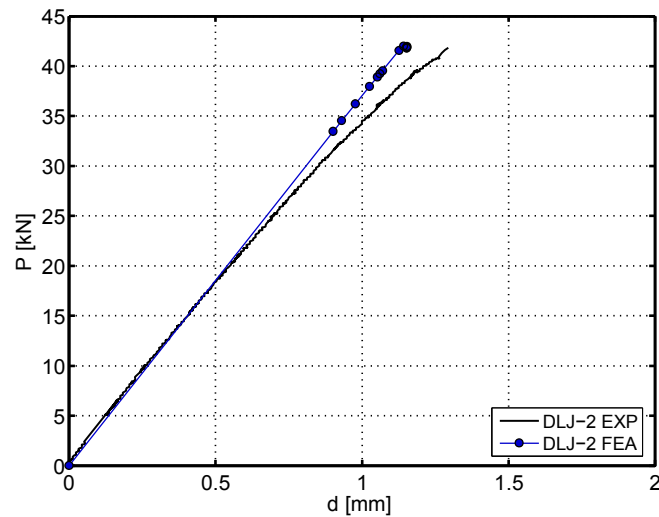


Figure 3. Load-elongation response, experimental and FEA, DLJ-2.

Table 2. Overview of experimental program and main results (* specimens with crack gages)

Specimen ID	Ultimate load [kN]	Crack initiation load [kN]	Elongation at ultimate failure [mm]	Elongation at crack initiation [mm]
SLJ-1*	10.3	3.6	1.01	0.22
SLJ-2*	10.3	4.7	1.05	0.32
SLJ-3*	11.1	4.4	1.04	0.32
SLJ-4	10.2	-	1.19	-
SLJ-5	10.0	-	1.22	-
Mean	10.4 ± 0.4	4.2±0.6	1.10 ± 0.10	0.29±0.06
DLJ-1*	43.2	38.4	1.37	1.13
DLJ-2*	42.0	33.5	1.30	0.96
DLJ-3*	42.6	35.9	1.42	1.07
DLJ-4	42.1	-	1.29	-
DLJ-5	47.5	-	1.59	-
Mean	43.5 ± 2.3	35.9±2.5	1.39 ± 0.12	1.05±0.09

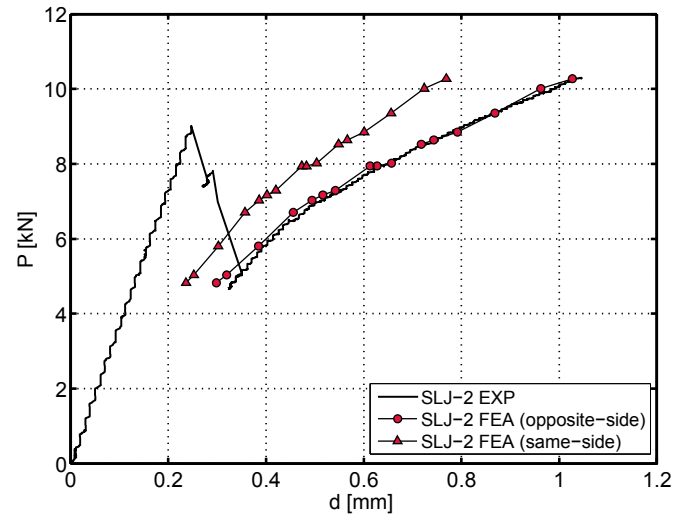


Figure 4. Load-elongation response, experimental and FEA, SLJ-2.



Figure 5. Typical failure mode of SLJ with same-side crack pattern.

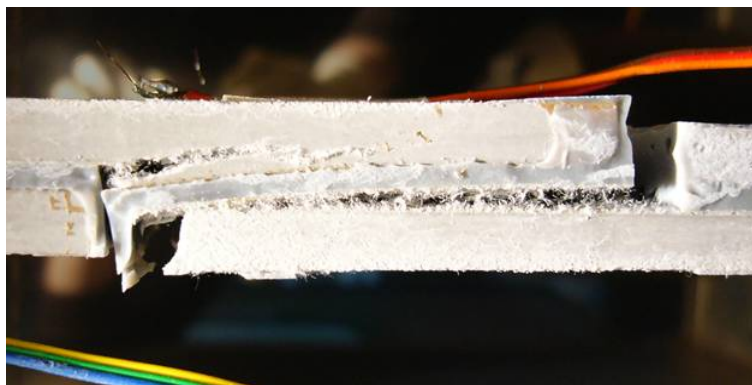


Figure 6. Typical failure mode of SLJ with opposite-side crack pattern.

2.4 Results of experimental compliance method

The compliance, C , of the DLJs and the SLJs was calculated as the ratio of the joint elongation, d , over the applied load, P , ($C = d/P$), and plotted vs. the total crack length, a_{tot} , in Fig. 7 (for DLJ-2/-3) and Fig. 8 (SLJ-2). For both joint types, the compliance exhibited an almost linearly increasing trend with crack propagation. The slope of the curves, however, was different: DLJs showed a very small compliance increase (approx. 2-3%) while a significant increase (approx. 50%) was observed for SLJs due to the much higher load eccentricity after gap failure.

The total strain energy release rate, G_{tot} , was calculated as:

$$G_{tot} = \frac{P^2}{2w} \frac{dC}{da} \quad (1)$$

where w is half of the specimen width, since half of the specimen's width is attributed to each crack gage. The calculated G_{tot} versus the crack length, a_{tot} , are presented in Fig. 9 for DLJ-2/-3 and Figs. 10 and 11 for SLJ-2/-3. For both joint types, the experimental C - a_{tot} relationships were fitted by straight lines to obtain a linear dC/da relationship. It had already been shown in a previous work by the authors [24] that linear fitting is the most appropriate for the examined joint types. Thus different strain energy release rate values are reported here compared to [22] due to the different compliance fitting method. Since structural joints do not contain a pre-crack, crack lengths $a_{tot} < 10$ mm and 16 mm for DLJs and SLJs were considered as belonging to the nucleation phase and excluded from the calculations. All curves exhibited an increasing trend without reaching a plateau however. Hence, G_{tot} , corresponding to $a_{tot} = 10$ mm (DLJs) and 16 mm (SLJs) was considered as being the representative value for crack initiation (designated INI), while the maximum G_{tot} was considered as being the strain energy release rate for crack propagation (PRO).

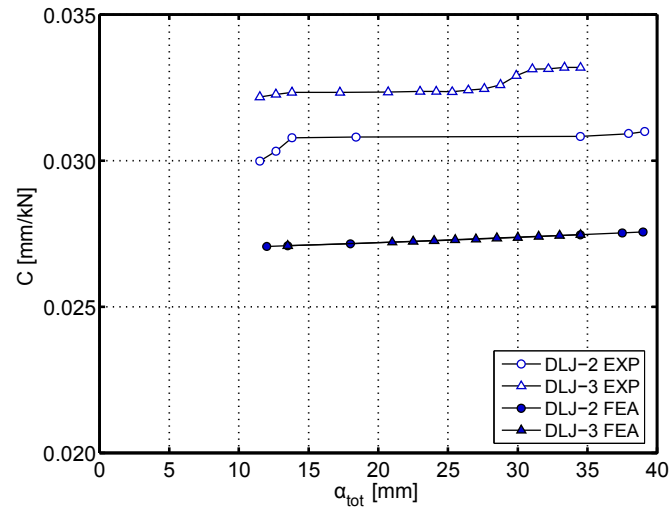


Figure 7. Compliance vs. total crack length, experimental and FEA, DLJ-2 and DLJ-3.

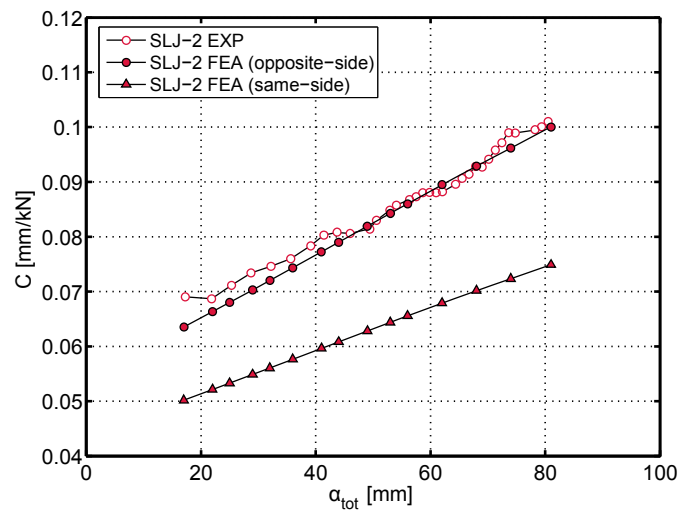


Figure 8. Compliance vs. total crack length experimental and FEA, SLJ-2 and SLJ-3.

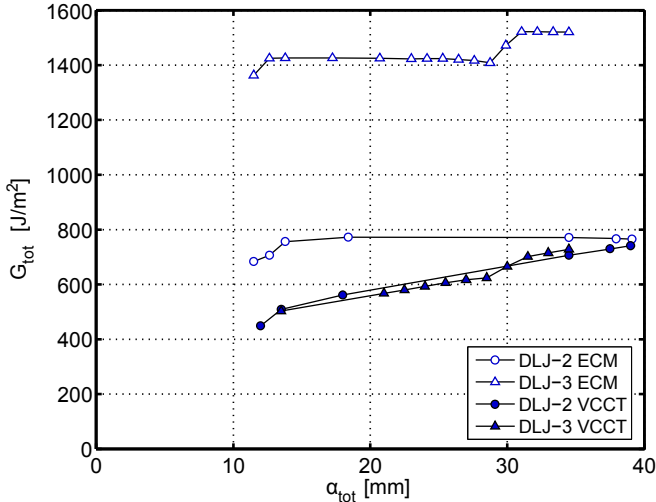


Figure 9. Strain energy release rate vs. total crack length, obtained from ECM and VCCT, DLJ-2 and DLJ-3.

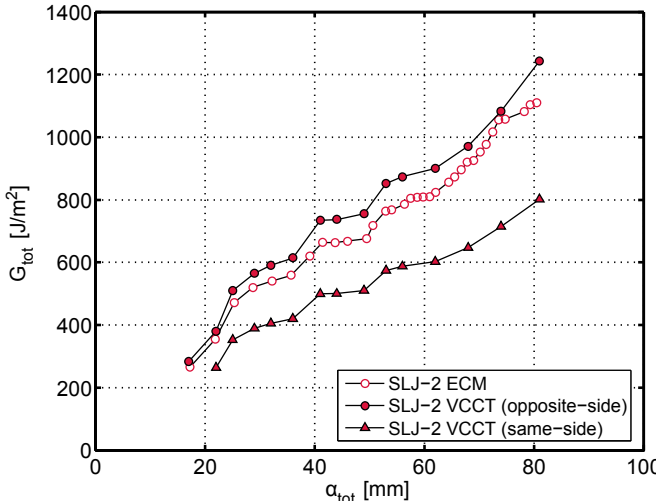


Figure 10. Strain energy release rate vs. total crack length, obtained from ECM and VCCT, SLJ-2.

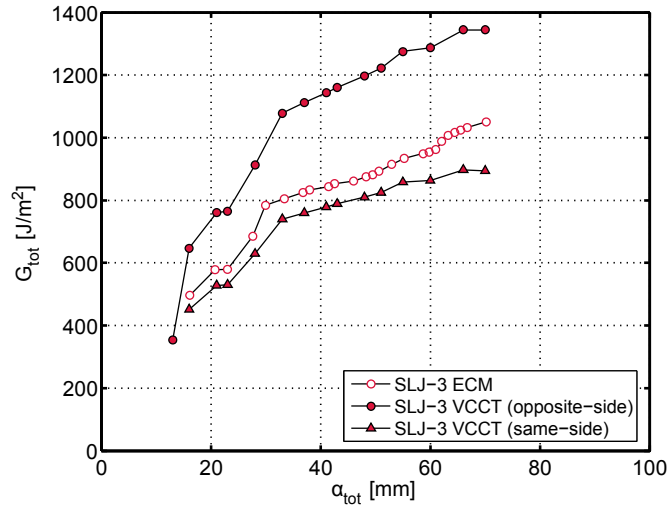


Figure 11. Strain energy release rate vs. total crack length, obtained from ECM and VCCT, SLJ-3.

3 FE MODELING AND VALIDATION OF VCCT

3.1 Overview

2D and 3D models were developed in ANSYS (version 10.0) in order to model the two joints under investigation. In 2D models, two cracks were introduced, according to what had been observed from experiments: for the DLJs between the two mat layers of the 12-mm laminates, on the upper side at one joint end and on the lower side at the opposite end (see Fig. 12). For the SLJs the cracks were introduced between the veil and the mat layer of the 6-mm laminates for opposite-side (Fig. 13) and same-side (Fig. 14) crack patterns.

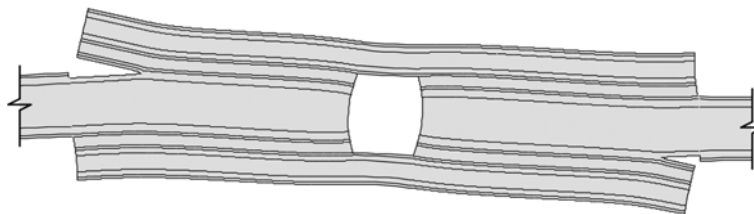


Figure 12. 2D-FE model for DLJs.

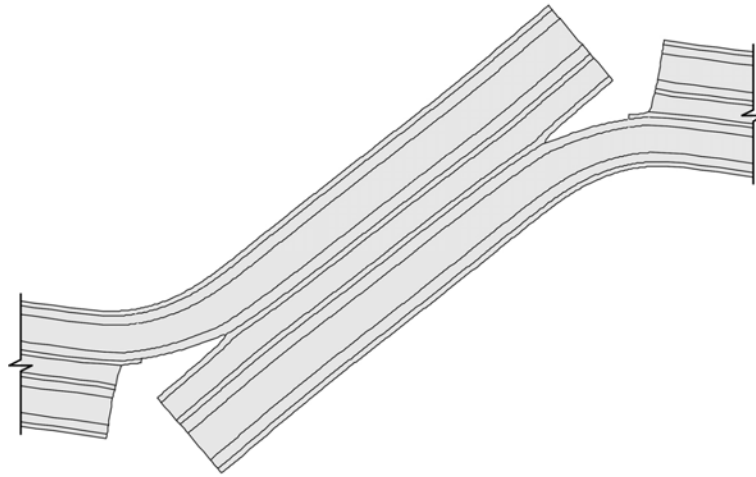


Figure 13. 2D-FE model for SLJs with opposite-side crack pattern.

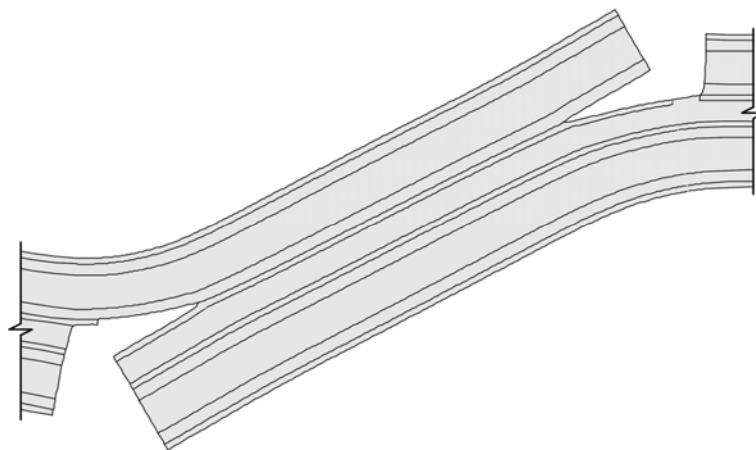


Figure 14. 2D-FE model for SLJs with same-side crack pattern.

All the layers of the laminates - veil, mat (one or two) and roving - were separately modeled; the material properties are given in Table 1. The FE models were meshed with manually controlled element size. The element types PLANE42 and SOLID 45 (2D four-node plane and 3D eight-node solid elements) were used for the 2D and 3D models respectively. One joint end was fixed, while the other was free in the load direction. Linear-elastic analysis was performed and the specimen elongations, nodal forces and nodal displacements were calculated.

3.2 Application of VCCT

The visual crack closure technique relies on accurate numerical calculation of the nodal forces at the crack tip ($F_{x,i}$ and $F_{y,i}$) and the displacements of the adjacent nodes j and k ($u_{x,j}$, $u_{y,j}$, $u_{x,k}$, $u_{y,k}$), as shown in Fig. 15 for a 2-dimensional (2D) model. G_I and G_{II} are then calculated as:

$$G_I = \frac{1}{2\Delta a} [F_{y,i} \cdot (u_{y,j} - u_{y,k})] \quad (2)$$

$$G_{II} = \frac{1}{2\Delta a} [F_{x,i} \cdot (u_{x,j} - u_{x,k})] \quad (3)$$

where Δa is the crack increment, which is equal to the element size at the crack tip. In the case of a 3D model, the product of the nodal forces and the displacement is calculated for all nodes through the width of the specimen as follows:

$$G_I = \frac{1}{2w\Delta a} \sum_{N=1}^N [F_{y_i,N} \cdot (u_{y_j,N} - u_{y_k,N})] \quad (4)$$

$$G_{II} = \frac{1}{2w\Delta a} \sum_{N=1}^N [F_{x_i,N} \cdot (u_{x_j,N} - u_{x_k,N})] \quad (5)$$

where N is the number of nodes in the specimen width direction. After crack initiation, a small angle, θ , was formed between the crack centerline and the x-axis due to unsymmetrical deformations, as shown in Fig.15. The nodal forces ($F_{\xi i}$ and $F_{\eta i}$) and displacements ($u_{\xi j}$, $u_{\eta j}$, $u_{\xi k}$, $u_{\eta k}$), expressed in the (ξ, η) coordinate system, were used thereafter.

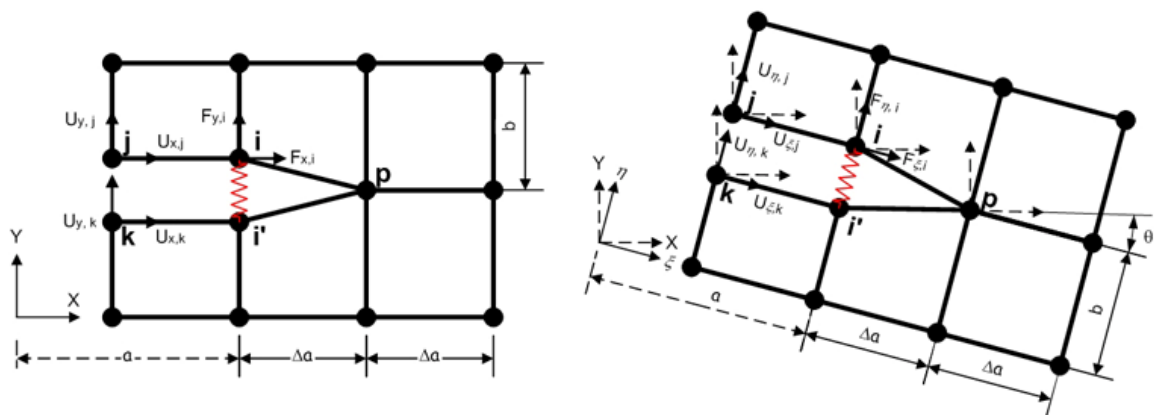


Figure 15. Nodal forces and displacements at crack tip for VCCT.

Table 3. Matrix of parametric investigations to validate VCCT

Model family	Model dimension	Element shape and size Δa and b [mm]	Crack length ratio a_2/a_1 [mm/mm]	Location of crack propagation path
1	2D, 3D	Square $\Delta a=b=0.25$	DLJ : 0.5 SLJ : 1.0	DLJ : Mat/Mat SLJ : Veil/Mat (opposite-side)
2	2D	Rectangular 9 combinations $\Delta a, b$ from 0.10/0.25/0.50	DLJ : 0.5 SLJ : 1.0	DLJ : Mat/Mat SLJ : Veil/Mat (opposite-side)
3	2D	Square $\Delta a=b=0.1/0.25/0.5$	DLJ : 0.5 SLJ : 1.0	DLJ : Mat/Mat SLJ : Veil/Mat (opposite-side)
4	2D	Square $\Delta a=b=0.25$	DLJ : 0, 0.2, 0.5, 0.8, 1 SLJ : 1.0	DLJ : Mat/Mat SLJ : Veil/Mat (opposite-side)
5	2D	Square $\Delta a=b=0.25$	DLJ : 0.5 SLJ : 1.0	DLJ : Mat/Mat, Mat/Roving, Veil/Mat SLJ : Veil/Mat, Mat/Roving (opposite-side)

3.3 FE model sensitivity analysis

3.3.1 Overview

To evaluate the effects of the FE model parameters on the VCCT results, a sensitivity analysis was performed. Five model families were created to investigate the influence of 1) the FE model dimension (2D or 3D), 2) the element shape, 3) the element size, 4) the left/right crack length ratio, a_2/a_1 , in DLJs, and 5) the location of the crack propagation path on the results. Table 3 gives an overview of the parameter combinations used. In each model, a constant load of 5 kN for SLJs and 30 kN for DLJs was applied and the total crack length was then increased stepwise from 12 mm to 92 mm. The upper limit (92 mm) was the maximum crack

length that could be measured by crack gages. Based on the crack length and applied load, the values of G_I , G_{II} and G_{tot} were then calculated using the VCCT method.

3.3.2 Sensitivity to FE model parameters

Comparison of the G_I , G_{II} and G_{tot} values obtained from the 2D and 3D models of the opposite-side SLJ vs. the crack length normalized by the total overlap length ($l_{tot} = 4.50 \text{ mm} = 200 \text{ mm}$), a_{tot}/l_{tot} , shown in Fig. 16, indicated that the dimension of FE models hardly affected the G results, with the maximum differences being less than 3%. Similar good agreement was obtained for DLJs.

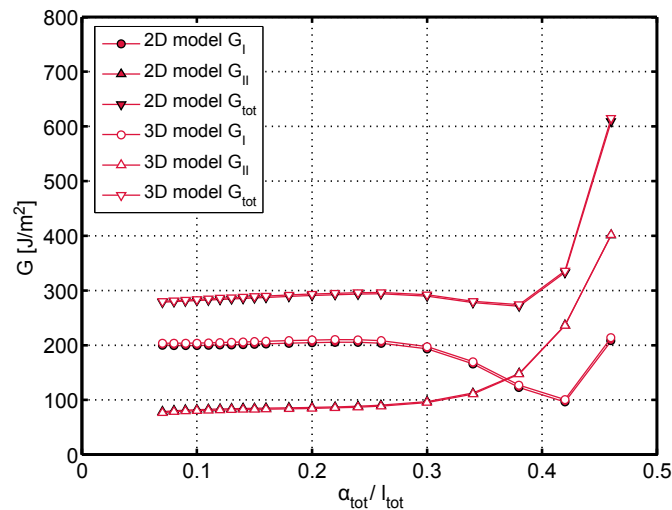


Figure 16. Comparison of strain energy release rates of 2D and 3D SLJ models.

The effects of element shape and element size on VCCT results were investigated using rectangular and square elements in model families 2 and 3 respectively. At the crack tip, the element length in the crack direction (equal to the crack increment), Δa , and the element height (transverse to the crack), b , were varied according to Table 3. The selected values are based on [25] where for DLJs of similar dimensions a height of 0.25 mm (eight element layers through the 2-mm adhesive thickness) provided stable results. The main results of this study are presented in Figs. 17 and 18 (for element shape) and Fig. 19 (for element size). Fig. 17 shows G_I , G_{II} and G_{tot} with increasing Δa (ranging between 0.1 and 0.5 mm) in the case of $a_{tot} = 36 \text{ mm}$ ($a_{tot}/l_{tot} = 0.18$) and $b = 0.25 \text{ mm}$ for both joint types. For this specific element height, the

varying element shape did not noticeably influence the G values. In Fig. 18, the fracture mode mixity G_I/G_{II} vs. Δa relationship is shown for SLJs and for different b values. When b became very small (0.10 mm), however, the effect of element shape on mode mixity cannot be ignored. This study showed that the element shape did not noticeably affect the G results (G values and ratio) unless the element height was much smaller than the element length. Fig. 19 shows G_I , G_{II} and G_{tot} with increasing Δa and square elements, again in the case of $a_{tot} = 36$ mm for both joint types. It can be seen that for both joint configurations the strain energy release rate is not affected by element size.

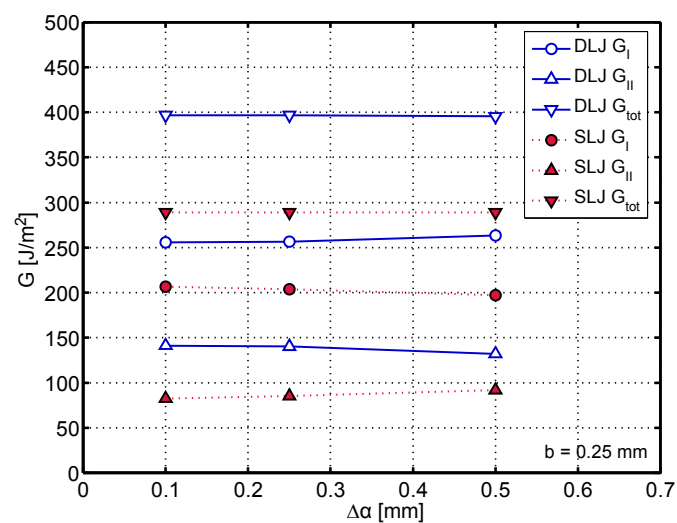


Figure 17. Comparison of strain energy release rates of FE models with different element shapes.

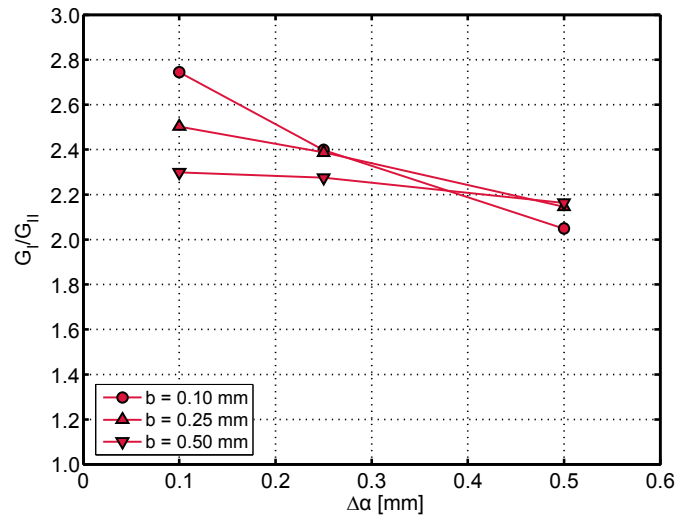


Figure 18. Comparison of fracture mode mixity for SLJs with different element shapes.

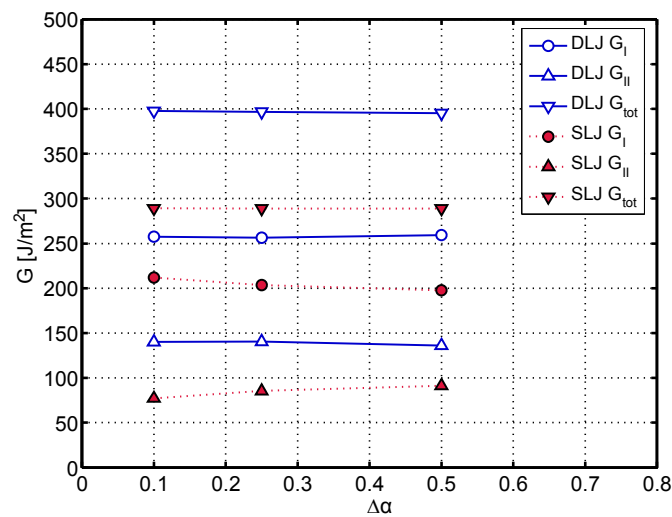


Figure 19. Comparison of strain energy release rates of FE models with different element sizes (square elements).

As described in Section 2.3, two cracks of different lengths a_1 and a_2 (long and short crack respectively) were observed in the DLJs. Based on the experimentally observed ratio range, five crack length ratios a_2/a_1 were therefore taken into account in model family 4, see Table 3. Fig. 20 shows that, if two cracks are present, the G -values only depended on the total crack length of the two cracks but not on the ratio between the two lengths.

The effect of the crack depth was also investigated (see Table 3, model family 5). Fig. 21 shows that the resulting G_{tot} for a propagating crack in DLJs significantly depends on the

location of the crack propagation paths. Highest values were obtained for a path between the mat and the roving layer, while the smallest values resulted from a path between the veil and first mat layer. Similar results were derived for the SLJs. Since the critical strain energy release rate (G_c) of the individual paths is unknown, however, no conclusion concerning the real location of the crack path (which was between the two mat layers) could be deduced from these results.

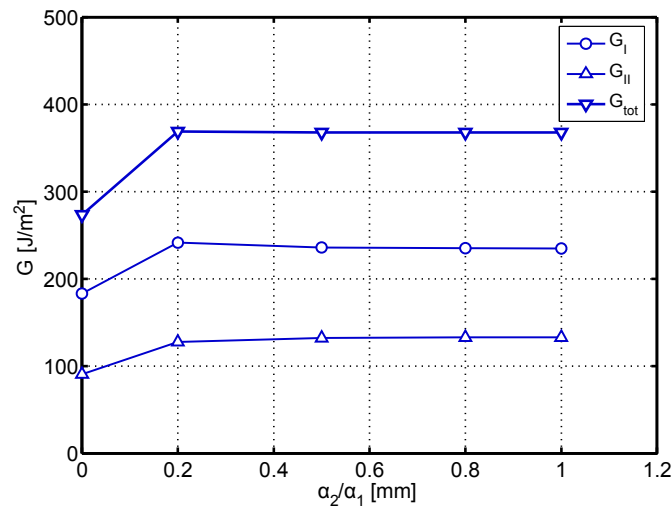


Figure 20. Comparison of strain energy release rates of FE models for DLJs with different crack length ratios.

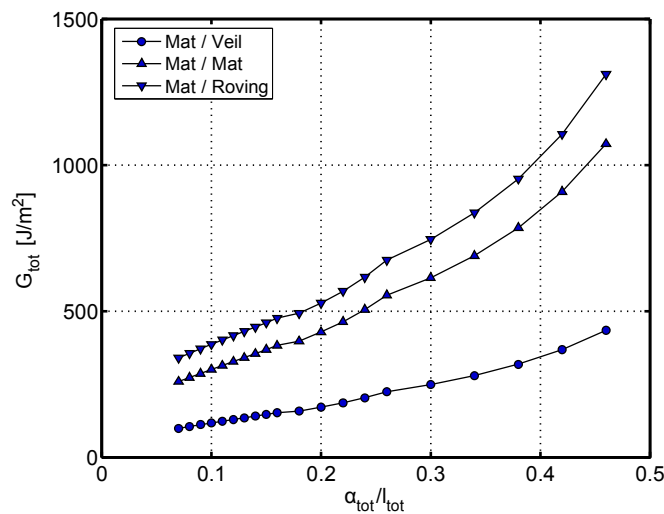


Figure 21. Comparison of strain energy release rates of FE models for DLJs with different crack location layers.

3.3.3 FE model selection and application

Based on the sensitivity analysis, the parameters of the three FE models used to simulate the behavior of the DLJs and the SLJs (opposite- and same-side model) and calculate the components of the strain energy release rate were selected as:

- 1) 2D model (due to insensitivity to model dimension),
- 2) Square elements (to fulfill the condition that height is not much smaller than length)
- 3) $\Delta a=b= 0.25$ mm in order to have an element size larger than 0.1 mm, but smaller than the thinnest material layer (here 0.5 mm (veil)),
- 4) Crack length ratio $a_2/a_1 = 0.5$ for DLJs (experimental mean value), identical crack lengths for the SLJs,
- 5) Crack position between two mat layers for the DLJs, and between the veil and mat layers for the SLJs (as observed in most cases).

The number of elements ranged from 16,000 to 33,000 based on the joint type (DLJ and SLJ) and crack pattern (opposite-side and same-side). In each model, 17 to 20 different total crack lengths, a_{tot} , ranging from 3 to 86 mm and the corresponding experimental loads were applied. The specimen elongation d , and the compliance C were obtained and compared to the measured values in order to validate the models. Based on the nodal solutions of forces and displacements, the values of G_I , G_{II} and G_{tot} were then calculated using VCCT and compared to the corresponding results obtained from ECM.

4 COMPARISON AND DISCUSSION

4.1 Comparison of DLJ results

The load-elongation behavior obtained from the FE model is compared to the experimental results obtained for specimen DLJ-2 in Fig. 3. The dots in the modeling curve correspond to the selected crack lengths a_{tot} , the lowest one corresponding to crack initiation. Experimental and FEA values compared well up to approximately 20 kN. Between this value and the assumed initiation of the first macrocrack (detected by crack gages, at approx. 33 kN in this specimen) an experimental stiffness decrease occurred, which was mainly attributed to microcracking of the GFRP laminates, which could not be simulated in the model since no crack had yet been introduced and the material properties were kept constant. The predicted stiffness decrease subsequent to crack initiation was furthermore lower than the measured

one and, finally, a total overestimation of stiffness at ultimate failure of 15-20% resulted for all five DLJs, as shown in Fig. 7 (underestimation of compliance in this case). It must be noted, however, that the total stiffness loss was very small, approximately 2-3%, well below the experimental scatter (see Section 2.3).

The values of strain energy release obtained from the ECM and VCCT are compared in Fig. 9. Only fairly good agreement was obtained for specimen DLJ-2, while in the case of DLJ-3 large deviations were observed. The disagreement can be attributed to the differences in the modeling of the joint stiffness (see Fig. 7). ECM proved to be very sensitive to the very low stiffness degradation, that is, to the slope of the compliance, dC/da . VCCT accuracy, moreover, was affected by the inaccurate FEA modeling of joint stiffness (see Fig. 3), which did not take the observed stiffness degradation before visual crack initiation into account.

4.2 Comparison of SLJ results

By using both the opposite- and same-side FE models, the load-elongation and compliance behavior was obtained for SLJ-2 and compared to the experimental results, see Figs. 4 and 8. SLJ-2 exhibited an opposite-side crack pattern and thus excellent agreement was obtained from the opposite-side model, while the same-side model results clearly deviated. The exact evaluation of crack location and pattern therefore proved significant for the accurate description of fracture behavior.

The same result was obtained for the strain energy release rate, as shown in Fig. 10 (SLJ-2, opposite-side pattern) and Fig. 11 (SLJ-3, same-side pattern). The results obtained from the corresponding models showed good agreement with the results obtained from ECM.

4.3 Fracture mode mixity

Based on VCCT, different mode mixities G_I/G_{II} , also varying with increasing crack length, resulted for the two joint types. The G_I/G_{II} ratio vs. the normalized crack length relationships for DLJ-2 and SLJ-2 (opposite-side pattern) and SLJ-3 (same-side pattern) are presented in Fig. 22.

The three cases exhibited a similar trend. For short crack lengths, G_I clearly exceeded G_{II} in all examined cases (with ratios between 1.7-2.5). For longer crack lengths, up to 40 mm, the

ratio decreased and reached a plateau at a high level for SLJ-2 (approx. 2.4), a medium level for DLJ-2 (approx. 1.8), and less pronounced at a lower level, but still above 1.0, for SLJ-3. Crack length measurements stopped at this point for DLJs while the ratio started decreasing for both SLJs and, for longer crack lengths of between 40 mm and 86 mm it dropped below 1.0, signifying that G_{II} exceeded G_I . The trend of these curves and the change in the dominant fracture mode from Mode I to Mode II for SLJs agreed well with results presented in the literature for joints with similar geometric configurations e.g. [2, 4].

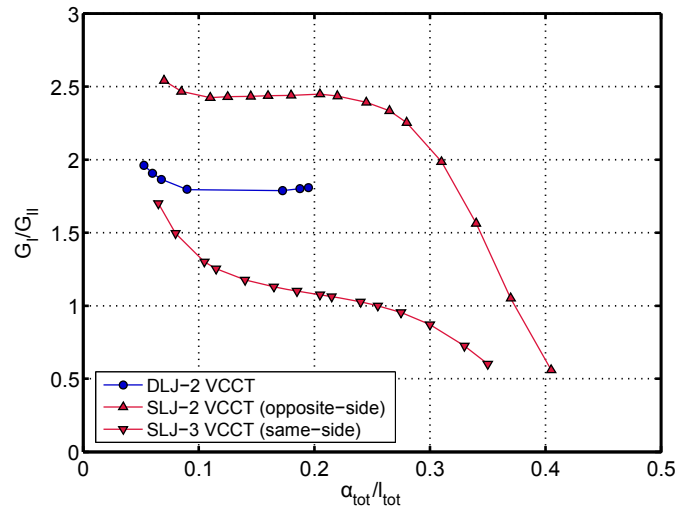


Figure 22. Fracture mode mixity for DLJs and SLJs vs. crack/overlap length ratio.

4.4 Mixed mode fracture criterion

Based on the fracture results for both structural joints (DLJs and SLJs) and for Mode I and II fracture joints composed of the same material, presented in [22], a mixed mode fracture criterion for crack initiation and propagation was established. The criterion is based on the following canonical elliptic equation:

$$\left(\frac{G_I}{G_{IC}}\right)^m + \left(\frac{G_{II}}{G_{IIC}}\right)^n = 1 \quad (6)$$

The initiation criterion expresses the critical mode ratio at which crack initiation occurs, while the propagation criterion indicates when unstable propagation occurs. Fig. 23 shows on the y- and x-axes the critical strain energy release rates G_{IC} and G_{IIC} obtained from the DCB and ELS specimens [21]. Values from visual observation of crack initiation (VIS) were

taken from [21], assumed as being equivalent to the values obtained from crack gages in this study. Furthermore, G_I and G_{II} obtained from VCCT for the DLJs and SLJs at initiation (INI) and propagation (PRO) are shown. The data points for the crack initiation of all DLJ and SLJ specimens are concentrated since the mode ratio at initiation was similar. For propagation, however, the differences are more pronounced, in accordance to Fig. 22.

By substituting $m = n = 1$ into Eq. (6), a linear upper bound for initiation and propagation was obtained, see Fig. 23 (dashed lines). Fitting Eq. (6) to the results led to similar values of $m=n=0.42$ for initiation and $m=n=0.47$ for propagation and, correspondingly, to non-convex criteria for initiation and propagation, as also shown in Fig. 23 and also observed in literature for FRP composites, e.g. [18-19]. This result, however, is based on a relatively small database and needs further confirmation.

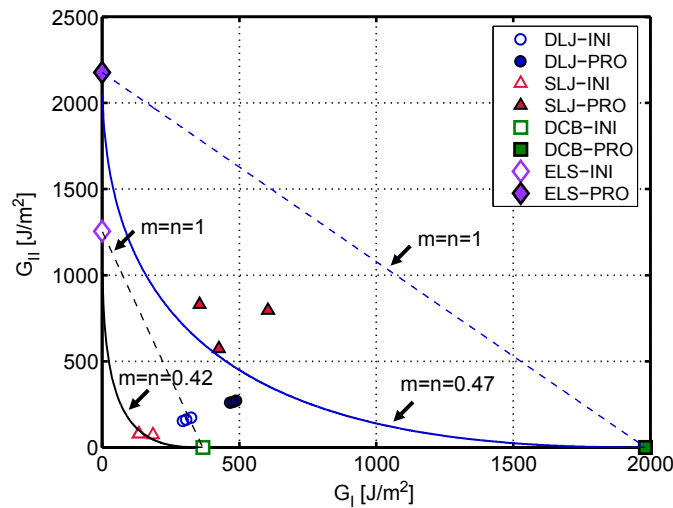


Figure 23. Mixed-mode fracture criterion for crack initiation and propagation.

5 CONCLUSIONS

The fracture behavior of adhesively-bonded DLJs and SLJs composed of pultruded GFRP laminates subjected to axial tension was experimentally investigated and numerically modeled using FE analysis. The strain energy release rate was obtained using both the experimental compliance method (ECM) and the virtual crack closure technique (VCCT). The fracture mode mixity was investigated and, combined with the results for pure Mode I and II fracture derived in a previous work by the authors, a mixed-mode fracture criterion for crack

initiation and propagation was established. The following conclusions were drawn:

1. The strain energy release rate obtained from VCCT proved insensitive to the main FE model parameters, including the model dimension, the element shape and size, the left/right crack length ratio and the location of the crack propagation path, unless the element height was much smaller than the element length.
2. The total strain energy release rate (G_{tot}) obtained from the ECM and VCCT agreed well for the SLJs while deviations were observed for DLJs due to low stiffness changes. ECM results were sensitive to these small changes and VCCT accuracy was affected by the inability of the FEA to accurately model the behavior before the initiation of the first measurable crack.
3. For both joint types, the fracture mode mixity (G_I/G_{II}) varied with increasing crack length. Fracture of the DLJs was Mode I-dominated up to failure, while the dominant mode changed from Mode I to Mode II in the case of SLJs for long crack lengths.
4. Combined with the results from DCB and ELS, a mixed mode fracture criterion was established for crack initiation and propagation, which exhibits a non-convex form. Similar values for the empirical parameters ($m=n\approx 0.5$) were obtained for crack initiation and propagation. This result, however, needs further experimental validation.
5. Existing methods for the interpretation of fracture mechanics data, such as the ECM and VCCT, proved applicable in the case of structural joints. Their accuracy, however, depends on their ability to accurately describe stiffness degradation during crack propagation.

ACKNOWLEDGEMENTS

The authors would like to thank the Swiss National Science Foundation (Grant No 200020-111702/1), Sika AG, Zurich (adhesive supplier) and Fiberline Composites A/S, Denmark (pultruded laminate supplier) for their support of this research.

REFERENCES

- [1] Keller T, Vallée T. Adhesively bonded lap joints from pultruded GFRP profiles, Part II: Joint strength prediction. *Composites Part B* 36/4 (2005) 341-350
- [2] Abdel wahab MM, Ashcroft IA, Crocombe AD, Smith PA. Finite element prediction of fatigue crack propagation lifetime in composite bonded joints. *Compos Part A-Appl S*,

2004;35(2):213-222.

- [3] Aymerich F, Onnis R, Priolo. Analysis of the fracture behaviour of a stitched single-lap joint. *Compos Part A-Appl S*, 2005;36(5):603-614.
- [4] Quaresimin M, Ricotta M. Stress intensity factors and strain energy release rate in single lap bonded joints in composite materials. *Compos Sci Technol*, 2006;66(5):647-656.
- [5] Yang C, Chadegani A, Tomblin JS. Strain energy release rate determination of prescribed cracks in adhesively-bonded single-lap composite joints with thick bondlines. *Compos Part B-Eng*, 2008;39(5):863-873.
- [6] Li HCH, Dharmawan F, Herszberg I, John S. Fracture behaviour of composite maritime T-joints. *Compos Struct*, 2006;75(1-4):339-350.
- [7] Cheuk PT, Tong L, Wang CH, Baker A, Chalkley P. Fatigue crack growth in adhesively bonded composite-metal double-lap joints. *Compos Struct*, 2002;57(1-4):109-115.
- [8] Mostovoy S, Crosley PB, Ripling EJ. Use of crack-line-loaded specimens for measuring plane strain fracture toughness. *J Mater* 1967;3(2):661-681.
- [9] Cheuk PT, Tong L, Rider AN, Wang J. Analysis of energy release rate for fatigue cracked metal-to-metal double-lap shear joints. *Int J Adhes Adhes* 2005;25(2):181-191.
- [10] Curley AJ, Jethwa JK, Kinloch AJ, and Taylor AC. The fatigue and durability behaviour of automotive adhesives. Part III: predicting the service life. *J Adhesion*, 1998;66(11):39-59.
- [11] Tay TE, Shen F, Lee KH, Scaglione A, Di Sciuva M. Mesh design in finite element analysis of post-buckled delaminating in composite laminates. *Compos Struct*, 1999;47(1-4):603-611.
- [12] Rybicki FE, Kaninen MF. A finite element calculation of stress intensity factor by a modified crack closure integral. *Eng Fract Mech* 1977;9(4):931-938.
- [13] Dakshina Moorthy CM, Reddy JN. Modelling of laminates using a layerwise element with enhanced strains. *Int J Numer Meth Engng*, 1998;43(4):755-779.
- [14] Raju IS, Crews JH, Aminpour MA. Convergence of strain energy release rate components for edge-delaminated composite laminates. *Eng Fract Mech* 1988;30(3):383-396.
- [15] Russell AJ, Street KN. Moisture and temperature effects on the mixed-mode delamination fracture of unidirectional graphite/epoxy. *Delamination and debonding of materials*, ASTM STP 876, W. S. Johnson, Ed., American Society for Testing Materials, Philadelphia, 1985, pp. 349-370.

-
- [16] Rikards R. Interlaminar fracture behaviour of laminated composites. *Compos Struct*, 2000;76(1-3):11-18.
- [17] Hashemi S, Kinloch and Williams JG. Mechanics and mechanisms of delamination in a poly(ether sulphone) – fibre composite. *Compos Sci Technol*, 1990;37(4):429-462.
- [18] Charalambides M, Kinloch AJ, Wang Y and Williams JG. On the analysis of mixed-mode failure. *Int J Fracture* 1992;54(3):269-291.
- [19] Hashemi S, Kinloch and Williams G. Mixed-mode fracture in fiber-polymer composite laminates. *Composite Materials. Fatigue and Fracture (Third volume)*, ASTM STP 1110, T.K. O'Brien., Ed., American Society for Testing and Materials, Philadelphia, 1991:143-168.
- [20] Mandell JF, Samborsky DD and Agastra P. Composite material fatigue issues in wind turbine blade construction. *SAMPE 2008*, Los Angeles, CA.
- [21] Zhang Y, Vassilopoulos AP and Keller T. Mode I and II fracture behavior of adhesively-bonded pultruded composite joints. *Eng Fract Mech*. In press.
- [22] Zhang Y, Keller T. Progressive failure process of adhesively bonded joints composed of pultruded GFRP. *Compos Sci Technol*, 2008; 68(2):461-470.
- [23] Ye Zhang, Anastasios P. Vassilopoulos and Thomas Keller. Effects of low and high temperatures on tensile behavior of adhesively-bonded GFRP joints. *Compos Struct*. In press.
- [24] Ye Zhang, Anastasios P. Vassilopoulos and Thomas Keller. Fracture of adhesively-bonded pultruded GFRP joints under constant amplitude fatigue loading. *Int J Fatigue*. In press.
- [25] De Castro J, Keller T. Ductile double-lap joints from brittle GFRP laminates and ductile adhesives, Part II : Numerical investigation and joint strength prediction. *Compos Part B*, 2008;39(2):282-291.

2.4 Environmental effects under quasi-static loading

Summary

Great efforts were made in Sections 2.1-2.3 to characterize the mechanical and fracture behavior of adhesively-bonded GFRP joints under quasi-static loading in the ambient laboratory conditions. Since they are used in real civil engineering structures, adhesively-bonded GFRP joints, however, are subjected to different environmental conditions in their service lifetime. Under elevated temperatures, the material properties of the matrix of GFRPs and the adhesive undergo significant changes caused by the glass transition. The high/low temperatures affect several aspects of the mechanical and fracture behavior of structural joints, e.g. strength, stiffness, crack initiation and propagation, and therefore cannot be neglected in the present research.

This paper, covering Task 1.4 and 2.7 in Fig. 1, attempts to evaluate the environmental effects, particularly temperature effects, on the mechanical and fracture behavior of structural joints under quasi-static loading. In this section, an experimental investigation was performed involving adhesively-bonded double-lap joints (DLJs) composed of pultruded GFRP adherends and an epoxy adhesive under temperatures ranging between -35°C and 60°C . The validated crack measurement techniques and calculation method for strain energy release rate were employed as in Section 2.2. The thermomechanical behavior of the adhesive, rather than that of the adherends, proved to be the prime factor influencing the mechanical and fracture behavior of joints. For temperatures above the adhesive glass transition temperature, T_g , the load-elongation response became non-linear, strength and stiffness significantly decreased and the failure mechanism changed from fiber-tear to adhesive failure. Concerning the fracture behavior, the crack initiation was unaffected as long as the temperature remained below the T_g of the adhesive, while the crack propagation rate was higher at low temperatures. Critical strain energy release rates, G_c , for crack initiation and propagation consistently rose as temperature increased.

In addition to the experimental investigation, this paper also includes the modeling of the temperature effect on joint stiffness by using two existing empirical models and finite element analysis (FEA). Good agreement was observed for both empirical and FE models compared to the experimental results. FEA offers an efficient means of modeling the

temperature-dependent stiffness of a structural component, e.g. the joint, when only the temperature-dependent properties of the constituent materials are known.

Reference details

This paper, “Effects of low and high temperatures on tensile behavior of adhesively-bonded GFRP joints” by Ye Zhang, Anastasios P. Vassilopoulos and Thomas Keller, was published in Composite Structures, in Press.

[doi:10.1016/j.compscitech.2009.01.024](https://doi.org/10.1016/j.compscitech.2009.01.024)

EFFECTS OF LOW AND HIGH TEMPERATURES ON TENSILE BEHAVIOR OF ADHESIVELY-BONDED GFRP

Ye Zhang, Anastasios P. Vassilopoulos and Thomas Keller

Composite Construction Laboratory (CCLab),
Ecole Polytechnique Fédérale de Lausanne (EPFL),
Station 16, Bâtiment BP, CH-1015 Lausanne, Switzerland

ABSTRACT

The tensile behavior of adhesively-bonded double-lap joints composed of pultruded glass fiber-reinforced adherends and an epoxy adhesive was investigated under temperatures ranging between -35°C and 60°C . The load-elongation response was influenced primarily by the thermomechanical behavior of the adhesive and much less so by that of the adherends. For temperatures above the adhesive glass transition temperature, strength and stiffness decreased with the former being less affected than the latter. The failure mechanism changed with increasing temperature from fiber-tear to adhesive failure. The crack initiation loads were unaffected as long as the temperature remained below the adhesive glass transition temperature. However, the crack propagation rate was higher at low temperatures. Critical strain energy release rates for crack initiation and propagation consistently rose as temperature increased. Modeling results obtained using existing empirical models and FEA compared well to the experimental data in the examined temperature range.

KEYWORDS

Adhesive bonding; Fiber-reinforced polymers; Joints; Temperature effects;
Thermomechanical response

1 INTRODUCTION

The temperature-dependent structural behavior of adhesively-bonded joints composed of metallic and composite adherends has been of interest to the scientific community since the early 1980s. Based on the specific service conditions related to different application fields, a number of experimental programs have been realized in order to correlate joint strength and stiffness with temperature fluctuations. However, most of the efforts were directed at investigating material behavior under predefined thermomechanical loading patterns and not aimed at developing any theoretical models for predicting the behavior of the examined materials under wide ranges of operating temperatures. In [1] it was shown that the strength of aluminum alloy single-lap joints bonded with an epoxide-polymide film adhesive decreased with increasing temperatures, while a drop in strength and change of failure mechanism was observed at very low temperatures (-40°C). The temperature and moisture effects on the strength of carbon fiber-reinforced polymer (CFRP) joints bonded with six different types of structural epoxy adhesives formed the subject of [2]. A decrease in strength was observed in the case of higher temperature and longer exposure time to humidity. The extent of the loss was dependent on the adhesive curing temperature: curing at 175°C resulted in lower joint strength losses at high temperatures than curing at 120°C . The failure mode at ambient temperature and the way in which this failure mode changed with temperature and moisture exposure depended on the adhesive type. While both higher temperature and moisture content were expected to increase the likelihood of failure in the adhesive, this was not always the case, suggesting that the failure mode was a result of a complex balance between adhesive, composite and interface properties. The influence of temperatures between -50°C and 200°C on the stress state and strength of adhesively-bonded titanium/titanium and titanium/CFRP joints has been studied in [3-5]. The effect of temperature on joint response depended on three factors: the cure shrinkage, the different thermal expansion of adherends and adhesive, and the stress-strain behavior at different temperatures. At high temperatures, the strain capacity was high but the load capacity was low and vice versa. Therefore, a combination of two types of adhesives in the joint was proposed for low and high temperatures. The stiffness reduction of composite/aluminum joints comprising flexible and rigid adhesives under tensile loading was compared at -40°C and 23°C [6]. The results showed that joint stiffness is affected more by the composite

adherend response to temperature than by the modulus of the adhesive due to its thin layer. The effects of temperature and strain rate on the quasi-static response of double-lap steel joints bonded with an epoxy adhesive were investigated in [7]. At high temperature (82°C), the joints exhibited a greater degree of strain rate sensitivity with a significant decrease in joint strength compared to joints at ambient temperature. These differences were attributed to the softening of the adhesive at high temperatures.

Temperature also affects the fracture behavior of adhesive joints. Fracture energy decreased at lower temperatures in [8] where Mode I fracture tests were performed on epoxy-bonded CFRP double cantilever beam (DCB) joints at three different temperatures (-50°C, 22°C and 90°C). The temperature also influenced the mode of fracture, which changed from stable, brittle fracture at low temperature to slip-stick fracture at ambient temperature and stable ductile behavior at elevated temperature.

Previous research focused mainly on qualitative comparisons of temperature-dependent behavior in terms of strength, stiffness and/or fracture process of specific joint specimens. The adherend types used were metallic strips or laminated composites. Corresponding empirical models to describe the temperature-dependent material stiffness and strength degradation were developed on the material level however [9, 10], although not for complex systems such as adhesive joints.

In the present work, the temperature-dependent quasi-static behavior of adhesively-bonded double-lap joints (DLJs) composed of GFRP laminates was experimentally investigated. Pultruded laminates, which are preferred in civil infrastructure and behave quite differently from laminated adherends [11] were used. Furthermore, fracture data was extracted from these structural joints and not from fracture joints, as recommended in several works, e.g. [12]. Stiffness degradation was modeled using Finite Element Analysis (FEA) and the required temperature-dependent material properties were obtained using Dynamic Mechanical Analysis (DMA), which is much easier and allows much more general modeling than specific model calibration through joint tests. The main objectives of this work were: 1) the characterization of the structural performance and fracture behavior of the examined DLJs over a wide range of temperatures, 2) the evaluation of temperature effects on specimen strength, stiffness and critical strain energy release rate for crack initiation and propagation, 3) the modeling of thermomechanical behavior based on

FEA and existing empirical models.

2 EXPERIMENTAL AND NUMERICAL INVESTIGATIONS

2.1 Specimen geometry and material properties

Balanced DLJs were manufactured from pultruded glass fiber-reinforced polymer (GFRP) laminates (supplied by Fiberline A/S, Denmark) and a two-component epoxy adhesive, as shown in Fig. 1. The laminate widths were 50 mm and the thicknesses 12 and 6 mm. The overlap length was 50 mm and the adhesive thickness 2 mm. A relatively thick adhesive layer was selected to simulate the situation in civil engineering applications where tolerances need to be compensated in the joints.

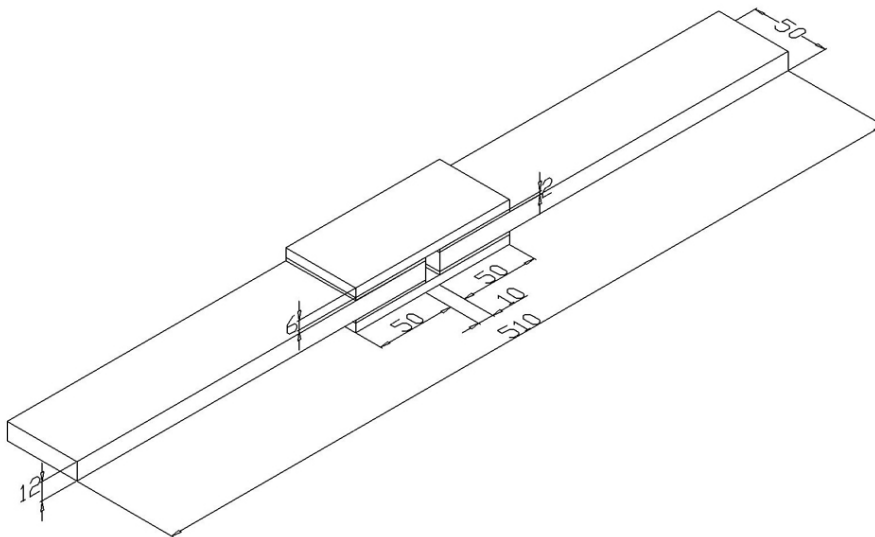


Figure 1. Geometry of double-lap joint specimen (dimensions in [mm]).

The laminates consisted of E-glass fibers embedded in an isophthalic polyester resin. The fiber architecture of both laminate types was similar as they were both composed of complex mat layers on the outside and rovings in the core region. The 12-mm-thick laminate comprised two mat layers on each side, while the 6-mm-thick laminate contained only one mat layer. A mat layer consisted of a chopped strand mat (CSM) and a woven mat $0^{\circ}/90^{\circ}$ stitched together. A polyester surface veil of 40 g/m^2 was also applied onto the outer surfaces. To determine the fiber volume fractions, burn-off tests were performed according to ASTM D3171-99. The veil layer totally decomposed, while the fibers of the mat and the roving

layers could easily be separated and weighed. The thicknesses of all layers were estimated using an optical microscope and the resulting average values are given in Table 1 [13]. Based on this data, the glass fiber volume fraction of each layer was estimated, see Table 2. The material properties of all layers were then estimated using the rule of mixture based on the fiber volume fractions and layer thicknesses or derived experimentally [14], see Table 2. In the case of the complex mat layers, only 35% of the fiber volume fraction was considered as being effective in the axial direction. This value has been estimated through comparison between experimental and FE results obtained for the laminates under tensile and bending loading. The determined total glass fiber volume fractions were 43.6% and 48.5% for 6-mm and 12-mm-thick laminates respectively. Due to the higher fiber content, the mean tensile strength and Young's modulus of the thicker laminates (355 MPa and 34.4 GPa) were higher than those of the 6-mm laminates (283 MPa and 31.4 GPa) [13].

Table 1. Estimated average layer thickness of 6-mm and 12-mm laminates

Layer	6-mm GFRP [mm]	12-mm GFRP [mm]
Veil	0.5	0.5
Mat	1.0	0.5+1.0
Roving	3.0	8.0

A two-component epoxy system was used (SikaDur 330 from Sika AG) which exhibited an almost elastic behavior and a brittle failure under axial quasi-static tensile loads at ambient temperature. The measured mean tensile strength was 38.1 MPa, the Young's modulus 4.6 GPa, and strain to failure 1.0% [15].

The glass transition temperature, T_g , of the adhesive and GFRP laminates was determined using DMA on specimens of $50 \times 10 \times 3$ -mm³ size. The adhesive specimens were fabricated in an aluminum mold and cured for ten days at ambient temperature and humidity. The GFRP specimens were cut from the roving part. The specimens were tested in a dual cantilever set-up at a constant frequency of 1 Hz within a 0°C-100°C temperature range for the adhesive and 0°C-220°C range for the laminate at two different heating rates, 2.5°C/min and 5°C/min. The dependence of the adhesive and laminate storage modulus on temperature variations is shown in Fig. 2. Following a slight decrease in the glassy state (below T_g), the

adhesive storage modulus decreased significantly during glass transition and stabilized at the onset of the leathery state at approximately 2% of the initial value. The glass transition temperature was estimated as being in the range between 40°C and 50°C. As from approximately 30°C, the laminate modulus exhibited a steady decrease and started stabilizing at approximately 20% of its initial value. The T_g of the laminate was in the range between 100°C to 150°, where the greatest change in modulus was observed. Higher heating rates were shown to result in higher stiffness and T_g values.

All specimens were manufactured under ambient laboratory conditions. Before manufacturing, the surfaces of the bonding region were mechanically abraded with a P60 sandblasting paper using a grinder and then chemically degreased using acetone. To ensure a constant thickness of the adhesive and good alignment of the GFRP laminates, a special aluminum frame was designed and employed for the production of the joints. After their manufacture, all specimens were cured under ambient laboratory conditions for ten days.

Table 2. Fiber volume fractions and properties used for FE modeling (* experimentally determined property)

	6-mm GFRP		12-mm GFRP		Veil	Adhesive
	Roving	Mat	Roving	Mat		
Fiber vol. fraction [%]	57.8	45.7	52.7	46.9	-	-
E_{11} [GPa]	42.9	18.9	39.5	19.3	3.2	4.6*
E_{22} [GPa]	3.5*	18.9	3.5*	19.3	3.2	4.6*
E_{33} [GPa]	3.5*	3.5*	3.5*	3.5*	3.2	4.6*
G_{12} [GPa]	2.7	7.4	2.4	7.1	1.2	1.7
G_{23} [GPa]	1.4	1.5	1.4	1.5	1.2	1.7
G_{31} [GPa]	2.7	1.5	2.4	1.5	1.2	1.7
ν_{12}	0.32	0.27*	0.33	0.27*	0.38	0.37
ν_{23}	0.27*	0.36	0.27*	0.36	0.38	0.37
ν_{31}	0.03	0.36	0.03	0.36	0.38	0.37

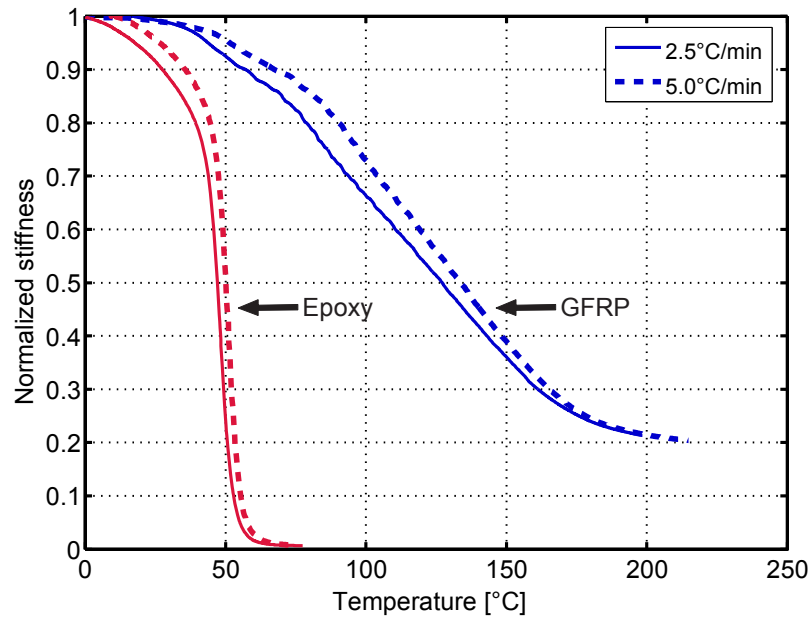


Figure 2. Thermomechanical behavior of epoxy adhesive and GFRP laminates (roving part).

2.2 Experimental program and instrumentation

A total number of 19 DLJs were examined under temperatures ranging between -35°C and 60°C . The temperature was controlled by a climatic chamber attached to an INSTRON 8800 testing machine of 100-kN capacity. Specimens were placed in the chamber for at least 90 min before mechanical loading to ensure a uniform through-thickness temperature profile. The 90-min time span was derived from a preliminary study in which temperatures in the adhesive layer were measured by thermal gages. All specimens were loaded up to failure at a displacement rate of 1 mm/min.

The temperature range was selected according to the operational conditions of the joints as parts of engineering structures and the glass transition temperature of the adhesive. A low temperature of -35°C simulated operation of the structure during wintertime, 23°C represented the baseline temperature, while 40°C represented summer days. However, to also investigate the joint behavior up to the adhesive glass transition temperature, the range was extended to an upper limit of 60°C , being just above glass transition and at the transition to the leathery material state. Unlike the adhesive, the laminates exhibited a stiffness decrease of less than 10% in this higher temperature range, see Fig. 2. At the operational conditions (-35 , 23 and 40°C , which presented the main interest of this study), five specimens were

investigated while only one specimen (at much shorter temperature steps however) was examined at higher temperatures (45, 50, 55 and 60°C). The resulting experimental matrix is shown in Table 3, with LT, AT and HT designating low, ambient and high temperature respectively. The specimens were labeled accordingly, with HT4001, for instance, signifying specimen 01 at 40°C.

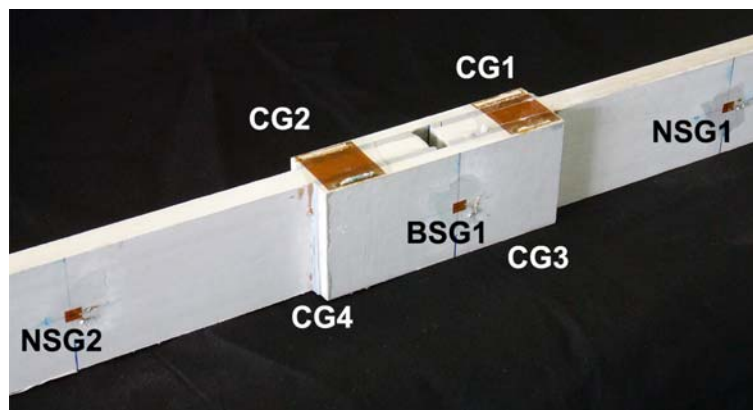


Figure 3. Instrumentation of double-lap joints (CG = crack propagation gage, NSG = normal strain gage, BSG = back-face strain gage).

All specimens were instrumented with four strain gages, see Fig. 3. Strain gages of the type 1,5/120LY18 (120 Ohm), manufactured by HBM, with a gage length of 6 mm were used. Two were placed in the middle of the thicker laminates (designated NSG1 and NSG2), 100 mm from the joint edge, to measure the axial strains outside the joint region (expected to be uniformly distributed through the thickness). The other two gages, designated back-face strain gages (BSG1 and BSG2), were placed above locations sensitive to crack initiation, as demonstrated in [13, 16]. A sudden change in strains due to stress redistribution after crack initiation was recorded at these locations in [13]. Specimens marked with an asterisk in Table 3 were additionally instrumented with four crack propagation gages to detect crack initiation and record crack propagation. The crack gages (HBM/RSD20, with a resistance of 13 Ohm) consisted of 20 wires spaced at 1.15-mm intervals perpendicular to the adhesive layer, and covered almost half of the overlap length where crack propagation was expected to occur. As the crack propagated, the wires were progressively broken, thereby increasing the electrical resistance of the gages. Theoretically, a crack could initiate at each joint end close to each of the two adhesive layers and therefore a total of eight cracks could develop, however, only one

crack initiated at one joint end in the experiments. Each crack gage was therefore crossed by only one crack and the sum of the four individually measured crack lengths was taken into account to describe crack propagation.

An HBM/Spider8 was used to record the measured experimental data with a frequency of 800 Hz for the specimens equipped with crack gages and a frequency of 200 Hz for the others. A strain channel was used to acquire crack gage measurements. The load was directly measured by the 100-kN load cell of the testing rig. The displacement of the stiff testing frame was used to record specimen elongation. Specimen rather than joint elongation was recorded since the effect of the laminates outside of the joint on joint behavior was considered as being small. Comparatively low stresses developed in the laminates (a maximum of 85 MPa or 30% of their tensile strength) and laminate properties remained virtually unaffected by temperature (as shown above, see DMA results).

2.3 FE models

A numerical analysis was performed to model temperature effects on stress distribution in the joint area and joint stiffness. A two-dimensional model of the whole DLJ was created using ANSYS software (academic version 10.0). Geometry, mesh and boundary conditions are shown in Fig. 4. The mesh size was optimized to obtain accurate results. A denser mesh (0.25×0.25 mm) was used in the overlap region to take stress concentrations into account. The laminates were modeled as laminated plates; the element type PLANE42, a 2D-four-node quadrilateral plane element having two degrees of freedom at each node, being used for the whole model. The number of nodes and elements in the models were 153152 and 50560 respectively. One end of the joint was completely fixed, while the other end, where the axial displacement was applied, was fixed only in the out-of-plane direction. Individual layer properties, given in Table 2, were used for ambient temperature and were decreased proportionally to the temperature curves at the lower heating rate, shown in Fig. 2. The fiber-dominated properties of the roving layer (E_{11}) and mat layers (E_{11} , E_{22}) were decreased according to the GFRP curve of Fig. 2, while all other properties, which were resin-dominated, were decreased proportionally to the epoxy resin curve. Previous results [17] showed that there is no obvious stiffness variation between -50°C and 23°C for the same GFRP material. Table 3. Overview of experimental program and main results (* specimens with crack gages)

Temp.	Specimen	Ultimate	Crack initiation	Elongation	Elong. at	Specimen
	ID	load	load, back-face / crack gage	at failure	crack initiation, back-face / crack gage	stiffness
[°C]		[kN]	[kN]	[mm]	[mm]	[kN/mm]
-35	LT3501*	40.9	33.2 / 35.4	1.11	0.89 / 0.95	38.3
	LT3502*	41.6	28.0 / 38.0	1.24	0.77 / 1.09	36.8
	LT3503*	41.0	30.3 / 37.9	1.28	0.90 / 1.15	33.7
	LT3504	44.4	30.7 / -	1.37	0.87 / -	35.0
	LT3505	44.6	30.1 / -	1.28	0.84 / -	36.4
	Mean	42.5±1.9	30.5 / 37.1	1.26±0.09	0.85 / 1.06	36.0±1.8
23	AT2301*	43.2	36.6 / 38.4	1.37	1.06 / 1.13	37.9
	AT2302*	42.0	25.5 / 33.5	1.30	0.71 / 0.96	35.5
	AT2303*	42.6	32.7 / 35.9	1.42	0.95 / 1.07	35.8
	AT2304	42.1	29.8 / -	1.29	0.89 / -	33.5
	AT2305	47.5	25.0 / -	1.59	0.77 / -	34.2
	Mean	43.5±2.3	29.9 / 35.9	1.39±0.12	0.88 / 1.05	35.4±1.7
40	HT4001*	47.9	35.5 / 37.3	1.50	1.08 / 1.13	33.5
	HT4002*	53.8	~40 / 36.4	2.77	~1.55 / 1.32	32.2
	HT4003*	50.9	~35 / 37.5	2.74	~1.25 / 1.37	31.2
	HT4004	37.5	29.2 / -	1.14	0.84 / -	34.9
	HT4005	40.6	32.4 / -	1.30	1.01 / -	34.2
	Mean	46.1±6.9	34.4 / 37.1	1.89±0.80	1.15 / 1.27	33.2±1.5
45	HT4501	39.8	- / -	2.64	- / -	27.0
50	HT5001	43.2	- / -	4.63	- / -	16.3
55	HT5501	32.1	~28 / -	5.31	~4.21	7.0
60	HT6001	29.6	~25 / -	4.83	~3.84	7.0

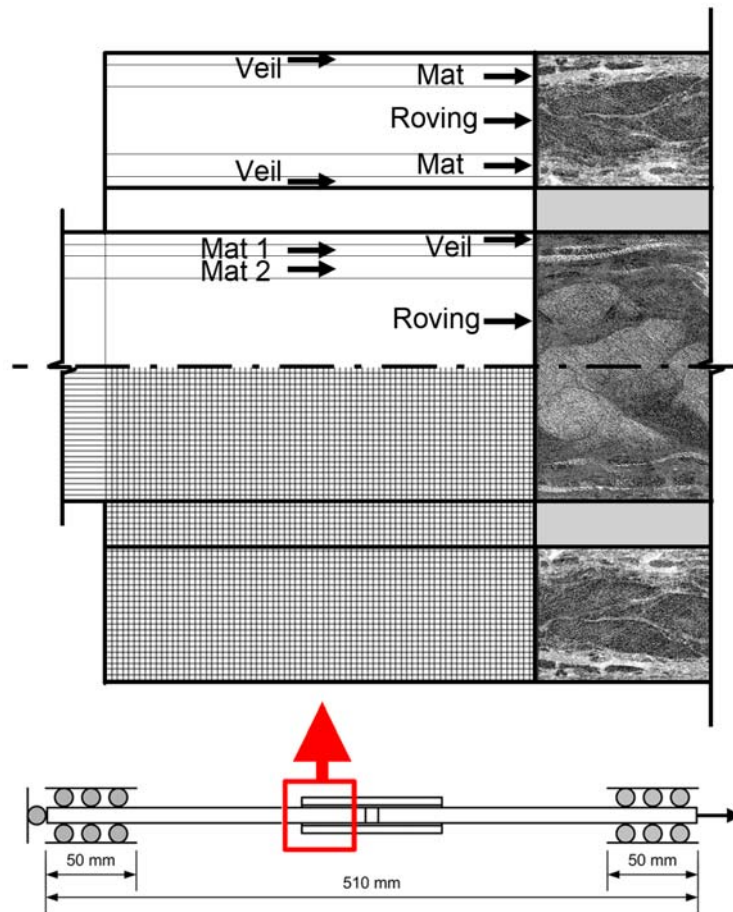


Figure 4. Layered FE model based on fiber architecture.

3 EXPERIMENTAL AND NUMERICAL RESULTS

3.1 Load vs. elongation response

The load vs. elongation response of selected specimens at each temperature level is presented in Fig. 5. At temperatures below the glass transition temperature of the adhesive (lower than 40°C) specimens exhibited an almost linear response up to an abrupt failure. Specimens at temperatures in the glass transition range (between 40°C and 50°C) exhibited linear (e.g. HT4001/04/05) or non-linear (HT4002/03, HT4501) behavior. Specimens where the adhesive was at the beginning of the leathery state (55°C and 60°C) again exhibited a linear behavior almost up to failure followed by a non-linear response shortly before failure.

Measured ultimate loads and specimen elongations at failure are given in Table 3 (mean values and standard deviations). The variation in the results increased at temperatures in the adhesive's glass transition range because adhesive properties were very sensitive to slight temperature changes in this range, see Fig. 2. Ultimate loads proved to be independent of

temperature and varied around 42.8 ± 2.8 kN in the range of -35°C to 40°C , the latter applying to specimens which maintained a linear response (HT4001/04/05) and small elongations at failure (between 1.0 and 1.5 mm). Specimens at 40°C , exhibiting a non-linear response (HT4002/003) and elongations at failure of approximately 2.8 mm, showed the highest ultimate loads (50.9 and 53.8 kN). As from this level, the ultimate loads gradually decreased with increasing temperature down to 29.6 kN at 60°C , while elongations at failure increased up to 5.4 mm.

Table 3 also shows the specimen stiffness, which was calculated in the linear range from the slope between 0.1 and 0.5 mm elongation. Specimen stiffness showed a different trend from that of ultimate load. The values remained almost constant (at approximately 35 kN/mm) up to 40°C , without exhibiting any maximum for non-linear specimens at this temperature. Subsequently, stiffness significantly decreased with increasing temperature down to very low values in the leathery state (7.0 kN/mm).

The stiffness decrease at temperatures above 40°C was greater than the drop in ultimate load, indicating that the elastic properties were more sensitive than strength within this temperature range, as shown in Fig. 6 (values at 23°C were used for the normalization). The drop in stiffness resulted in a significant increase of elongation at failure with increasing temperature. All values changed considerably in the range between 40°C and 50°C , i.e. around the T_g of the adhesive.

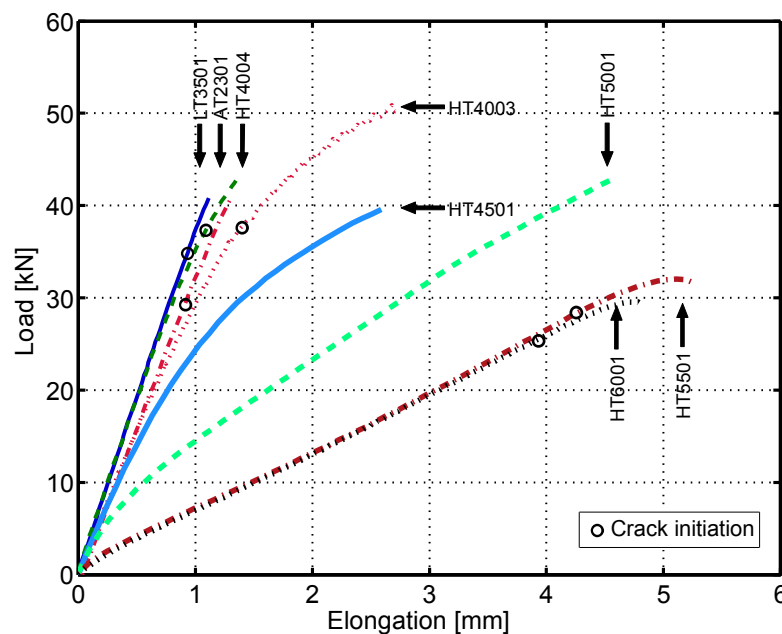


Figure 5. Load vs. elongation response of specimens at different temperatures.

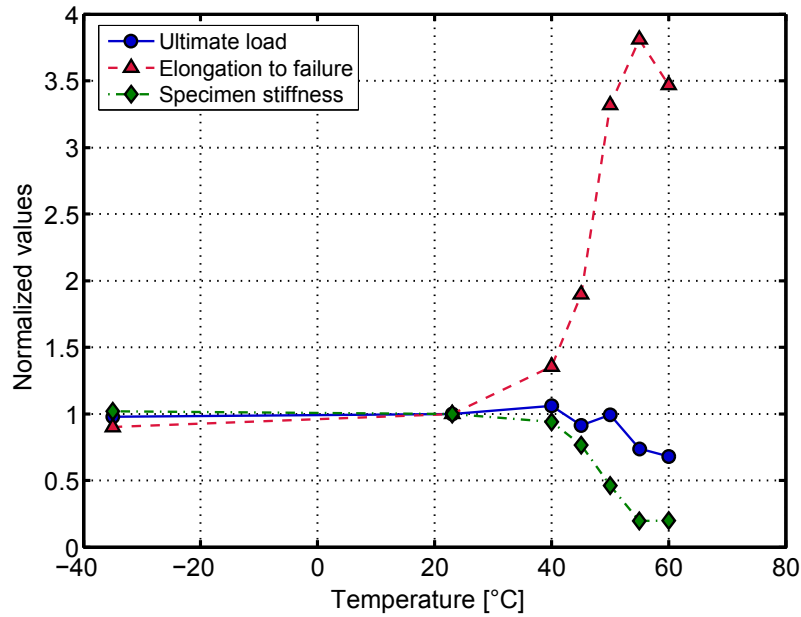


Figure 6. Normalized ultimate load, elongation and specimen stiffness vs. temperature.

3.2 Failure mechanism

Significant differences in failure mechanisms were observed at different temperatures. Although in all cases cracks nucleated and propagated at all four crack gage locations, the failure processes could be classified into three distinct categories: for -35°C , failure occurred mainly inside the 12-mm adherend, following a path between the mat layers or even extending into the roving layer, as shown in Fig. 7. A number of cracks in the adhesive in the through-thickness direction were also observed. For temperatures between 23°C and 40°C , a fiber-tear failure in the outer mat layers of the 12-mm laminate was observed, but in this case the crack did not penetrate into the roving layer. When temperature increased, especially above 50°C , the failure mode changed to adhesive failure, with the crack propagating along the interface between the adherend and the adhesive layer (see Fig. 7, 60°C). According to results presented in [11], fiber-tear failure in pultruded GFRP profiles at ambient temperature occurs because the adherend through-thickness material strength is lower than the adhesive-adherend interface strength. The present results showed, however, that the interface strength was lower than adherend strength at higher temperatures.

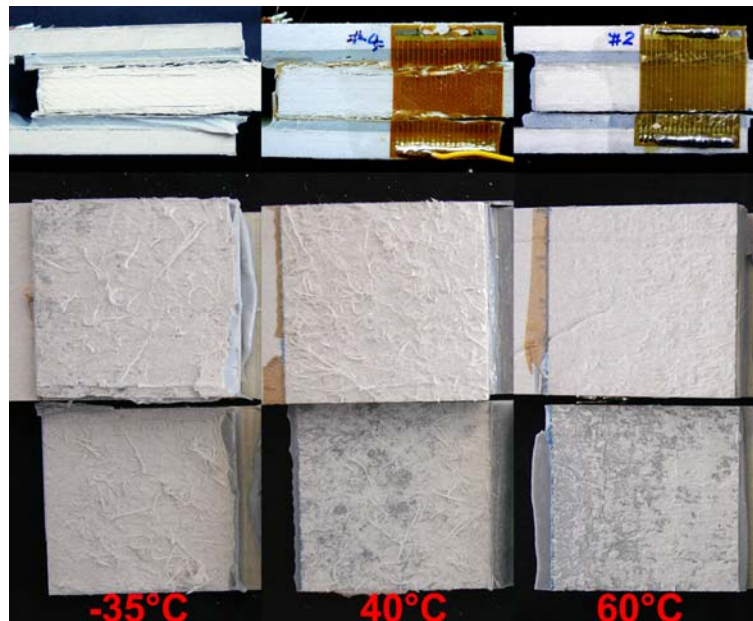


Figure 7. Failure modes at different temperatures.

3.3 Crack initiation and propagation

Both back-face strain and crack propagation gages were able to identify crack initiation when the temperature was lower than 40°C. Back-face gage measurements vs. load are shown in Fig. 8 for all temperatures. Depending on the location of the propagating cracks, measurements were positive or negative. Since only the change in the load-strain response was of interest however, the absolute values of strain are presented in Fig. 8. Two types of strain changes were observed which were associated with crack initiation: Between temperatures of -35°C and 40°C specimens with linear response showed a sudden offset in strain (similar to that observed in [13]), while at higher temperatures (and for non-linear 40°C specimens), where the adhesive was much softer, much smoother changes in strain were observed. In this case, the change in sign of the curve slope was attributed to crack initiation. Thus determination of crack initiation was much more accurate at lower temperatures (clear offset) than at higher temperatures (smooth transition). In some cases (HT4501, HT5001), back-face strain gages even failed to provide a clear indication of crack initiation. The obtained loads and elongations at crack initiation are listed in Table 3.

Load and elongation values at crack initiation determined by crack gages were defined as being those measured when the first wire of any one of the four gages was broken. The corresponding results are given in Table 3. The crack gages, however, failed to work correctly

for temperatures above 40°C; and therefore the corresponding results are not shown. Wires were broken due to large joint deformations caused by the softening of the adhesive and not by the propagating cracks. The total crack length (sum of all four gages, see Section 2.2) vs. specimen elongation response is shown in Fig. 9. Since the same displacement rate was employed for all experiments, the elongation was proportional to time and the slope of the curves could be considered as the crack propagation rate. The crack propagation rate was highest for -35°C, while it was lowest at 40°C for specimens exhibiting a non-linear response (HT4002/03). For specimens at 23°C and 40°C (linear specimens) a similar intermediate rate was observed. The longest total crack lengths (approximately 60-70 mm) were found for non-linear specimens at 40°C.

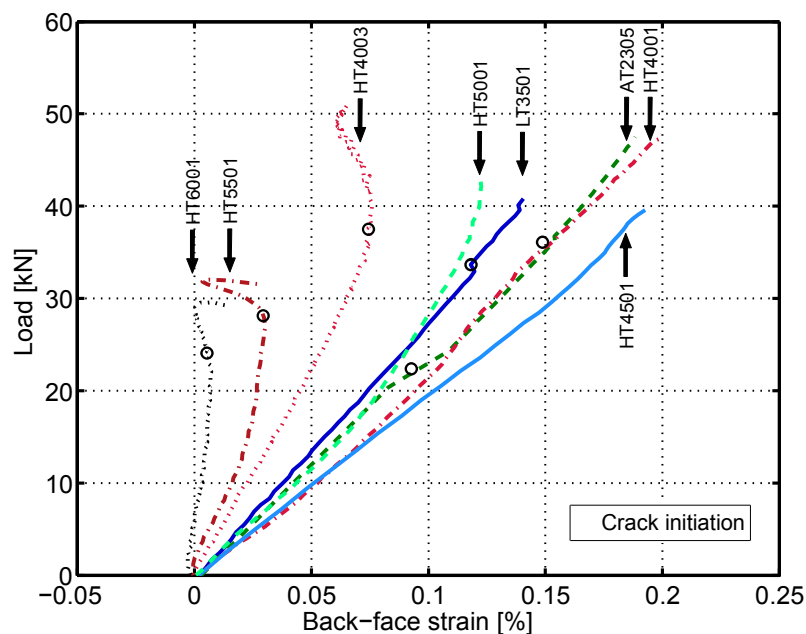


Figure 8. Load vs. back-face strain at different temperatures (absolute strain values).

Back-face gages consistently gave 10-20% lower loads and elongations at crack initiation than crack gages (see values in Table 3). These differences were caused by the lower sensitivity of the crack gages due to stepwise measurements taken at the 1.15-mm distances between the wires. Regardless of the measuring method, similar loads and elongations at crack initiation were observed up to 40°C, while loads decreased and elongations significantly increased with higher temperatures, see Table 3 and Fig. 5. Crack initiation also caused the transition from linear to non-linear joint behavior. Stiffness progressively decreased with the propagating cracks and the associated deviation from a balanced joint

configuration. At temperatures below 40°C, the non-linearity above crack initiation remained insignificant (specimen's behavior still designated as linear), while it became much more pronounced with increasing temperature.

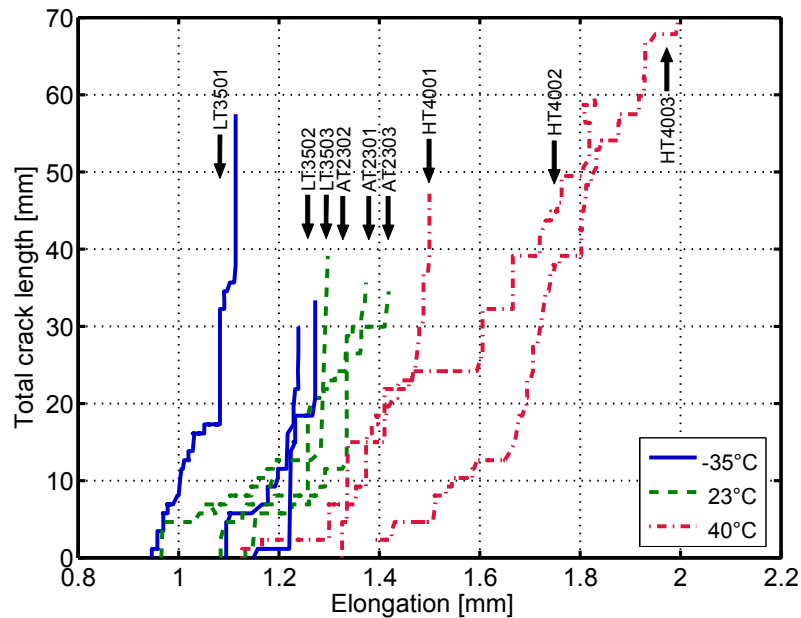


Figure 9. Total crack length vs. elongation at three specific temperatures.

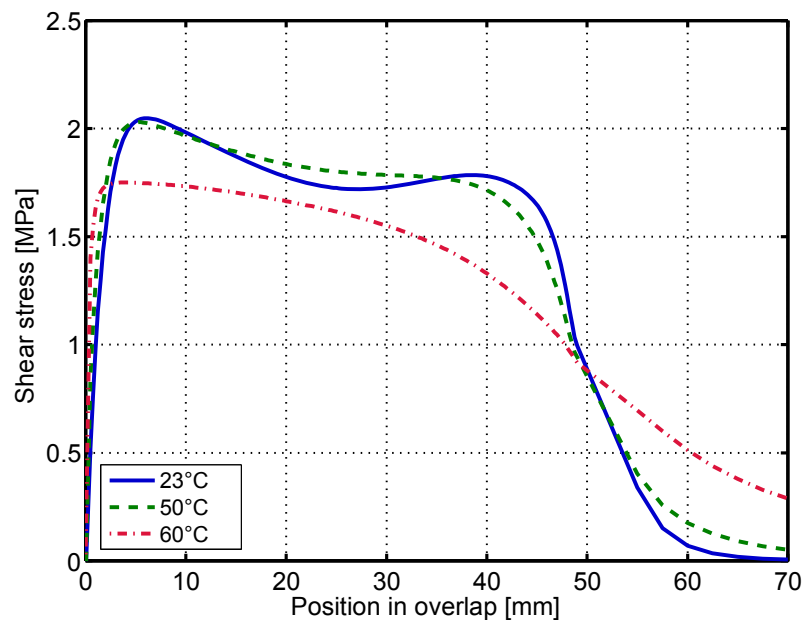


Figure 10. Shear stress distribution along overlap length at different temperatures.

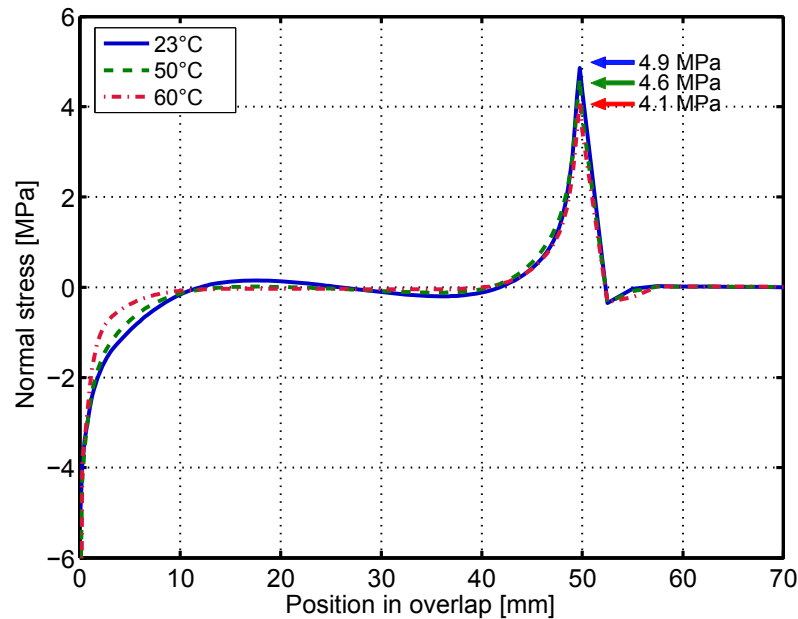


Figure 11. Normal stress distribution along overlap length at different temperatures.

3.4 Stress distribution in joint

The shear and normal stresses in the failure location layer (assumed as being at a depth of 1.0 mm between the two mat layers of the 12-mm laminate), obtained from FEA with an applied load of $P = 10$ kN, are shown in Figs. 10-11. The peak values at the edge where shear and tensile normal stresses occurred simultaneously (and failure initiated) are indicated as a function of temperature. Since no significant difference between the curves for temperatures up to 40°C was obtained, curves at 23, 50 and 60°C are shown. The softening of the adhesive above 40°C reduced stress peaks in both cases and led to a more uniform shear stress distribution along the overlap. This observation agreed well with results obtained in [15] for similar joints.

4 DISCUSSION AND MODELING

4.1 Temperature effects on joint behavior

Temperatures below the glass transition temperature range (40-50°C), even if they were very low (-35°C), did not noticeably influence the joint behavior, in other words, stress state in the overlap, joint strength and stiffness, linear joint behavior, and loads and elongations at crack initiation remained unaffected by temperature.

When the glass transition range was reached and exceeded, more uniform stress distributions occurred in the joint, with reduced stress peaks. Joint stiffness decreased prior to crack initiation due to the softer adhesive and subsequent to crack initiation, which also occurred at a lower load level due to a more pronounced non-linearity. In contrast to stiffness, joint strength exhibited a maximum at approximately 40°C (in the case of non-linear specimens). This maximum could be explained by a statistical size effect as described in [18]. Strength depends not only on the peak values of combined shear-tensile stresses, but also on the volume of material that is exposed to these stresses. The decrease in stress peaks and increase in the amount of material subjected to stresses seemed to attain an optimum resulting in maximum joint strength at around 40°C (for non-linear behavior). The significantly different behavior of specimens at 40°C (linear or non-linear) could be attributed to the sharp decrease in adhesive stiffness shown in Fig. 2, which made joint behavior very sensitive to small temperature differences. Temperatures above glass transition also weakened the adhesive-adherend interface and changed the failure mode from fiber-tear to adhesive failure.

4.2 Fracture data reduction

In order to describe the crack propagation process, the specimen compliance, C , defined as the ratio of specimen elongation, δ , over the corresponding load, P , $C=\delta/P$, was plotted against the total crack length, a , as shown in Fig. 12. The compliance increased with longer crack length at an almost constant rate. Therefore, the compliance was linearly fitted to the total crack length as follows:

$$C = k \cdot a + c_t \quad (1)$$

where k and c_t are the slope and the y-axis intercept of the fitted straight line. Fitted curves are presented in Fig. 12 and show good agreement with the measurements (R^2 -values between 0.83 and 0.98). At higher temperatures compliance values were higher, in accordance with the lower stiffness under these conditions (see Fig. 5). At 40°C, the compliance of the non-linear specimens was higher than that of the linear specimens.

Crack propagation was always located in the mat layers of the GFRP laminates, whose material properties remained linear-elastic in the examined temperature range. Therefore, linear-elastic fracture mechanics (LEFM) was assumed to be applicable and the strain energy

release rate, G , was calculated accordingly:

$$G = \frac{P^2}{2B} \frac{dC}{da} = \frac{kP^2}{2B} \quad (2)$$

where P is the applied load, B the crack width, a the total crack length and C the compliance, as estimated by Eq. (1). Since the total crack length obtained from the four crack gages was used, only half of the specimen width had to be taken into account: $B = 25$ mm.

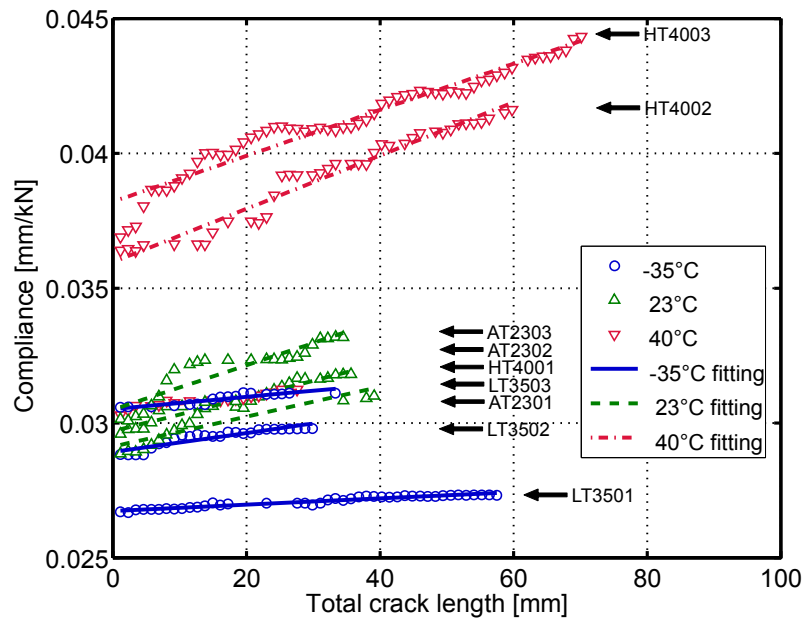


Figure 12. Compliance vs. total crack length (measurements and fitted lines).

Fig. 13 shows the resulting strain energy release rate as a function of total crack length. For all temperatures, G gradually increased with longer crack length until it reached a plateau, representing the trend of a typical R-curve. The G -value corresponding to the first measured crack length was defined as being the critical strain energy release rate, G_c , for crack initiation. Moreover, the mean value of G in the plateau region was defined as being the G_c for crack propagation. The resulting values of G_c are listed in Table. 4.

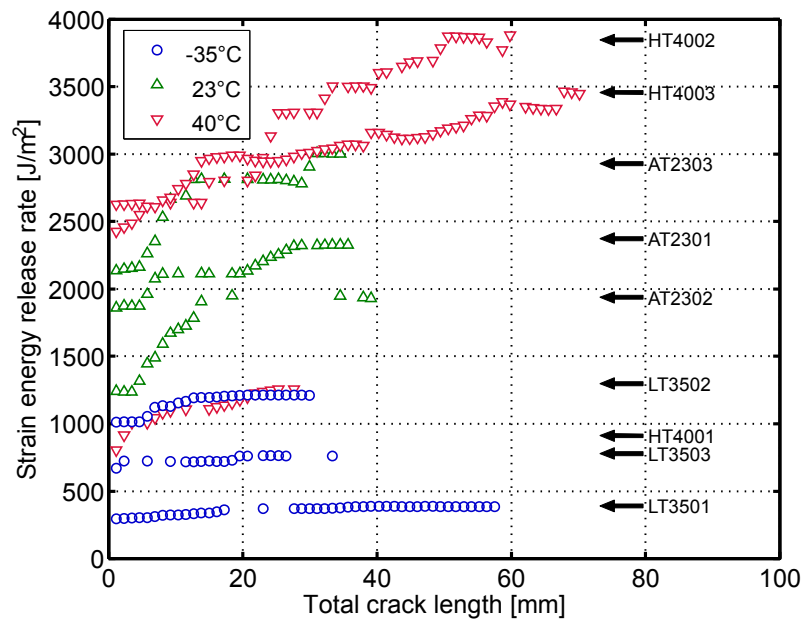


Figure 13. Strain energy release rate vs. total crack length.

Table 4. Critical strain energy release rates for crack initiation and propagation.

Temperature [°C]	Specimen	G_c [J/m ²]	
		for crack initiation	for crack propagation
-35	LT3501	295.0	382.1±6.3
	LT3502	1012.6	1207.4±8.3
	LT3503	669.3	737.9±20.1
23	AT2301	1860.4	2323.9±3.3
	AT2302	1242.2	1882.9±89.9
	AT2303	2135.1	2865.9±89.9
40	HT4001	561.6	889.8.0±6.7
	HT4002	2627.0	3853.8±36.9
	HT4003	2426.4	3259.6±115.5

At 23°C, the mean value of G_c for crack initiation was 1746 J/m² while G_c at -35°C was approximately 62% lower (mean of 659 J/m²). At 40°C, the linear specimen HT4001 had a significantly lower G_c value (561 J/m²) compared to the non-linear specimens HT4002/03 (mean of 2527 J/m²), whose values exceeded the mean value at 23°C by approximately 45%. Taking into account the scatter due to the relatively small number of specimens, a clear trend

towards higher G_c -values for crack initiation with increasing temperature and softening of the adhesive could be observed. A similar trend was observed for G_c -values for crack propagation. The mean value at -35°C (776 J/m^2) was approximately 67% lower than the mean value at 23°C (2358 J/m^2), while the mean value of the non-linear specimens at 40°C (3557 J/m^2) was approximately 51% higher than the 23°C values. However, the effect of changing failure mode (from fiber-tear to adhesive failure) above glass transition must also be taken into account in these comparisons.

The G -values obtained at 23°C differed from the corresponding results given in [13] for similar joints and materials due to different methods of crack gage measurement and fitting of the compliance. In the present work, more accurate strain channels were employed instead of the resistance channels with limited resolution used in [13]. As a result, the linear fitting of the compliance provided better correlation with experimental results than the Berry fitting used in [13].

4.3 Modeling of thermomechanical behavior

The stiffness and strength properties vs. temperature relationship across the adhesive glass transition range could be described by a polynomial of at least the 6th order. However, such a relationship would only be valid within the range of the fitted data. Another model was proposed by Mahieux et al. in [9], according to which bond strength follows a cumulative Weibull distribution as follows:

$$P(T) = P_R + (P_U - P_R) \exp\left(-\left(\frac{T}{T_0}\right)^m\right) \quad (3)$$

where $P(T)$ is a particular property, and P_U and P_R are the un-relaxed (low temperature) and relaxed (high temperature) values of the property respectively. T_0 is the relaxation temperature (the glass transition temperature of the joint herein, in [K]) and m is the Weibull exponent. Mahieux's model was initially proposed for polymers and later its applicability was validated for tensile properties of polymer matrix composites. A Weibull exponent of $m = 20$ was selected, which was found to be valid for the majority of polymers [9]. An improvement on this model based on the hyperbolic \tanh function was proposed by Gibson et al. in [10] as follows:

$$P(T) = \left(\frac{P_U + P_R}{2} - \frac{P_U - P_R}{2} \tanh(k(T - T_0)) \right) \quad (4)$$

where k is a material constant describing the temperature range over which the stiffness is reduced during the thermal softening process, and P_U , P_R and T_0 are as in Eq. (3). In this work Mahieux's (Eq. 3) and Gibson's (Eq. 4) models were employed to characterize the temperature-dependent normalized joint stiffness. P_U denotes the initial normalized stiffness (normalized by the value at 23°C), which is equal to 1.0, and parameters T_0 , P_R and k were determined by fitting Eq. (4) to the experimental data

The results obtained from the application of both empirical models to joint stiffness are shown in Fig. 14. Values of 49.2°C and 48.4°C were derived for T_0 from Mahieux's and Gibson's models respectively, which were in the range of T_g of the adhesive (40-50°C), see Section 2.1. As expected, the model by Gibson et al. perfectly represented the experimental data (parameters used and obtained were $P_R = 0.158$, $k = 0.163$), while the model by Mahieux et al. (with $m = 20$, $P_R = 0.209$) was slightly less accurate and produced a rather sharp change of slope in the stiffness-temperature plot at the beginning and end of the transition.

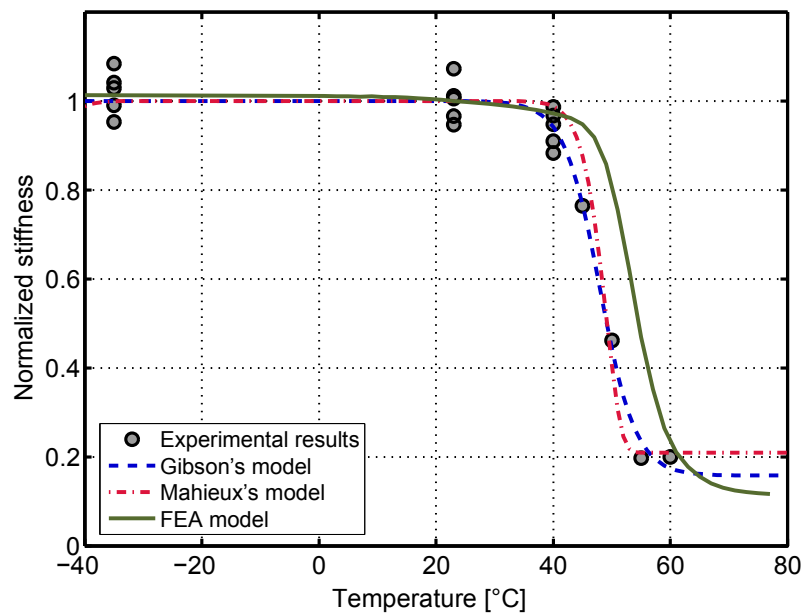


Figure 14. Comparison of empirical models vs. FE for predicting specimen stiffness as function of temperature.

FEA offers a means of modeling the temperature-dependent stiffness of a joint when only the temperature-dependent properties of the constituent materials are known. The

results obtained from the FEA model described in Section 2.3 are shown in Fig. 14 and compare well to experimental results. The drop in stiffness, however, occurred at slightly higher temperatures than measured and predicted by the other models. The lack of DMA results for the veil and mat layers is the main reason for this discrepancy.

5 CONCLUSIONS

The quasi-static tensile behavior of adhesively-bonded double-lap joints, composed of pultruded GFRP laminates and an epoxy adhesive, was investigated under temperatures ranging between -35°C and 60°C . The following conclusions were drawn:

1. The load-elongation response was mainly influenced by the thermomechanical behavior of the adhesive and much less so by that of the adherends. While the response was almost linear for adhesives in the glassy state (from -35°C up to 40°C) and the leathery state (above 50°C), it was non-linear in the glass transition temperature range (between 40 and 50°C).
2. The strength and stiffness of the joint were not affected by temperatures in the operational range of -35°C to 40°C , below the glass transition temperature of the adhesive. The highest strength was obtained at 40°C due to a statistical size effect caused by the smoothing of the normal tensile and shear stress peaks. At temperatures above glass transition, strength and stiffness decreased following the trend of the thermomechanical behavior of the adhesive.
3. The failure mechanism changed with increasing temperature at glass transition from fiber-tear to adhesive failure. The strength of the adherend-adhesive interface appeared to be more affected by temperature than the adherend strength.
4. The crack initiation load was not affected by temperatures below glass transition, while it decreased during and above glass transition. At the low temperature, the crack propagation phase was shorter and the crack propagation rate higher than at ambient and high temperatures.
5. The strain energy release rate showed a typical R-curve. Critical strain energy release rates for crack initiation and propagation consistently increased from low to ambient to high temperatures with corresponding softening of the adhesive.

6. The thermomechanical behavior was modeled using existing empirical models and FEA. The FE modeling took into account the temperature-dependent stiffness of adhesive and adherends, obtained from DMA. The results obtained from both types of models compared well to experimental results in the considered temperature range. However, the ability of the FE method to model different joint configurations without the need for more experimental input establishes it as being the most appropriate method for this purpose.

ACKNOWLEDGMENT

The authors would like to thank the Swiss National Science Foundation (Grant No 200020-111702), Sika AG, Zurich (adhesive supplier) and Fiberline Composites A/S, Denmark (pultruded laminate supplier) for their support of this research.

REFERENCES

- [1] Brewis DM, Comyn J, Shalash RJA. The effect of moisture and temperature on the properties of an epoxide-polymide adhesive in relation to its performance in single lap joints. *Int J Adhes Adhes* 1982; 2(4):215-222.
- [2] Parker BM. Some effects of moisture on adhesive-bonded CFRP-CFRP joints. *Compos Struct* 1986; 6(1-3):123-139.
- [3] Adams, RD, Coppendale J, Mallick V. The effect of temperature on the strength of adhesive joints. *Int J Adhes Adhes* 1992; 12(3):185-190.
- [4] Da Silva FML, Adams RD. Adhesive joints at high and low temperatures using similar and dissimilar adherends and dual adhesives. *Int J Adhes Adhes* 2007; 27(3):216-226.
- [5] Da Silva FML, Adams RD. Joint strength predictions for adhesive joints to be used over a wide temperature range. *Int J Adhes Adhes* 2007; 27(5):362-379.
- [6] Owens JFP, Lee-Sullivan P. Stiffness behaviour due to fracture in adhesively bonded composite-to-aluminium joints. *Int J Adhes Adhes* 2000; 20(1):47-58.
- [7] Deb A, Malvade I., Biswas P, Schroeder J. An experimental and analytical study of the mechanical behavior of adhesively bonded joints for variable extension rates and temperatures. *J Adhes Adhes* 2008; 28(1):1-15.

-
- [8] Ashcroft IA, Hughes DJ, and Shaw SJ. Mode I fracture of epoxy bonded composite joints: 1. Quasi-static loading. *Int J Adhes Adhes* 2001; 21(2):87-99.
- [9] Mahieux CA, Reifsnider KL, Case SW. Property modeling across transition temperatures in PMC's: part I. Tensile properties. *Appl Compos Mater* 2001;8(4):217-234.
- [10] Gibson AG, Wu YS, Evans JT, Mouritz AP. Laminate theory analysis of composites under load in fire. *J Compos Mater* 2006; 40(7):639-658.
- [11] Keller T, Vallée T. Adhesively bonded lap joints from pultruded GFRP profiles, Part I: Stress-strain analysis and failure modes. *Compos Part B-Eng* 2005; 36(4):331-340.
- [12] Abdel-Wahab MM, Ashcroft IA, Crocombe AD, Smith PA. Finite element prediction of fatigue crack propagation lifetime in composite bonded joints. *Compos Part A-Appl S* 2004; 35(2):213-222.
- [13] Zhang Y, Keller T. Progressive failure process of adhesively bonded joints composed of pultruded GFRP. *Compos Sci Technol* 2008; 68(2):461-470.
- [14] Keller T, Vallée T. Adhesively bonded lap joints from pultruded GFRP profiles, Part II: Joint strength prediction. *Compos Part B-Eng* 2005; 36(4):341-350.
- [15] De Castro J, Keller T. Ductile double-lap joints from brittle GFRP laminates and ductile adhesives. Part I: Experimental investigation. *Compos Part B-Eng* 2008; 29(2):271-281.
- [16] Curley AJ, Hadavinia H, Kinloch AJ, Taylor AC. Predicting the service-life of adhesively-bonded joints. *Int J Fract* 2000; 103:41-69.
- [17] Bai Y, Keller T. and Vallée T. Modeling of stiffness of FRP composites under elevated and high temperatures. *Compos Sci Technol* 2008;68(15-16):3099-3106.
- [18] Vallée T, Correia JR, Keller T. Probabilistic strength prediction for double lap joints composed of pultruded GFRP profiles part I: Experimental and numerical investigations. *Compos Sci Technol* 2006; 66(13):1903-1914.

2.5 Mechanical behavior under fatigue loading

Summary

The mechanical and fracture behavior of structural joints under quasi-static loading and environmental effects on joint behavior were discussed in Section 2.1-2.4. In the following three sections (Section 2.5-2.7), investigations will focus on the mechanical and fracture behavior of adhesively-bonded structural joints, i.e. DLJs and SLJs, under cyclic axial tensile loading. Generally speaking, there are three main categories of approaches for characterizing the fatigue behavior of structural joints (see Section 1.1). Besides the establishment of $F-N$ curves, the stiffness/strength degradation approach was employed in this paper to cover Task 3.1-3.4 in Fig. 1. The residual stiffness of structural joints was selected as the damage matrix to describe fatigue lifetime.

An experimental investigation was performed involving DLJs and SLJs composed of pultruded GFRP laminates under cyclic axial tensile loading. A critical stiffness was found for DLJs and a critical elongation for SLJs at which failure occurs independently of load level. With regard to the decreasing joint stiffness after crack initiation, a linear stiffness degradation model was established for DLJs and a non-linear sigmoid model for SLJs, in which stiffness decreased at a higher rate during the initial and final stages of crack propagation. Both these models provided good agreement compared to experimental results and enable the fatigue life prediction corresponding to the allowable stiffness degradation.

Reference details

The paper, "Stiffness degradation and fatigue life prediction of adhesively-bonded joints for fiber-reinforced polymer composites" by Ye Zhang, Anastasios P. Vassilopoulos and Thomas Keller, was published in International Journal of Fatigue 2008, volume 30, pages 1813-1820.

[doi:10.1016/j.ijfatigue.2008.02.007](https://doi.org/10.1016/j.ijfatigue.2008.02.007)

STIFFNESS DEGRADATION AND LIFE PREDICTION OF ADHESIVELY-BONDED JOINTS FOR FIBER-REINFORCED POLYMER COMPOSITES

Ye Zhang, Anastasios P. Vassilopoulos and Thomas Keller

Composite Construction Laboratory (CCLab),
Ecole Polytechnique Fédérale de Lausanne (EPFL),
Station 16, Bâtiment BP, CH-1015 Lausanne, Switzerland

ABSTRACT

Adhesively-bonded joints, including double- and stepped-lap joints (DLJs and SLJs), were experimentally investigated under cyclic tensile loading. The joints were composed of pultruded GFRP laminates and epoxy adhesive. A critical stiffness was found for DLJs and a critical elongation for SLJs at which failure occurs independently of load level. Based on measured uniform stiffness degradation during the fatigue life of DLJs, a linear model of stiffness degradation was established. For SLJs, after crack initiation, stiffness decreased at a higher rate during the initial and final stages of crack propagation. A non-linear sigmoid model was established. Results of both models compared well to experimental results and enabled F-N curves suitable for design to be established.

KEYWORDS

Adhesive joints; Fatigue; Life prediction; S-N curves; Stiffness degradation

1 INTRODUCTION

The fatigue of adhesively bonded composite joints was initially investigated for aerospace and aircraft structure applications. Nowadays adhesively bonded joints, especially joints composed of pultruded GFRP laminates, are also used in civil engineering. In these applications joints are exposed to complex loading patterns, and frequently fail due to fatigue loads. It is therefore important to understand the fatigue behavior of these structural elements and establish models to predict the fatigue damage accumulated in the material.

Different approaches have been adopted, based on different damage metrics for measuring fatigue damage accumulation. The aim of these studies was to establish a procedure that could reliably predict material fatigue behavior material with a minimum of experimental work. Existing fatigue theories fall into four categories [1].

(a) Macroscopic failure theories based on static strength criteria modified to take cyclic loading into account.

(b) Strength degradation fatigue theories, where the damage metric is the residual strength of the composite material after a cyclic program. According to these, failure occurs when residual strength decreases to the maximum applied cyclic stress.

(c) Stiffness degradation fatigue theories, where the damage metric is the residual stiffness (the stiffness of the material after N loading cycles).

(d) Damage mechanism fatigue theories, based on the modeling of intrinsic defects in the matrix of the composite material that can be considered as matrix cracks. Studying the development of these cracks provides information on fatigue damage.

The stiffness/strength-based models were mostly established as phenomenological models since they propose an evolutionary law to describe the gradual degradation of the specimen's stiffness or strength in terms of macroscopically measurable properties [2]. The modeling of the varying damage metric reflects the damage accumulation in specimens during fatigue. The damage metric depends on many factors, including applied cyclic stress, number of fatigue cycles, loading frequency and environmental conditions.

The stiffness-based model is based upon the change in stiffness of a material or a structural component undergoing fatigue. The residual stiffness is expressed as a function of initial stiffness and number of cycles. The relation between these three parameters can be in any mathematical form, e.g. linear, power, sigmoid, depending on the experimental data.

Similar models were developed using residual strength as the damage metric. However, stiffness offers certain advantages compared to strength: it can be measured using non-destructive methods and presents less scatter on the measured results than strength data. Furthermore, residual strength exhibits only minimal decreases with the number of cycles until it begins to change rapidly close to the end of lifetime, while stiffness exhibits greater changes during fatigue life [1, 3-5] and thus a higher sensitivity to damage progression.

A power law relation has been used in [6, 7] to describe the stiffness degradation of a glass- fiber cloth composite laminate. The concept of fatigue modulus has been introduced. It was defined as the ratio of maximum stress over maximum strain at a specific cycle. Fatigue modulus measured during the first loading cycle was assumed to be the same as the elastic modulus. The fatigue modulus at failure was dependent on the applied cyclic stress level.

A modified exponential model was introduced in [8] to describe the behavior of AS4/3501-6 graphite/epoxy laminates. Stiffness at any loading cycle was expressed as a function of the initial stiffness, ultimate strength of the laminate, applied stress level and two constants that should be adjusted by fitting the model to the experimental data.

Although a number of studies were presented on the modeling of the stiffness degradation of several materials, fewer were presented on the investigation of the fatigue behavior of structural components such as structural joints, e.g. [9-10].

The concept of the shear stiffness modulus has been introduced in [9] for study of the fatigue life of adhesive lap joints produced from bi-directional woven E-glass fibers and polypropylene matrix. The shear stiffness modulus was defined as the ratio between shear stress in the bond and axial strain. Experimental results showed that the joints exhibited little and almost linear stiffness degradation throughout most of the life, followed by a sudden decrease between $0.95 < N/N_f < 1$. A similar tendency was observed in [10] for double-lap joints of GFRP pultruded laminates. Although GFRP laminates exhibited considerable stiffness degradation under low cyclic loads, the joint specimens showed degradation of less than 5% up to failure.

The above studies proved that residual stiffness could be an efficient damage metric for description of the fatigue behavior of composite materials and structures. However, most of the existing works on adhesively-bonded joints do not propose any methodology to connect

stiffness degradation with fatigue life. Experimental data from a testing program consisting of static and fatigue tests on double-lap and stepped lap joints are presented here. The dependence of stiffness changes on applied stress level and joint type was systematically investigated and theoretical models for monitoring the damage accumulation in these structural elements were developed and design allowables established.

2 EXPERIMENTAL INVESTIGATION

2.1 Material and specimen description

Two types of specimens were considered: balanced double-lap joints (DLJs) and stepped lap joints (SLJs), both composed of pultruded GFRP laminates of 50 mm width and 6 or 12 mm thickness. The adhesive layer was 2 mm thick. The pultruded GFRP laminates (supplied by Fiberline A/S, Denmark) were composed of E-glass fibers embedded in an isophthalic polyester resin. In accordance with ASTM D3171-99, burn-off tests were performed in an oven where the highest temperature reached was 600°C. The glass fiber density was 2560kg/m³ as specified by the manufacturer. The determined glass fiber volume fractions were 43.6% and 48.5% respectively for 6- mm and 12 mm thick GFRP laminates. The fiber architecture of the two laminates was similar as they both comprised mat layers on the outside and roving in the core region. The 12 mm thick laminate comprises two mat layers on each side, while the 6 mm thick laminate contains only one mat layer. A mat layer consists of a chopped strand mat (CSM) and a woven mat 0°/90°, stitched together. A polyester surface veil of 40 g/m² was also applied on the outer surfaces of the pultruded laminates. A two-component epoxy system was used (SikaDur 330 from Sika AG) to manufacture the specimens. This epoxy system showed an almost elastic behavior and a brittle failure under axial quasi-static tensile loads as presented in [11].

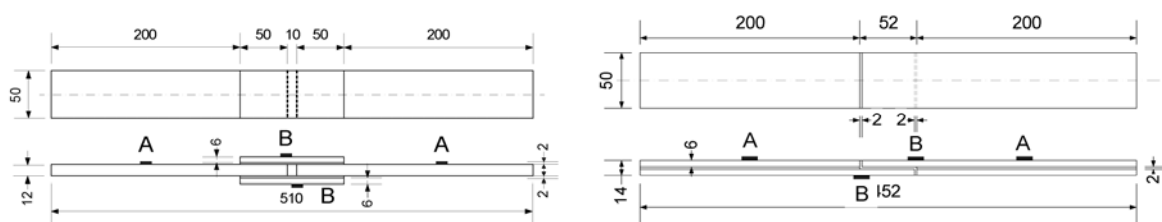


Figure 1. Dimensions and instrumentation of DLJs and SLJs.

The dimensions of the specimens are shown in Fig. 1. All specimens were manufactured in ambient laboratory conditions and subsequently cured for ten days. All surfaces subjected to bonding were mechanically abraded with sandblasting paper using a hand grinder and then chemically degreased using acetone before manufacture. To ensure constant adhesive thickness and good alignment of specimens, a special aluminum-laying frame was employed for both types of joints. In addition, 2 mm thick steel bolts were used to support the GFRP laminates in order to keep the adhesive thickness constant. These spacers were placed outside potential crack initiation regions to avoid any influence on the mechanical behavior of the joints.

2.2 Experimental set-up

Constant amplitude fatigue tests of sinusoidal waveform were realized for both DLJs and SLJs. Tension fatigue ($R=0.1$) was selected. Four different maximum load levels, including 45% (48% for SLJ), 55%, 65%, and 80% of ultimate static loads of each type of joints were selected in order to reach fatigue lives between 10^2 and 10^7 cycles. For each joint type 12 specimens were tested, three at each load level, for the determination of each Load- N curve, henceforth designated $F-N$ curve. For all tests frequency was kept constant at 10 Hz, while temperature and humidity levels were controlled to 23°C and 50% accordingly. An INSTRON 8800 hydraulic test rig of 100 kN capacity and a climate chamber were used for all tests. Two HBM spider8 measuring devices were used for data acquisition. Four strain gages were glued onto each specimen at the locations designated A and B in Fig. 1. Strain gages at location A were measuring the uniformly distributed strain of the laminate, while those at location B were used as back-face strain gages. They were placed above locations where any crack initiation would be expected to considerably influence the strain field. The back-face strain gages were used, therefore, to identify crack initiation. It was anticipated that a sudden change in strains would be recorded due to stress redistribution after crack initiation or after the failure of the small gap in the SLJ components.

2.3 Experimental results and discussion

The dominant failure mode of both joint types was a fiber-tear-off failure. For DLJs, failure initiation occurred in the outer mat layers of the 12 mm laminates at the ends of the bonded

surface. The initial crack developed with fatigue loading and propagated until the load transfer area was too small to sustain the applied load. Then final failure occurred in a brittle manner. A similar failure process was observed for the stepped lap joints, with the small transverse gap filled with adhesive failing first. The crack then entered into the outer mat layer of the pultruded laminate at this location and propagated in this layer until reaching the small gap on the opposite side of the joint. For both joint types, crack opening was visible during fatigue loading. The SLJ thus became a single-lap joint as soon as the small gaps failed. Then, due to the unbalanced joint configuration, mode I fracture became dominant and peeling (or through-thickness tensile) stresses were leading the failure. In the case of the DLJ configuration however, symmetry was maintained even after initiation of the crack(s) and it could thus be concluded that failure was led by mode II fracture, or shear stresses in the bonding area. The dominant failure mechanism and the failure process were the same as under quasi-static loads, presented in [12]. However, in the case of quasi-static loading it was not possible to follow damage development without measuring devices, since failure occurred very suddenly with no prior notice or even appearance of any visible cracks. Typical failure modes of DLJ and SLJ specimens are depicted in Figs. 2-3 accordingly.

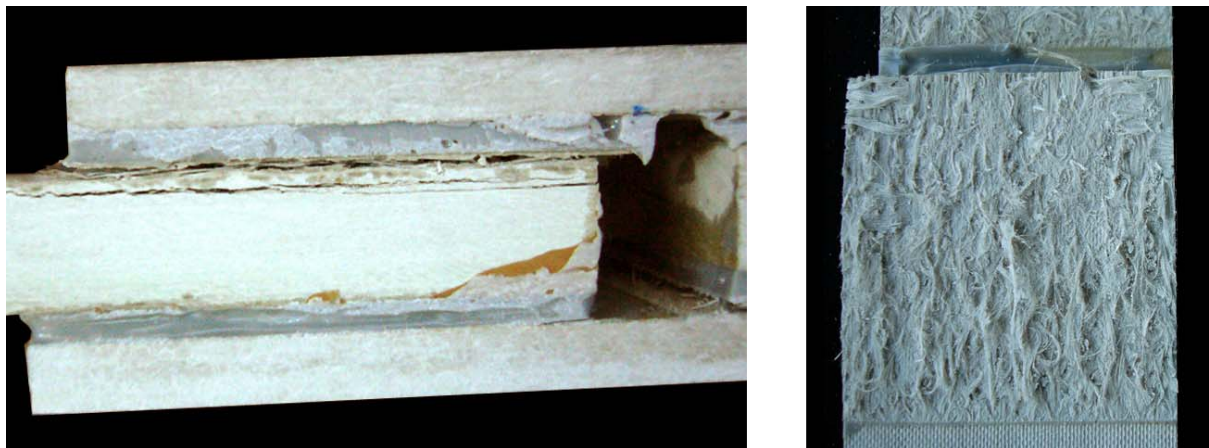


Figure 2. Typical failure mode of DLJ specimens, failure surface shown on the right.

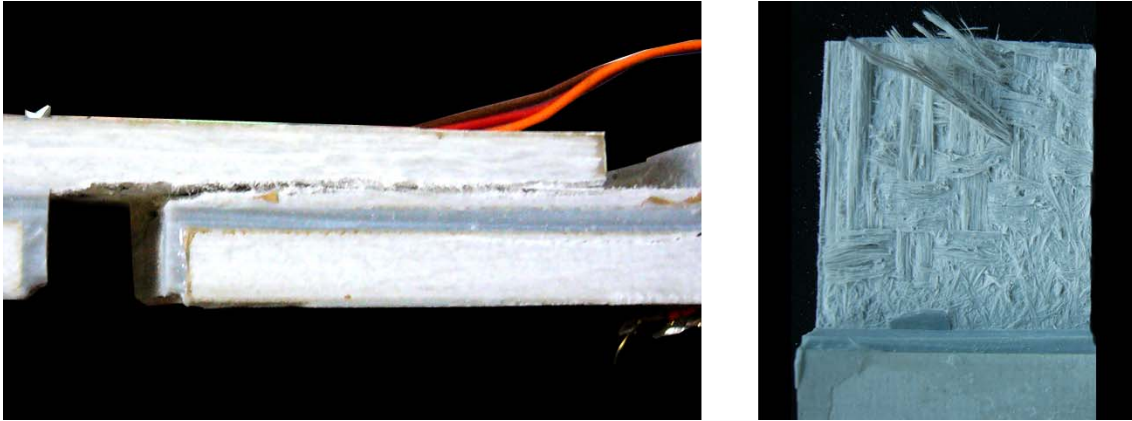


Figure 3. Typical failure mode of SLJ specimens, failure surface shown on the right.

$F-N$ curves derived experimentally for DLJ and SLJ specimens are shown in Fig. 4, the solid line corresponding to the DLJs and the dashed to SLJs. Normalized load data were used in both cases, as maximum applied load, F , was divided by the corresponding ultimate tensile load, F_u , in order to produce comparable results. Slight differences can be observed between the real load output from the testing machine, which is presented in Fig. 4, and the predetermined load levels for the tests. However, as can be seen, the SLJs exhibited longer lives for the same normalized load level.

Structural stiffness changes during fatigue life were recorded for both types of joints. Different patterns of stiffness degradation were observed for the two different joint configurations. For the DLJs failure occurred after slight stiffness degradation, less than 5-7%, irrespective of load level, as indicated by the experimental results in Fig. 5. Here, the structural stiffness of the joint during the N^{th} cycle, $E(N)$, was normalized over the value measured during the first loading cycle, $E(0)$. The number of loading cycles, N , was normalized over the life at failure, N_f . In DLJs, almost linear stiffness degradation was observed during most of the fatigue process, i.e. in the $0.05 < N/N_f < 0.95$ range. Close to the final fatigue failure, when crack propagation was unstable, stiffness degradation rate increased significantly. A linear relation is established if the maximum cyclic load is plotted against elongation at failure, see Fig. 6. In addition to fatigue data, this figure also shows the static ultimate loads and corresponding elongation. In this case, the residual stiffness can be considered as a critical structural stiffness, the same for all load levels, and once it is reached, final failure occurs. This critical stiffness value was established as 32.2 ± 1.6 kN/mm by the tests.

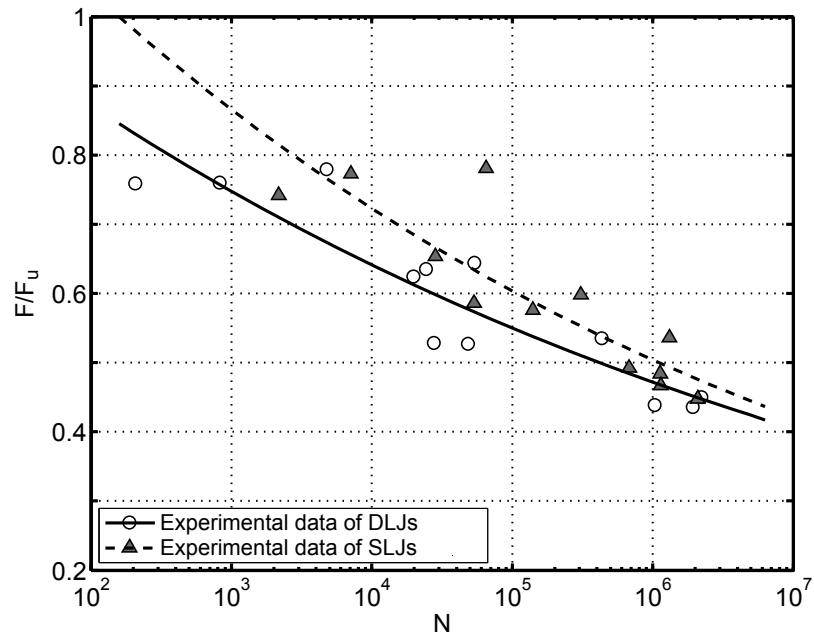


Figure 4. F-N curves of DLJs and SLJs.

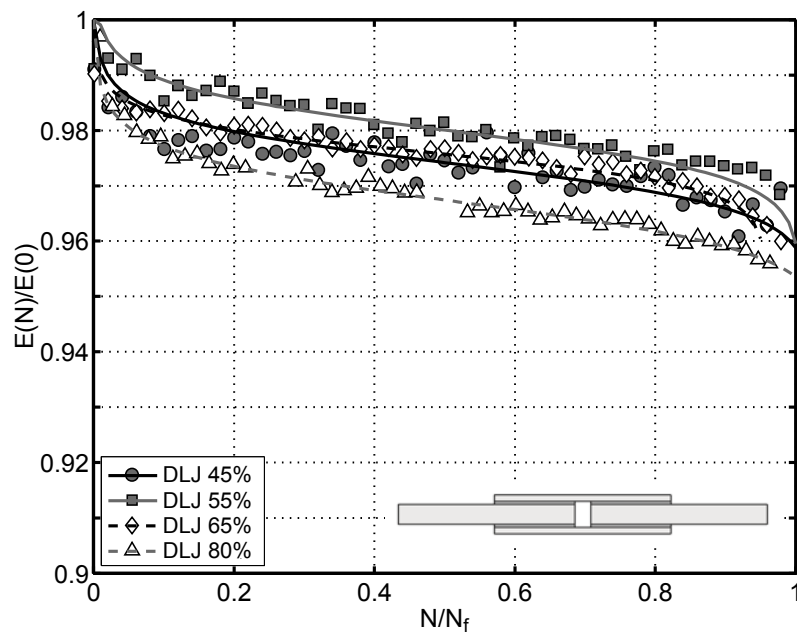


Figure 5. Stiffness degradation of DLJs during fatigue.

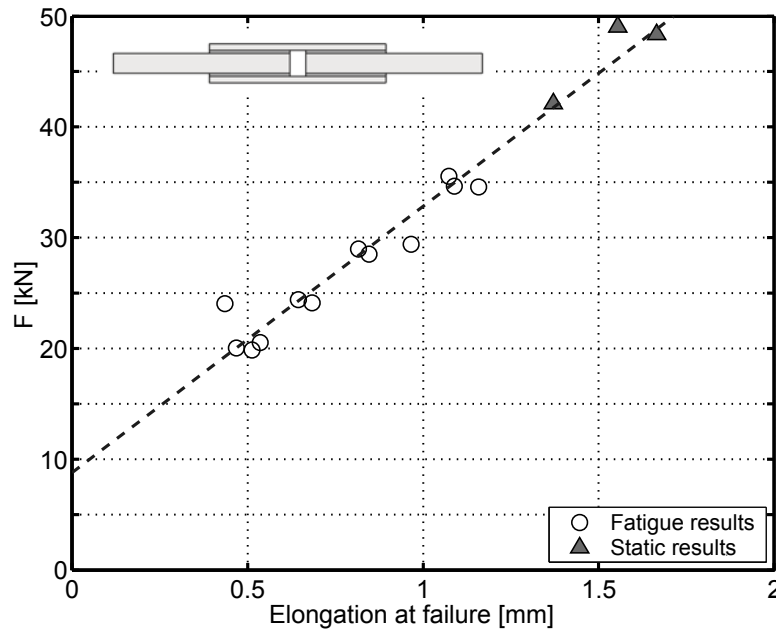


Figure 6. Maximum elongation of DLJs at failure in static and fatigue experiments.

For the SLJs the results were different as stiffness degradation was dependent on the failure of the small gaps filled by adhesive. As shown in Fig. 7, the failure of the gap was always followed by a considerable stiffness decrease of the order of 55-60% of initial stiffness, independent of applied load level. This failure was not correlated to the final failure of the specimens, but only to the initiation of damaging cracking in the adhesively-bonded area. After initiation of the crack(s), life depended on the crack propagation rate and therefore the applied load level. Fig. 8 shows the normalized stiffness fluctuations during crack propagation $(N-N_i)/(N_f-N_i)$, where N_i denotes the life for crack initiation, for all corresponding load levels. Fitted curves are used to show the tendency of the experimental data. It is shown that stiffness reductions of 15-25% were recorded for different specimens. These curves can be partitioned into three parts with respect to the fatigue life for the crack propagation: one part for lives between $0.2 < (N-N_i)/(N_f-N_i) < 0.8$ which is characterized by a low-rate uniform stiffness degradation and two other parts, one at the beginning for $0 < (N-N_i)/(N_f-N_i) < 0.2$ and the other at the end of life that are characterized by their high stiffness degradation rate. For this type of specimens, a similar failure elongation was measured independent of applied load level. The maximum cyclic elongation at failure was 1.02 ± 0.11 mm and, as can be seen in Fig. 9, is the same as elongation at failure under quasi-static loading.

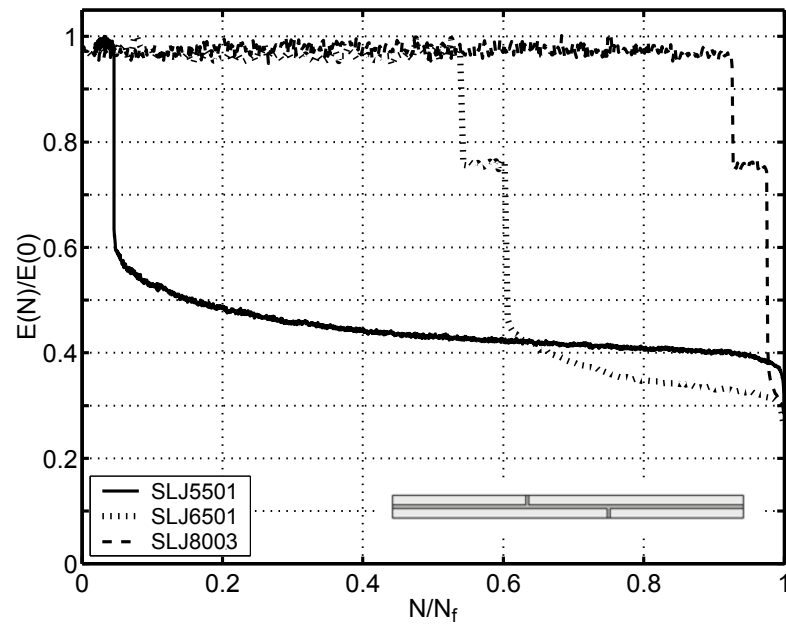


Figure 7. Stiffness degradation of SLJs during fatigue.

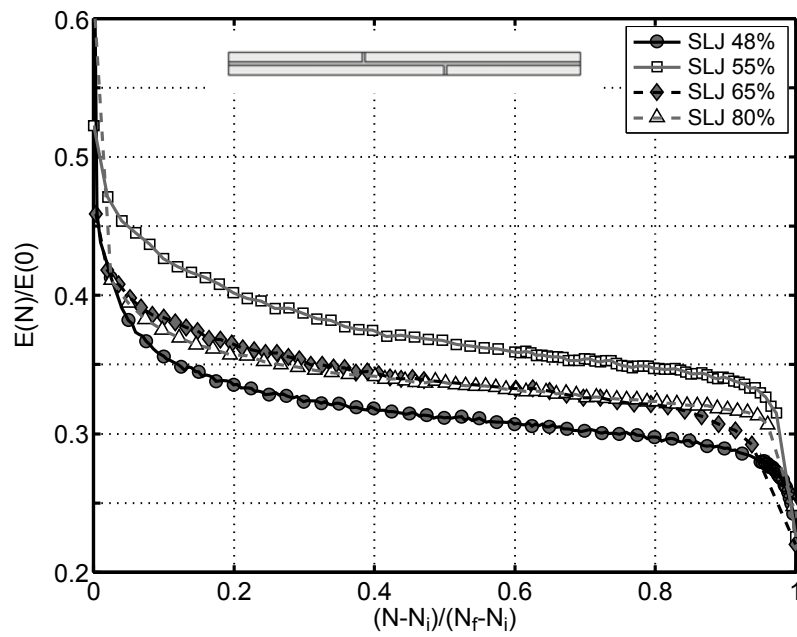


Figure 8. Stiffness degradation of SLJs during crack propagation.

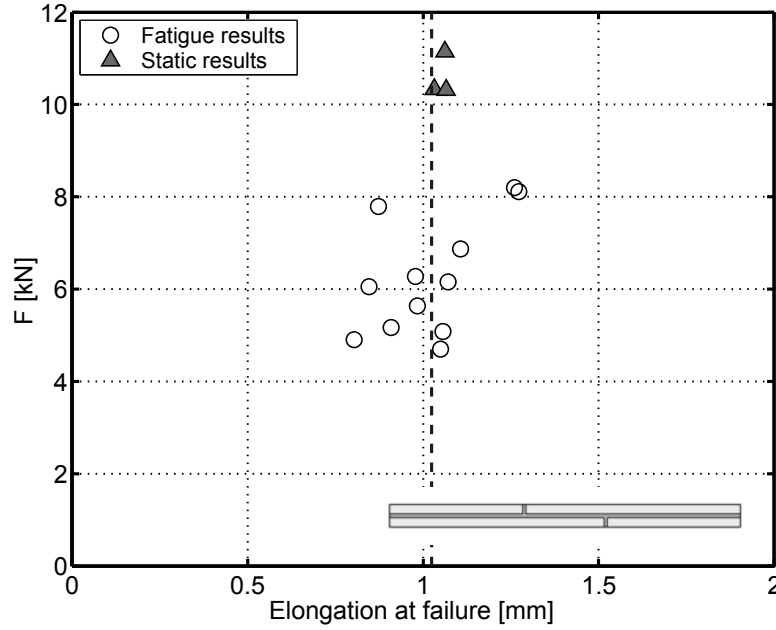


Figure 9. Maximum elongation of SLJs at failure in static and fatigue experiments.

3 STIFFNESS DEGRADATION MODELS

Two empirical models - a linear and a non-linear - are introduced for modeling the stiffness degradation of the two types of joints and the subsequent prediction of fatigue life. The term fatigue life prediction is used in this paper since the load-life curve ($F-N$ curve) is derived based only on stiffness degradation measurements. The curve corresponds to failure data, but no failure is needed for its derivation. In that context the process can be characterized as a predictive one.

The degree of damage in each type of joint was evaluated by measuring stiffness degradation $E(N)/E(0)$. The dynamic stiffness $E(0)$ at the first cycle is, in general, different from the one measured under quasi-static loading due to the different loading rate for fatigue and static tests.

In the case of the DLJs, where tests showed that stiffness degradation is almost linear up to failure, the following model was established:

$$\frac{E(N)}{E(0)} = 1 - k_1 \left(\frac{F}{F_u} \right)^{k_2} N \quad (1)$$

where F denotes the applied load level and could correspond to its amplitude, maximum value, or a normalized value of it. Throughout this work, F denotes the maximum applied

cyclic load and F_u corresponds to the ultimate tensile load of the joint. Model parameters k_1 and k_2 are dependent on available experimental data for stiffness degradation and it is assumed that they depend on the number of stress cycles and level of the applied load.

Eq. (1) also establishes a stiffness-based design criterion since for a preset value of stiffness degradation, $E(N)/E(0) = p$, N can be solved for to obtain an alternative form of the F-N curve, corresponding not to material failure but to a specific stiffness degradation percentage:

$$N = \frac{E(N) - E(0)}{E(0)k_1 \left(\frac{F}{F_u} \right)^{k_2}} \quad (2)$$

The term “stiffness-controlled curves” or “stiffness-based curves” was initially introduced in [13]. A heuristic procedure was established to define the so-called Sc-N curves, where Sc denotes “stiffness-controlled”. Compared to conventional S-N curves, they offer a significant advantage since they provide information concerning both allowable stiffness degradation and probability of survival.

The non-linear model is based on the assumption that stiffness degradation curves follow a sigmoid path: a high rate initially, a lower linear and constant rate for the most part of life, and finally a sharply increasing rate at the end of life. Based on this hypothesis the following equation was introduced to model the stiffness degradation data of the SLJs during crack propagation:

$$\frac{E(N)}{E(0)} = \left(\frac{N \cdot k^m}{V - N} \right)^{\frac{1}{m}} \quad (3)$$

In Eq. (3) N obtains values between the cycle at which the crack started to propagate and failure, according to the experimental data. V , k , m are parameters that should be estimated by fitting Eq. (3) to the available experimental data.

The usefulness of this model is based on the accurate estimation of the three fitting parameters, V , k and m . Analysis of the experimental data showed that V , which corresponds to the lifetime of each coupon, is strongly dependent on the applied load level. However, neither of the other fitting parameters, m that is connected to the slope of the median, linear part of the stiffness degradation curve, and k that is an estimation of the center of gravity of

the stiffness degradation curve, is significantly influenced by the cyclic load level. Therefore, to simplify the model, only the V parameter was considered as varying with load level, while m and k were attributed constant values.

By solving Eq. (3) for N , an alternative form of the F-N curve is obtained which, like Eq. (2), can be used to establish design allowables, that is, F-N curves corresponding to specific stiffness degradation percentages, $E(N)/E(0) = p$:

$$N = V \left(\frac{\left(\frac{E(N)}{E(0)} \right)^m}{k^m + \left(\frac{E(N)}{E(0)} \right)^m} \right) \quad (4)$$

4 MODELING RESULTS AND DISCUSSION

With exception of the initial and final periods, the stiffness of DLJs exhibited a constant degradation rate until final fatigue failure, see Fig. 5. Therefore, the linear model was selected to describe the behavior of this type of joints. For a given specimen, the residual stiffness is assumed to follow Eq. (1) with the term $k_1(F/F_u)^{k_2}$ representing the rate of stiffness degradation and assumed to depend on the applied load level. Model parameters are estimated by plotting the stiffness degradation rate against the relevant load levels for all the available experimental data, i.e. 12 specimens for the DLJs, as presented in Fig. 10. The resulting estimations of parameters k_1 and k_2 are: $k_1 = -0.00126$ and $k_2 = 14.176$.

After derivation of the model parameters k_1 and k_2 the expected $F-N$ behavior can be extrapolated using Eq. (2). The results are presented in Fig. 11 and are compared to the experimentally determined F-N data. As shown in Fig. 11 the linear model can produce theoretical predictions that compare well with experimental data. The slight overestimation of fatigue life is attributed to the ignorance of the initial and final periods of stiffness degradation. However, for the DLJs, the effect of these two periods on the entire life is almost negligible. In addition to the F-N curves, Sc-N curves corresponding to predetermined stiffness reduction and not to failure data can be plotted and used as design allowables. For DLJs where total stiffness degradation at failure was less than 7%, Sc-N curve for 2% decrease of stiffness is plotted, based on the linear model.

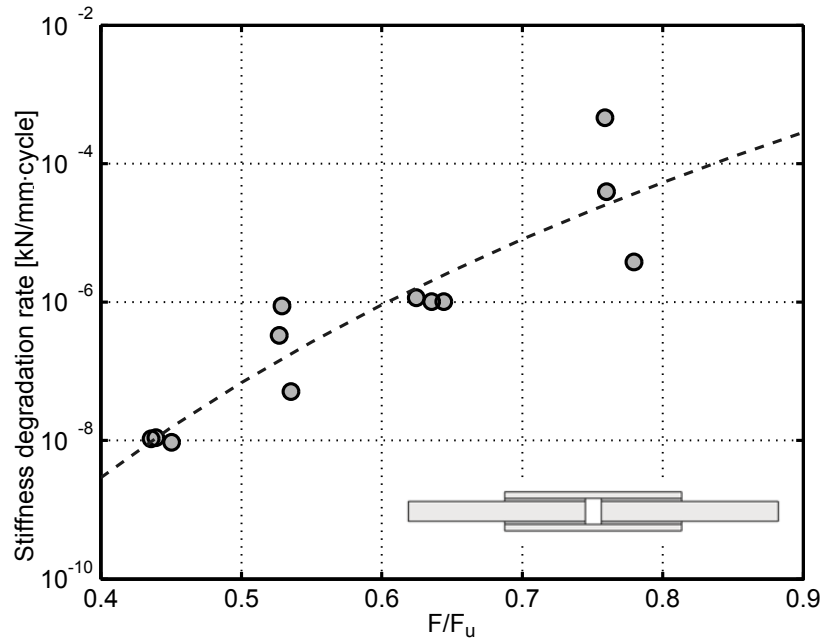


Figure 10. Stiffness degradation rate (absolute value) of DLJs at different load levels.

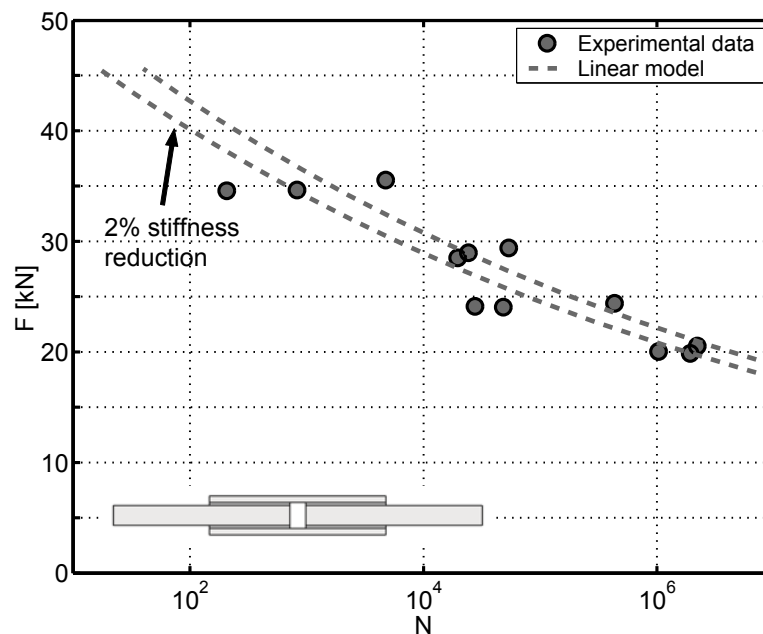


Figure 11. Comparison between predicted $F-N$ curve of DLJs and experimental results, design allowable corresponding to 2% stiffness reduction.

This linear model (Eq. (2)) was also used for the derivation of $F-N$ curves that correspond to the life for crack propagation in the SLJs. Model parameters were estimated by plotting the assumed linear stiffness degradation rate versus the corresponding load levels.

Their values were found to be: -0.00140 for k_1 and 9.139 for k_2 . However, as presented in Fig. 12, stiffness changes were more severe in this case and the linear model was able to accurately represent only the period between 20% and 80% of life for crack propagation.

The non-linear Eq. (3) was therefore considered for modeling the stiffness degradation of the SLJ specimens and the subsequent derivation of stiffness-controlled F-N curves. The three model parameters were estimated by fitting Eq. (3) to the available data for all SLJ specimens. The estimated values of all three model parameters are plotted in Fig. 13 against the normalized load levels. As depicted, V parameter is strongly dependent on the applied load level, and the two others appear unaffected by load changes. Their values were estimated as -21.80 for m and 0.34 for k . Parameter V however was assumed to be a power function of the load level. Typical curves from the non-linear model are presented in Fig. 12. It is shown that the model can effectively fit the experimental results for all cases.

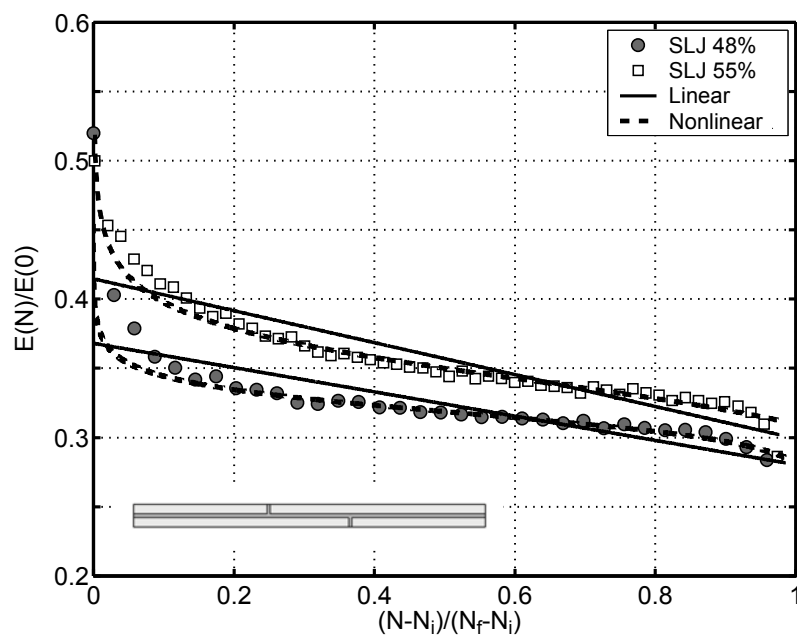


Figure 12. Linear and non-linear modeling of SLJ stiffness degradation during crack propagation.

The resulting $F-N$ curves, from both linear and non-linear models, are presented in Fig.14 together with the available test data. Only fatigue behavior in the crack propagation stage was taken into account. Compared to the experimental results, the fatigue life was overestimated by the linear model since the influence of the initial and final periods of stiffness degradation

was ignored. The non-linear model worked successfully and good agreement between experimental data and theoretical predictions was obtained. Furthermore, Sc-N curves based on the non-linear model and corresponding to 10% and 15% stiffness reduction are presented in Fig. 14 for the SLJ specimens.

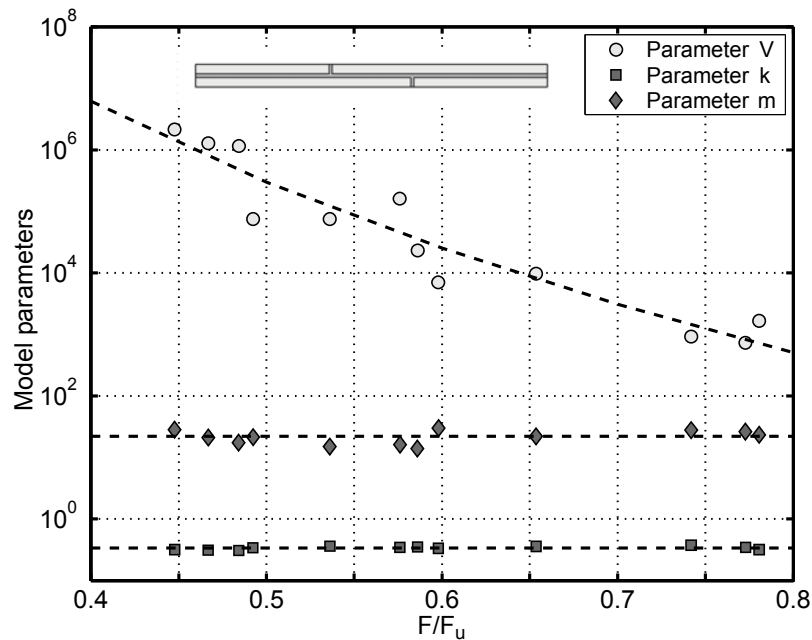


Figure 13. Model parameters for SLJs at different load levels.

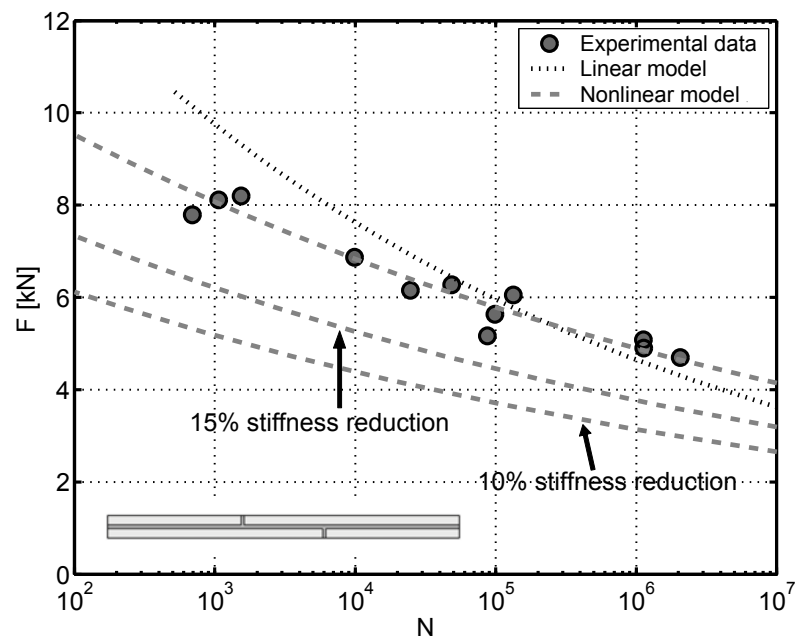


Figure 14. Comparison between predicted F-N curves for crack propagation of SLJs and experimental results, design allowables corresponding to 10% and 15% stiffness reduction.

Use of stiffness reduction as a damage metric offers several potential applications in civil engineering fields. As already pointed out, it is a non-destructive detection method and the stiffness of the structural component is a parameter that can easily be monitored. The stiffness-based life prediction method can predict the residual life of structures regardless of their loading history. This is one of the advantages compared to the general stress-based life prediction methods. Another advantage of this method is its conformity to design code designations, since the allowable stiffness reduction is a widely used criterion. Derivation of stiffness-based curves corresponding to stiffness reduction and not final failure provides useful input for designing structures based on such criteria.

5 CONCLUSIONS

The fatigue behavior of adhesively-bonded joints from GFRP laminates was experimentally investigated under the cyclic tensile loads. The following conclusions were drawn:

1. DLJs exhibit a critical stiffness and SLJs a critical elongation at which failure occurs independently of load level.
2. DLJs exhibited almost linear stiffness degradation during fatigue, which however remained low at only around 5-7%. Moreover, the rate was constant independent of the applied cyclic load level. A linear model well represented the residual stiffness.
3. Constant stiffness degradation was observed in SLJs only between 20% and 80% of life for crack propagation. At the beginning, after failure of the small gaps and at the end, close to fatigue failure, stiffness degradation was more pronounced. Results of a non-linear sigmoid model compared well to the experimental results.

Although this type of modeling requires more effort than the simpler stress-based approach (in terms of equipment, complicated recording set-up and calculations) it has the merit of also being able to specify allowable stiffness reduction levels. Moreover, since these methods are based on stiffness measurements that can be performed during the operational life of structures without interruptions and in a non-destructive manner, they can be adapted by design codes as on-line health monitoring tools.

REFERENCES

- [1] Sendeckyj GP. Life prediction for resin-matrix composite materials, *Fatigue of composite materials, composite materials series, 4*, KL Reifsneider, Ed., Elsevier, 1991.
- [2] Degrieck J, Paepegem WM. Fatigue damage modeling of fiber-reinforced composite materials: a review. *Applied Mechanics Reviews* 2001;54(4):279-300.
- [3] Highsmith, AL, Reifsneider KL. Stiffness Reduction Mechanisms in Composite Laminates, *Damage in Composite Materials, ASTM STP 775*, KL Reifsneider, Ed., American Society for Testing and Materials, 1982:103-117.
- [4] Talreja R. *Fatigue of Composite Materials*, Technomic, Lancaster Pennsylvania, 1987.
- [5] Andersen SI, Brondsted P, Lilholt H. Fatigue of polymeric composites for wingblades and the establishment of stiffness-controlled fatigue diagrams. *Proceedings of 1996 European Union Wind Energy Conference, Göteborg, Sweden, 20-24 May 1996*:950-953.
- [6] Hwang W, Han KS. Cumulative damage models and multi-stress fatigue life prediction. *J Compos Mater* 1986;20(2):125-153.
- [7] Hwang W, Han KS. Fatigue of composites – fatigue modulus concept and life prediction. *J Compos Mater* 1986;20(2):154-165.
- [8] Whitworth HA. A stiffness degradation model for composite laminates under fatigue loading. *Compos Struct* 1997;40(2):95-101.
- [9] Ferreira JAM, Reis PN, Costa JDM, Richardson MOW. Fatigue behavior of composite adhesive lap joints. *Compos Sci Technol* 2002;62(10-11):1373-1379.
- [10] Keller T, Zhou A. Fatigue behavior of adhesively bonded joints composed of pultruded GFRP adherends for civil infrastructure applications. *Compos Part A-Appl S* 2006;37(8):1119–1130.
- [11] De Castro J, Keller T. Ductile double-lap joints from brittle GFRP laminates and ductile adhesives. Part I: Experimental investigation. *Compos Part B-Eng* 2007, in press.
- [12] Zhang Y, Keller T. Progressive failure process of adhesively bonded joints composed of pultruded GFRP. *Compos Sci Technol* 2008;68(2):461-470.
- [13] Philippidis TP, Vassilopoulos AP. Fatigue design allowables for GFRP laminates based on stiffness degradation measurements. *Compos Sci Technol* 2000;60(15):2819-2828.

2.6 Fracture behavior under fatigue loading

Summary

As an alternative to Section 2.5, this paper also attempts to understand and model the long-term performance of structural joints under fatigue loading, covering Task 4.1-4.4 in Fig. 1. However, it focuses on the characterization of the fracture rather than mechanical behavior (presented in Section 2.5) by adopting linear-elastic fracture mechanics (LEFM) approach. Fatigue Crack Growth (FCG) curves are employed to describe the fatigue lifetime and the fracture parameters can then be determined.

In this paper, an experimental investigation was performed involving adhesively-bonded DLJs and SLJs composed of pultruded GFRP laminates. Having been validated in Section 2.2, crack propagation gages were employed to record crack initiation and propagation and ECM was used to calculate the maximum strain energy release rate, G_{max} , during fatigue cycles. A linear trend of crack growth and compliance was observed for the DLJs whereas a sigmoid trend was found for SLJs. The crack propagation rate, da/dN , was calculated using the 5-point incremental polynomial method. Combining the results of G_{max} and da/dN , FCG curves were established for both joint types. The resultant fracture parameters proved greatly dependent on joint configuration. Based on the modeling of the fracture behavior of structural joints, the fatigue lifetime corresponding to allowable crack length was predicted.

Reference details

This paper, "Fracture of adhesively-bonded pultruded GFRP joints under constant amplitude fatigue loading" by Ye Zhang, Anastasios P. Vassilopoulos and Thomas Keller, was published in International Journal of Fatigue, in Press.

[doi:10.1016/j.ijfatigue.2009.11.004](https://doi.org/10.1016/j.ijfatigue.2009.11.004)

FRACTURE OF ADHESIVELY-BONDED PULTRUDED GFRP JOINTS UNDER CONSTANT AMPLITUDE FATIGUE LOADING

Ye Zhang, Anastasios P. Vassilopoulos and Thomas Keller

Composite Construction Laboratory (CCLab),
Ecole Polytechnique Fédérale de Lausanne, (EPFL),
Station 16, Bâtiment BP, CH-1015 Lausanne, Switzerland

ABSTRACT

The fracture behavior of adhesively-bonded structural joints under tensile constant amplitude fatigue has been investigated. Double-lap joints (DLJs) and stepped-lap joints (SLJs) composed of pultruded GFRP laminates and an epoxy adhesive were examined. Both joint types exhibited a fiber-tear failure with cracks that initiated at the joint edges in the adhesive-laminate interface and then propagated in the laminates' mat layers. A linear trend of crack growth and compliance was observed for the DLJs whereas a sigmoid trend was found for SLJs. The experimental compliance method was used for the calculation of the maximum strain energy release rate, G_{max} , and the incremental polynomial method for the calculation of the crack propagation rate, $d\alpha/dN$. Fatigue crack growth (FCG) curves established for both joint types showed that empirical constants are dependent on the joint configuration. Based on this fatigue life modeling, design allowables that correlate the developed damage with fatigue life were derived

KEYWORDS

Glass fibers; Fatigue; Fracture; Pultrusion; Joints/joining

1 INTRODUCTION

Pultruded glass fiber-reinforced polymer (GFRP) materials are beginning to be used as a structural replacement for conventional materials like steel and wood in many civil engineering applications, such as bridge and building construction. Nevertheless, little progress has been made with regard to joining techniques; bolted joints are still used in most applications to connect different pultruded shapes. In this respect, adhesive bonding is often seen as a much more material-tailored joining technique for FRP materials in terms of structural efficiency and manufacturing cost [1].

Adhesives are currently used in many areas of structural engineering, basically as sealant materials or secondary structural connections, but rarely as primary structural connections. The advances made in polymers enable structural adhesives to meet a wide range of structural needs. However, the lack of reliable design methods and knowledge regarding their fatigue and durability behavior have resulted in reluctance to use adhesives in primary structures.

Single-lap joints and double-lap joints are the two main types of structural joints found in many structural applications. During the loading of a structural joint, a crack or cracks initiate naturally and propagate along the weakest path within the joint. This uncontrollable phenomenon led scientists to focus on the investigation of fracture mechanics joints, i.e. pre-cracked joints, to produce pure Mode I crack propagation (e.g. double-cantilever beam (DCB)) or Mode II fracture (e.g. End-Notched Flexure (ENF) or End-Loaded Split (ELS) beam) [2-4]. Fracture mechanics data can thus be derived, i.e. crack length, a , crack propagation rate, da/dN , and strain energy release rate, G_{max} , in a fatigue cycle under a specific applied load F_{max} .

When structural joints are used instead of fracture joints, the situation becomes more complicated as the failure mode is not pure Mode I or Mode II failure but a mixed-mode failure. The proportion of each failure mode depends on the material, joint geometry, type of loading, and environmental conditions. The strain energy release rate calculated for this mixed-mode failure is designated the total strain energy release rate [5] and is assumed to be equal to the sum of G_I and G_{II} , $G_{tot}=G_I+G_{II}$. Moreover, the crack initiates naturally and propagates in an uncontrollable way in a structural joint without a pre-crack.

Fracture mechanics theory has been used to study the fatigue behavior of structural joints by a number of researchers. Analytical solutions and, more frequently, numerical methods were used to model the fatigue life of the examined material and joint configurations. However, the results obtained from theoretical modeling are rarely compared to experimental data. A review of previous works [5-8] revealed that fracture mechanics data should be directly obtained from structural joints rather than from fracture mechanics joints. Attempts to model the fatigue life of structural joints by using fracture mechanics data obtained from fracture mechanics joints (DCB) were proposed, but modeling accuracy was very low [6]. It was concluded in [6] that the mixed-mode failure, expressed by the ratio G_I/G_{II} , should be taken into account for the calculation of reliable values of the strain energy release rate of double- and single-lap joints. Other studies support this opinion: adhesively-bonded composite-metal double-lap joints [7], or carbon/epoxy laminates bonded with epoxy adhesive to form single-lap joints [8], were tested directly to obtain fracture mechanics data rather than using DCB and/or ENF specimens.

The fatigue of adhesively-bonded joints composed of FRP composite components was initially investigated for aerospace applications [9]. However, there are fundamental structural differences between aerospace and civil engineering applications with regard to manufacturing process, material architecture, component dimensions, operational conditions, and service life. It is therefore essential that more knowledge be obtained regarding the fatigue and fracture behavior of structural joints in the civil engineering domain.

In this study, adhesively-bonded double-lap joints (DLJs) and stepped-lap joints (SLJs) composed of pultruded GFRP laminates have been experimentally investigated under cyclic tensile loading. Stiffness degradation was proved to be a valuable parameter for fatigue life modeling and the derivation of fatigue design allowables [10]. However, this method provides no information concerning damage and the way in which it develops in the material. Fatigue behavior is therefore investigated in this paper using fracture mechanics data obtained directly from the examined specimens. Fatigue life is calculated and fatigue design allowables are derived that conform to a damage tolerance design concept.

2 EXPERIMENTAL PROGRAM

Both specimen types, DLJs and SLJs, were composed of pultruded GFRP laminates bonded by an epoxy adhesive system. Full-scale dimensions were chosen to exclude size effects. The pultruded GFRP laminates (supplied by Fiberline A/S, Denmark) consisted of E-glass fibers embedded in an isophthalic polyester resin. Laminates of 50-mm width and thicknesses of 12 and 6 mm were used to form balanced joints. In addition to the unidirectional rovings in the center, the 12-mm and 6-mm laminates comprised two mat layers and one mat layer on each side, respectively. A mat layer consisted of a chopped strand mat (CSM) and a $0^{\circ}/90^{\circ}$ woven mat stitched together. On the outside, a polyester surface veil (40 g/m^2) was added to protect against environmental attack. The fiber content, determined according to ASTM D3171-99, was 48.5 vol.-% for the 12-mm laminate and 43.6 vol.-% for the thinner one. Due to the higher fiber content, the mean tensile strength and Young's modulus of the thicker laminate (355 MPa and 34.4 GPa) were higher than those of the thinner laminate (283 MPa and 31.4 GPa) [10]. A two-component epoxy adhesive was used (SikaDur 330, Sika AG Switzerland) as bonding material. Axial tensile tests were performed according to EN ISO 527-1 to characterize the epoxy adhesive. The epoxy showed an almost linear elastic behavior and a brittle failure. The mean tensile strength was 38.1 MPa, and the mean Young's modulus 4.55 GPa. [11].

The geometry of the two joint configurations is schematically shown in Fig. 1. The overlap length was 50 mm for both joint types and the adhesive thickness was 2 mm. No adhesive fillet was formed in order to simulate the worst case that can occur in practice. The transverse gaps in the SLJs were also 2 mm thick. Before manufacturing, all surfaces subjected to bonding were mechanically abraded with sanding paper using a grinder, and then chemically degreased using acetone. To ensure constant adhesive thickness and good alignment of the laminates, a special aluminum frame was designed and employed for both joint types. After manufacture, all specimens were cured in laboratory conditions for ten days.

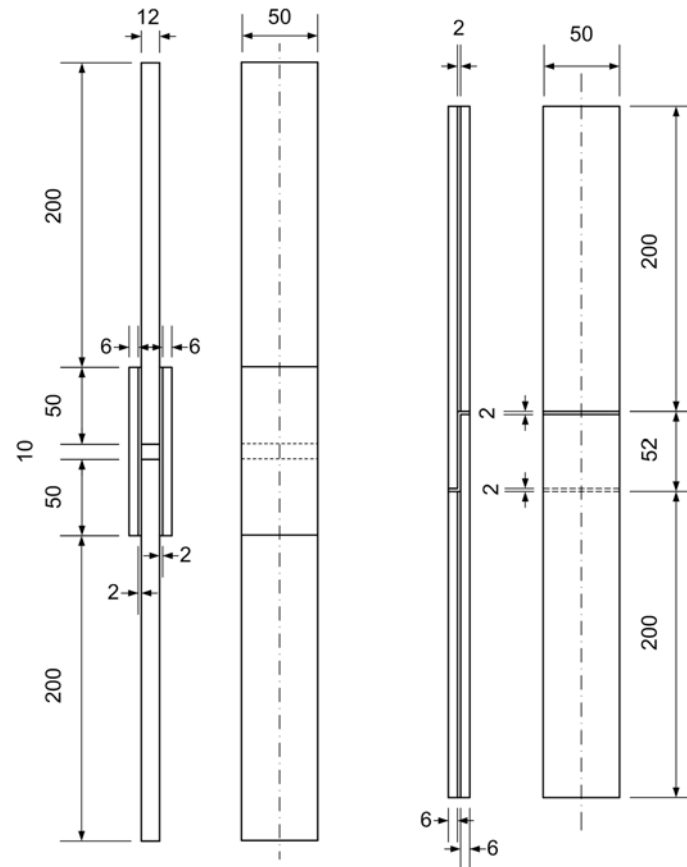


Figure 1. DLJ and SLJ geometries.

All specimens were instrumented with strain gages, while one specimen per load level was additionally instrumented with four crack gages to detect crack initiation and record crack length during propagation. Fig. 2 shows specimens with instrumentation prior to testing for the DLJ configuration and Fig. 3 for the SLJ configuration. The crack gages (HBM/RSD20) consisted of 20 wires spaced at 1.15-mm intervals perpendicular to the adhesive layer, and covered almost half of the overlap length where stable crack propagation was expected to occur. As the crack propagated, the wires were progressively broken, thus increasing the electrical resistance of the gage. In the SLJs, the crack gages were placed on both sides of the overlap where cracks could initiate and propagate after the adhesive gap failure. In the DLJs, there were four possible locations at the overlap edges where cracks could initiate and propagate. Therefore, the total crack length, measured with the four crack gages, was taken into account to describe crack propagation, rather than the crack length of one single crack. Two of the total of four strain gages per specimen were placed on the laminates, 100 mm from the joint edge, to measure axial strains outside the

joint where stresses were expected to remain uniformly distributed across the laminate width and depth. The other two strain gages, designated back-face strain gages, were placed above locations sensitive to crack initiation (see Figs. 2 and 3) to identify crack initiation. It was anticipated that a sudden change in strain would be recorded due to stress redistribution after crack initiation. This technique has successfully been employed for the identification of crack initiation in similar DLJs and SLJs under quasi-static loading [12].

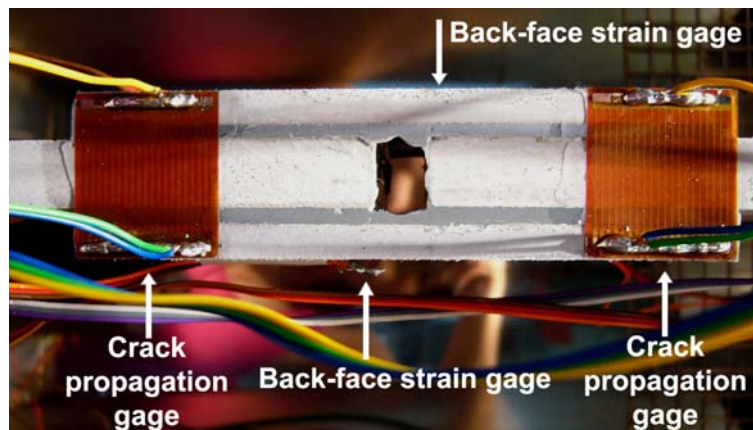


Figure 2. Instrumentation of DLJs (same configuration of crack gages on rear side).

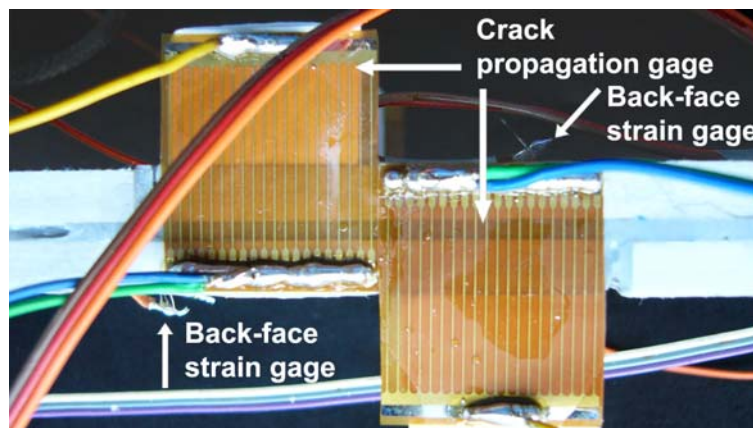


Figure 3. Instrumentation of SLJs (same configuration of crack gages on rear side).

Experiments were carried out on an INSTRON 8800 universal testing rig of 100-kN capacity under load control and laboratory conditions ($23\pm 2^\circ\text{C}$, RH $50\pm 5\%$). The frequency was kept constant at 10 Hz for all specimens, while the load ratio ($R=F_{min}/F_{max}$) was 0.1, corresponding to a tension-tension fatigue loading. Experiments were continued until

ultimate failure of the joint or 10^7 cycles, whichever occurred first. An HBM/Spider8 was used to record the measured fatigue data.

Four different nominal load levels were selected for each joint type in order to determine the load-cycle or $F-N$ curve. Load levels were selected at 45% (48% for SLJs), 55%, 65%, and 80% of the ultimate tensile load (UTL) of each joint configuration in order to obtain representative experimental data in the range between 10^2 and 10^7 cycles. Each $F-N$ curve was derived from 12 specimens, three at each of the four load levels. The specimens were labeled accordingly, with DLJ4501 signifying double-lap joint specimen 01 at 45% load level for example.

3 EXPERIMENTAL RESULTS

A set of experimental data was collected for each type of structural joint. The data measured by the machine comprised load level and amplitude, as well as cycles to crack initiation (N_i), crack propagation ($N-N_i$) and failure (N_f), see Table 1. The errors in the test waveform were compensated by means of an “amplitude control mode” of the testing machine. As a result, the load amplitude, $(F_{max} - F_{min})/2$, was perfectly controlled while the absolute values of F_{min} and F_{max} varied slightly, less than 7%, during each test. Furthermore, strains from strain gages and resistances from crack gages were obtained. In the following paragraphs, the fatigue data is presented and the fracture fatigue behavior of the structural components analyzed.

3.1 Failure modes

For both joint types, cracking was visible during fatigue loading. The dominant failure mode was a fiber-tear failure as shown in Fig. 4 for the DLJs and Fig. 5 for the SLJs, similar to that observed under quasi-static loads [12]. In the latter case, however, it was not possible to visually observe the damage development, since failure occurred very suddenly.

Failure initiation in DLJs occurred in the adhesive-adherend interface at one joint end. The crack then rapidly penetrated into the 12-mm laminate over a length of approximately 1 mm and propagated in the outer mat layers. Other, less damaging, cracks developed simultaneously from the opposite joint end. The initial dominant crack developed with fatigue loading and propagated until the load transfer area was too small to sustain the applied load and final failure occurred in a brittle manner.

Table 1. Recorded fatigue data for DLJs and SLJs.

Nominal load level [%UTL]	Specimen ID	Maximum cyclic load, F_{max} [kN]	Cycles to failure, N_f	Cycles to crack initiation, N_i	Cycles for crack propagation, $N_f - N_i$	Cycle ratio to crack initiation, N_i / N_f [%]	Cycle ratio for crack propagation, $(N_f - N_i) / N_f$ [%]		
DLJ	45	DLJ4501#	20.5	2215704	161100	2054604	7.3	92.7	
		DLJ4502	20.0	1030600	990835	39765	96.1	3.9	
		DLJ4503	19.9	1927124	1340300	586824	69.5	30.5	
	55	DLJ5501#	24.4	432844	6888	425956	1.6	98.4	
		DLJ5502	24.0	48180	22421	25759	46.5	53.5	
		DLJ5503	24.1	27647	5391	22256	19.5	80.5	
	65	DLJ6501#	28.5	19788	2880	16908	14.6	85.4	
		DLJ6502	29.0	24306	-	-	-	-	
		DLJ6503	29.4	53664	37178	16486	69.3	30.7	
80		DLJ8001#	34.7	823	35	788	4.3	95.7	
		DLJ8002	34.6	207	-	-	-	-	
		DLJ8003	35.5	4731	3724	1007	78.7	21.3	
	SLJ	48	SLJ4801*#	4.7	2089194	22405	2066789	1.1	98.9
			SLJ4802*	5.1	1130205	7315	1122890	0.6	99.4
			SLJ4803*	4.9	1140139	8338	1131801	0.7	99.3
55		SLJ5501#	6.0	139917	6219	133698	4.4	95.6	
		SLJ5502	5.6	1313070	1214300	98770	92.5	7.5	
		SLJ5503	5.2	679530	592580	86950	87.2	12.8	
65		SLJ6501#	6.2	53317	28581	24736	53.6	46.4	
		SLJ6502	6.3	307710	259100	48610	84.2	15.8	
		SLJ6503	6.9	28300	18407	9893	65.0	35.0	
80		SLJ8001#	7.8	2171	1481	690	68.3	31.8	
		SLJ8002	8.1	7089	6026	1063	85.0	15.0	
		SLJ8003	8.2	64933	63395	1538	97.6	2.4	

* with 2-mm-deep notch in adhesive gap.

with four crack propagation gages

A similar failure process was observed for the SLJs, in which the small transverse gap filled with adhesive failed first. The crack then entered into the outer mat layer of the laminate at this location and propagated in this layer until it reached the small gap on the opposite side of the joint. In some cases, cracks penetrated into the roving layer, below the mat layers. The specimens that were subjected to the low load level of 48% of UTL were an exception to this rule however. The adhesive in the transverse gap did not fail, even after the application of more than 5 million loading cycles. To initiate failure of these joints, a 2-mm deep notch was cut into the adhesive of the transverse gap prior to testing.

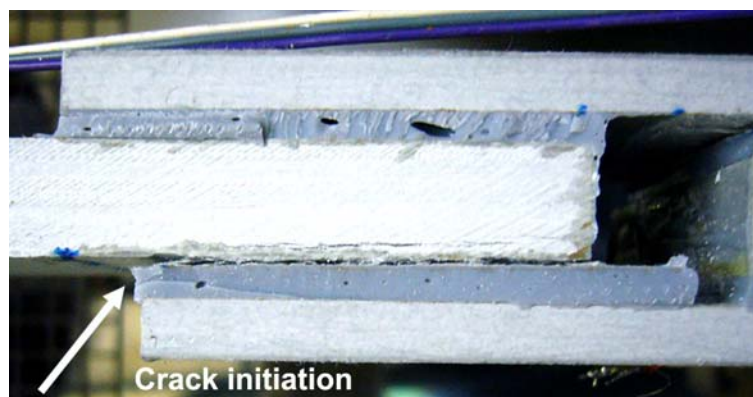


Figure 4. Fiber-tear failure mode of specimen DLJ5503.

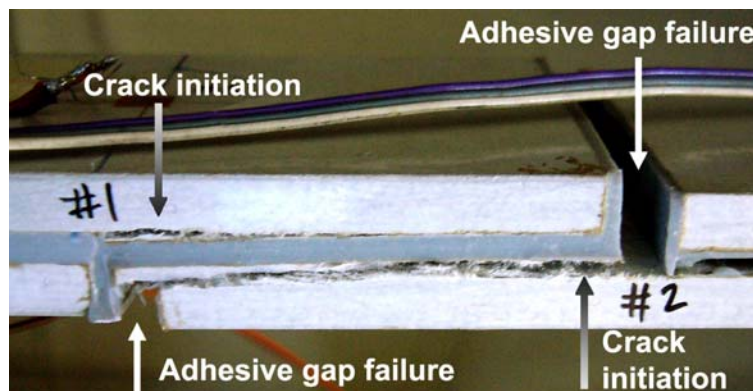


Figure 5. Fiber-tear failure after adhesive gap failure of specimen SLJ8003.

3.2 Crack initiation and propagation

The strains measured by the two back-face strain gages are plotted in Fig. 6 against the normalized life for representative DLJ and SLJ specimens. In contrast to the quasi-static results, the back-face strain gages proved to be sensitive to crack initiation only in the case of SLJs. Strains suddenly decreased due to stress redistribution after adhesive failure in the small gaps of the SLJ specimens. The much higher eccentricity of the axial load in the new

unbalanced single-lap joint configuration caused bending moments that changed the sign of the back-face strains from tension to compression. No significant changes in strains were exhibited during fatigue life in DLJs however. This difference in relation to the static loading was attributed to the limits of the measuring set-up. Continuous measurements at a frequency of 800 Hz could be performed during the static loading, while only periodical measurements could be recorded during fatigue loading due to the large amount of data to be collected.

The present study concentrates on the crack propagation phase because life to crack initiation showed a high degree of variation, reaching from 0.7% to 96.7% of total life, see Table 1. This variation can be explained by the fact that the examined structural joints contained no pre-crack and no special care was taken to precisely shape the adhesive edge (no fillet was formed, see above) during fabrication. Therefore, the crack could initiate at different locations in the joint, caused by existing defects, possible small asymmetries due to fabrication and/or loading misalignment. In contrast to aerospace applications, it is often not possible in civil engineering to precisely shape and control details such as adhesive fillet geometry for economic reasons. To remain on the safe side, it is therefore assumed that crack initiation already occurs at the beginning of life and that only crack propagation should be taken into account for design purposes.

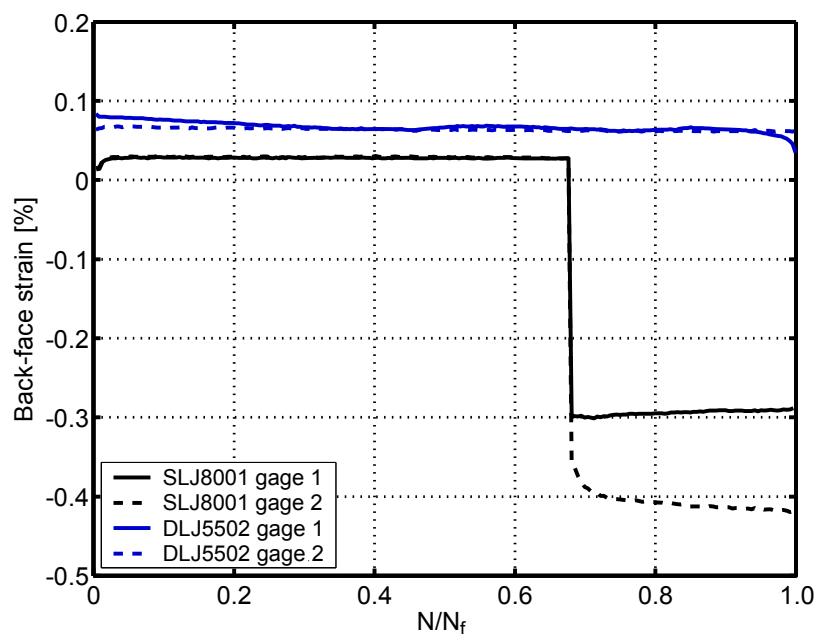


Figure 6. Back-face strain vs. normalized number of cycles for specimens DLJ5502 and SLJ8001.

Fig. 7 shows the total crack length (sum of the four crack gages) measured on DLJ specimens at different load levels, while Fig. 8 shows the corresponding values for SLJs during fatigue life. The total crack length in the DLJs increased almost linearly and reached a value of 60-75 mm at the end of the fatigue life. A different trend was observed for the SLJ configuration where the crack propagation rate was initially high (between 0% and 30% of cycles for crack propagation), diminished considerably between 30% and 90% of the cycles for crack propagation, and greatly increased again just before failure. The final total crack length for SLJs was between 70 and 90 mm, approximately 15% longer than that measured for DLJs.

4 MANIPULATION OF FRACTURE MECHANICS DATA

4.1 Overview

Two categories of fracture mechanics data can be distinguished: The first contains data that can be directly measured and recorded, such as crack length under specific load for a certain number of loading cycles. The second category contains data to be calculated using the recorded data, such as crack propagation rate, system compliance and its fluctuations during fatigue life and strain energy release rate as a function of crack length and/or crack propagation rate.

If the crack length can be measured during loading, the life of the examined structure can be modeled directly by integration of the crack propagation rate between two different crack lengths:

$$N - N_i = \int_{N_i}^N dN = \int_{a_i}^a \frac{1}{(da/dN)} da \quad (1)$$

where N_i denotes number of cycles for crack initiation, and a_i denotes initial crack length. $N - N_i$ corresponds to the number of cycles for crack propagation between crack lengths a_i and a . The application of Eq. (1) is straightforward, since only a method for the calculation of the crack propagation rate, da/dN , has to be selected.

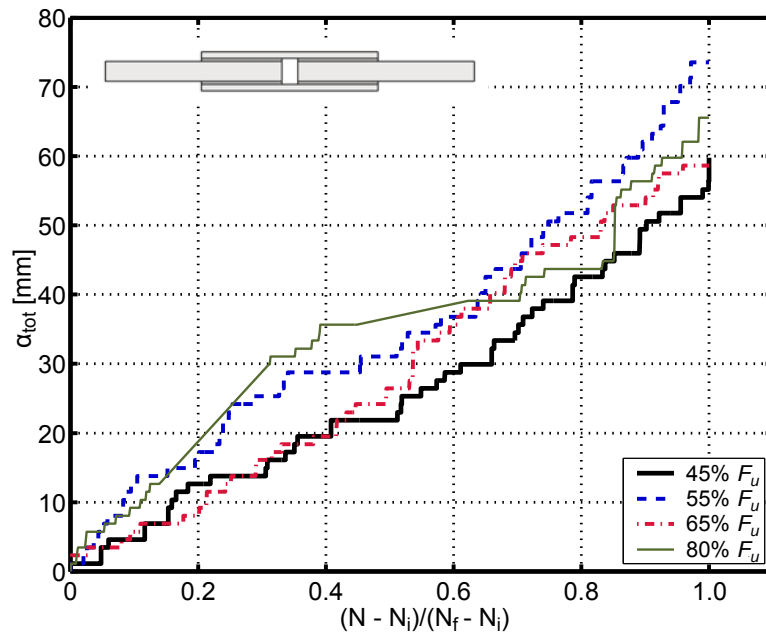


Figure 7. Total crack length vs. normalized number of cycles for crack propagation for DLJs.

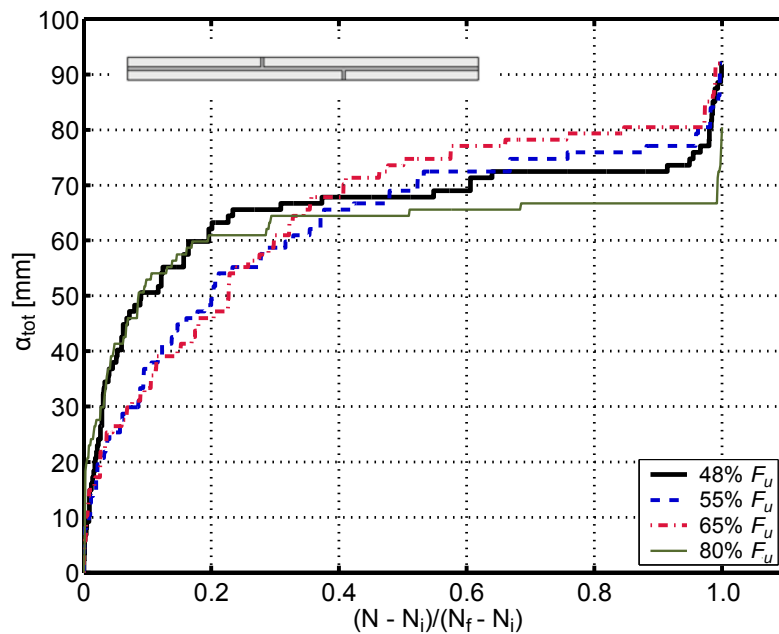


Figure 8. Total crack length vs. normalized number of cycles for crack propagation for SLJs.

This application is directly linked to the specific experimental data and does not take into account the materials and/or geometry of the structural element. Based on fracture mechanics data, however, predictive methods can be developed that combine the experimental evidence obtained from one type of structural element and analytical or numerical solutions for other types of structural elements, made from the same materials, in order to predict the strength or

fatigue life of the latter [13]. One parameter that is often used for this purpose is the strain energy release rate, G . For an isotropic or anisotropic plate of constant thickness, B , and a crack with length, a , the strain energy release rate is a function of the applied load, F , and the rate of compliance change, dC/da :

$$G = \frac{F^2}{2B} \frac{dC}{da} \quad (2)$$

In the case of cyclic loading, the maximum value of the strain energy release rate during one fatigue cycle can be deduced accordingly:

$$G_{\max} = \frac{F_{\max}^2}{2B} \frac{dC}{da} \quad (3)$$

where F_{\max} is the maximum cyclic load during the fatigue cycle. If G_{\max} is plotted against the crack propagation rate da/dN using logarithmic axes to derive Fatigue Crack Growth (FCG) graphs, the major part of the relationship is linear and can be fitted by the following equation:

$$\frac{da}{dN} = D(G_{\max})^m \quad (4)$$

where D and m are empirical constants for the given loading ratio, frequency of testing and environment [13]. In previous studies [3, 6], D and m were considered as material constants that do not depend on joint configuration. This assumption allowed their estimation from standardized DCB tests [6, 13, 14] and the subsequent application of the same values to estimate life for more complex joint configurations. Despite the fact that this argument seems rational, it was not supported by experimental evidence. As shown in [6], the adoption of this assumption led to an overprediction of the fatigue life of carbon fibre composite joints bonded with an epoxy adhesive.

By substituting da/dN with its equivalent from Eq. (4), Eq. (1) becomes:

$$N - N_i = \int_{a_i}^a \frac{1}{D(G_{\max})^m} da \quad (5)$$

Depending on the values of G_{\max} and the corresponding limits of the integration, Eq. (5) allows the calculation of conservative or non-conservative design allowables in line with a damage tolerance design philosophy (e.g. estimation of the number of cycles required to attain a specific crack length under a specific applied load).

4.2 System compliance

Load, displacement and crack length were recorded. To calculate the strain energy release rate, the only undefined term in Eq. (3) is the differential of system compliance with respect to crack length dC/da . The system compliance is determined as the ratio of the axial joint displacement amplitude, $\delta_{max}-\delta_{min}$, to the applied load amplitude, $F_{max}-F_{min}$, in one cycle. Compliance increase (or stiffness degradation) results from crack propagation and the degradation of laminate stiffness. However, previous experimental work on similar adherends proved that degradation of laminate stiffness is insignificant at the low load levels applied here [15] and therefore, degradation is entirely attributed to crack propagation. Since compliance increase is caused by crack propagation, it is assumed that its relationship to crack length is independent of load level. A unique dC/da can therefore be calculated for each joint type by using all available test data. The corresponding compliance vs. crack length relationship is presented in Figs. 9 and 10 for DLJs and SLJs. The bending, introduced by the unbalanced geometry of the SLJs after the gap failure, led to the lower initial stiffness and the greater stiffness degradation during crack propagation compared to the DLJs. The resulting curves exhibit similar trends to those observed in Figs. 7 and 8 for the crack length vs. number of cycles relationship and for the stiffness degradation shown in [10]: linear for DLJs and sigmoid for SLJs.

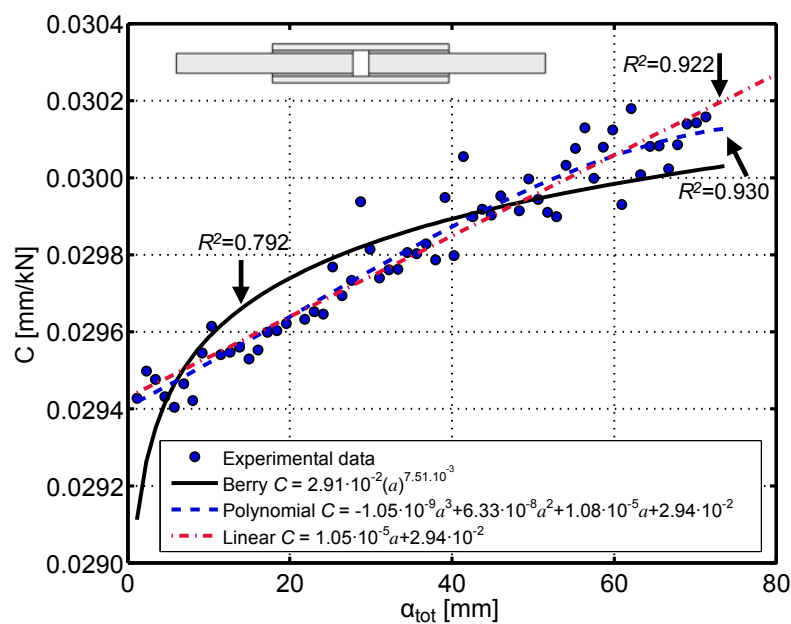


Figure 9. Compliance vs. total crack length for DLJs; comparison of fitting ability of three different methods.

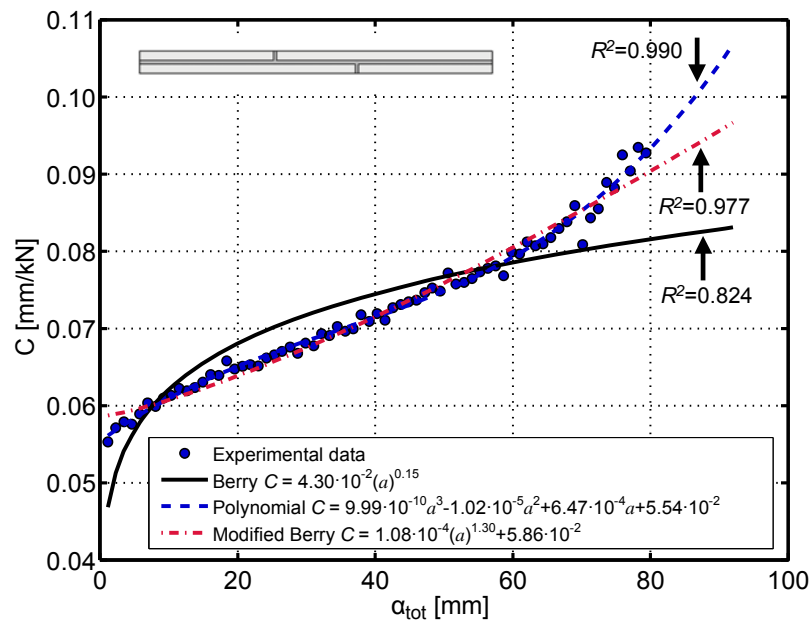


Figure 10. Compliance vs. total crack length for SLJs; comparison of fitting ability of three different methods.

To derive $dC/d\alpha$, the experimental data shown in Figs. 9 and 10 was fitted using four methods: the Berry method representing a power curve ($C=k \cdot (a)^n$), a polynomial fitting, and, based on the experimental results, a linear fitting ($C=k \cdot a + c_i$) for the DLJs and a modified Berry method, representing a power curve with a constant ($C=k \cdot (a)^n + c_i$), for the SLJs, see Figs. 9 and 10. In previous relationships, k , n and c_i are regression parameters that can be determined based on the fitting of C versus a .

Comparison of the different methods with experimental results revealed that the Berry method did not produce accurate results (R^2 -value of around 0.80 for both joint types). For DLJs, the fitting using polynomial and linear curves was more accurate with R^2 -values in the range between 0.92 and 0.93. The use of the polynomial or modified Berry method improved the fitting quality for the SLJs as well. The third-order polynomial method, however, led in this case to a subsequent calculation of negative values of G_{max} . The linear and the modified Berry methods were therefore selected as being the best fitting methods for the compliance of the DLJs and SLJs respectively.

4.3 Maximum strain energy release rate

The maximum strain energy release rate per cycle can be calculated by incorporating the

derivative dC/da into Eq. (3). Based on the selected fitting methods and the corresponding equations given in Figs. 9 and 10, G_{max} for DLJs results from:

$$G_{max} = \frac{F_{max}^2}{2B} \frac{dC}{da} = \frac{F_{max}^2}{2B} \cdot 1.05 \cdot 10^{-5} \quad (6)$$

and for SLJs:

$$G_{max} = \frac{F_{max}^2}{2B} \frac{dC}{da} = \frac{F_{max}^2}{2B} \cdot 1.40 \cdot 10^{-4} \cdot a^{0.30} \quad (7)$$

The slope of the linear DLJ compliance vs. crack curve is independent of the crack length, i.e., dC/da is represented by a constant value in $[1/N]$. For the SLJs, however, the fitting with the modified Berry method results in a dC/da that depends on the crack length. For both Eqs. (6-7), the unit of F_{max} is in $[N]$, B and a in $[m]$, dC/da in $[1/N]$, and G_{max} in $[J/m^2]$. The maximum strain energy release rate vs. the crack length for both DLJ and SLJ specimens is shown in Figs. 11 and 12. For DLJs, following Eq. (6), G_{max} is almost constant during fatigue while a power curve, as defined by Eq. (7), was derived for the SLJs. Due to the significantly higher stiffness degradation [10] and corresponding higher slope of the compliance curve (see Figs. 9-10), SLJs exhibit higher G_{max} values than DLJs, although SLJs were almost four times less loaded than DLJs.

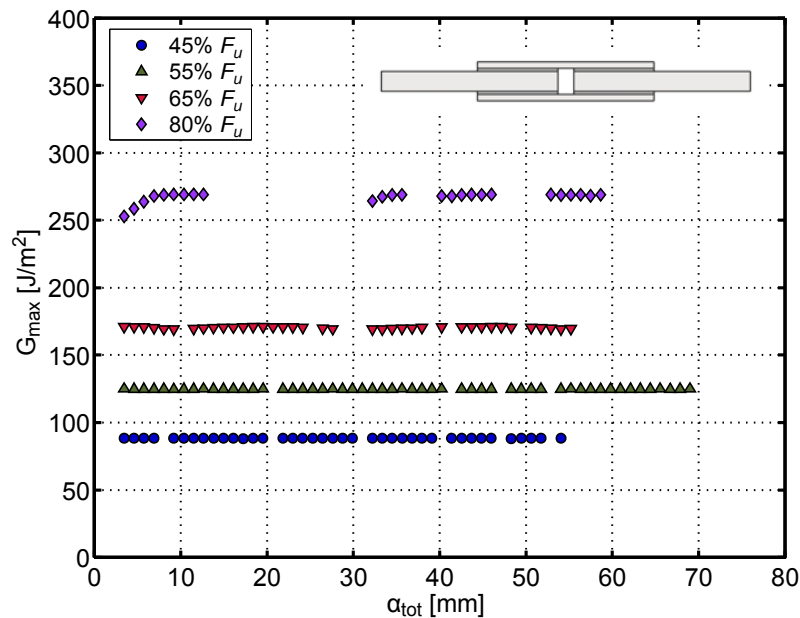


Figure 11. Maximum strain energy release rate vs. total crack length for DLJs.

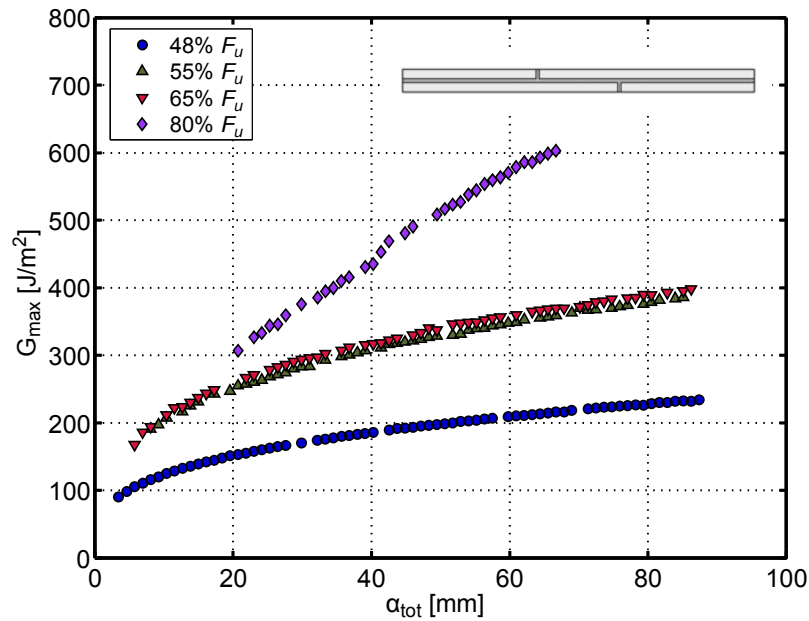


Figure 12. Maximum strain energy release rate vs. total crack length for SLJs.

4.4 Crack propagation rate

The secant method and the incremental polynomial fitting (according to ASTM E647-99) were used to calculate the crack propagation rate. According to the secant or point-to-point technique, the crack propagation rate can be determined by calculating the slope of a straight line connecting two contiguous data points on the a vs. N curve. The incremental polynomial method fits a second-order polynomial to sets of a specified number of successive data points, usually 3, 5, 7 or 9. The slope of the determined equation at any point corresponds to the crack propagation rate. The secant method is simple and accurately represents experimental data, but is sensitive to scatter in the latter [14]. The incremental polynomial method can reduce the scatter but involves the risk of masking real effects, especially when only small data sets are available [14]. The curve is expected to become smoother when more points are used for the calculations, but there is a risk of inadequate modeling, usually at the start or end of the lifetime.

Both methods were applied, as presented in Figs. 13 and 14 for representative DLJ and SLJ specimens. The incremental polynomial method (5 and 7 points were used) better represented the experimental data. It reduced scatter by providing smoother da/dN vs. N curves throughout the fatigue life. The 5-point version ($m=2$) was finally employed to not exclude information concerning the crack propagation rate in the initial and final stages of life.

The crack propagation rate was almost constant for DLJs, while it was high at the beginning and end of the fatigue life for SLJs in accordance with Figs. 7 and 10 and the stiffness degradation pattern of both joint configurations [10]. For the following analysis of fatigue life, an initial crack length (subsequent to crack nucleation) was assumed as being 4.6 mm for DLJs, corresponding to the failure of four wires of the crack propagation gages, one for each potential crack initiation location. For SLJs, the initial sharp drop of stiffness due to failure of the transverse adhesively-bonded gap led to an unrealistically high crack propagation rate (see Fig. 14) and therefore only crack lengths greater than 23 mm were considered in the calculations (see Fig. 8). Crack lengths greater than 80 mm were not considered in the calculations either since, as shown in Fig. 8, they correspond to an unstable crack propagation phase.

5 FATIGUE LIFE MODELING AND DISCUSSION

The FCG curves were derived by fitting Eq. (4) to the experimental data and determining the empirical constants D and m for both joint types. For the calculations, the mean values of da/dN and G_{max} over the selected crack length ranges (see Section 4.4) were considered for each load level to derive the FCG curves presented in Fig. 15. Higher cyclic loads led to higher crack propagation rates and higher G_{max} values for both joint types. Furthermore, the crack propagation rate was higher by almost one order of magnitude for the SLJs (in the range between 10^0 and 10^{-4} mm/cycle) compared to the corresponding values for the DLJs (in the range between 10^{-1} and 10^{-5} mm/cycle).

The D and m constants and the corresponding R^2 -values of the fitting are listed in Table 2 for both joint types. Similar slopes (m -values) of the FCG curves were obtained for both joint types. The slope for SLJs was only 10% steeper than that for the DLJs. The D value was higher for DLJs than for SLJs. However, this fitting parameter has no physical meaning since the FCG curve is limited to the left hand side by the fatigue threshold. The results shown in Table 2 prove that the values of these constants are not independent of joint type. This can be attributed partly to the different fracture mode ratio, which changes with increasing crack length and is strongly dependent on joint type, as presented in [6]. In addition, although the crack propagated in the mat layers of both laminates, their architecture was not identical (two vs. one mat layer in 12- and 6-mm laminates respectively) and this probably further contributed to the differences obtained.

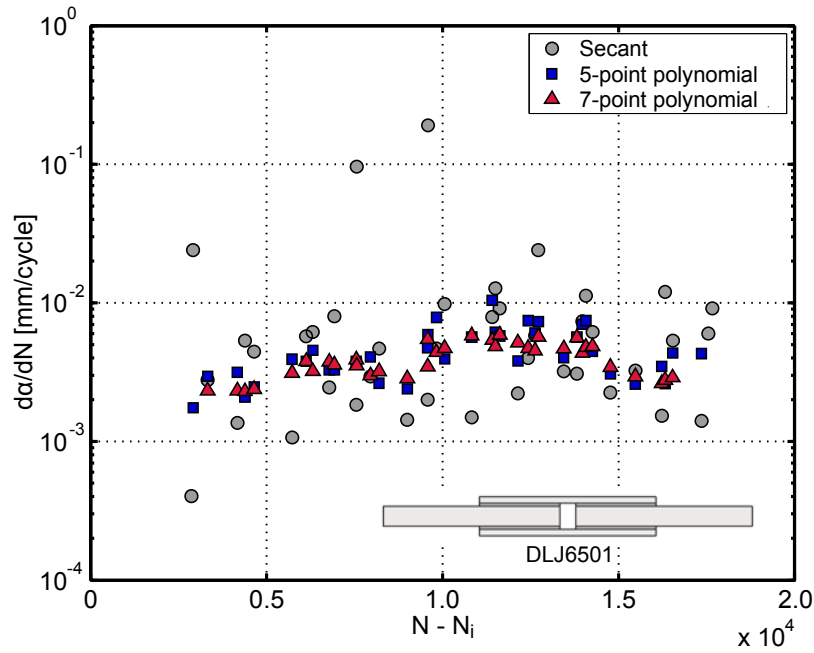


Figure 13. Comparison between secant and incremental polynomial fittings for calculation of fatigue crack propagation rate for DLJs.

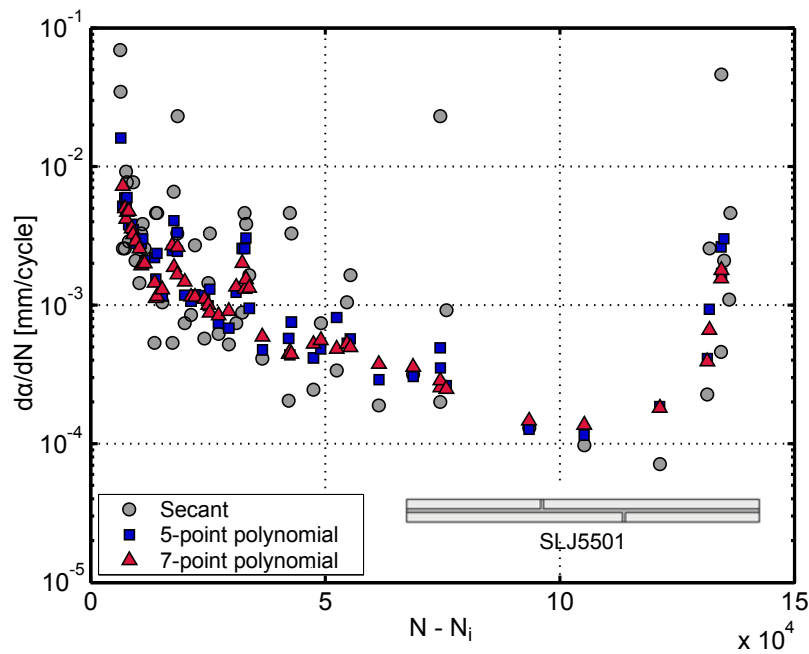


Figure 14. Comparison between secant and incremental polynomial fittings for calculation of fatigue crack propagation rate for SLJs.

When D and m are known for each joint type, the fatigue life for crack propagation can be calculated based on Eq. (5). $F-N$ curves that correspond to failure or a predetermined crack length can then be easily calculated, thus establishing a method for the determination

of damage tolerant design allowables. Corresponding curves are presented in Figs. 16 and 17 for DLJs and SLJs. Curves corresponding to joint failure agree well with the experimental data (data from specimens with crack gages are designated CG). In addition, design allowables corresponding to predetermined crack lengths were derived and compared to design allowables derived from stiffness degradation measurements in [10] where a stiffness degradation of 2% and 15% was considered for the DLJs and SLJs respectively. As shown in Figs. 9 and 10, each crack length can be attributed to a specific compliance increase and consequently to a specific stiffness degradation of the joint. The crack length corresponding to a 2% DLJ stiffness degradation was estimated as being 20 mm while a value of 27 mm was obtained for a 15% SLJ stiffness degradation. For each joint configuration, the crack length was calculated as the mean value of the experimentally measured a of the specimens at the four different load levels. The resulting $F-N$ curves derived from the fracture model, corresponding to 2% (DLJ) and 15% (SLJ) stiffness reduction, are shown in Figs. 16 and 17 (solid lines) together with the corresponding curves obtained from the stiffness degradation model [10] (dashed lines). The stiffness models show systematically steeper $F-N$ curves that tend to give more conservative results, especially towards the high cycle fatigue region. However, results from both models for both joint types seem reasonable and accurate, proving their potential use for the derivation of reliable design allowables.

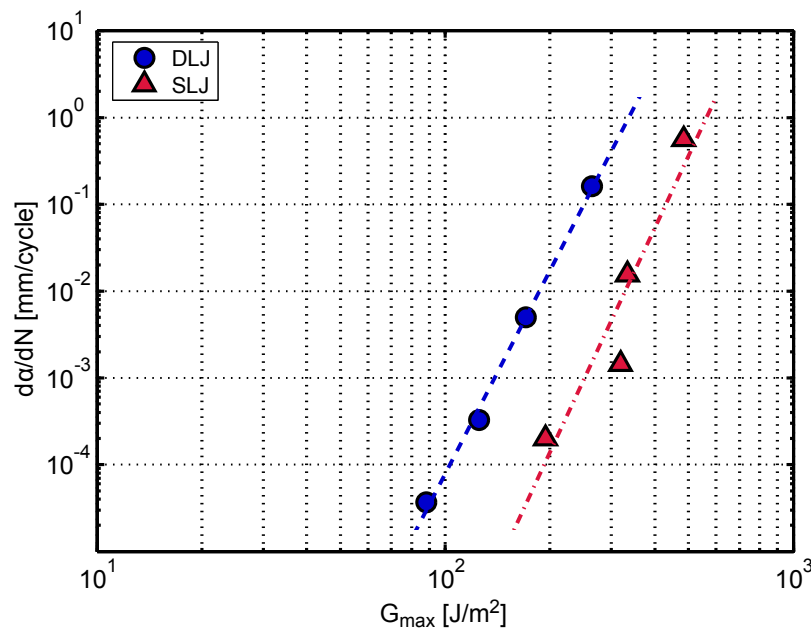


Figure 15. Crack propagation rate vs. maximum strain energy release rate for DLJs and SLJs.

Table 2. Estimated D and m parameters.

Joint type	D	m	R^2
DLJ	$2.18 \cdot 10^{-20}$	7.78	0.99
SLJ	$2.42 \cdot 10^{-24}$	8.59	0.90

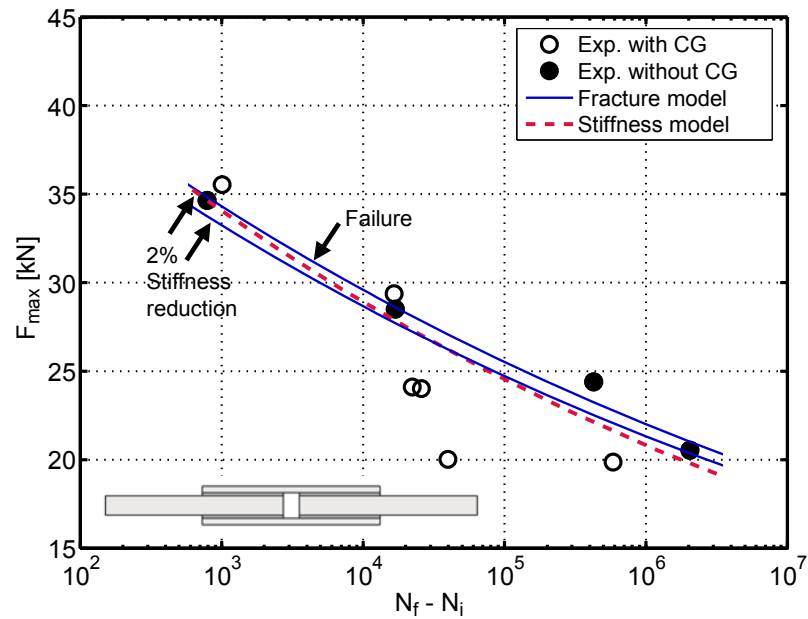


Fig. 16. $F-N$ curves obtained from fracture and stiffness models [10] for DLJs (CG= crack gage).

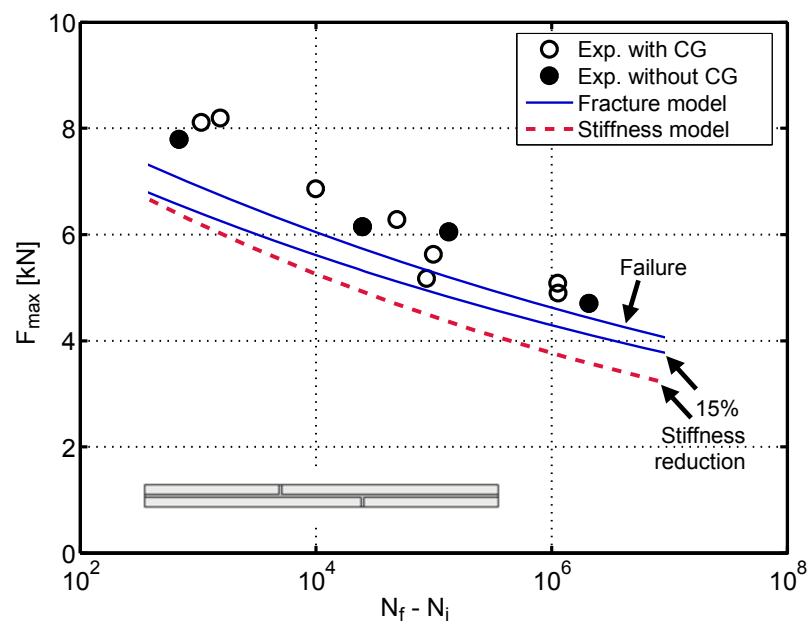


Fig. 17. $F-N$ curves obtained from fracture and stiffness models [10] for SLJs (CG= crack gage).

6 CONCLUSIONS

The fatigue behavior of adhesively-bonded double-lap and stepped-lap joints composed of pultruded GFRP laminates has been studied. The following conclusions were drawn regarding the fatigue life modeling based on fracture mechanics data:

1. For both joint configurations, fiber-tear failure was the dominant failure mechanism. It was possible to visually identify crack initiation and observe propagation during fatigue life, in contrast to the quasi-static behavior, where the same failure mode occurred in a brittle and sudden manner.
2. A linearly increasing trend of compliance was observed during the fatigue life of the DLJs in agreement with the linear development of the crack length and the stiffness degradation during fatigue life. A sigmoid trend was observed for the SLJs that also conforms to the crack growth pattern and stiffness measurements during the fatigue life of SLJs. SLJs exhibited a significantly higher compliance increase due to the unbalanced single-lap configuration after crack initiation.
3. The crack propagation rate for the DLJ specimens remained almost constant throughout the fatigue life. For SLJs, however, it was initially high but then decreased until very close to failure when the rate increased again. Crack propagation rate was lower for the DLJs than for the SLJs by one order of magnitude. The incremental polynomial fitting, using sets of five adjacent points, proved to be the best method for deriving the relationship of the crack propagation rate vs. number of cycles.
4. Fatigue crack growth curves were obtained for both joint types. The empirical constants D and m depended on joint configuration. Similar slopes m for both joint types were obtained. However, a significantly higher value of D was estimated for the DLJs than for SLJs. This discrepancy was probably caused by the different fracture mode ratio exhibited by each joint configuration and possible differences in the composition of the mat layers where the cracks propagated.
5. Based on the measured fracture mechanics data, the fatigue life of the examined joints was modeled and reliable design allowables were derived. The derived fatigue life curves compared well to similar curves based on stiffness degradation measurements with the latter being conservative especially in high cycle fatigue.

ACKNOWLEDGEMENTS

The authors would like to thank the Swiss National Science Foundation (Grant No 200020-111702/1), Sika AG, Zurich (adhesive supplier) and Fiberline Composites A/S, Denmark (pultruded laminate supplier) for their support of this research.

REFERENCES

- [1] Ascroft IA, Hughes DJ, Shaw SJ. Adhesive bonding of fibre reinforced polymer materials. *Assembly Autom* 2000;20(2):150-161.
- [2] Ashcroft AI, Hughes DJ, Shaw SJ. Mode I fracture of epoxy bonded composite joints: 1. Quasi-static loading. *Int J Adhes Adhes* 2001;21(2):87-99.
- [3] Hadavinia H, Kinloch AJ, Little MSG, Taylor AC. The prediction of crack growth in bonded joints under cyclic-fatigue loading. I. Experimental studies. *Int J Adhes Adhes* 2003;23(6):449-61.
- [4] Blackman BRK, Hadavinia H, Kinloch AJ, Paraschi M, Williams JG. The calculation of adhesive fracture energies in mode I: revisiting the tapered double cantilever beam (TDCB) test. *Eng Fract Mech* 2003;70(2):233-48.
- [5] Mall S, Ramamurthy G, Rezaizadeh MA. Stress ratio effect on cyclic debonding in adhesively bonded composite joints. *Compos Struct* 1987;8(1):31-45.
- [6] Abdel-Wahab MM, Ashcroft IA, Crocombe AD, Smith PA. Finite element prediction of fatigue crack propagation lifetime in composite bonded joints. *Compos Part A-Appl S* 2004;35(2):213-222.
- [7] Cheuk PT, Tong L, Wang CH, Baker A, Chalkley P. Fatigue crack growth in adhesively bonded composite-metal double-lap joints. *Compos Struct* 2002;57(1-4):109-115.
- [8] Quaresimin M, Ricotta M. Fatigue behaviour and damage evolution of single lap bonded joints in composite material. *Compos Sci Technol* 2006;66(2):176-187.
- [9] Renton WJ, Vinson JR. Fatigue behavior of bonded joints in composite material structures. *J Aircraft* 1975;12(5):442-447.
- [10] Zhang Y, Vassilopoulos AP, Keller, T. Stiffness degradation and life prediction of adhesively-bonded joints for fiber-reinforced polymer composites, *Int J Fatigue*, 2008;30(10-11):1813-1820.

-
- [11] De Castro J, Keller T. Ductile double-lap joints from brittle GFRP laminates and ductile adhesives. Part I: Experimental investigation. *Compos Part B-Eng*, 2008; 29(2):271-281.
- [12] Zhang Y, Keller T. Progressive Failure Process of Adhesively Bonded Joints Composed of Pultruded GFRP. *Compos Sci Technol*, 2008; 68(2):461-470.
- [13] Curley AJ, Jethwa JK, Kinloch AJ, and Taylor AC. The fatigue and durability behaviour of automotive adhesives. Part III: predicting the service life. *J. Adhesion*, 1998;66(11):39-59.
- [14] Ashcroft IA, Shaw SJ. Mode I fracture of epoxy bonded composite joints: 2. Fatigue loading. *Int J Adhes Adhes*, 2002;22(2):151-167.
- [15] Keller T, Tirelli T, Zhou A. Tensile fatigue performance of pultruded glass fiber reinforced polymer profiles, *Comp Struct* 2005;68(2):235-245.

2.7 Environmental effects under fatigue loading

Summary

In practice, the structural joints used in civil engineering structures may experience the combined effects of cyclic loading together with various environmental conditions. Under fatigue loading, structural joints are subjected to various combined temperatures and humidity levels throughout their service life, and therefore environmental effects merit more attention than effects occurring under quasi-static loading (discussed in Section 2.4). Furthermore, the damage caused by high humidity levels is mainly dependent on the exposure time. The humidity effects might be negligible on the short-term performance but cannot be disregarded for the long-term performance of structural joints under fatigue loading.

Based on the knowledge concerning the mechanical and fracture behavior of structural joints obtained from Section 2.5 and 2.6, this paper extends the experimental investigation of fatigue behavior from that exhibited under ambient conditions to that exhibited under various environmental conditions, covering Task 3.5 and 4.5. Three sets of experiments were performed at -35°C, 23°C and 40°C while the fourth set of data was collected at 40°C and 90% relative humidity for preconditioned specimens. The $F-N$ curves were established based on four sets of data and a wear-out model was employed to link fatigue lifetime to quasi-static joint strength under different environmental conditions. During fatigue, stiffness degradation, crack initiation and propagation were monitored using the techniques/methods validated in Section 2.4 and 2.5. In the presence of high humidity, the failure shifted to the adhesive/composite interface. The effect of high temperature was exaggerated by the presence of humidity in terms of the fatigue life, cycles for crack initiation, crack propagation rate and failure crack length.

Reference details

This paper, "Environmental effects on fatigue behavior of adhesively-bonded pultruded structural joints" by Ye Zhang, Anastasios P. Vassilopoulos and Thomas Keller, was published in Composites Science and Technology 2009, volume 69, pages 1022-1028.

[doi:10.1016/j.compscitech.2009.01.024](https://doi.org/10.1016/j.compscitech.2009.01.024)

ENVIRONMENTAL EFFECTS ON FATIGUE BEHAVIOR OF ADHESIVELY-BONDED PULTRUDED STRUCTURAL JOINTS

Ye Zhang, Anastasios P. Vassilopoulos and Thomas Keller

Composite Construction Laboratory (CCLab),
Ecole Polytechnique Fédérale de Lausanne, (EPFL),
Station 16, Bâtiment BP, CH-1015 Lausanne, Switzerland

ABSTRACT

The fatigue response of adhesively-bonded pultruded GFRP double-lap joints has been investigated under different environmental conditions. Tests were performed at -35°C , 23°C and 40°C . A fourth set of fatigue data was collected from tests on preconditioned specimens in warm (40°C) water. The tests were performed at 40°C and at 90% relative humidity. Specimens were instrumented with strain and crack gages to record fatigue data. In addition to the S-N curves, stiffness fluctuations and crack initiation and propagation during fatigue were monitored. The dominant failure mode was a fiber-tear failure that occurred in the mat layers of the GFRP laminates. In the presence of high humidity, the failure shifted to the adhesive/composite interface. Although the testing temperature was lower than the glass transition temperature of the adhesive, its influence on the fatigue life and fracture behavior of the examined joints was apparent and was aggravated by the presence of humidity.

KEYWORDS

Adhesive joints; Structural composites; Fatigue; Environmental degradation; Thermomechanical properties

1 INTRODUCTION

The majority of engineering structures comprise parts subjected to cyclic loading patterns. In fact, most structural failures occur due to mechanisms driven by fatigue loading, whereas purely static failure is rarely observed [1]. In civil engineering infrastructures, joints are the most likely locations of failure initiation and, since their function is to transfer loads from one part of the structure to another, their structural integrity is of high importance for the viability of the entire system.

The fatigue of adhesively-bonded joints was initially investigated for aerospace applications since they offer many advantages compared to riveting and bolting, such as considerable mass saving, cheaper fabrication, improved aerodynamics and the avoidance of holes that act as areas of stress concentration [2] and potential moisture ingress along cut fibers. There are however fundamental structural differences between aerospace and civil engineering applications concerning the manufacturing process, material architecture, dimensions of components and operational conditions. Although bonded joints are already used even as primary structural connections in aerospace applications, their potential has yet to be achieved in civil engineering. The main reason for this is lack of confidence in the ability of bonded joints to act as structural connections. This skepticism is even more pronounced when the structure has to operate under fatigue loads and is subjected to aggressive environments such as high temperature and humidity. In these cases, the lack of knowledge concerning adhesive joints leads to a lack of confidence in their ability to retain their structural integrity.

During loading of a structural joint, a crack or cracks initiate naturally and propagate along the least resistant path inside the component. Therefore, the development of damage in a joint is very much dependent on the constituent materials. The presence of aggressive environments, low or high temperatures and high humidity levels also affect the fatigue behavior of structural joints. Temperature and humidity can influence the mechanical properties of the adhesive and the matrix material of the composite adherends. As a result, the interface between the fibers and the matrix may be weakened in the presence of humidity [3]. These synergistic effects of different loading factors cause complex fracture surfaces and make the analysis of the failure of composite joints a very challenging task.

The effect of the environment on the behavior of adhesively-bonded joints has formed the subject of several investigations in the past, e.g. [2, 3-7], although most existing studies

concern joints used specifically in the aerospace and/or automotive engineering domains. Simulated aircraft structural joints comprising CFRP adherends and an epoxy adhesive were fatigued under five different combinations of temperature and humidity and the results were reported in [2]. These showed that the fatigue behavior of the joints was considerably affected by environmental conditions. In addition, different failure modes were observed under different conditions. Cohesive failure of the adhesive occurred under hot, humid conditions. The failure mode changed to substrate failure for ambient temperature, while very rapid propagation was observed when testing at -50°C . The authors attributed this behavior to the increased rigidity of the adhesive as it cooled. The static and fatigue behavior of different joint types used in the aerospace industry were investigated in [3] (composite joints with film or paste adhesives, composite-to-metal joints). The same group investigated the temperature-dependent fatigue behavior of CFRP/epoxy double-lap joints over a wide temperature range of -50 to 90°C [4]. Unidirectional (UD) and multidirectional (MD) adherends were used. The MD joints were shown to be stronger at low temperatures, at which, according to the authors, joint strength was determined by the peak stresses. UD joints on the other hand were stronger at high temperatures where the strength was controlled by the creep of the joints, determined by the minimum developed stresses. The fatigue damage and failure mechanism of single-lap joints composed of E-glass/polyethylene adherends and an ethyl-cyanoacrylate adhesive were investigated in [5]. The specimens were preconditioned for up to 90 days in water at different temperatures prior to testing. A significant reduction in fatigue strength was observed with increased immersion time and when the water temperature exceeded the glass transition temperature of the adhesive this reduction was accelerated.

The influence of the environment on the fatigue fracture behavior of adhesively-bonded joints was the subject of [6, 7]. The Mode I fracture behavior of double cantilever beams, comprising carbon/epoxy adherends and the same epoxy as the adhesive, was investigated in [6]. Shorter fatigue life was observed at higher temperatures. The fatigue crack growth behavior of structural adhesive joints was examined over a range of temperatures in air and salt water [7]. The specimens consisted of swirled glass fiber/isocyanurate matrix composite adherends bonded with a urethane adhesive. A pre-cracked lap shear configuration under 4-point bending was used to provide mixed-mode levels typical of bonded joints. The lowest crack growth rate and highest fatigue threshold value occurred at room temperature. Lower

and higher temperatures both lowered thresholds and increased crack growth rates. The salt water led to a decrease in threshold values and increase in crack growth rate with increasing temperature. Overall, salt water at 90°C was the most severe environment in terms of threshold values and crack growth rate. Temperature and humidity also affected the fracture performance of adhesively-bonded double-lap joints during quasi-static loading at high temperatures (50-60°C) [8]. The adhesive became more viscous and its yielding strength rather than fracture resistance controlled the failure. When the temperature increased, especially beyond 50°C, the failure mode changed from fiber-tear to adhesive failure, with the crack propagating along the interface between the adherend and the adhesive layer.

The literature review showed that most of the studies made to date focused on adhesively-bonded joint for aerospace and automotive engineering. The most commonly used materials for these studies are graphite/epoxy adherends, and epoxy (thin film or paste) adhesives. To the authors' knowledge no study has been made on effects of temperature and humidity on the fatigue behavior of structural joints for civil engineering applications however. In the present work, the fatigue behavior of double-lap joints, comprising pultruded GFRP laminates, bonded by a paste epoxy adhesive system, is investigated. Axial cyclic tests were performed under four environmental conditions and the effects of low and high temperatures and high humidity were evaluated.

2 EXPERIMENTAL PROGRAM

Balanced adhesively-bonded double-lap joints (DLJs), composed of pultruded GFRP laminates bonded by an epoxy adhesive system, were tested under axial tensile fatigue loads in four different environments. The objective was to demonstrate the influence of temperature and humidity on the fatigue behavior of the examined structural components. For all the cases investigated, S-N curves were derived, while nominal section stresses were used (load divided by the laminate cross section, 50x12 mm² in this case, see below). Furthermore, stiffness fluctuations and crack lengths were recorded during fatigue.

The pultruded GFRP laminates (supplied by Fiberline A/S, Denmark) consisted of E-glass fibers embedded in an isophthalic polyester resin. Two different laminate geometries with thicknesses of 12 and 6 mm were used, both being 50 mm wide. The 12-mm-thick laminate comprised two mat layers on each side (in addition to the unidirectional rovings in the center), while the 6-mm-thick laminate comprised only one mat layer on each side. A mat

layer consisted of a chopped strand mat (CSM) and a woven mat $0^\circ/90^\circ$ stitched together. A polyester surface veil (40 g/m^2) was added on the outside to protect against environmental attacks. The fiber content, determined by burn-off tests in accordance with ASTM D3171-99, was 48.5 vol.-% for the thicker and 43.6 vol.-% for the thinner laminates. Due to the higher fiber content, the tensile strength and Young's modulus of the thicker laminate ($355 \pm 15 \text{ MPa}$ and $34.4 \pm 2.3 \text{ GPa}$) were higher than the corresponding properties of the 6-mm laminate ($283 \pm 7 \text{ MPa}$ and $31.4 \pm 1.6 \text{ GPa}$). A two-component epoxy adhesive was used (SikaDur 330, Sika AG Switzerland) as bonding material. Axial tensile tests were performed according to EN ISO 527-1 to characterize the epoxy adhesive. The epoxy showed an almost elastic behavior and a brittle failure. The measured tensile strength was $38.1 \pm 2.1 \text{ MPa}$, and the Young's modulus was $4.56 \pm 0.1 \text{ GPa}$. [9]. The glass transition temperature, T_g , of the adhesive when cured at room temperature for approximately 10 days was estimated as being in the range between 45°C and 55°C by means of dynamic mechanical analysis (DMA) [8].

The geometry of the examined joint configuration is shown schematically in Fig. 1. All specimens were manufactured in ambient laboratory conditions. Before manufacturing, all surfaces subjected to bonding were mechanically abraded with sandblasting paper using a grinder and then chemically degreased using acetone. Spacers of 2-mm thickness were used to ensure a constant thickness of the adhesive and a special aluminum frame was designed for the easy alignment of the GFRP laminates during the manufacture of each specimen. After manufacture, all specimens were cured in ambient laboratory conditions ($23^\circ\text{C} \pm 5^\circ\text{C}$, $50\% \pm 10\%$ RH) for ten days.

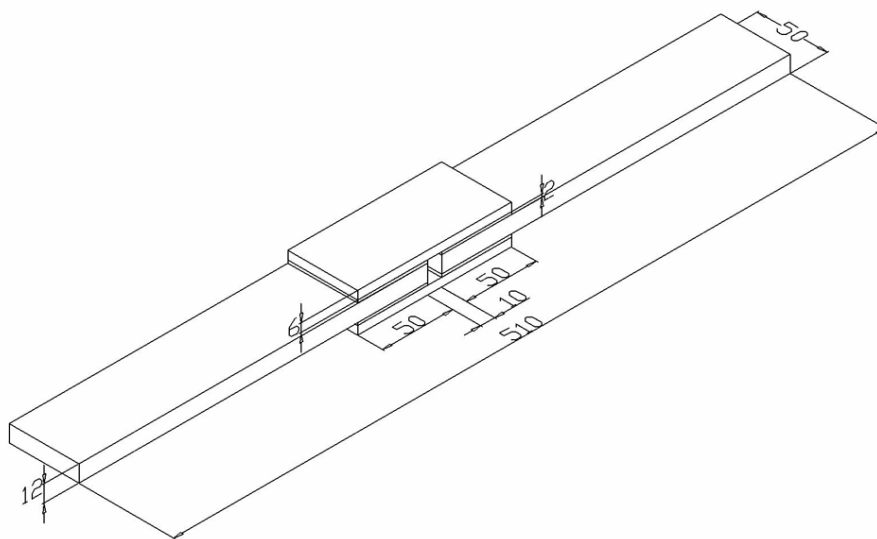


Figure 1. Geometric configuration of test specimen.

Each specimen was instrumented with a number of strain gages and one specimen per stress level was instrumented with four crack gages to capture the crack initiation and record crack propagation. A photo of a specimen with instrumentation prior to testing is shown in Fig. 2. The crack propagation gages (HBM/RSD20) consisted of 20 wires spaced at 1.15- mm intervals perpendicular to the adhesive layer, and covered almost half of the overlap length, the part where crack propagation was expected to occur. As the crack propagated, the wires were broken progressively and the electrical resistance of the gage increased. Theoretically, a crack could initiate close to each of the two adhesive layers of each joint end and, therefore, eight cracks could develop. However, experiments evidenced that only one crack initiated at one joint end. The high stresses developed around the crack tip imposed propagation of this crack and impeded any other crack nucleation at this joint end. Each crack gage was therefore crossed by only one crack and the sum of the four individually measured crack lengths was taken into account to describe crack propagation. The measured crack lengths on each side were assumed to be constant over half of the joint width and, therefore, half of the specimen width was allocated to each crack measurement. Each specimen was also instrumented with four strain gages. Two were placed on the laminate, away from the joint area, to measure the axial strains outside the joint where the stresses were expected to remain uniformly distributed across its width and depth. Two more were placed above the locations considered sensitive to crack initiation. These gages, designated back-face strain gages (see Fig. 2), were used to identify crack initiation. It was anticipated that a sudden change in strains would be recorded due to stress redistribution immediately after crack initiation. This technique has been successfully adopted by other researchers in the past, e.g. [10], as well as for the capture of crack initiation during quasi-static loading of the same joint type as used in this study [8].

All tests were carried out on an INSTRON 8800 universal testing rig of 100 kN capacity under load control. An environmental chamber was used to control temperature and humidity during testing. Deviations of approximately $\pm 1^\circ\text{C}$ were recorded for the temperature, while $\pm 2\%$ differences in relative humidity were observed. Frequency was kept constant at 10 Hz for all coupons, while the stress ratio ($R = \sigma_{min}/\sigma_{max}$) was equal to 0.1, resulting to a tension-tension fatigue loading. The frequency of 10 Hz was chosen as a compromise between testing time and hysteretic heating effects. Preliminary test results proved that the fatigue performance of the examined specimens is not affected by the frequency when it lies within the range between 2 and 10 Hz. The temperature of the specimens was measured

during fatigue testing and no significant increase (more than 2°C) was recorded throughout fatigue life. All tests were continued until ultimate failure (separation) of the joint. An HBM/Spider8 was used to record the measured experimental fatigue data with a frequency of 200 Hz.

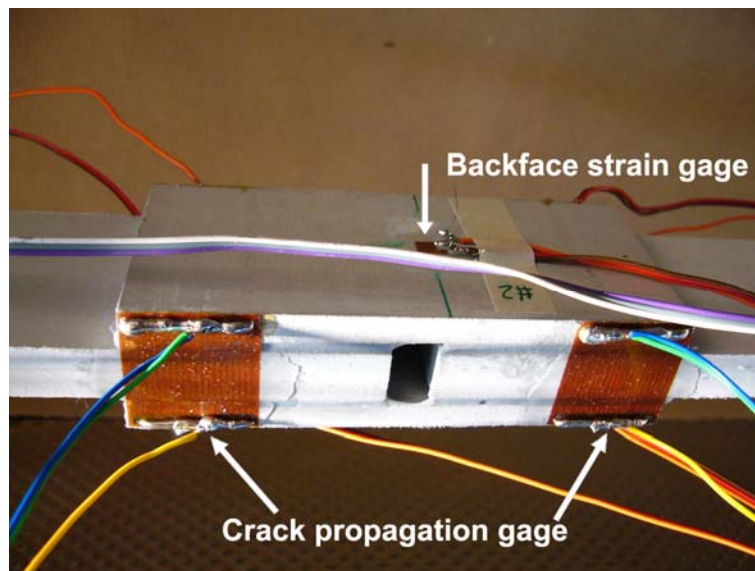


Figure 2. Experimental instrumentation for double-lap joint.

The tests were performed under four different controlled environmental conditions: a temperature of $-35^{\circ}\text{C}\pm 1^{\circ}\text{C}$ (humidity cannot be controlled for negative temperatures), a temperature of $23^{\circ}\text{C}\pm 1^{\circ}\text{C}$ and relative humidity of $50\%\pm 2\%$, a temperature of $40^{\circ}\text{C}\pm 1^{\circ}\text{C}$ and relative humidity of $50\%\pm 2\%$ and finally, a temperature of $40^{\circ}\text{C}\pm 1^{\circ}\text{C}$ and relative humidity of $90\%\pm 2\%$. The temperature and humidity ranges were selected in accordance with the properties of the adhesive (ASTM D1151-90, Standard test method for effect of moisture and temperature on adhesive bonds) and the operational conditions of the joints as parts of engineering structures (Swisscode 261, Actions on structures). The low temperature of -35°C was selected to simulate the performance of the structure during wintertime, 23°C to represent the ambient temperature during normal weather conditions, with the limit of 40°C representing summer days and being below the glass transition temperature of the adhesive. The addition of the 90% humidity to the high temperature represents the worst loading case for the structure.

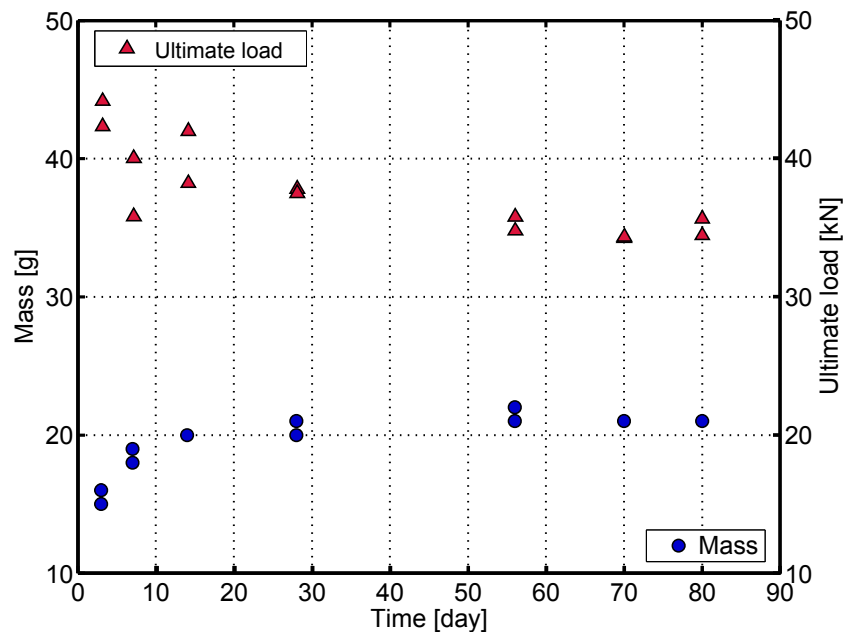


Figure 3. Moisture absorption and ultimate tensile loads after preconditioning.

Prior to testing, the specimens were placed inside the chamber for an appropriate time period (approximately 90 min for temperatures above zero and 150 min for the negative temperature) in order to attain the predetermined temperature and humidity levels. Special preconditioning was required for the specimens that were tested at high temperature and high relative humidity. Preliminary quasi-static tests showed that moisture absorption was initially rapid and reached saturation after 70 days. The ultimate load of the joints decreased with increased moisture concentration and also reached a plateau after 70 days (see Fig. 3). Based on these tests, the fatigue specimens were preconditioned for 70 days in a warm water bath at a temperature of 40°C.

After preliminary testing, four different stress levels were determined as a percentage of the static joint strength, f_u , (ultimate joint load divided by the laminate cross section) for each condition to collect experimental data in the range between 10^2 and 10^7 cycles. This range can be considered representative of a real structure, which may be subjected to 10 million cycles during its lifetime.

3 EXPERIMENTAL RESULTS AND DISCUSSION

A set of experimental data was gathered after testing the joint specimens under each environmental condition. In the following paragraphs, the fatigue data is presented and the

environmental effects on fatigue behavior are analyzed.

3.1 Failure modes and fatigue data

Fig. 4 shows typical detailed views of failed specimens under different environmental conditions. As can be seen, all joints exhibited a typical fiber-tear failure: a crack propagated in the region of the interface, with the majority of the cracks located inside the inner GFRP laminate. As reported in [11], fiber-tear failure in pultruded GFRP profiles at ambient temperature occurs because the adherend interlaminar strength is lower than the adhesive/adherend interfacial strength. This conclusion corresponds with the joint design recommendation according to which joint proportions must be such that the bond never constitutes the weak link in the joint. The strength of the adhesive bond across the bonded area must be greater than the interlaminar strength of the adherends [12].

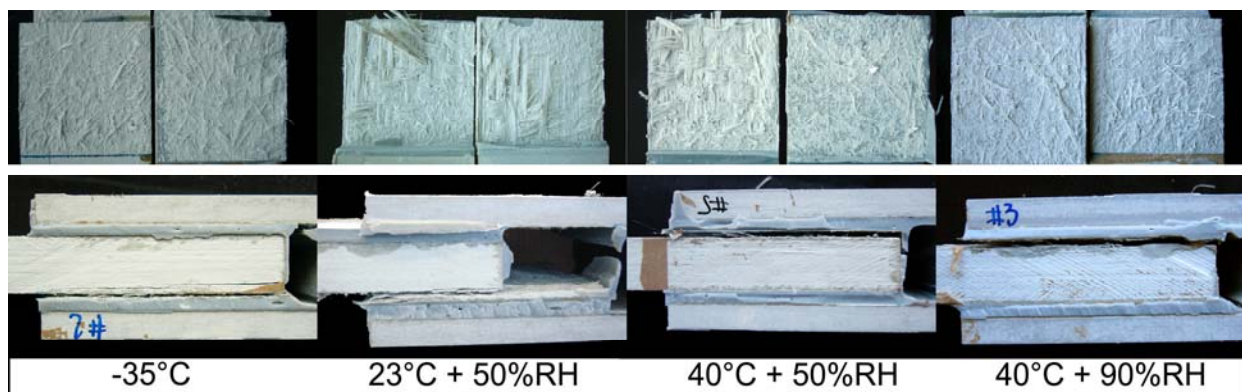


Figure 4. Failure modes under different environmental conditions.

The crack opening was visible during fatigue loading under all environmental conditions. The dominant failure mechanism and the failure process were similar to those exhibited under quasi-static loading, as presented in [8], although for quasi-static loading it was not possible to observe the damage development, since failure occurred very suddenly without prior warning or even the prior appearance of any visible cracks. Temperature (in the range between -35°C and 40°C) had no noticeable influence on the failure process of the joints; cracks propagated through the mat layers of the 12-mm laminate in all the studied cases. The presence of 90% RH, however, shifted the crack from the adherend to the interface (adhesive crack).

Table 1. Fatigue data for double-lap joints (actual measured stress level values are reported).

Specimen No.	-35°C		23°C + 50%RH		40°C + 50%RH		40°C + 90%RH	
	Stress level [% of f_u]	Fatigue life [No. of cycles to failure]	Stress level [% of f_u]	Fatigue life [No. of cycles to failure]	Stress level [% of f_u]	Fatigue life [No. of cycles to failure]	Stress level [% of f_u]	Fatigue life [No. of cycles to failure]
1*	53.7	191251	45.0	2215704	43.7	1909376	43.7	1313940
2	53.4	1266390	43.9	1030600	47.0	1667768	43.6	553739
3	53.7	651059	43.6	1927124	44.3	484288	43.6	1055244
4*	63.6	259708	53.5	432844	53.4	149005	53.4	145871
5	63.3	85879	52.7	48180	53.8	124173	53.7	96773
6	63.7	55178	52.9	27647	54.1	131288	53.8	73037
7*	73.3	6355	62.5	19788	63.2	17361	63.2	5751
8	73.3	23765	63.5	24306	63.4	6731	62.7	10446
9	73.3	35569	64.4	53664	63.5	25723	63.9	7905
10*	83.0	6513	76.0	823	73.3	8861	73.5	1780
11	82.3	7171	75.9	207	73.6	9797	72.2	1124
12	82.9	2060	78.0	4731	73.2	5813	72.1	1105

*: specimen equipped with crack propagation gages.

Table 2. Estimated statistical parameters for examined fatigue data and static strength.

Parameter	-35°C	23°C + 50%RH	40°C + 50%RH	40°C + 90%RH
α_f	22.82	15.57	17.40	24.02
β	72.72	76.67	76.12	64.15
G	0.080	0.081	0.088	0.074
C	0.0022	0.0106	0.0158	0.1520
f_u [MPa]	72.2±3.5	77.2±6.2	70.0±8.8	59.7±4.3

The aforementioned environmental influence is reflected in the collected fatigue data listed in Table 1. All fatigue data sets were subjected to statistical analysis according to the wear-out model proposed in [13]. The wear-out model assumes that the stronger specimen in fatigue should also be the stronger one under quasi-static loads and that therefore a relationship exists between the equivalent static strengths and cyclic stresses and number of cycles to failure. This relationship can be expressed mathematically by the following deterministic equation:

$$\sigma_e = \sigma_{\max} \left[\left(\sigma_r / \sigma_{\max} \right)^{\frac{1}{G}} + (n-1)C \right]^G \quad (1)$$

where σ_e is the equivalent static strength, σ_{\max} denotes the maximum cyclic stress level, σ_r is the static residual strength, n is the number of loading cycles and S and C are the fatigue model parameters to be determined.

The initial values of G and C should be selected based on available fatigue data with G being the slope of the S-N curve and C a constant defining the shape of the S-N curve for a low-cycle fatigue region. By using the selected G and C values, all data is converted into equivalent static strengths, σ_e , using Eq. (1). A Weibull distribution is then fitted to the equivalent static strength data by using maximum likelihood estimators (MLE):

$$P(\sigma_e) = \exp \left[- \left(\frac{\sigma_e}{\beta} \right)^{\alpha_f} \right] \quad (2)$$

This process is performed iteratively for different values of S and C , until the maximum value of the shape parameter, α_f , is obtained [13].

Using the selected/estimated set of parameters G , C , β , α_f , the fatigue curve can be plotted for any desired reliability level $P(N)$ (including 50%, which represents the mean value of the experimental data) by using the following equation:

$$\sigma_{\max} = \beta \left[-\ln P(N)^{\frac{1}{\alpha_f}} \right] \left[(N-A)C \right]^{-G}, \quad (3)$$

with $A = -(1-C)/C$.

The estimated parameters for all fatigue data sets (and ultimate strength f_u [8]) are listed in Table 2. The entire set of fatigue data is presented in Fig. 5. S-N curves based on Eq (3) were derived and plotted (as lines) with experimental fatigue data (symbols) for better visualization and comparison between the four different loading cases. As presented in Fig. 5,

the fatigue life of the examined joints was longer at low temperatures, even if the static strength of the joints at low temperature was lower than the corresponding value under ambient conditions [8]. Analysis showed that, irrespective of loading condition, all curves have similar slopes with an average of 0.081 and a very low standard deviation of 0.005. The increased temperature (from ambient to 40°C) seems to influence the fatigue life by a factor of approximately 5% for low cycle fatigue (up to 1000 cycles), while this difference increases to 10% for longer lifetime. The presence of humidity is even more critical as the derived S-N curve is situated lower than all the others in the S-N plane, although it presents the least steep slope (G parameter in Table 2). Compared to the life of the specimens tested at 40°C and 50% RH, a significant decrease of roughly one decade of life can be observed when 90% RH is present.

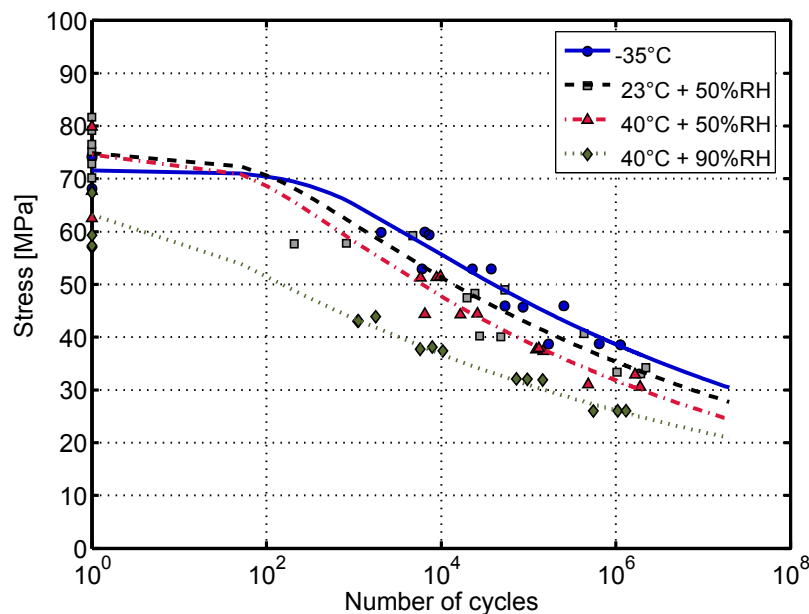


Figure 5. Derived S-N curves for examined fatigue data sets.

3.2 Stiffness degradation

Stiffness fluctuations during fatigue life were also recorded since stiffness can be used as a non-destructive damage metric for evaluating the structural integrity of constructions. The development of phenomenological models, capable of describing gradual stiffness degradation in terms of macroscopically measured properties, permits the establishment of fatigue design allowables, which can easily be incorporated into design codes [6].

During fatigue life, the peak and valley forces and corresponding displacements, Δl ,

were recorded for each cycle. The secant structural modulus was calculated as:

$$E(N) = \frac{F_{\max}(N) - F_{\min}(N)}{\Delta l_{\max}(N) - \Delta l_{\min}(N)} \quad (4)$$

where the subscripts max and min indicate the maximum and minimum values of F and Δl of the N^{th} cycle. Normalized values for number of cycles and stiffness were used for comparison with the available stiffness data. The initial fatigue modulus $E(1)$ was calculated using Eq. (4) for the first cycle of each test. All stiffness measurements were then normalized with respect to $E(1)$. The number of cycles was divided by the number of cycles to failure.

Table 3. Residual stiffness at fatigue failure of DLJs under different environmental conditions.

-35°C		23°C + RH50%		40°C + RH50%		40°C + RH90%	
Av. stress level [% of f_u]	Failure $E(N)/E(1)$ [%]	Av. stress level [% of f_u]	Failure $E(N)/E(1)$ [%]	Av. stress level [% of f_u]	Failure $E(N)/E(1)$ [%]	Av. stress level [% of f_u]	Failure $E(N)/E(1)$ [%]
53.6	95.5	44.2	94.3	44.0	92.5	43.6	92.8
63.5	96.0	53.0	95.0	53.8	93.8	53.7	94.0
73.3	96.1	63.5	95.9	63.4	95.0	63.3	92.7
82.7	96.8	76.6	95.9	73.4	94.7	72.6	94.3
Average	96.1±0.5	-	95.3±0.8	-	94.0±1.1	-	93.4±0.8

Basically, stiffness degradation results from crack propagation and degradation of laminate stiffness. However, previous experiments on similar adherends showed that degradation of laminate stiffness is almost insignificant at the low stress levels applied herein [14] and that, therefore, degradation primarily can be attributed to crack propagation in this case. Stiffness degradation was low, with less than 6-7% being observed for all the investigated cases. As shown in Fig. 6, for the 40°C with 50% RH case, the longer part of the curves exhibits a linear trend, although there are short regions at the beginning and end of life where stiffness changes rapidly. This phenomenon can be attributed to the failure process itself. The damage developed gradually (which can be explained by the stable crack propagation) until close to failure where rapid changes in stiffness indicated unstable crack

development. The same trend was exhibited by the specimens tested under other environmental conditions. Nevertheless, increased temperatures were found to cause more fatigue damage, which is reflected, albeit slightly, in more stiffness degradation while the addition of humidity aggravated damage development. As presented in Table 3, averaged stiffness values at failure are lower for higher testing temperatures and increased humidity levels.

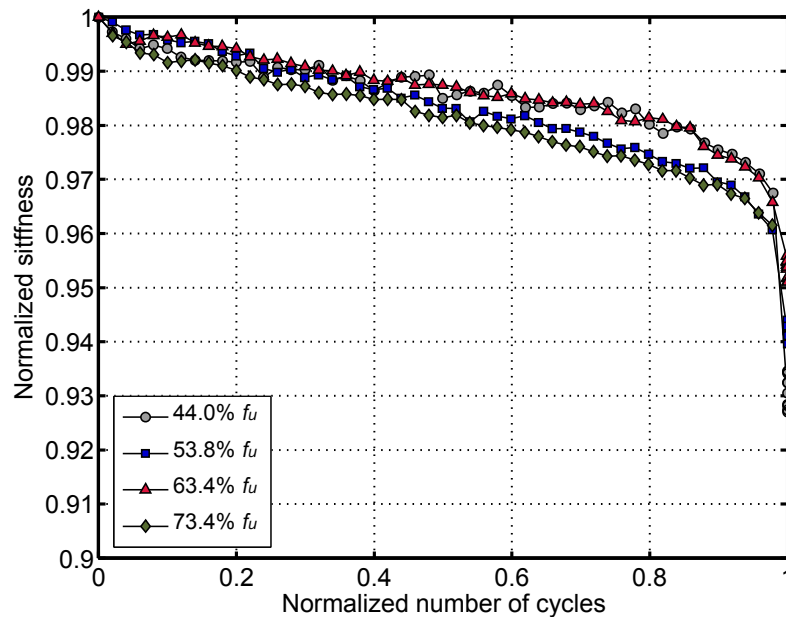


Figure 6. Normalized average stiffness degradation vs normalized fatigue life (specimens at 40°C + 50%RH).

3.3 Crack initiation and propagation

The failure of the examined joint configurations was lead by the initiation and propagation of one or more cracks. Thus, in order to draw safe conclusions regarding the behavior of these structural elements it was considered necessary to also record crack development during lifetime. In the case of quasi-static loads, it was shown that crack initiation in the laminate could be identified by means of either crack propagation gages or back-face strain gages [8]. The same instrumentation was therefore used for the fatigue loading. However, specimens exhibited no remarkable changes in strains during fatigue life. Some indications were present, but were insufficiently pronounced to constitute reliable proof. This difference in relation to the static experiments was attributed to the limits of the measuring set-up. Continuous measurements at a frequency of up to 800 Hz could be performed for the static experiments,

whereas only periodical measurements could be recorded during the fatigue experiment due to the large amount of data to be collected. Therefore, only the measurements obtained from the crack gages were considered for the identification of crack initiation and recording of crack length. Cycles for crack initiation, as a percentage of cycles to failure, are given in Table 4 for all environmental conditions. In general, crack initiation is shown to be delayed with increased temperature, as the average value of the initiation increased from 2.1% for -35°C to 14.9% when tested at 40°C with 90% RH. However, the scatter was too high to enable reliable conclusions to be drawn. Nevertheless, this observation coincides with the corresponding results for quasi-static loading reported in [8]. The apparent delay in crack initiation is attributed to the softening of the adhesive under higher temperatures, resulting in a less stiff system with less pronounced stress peaks.

Fig. 7 shows the crack length of a representative specimen measured by the four crack gages. Crack gages 1 and 3 were always applied to one joint end (one on each side), while gages 2 and 4 were applied to the opposite joint end. Cracks did not initiate simultaneously at all four potential locations. A crack always initiated at one joint end first (at gage 1 in Fig. 7) before a second crack initiated on the opposite end (at gage 4). The first crack was always dominant and its length was much greater than that of the crack on the other side.

Table 4. Cycles for crack initiation as percentage of lifetime.

	-35°C		23°C+50%RH		40°C+50%RH		40°C+90%RH	
Stress level [% of f_u]	Cycles for crack initiation [% of cycles to failure]	Stress level [% of f_u]	Cycles for crack initiation [% of cycles to failure]	Stress level [% of f_u]	Cycles for crack initiation [% of cycles to failure]	Stress level [% of f_u]	Cycles for crack initiation [% of cycles to failure]	
53.7	0.7	45.0	7.3	43.7	8.4	43.7	12.9	
63.6	2.4	53.5	1.6	53.4	11.7	53.4	0.5	
73.3	2.9	62.5	14.6	63.2	17.3	63.2	32.0	
83.0	2.6	76.0	4.3	73.3	1.1	73.5	14.6	
Average	2.1±1.0	-	6.9±5.6	-	9.6±6.8	-	14.9±13.0	

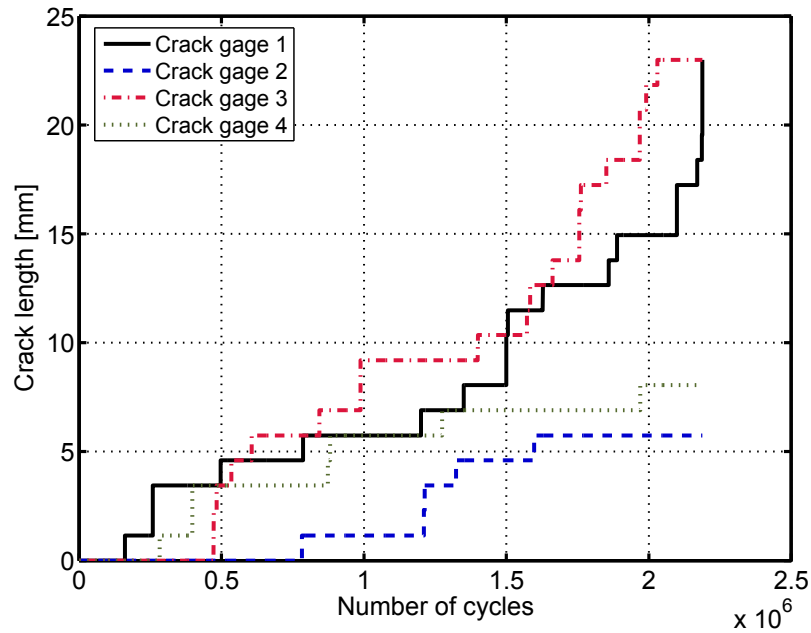


Figure 7. Typical crack length measurements from four crack gages (specimen 1 at 23°C + 50%RH).

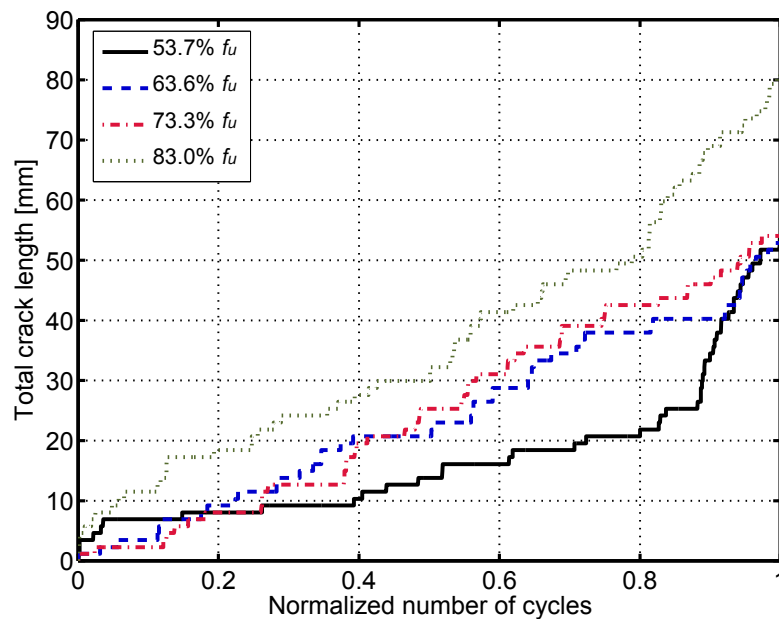


Figure 8. Crack propagation against normalized life for propagation (specimens at -35°C).

The total crack length (calculated as the sum of all the recorded cracks), as a function of the normalized life for crack propagation, propagated in the same manner during the fatigue life, regardless of stress level and environmental condition. A typical graph (for the -35°C case) is shown in Fig. 8. The shape of the curves corresponds to the observed linear stiffness

degradation trend; almost linear up to a certain point, after which rapid crack propagation occurs. Increasing temperature seems to provoke longer crack lengths at failure since the adhesive becomes more viscous and undergoes longer elongations during loading (average total crack length of 64.4 mm at 23°C+50%RH vs. 92.0 mm at 40°C+50%RH). The presence of humidity inverts this effect however and a short crack length is observed for the specimen tested after preconditioning at high temperature and humidity level (55.5 mm at 40°C+90% RH). In the presence of humidity, the interface becomes weaker and the crack propagates along this least resistant path.

4 CONCLUSIONS

The fatigue behavior of adhesively-bonded pultruded GFRP double-lap joints subjected to a constant amplitude fatigue loading under different environmental conditions has been examined. The influence of temperature and humidity on the damage accumulation and fatigue life of the examined specimens was evaluated. The following conclusions can be drawn:

1. Environment has a considerable effect on the fatigue behavior of the examined joints. Increased temperature seems to shorten specimen fatigue life. This phenomenon is more pronounced in the presence of high humidity levels. The derived F-N curves had almost the same slope, which indicates that joint fatigue behavior is very much dependent on its static strength.
2. When tested at -35°C, 23°C and 40°C, cracks leading to the failure of the joints propagated through the outer layer of the pultruded adherends. However, in the presence of high humidity the failure shifted from an adhesive to an interfacial failure, which implied that the adhesive/composite bond was weaker than the fiber/matrix bond in the composite itself.
3. Almost linear stiffness degradation was observed up to failure irrespective of the applied stress level. Very close to failure, a rapid decrease in stiffness was observed for all the investigated cases. An increase in temperature was found to provoke higher stiffness degradation, aggravated by the addition of humidity. However, only a small stiffness degradation of 6%-7% was measured for all the specimens prior to ultimate failure.

4. Crack propagation gages were used to identify crack initiation and record crack propagation during fatigue life. Crack propagation was almost linear for all the examined cases, irrespective of environmental conditions. Nevertheless, longer cracks were measured for higher temperatures, due to the softening of the adhesive and greater elongations exhibited under loading. The presence of high humidity reversed this effect. In this case, the adhesive/composite interface weakened and the joint failed after the occurrence of even short cracks.

REFERENCES

- [1] Halfpenny A. A practical introduction to fatigue. nCode International Ltd., Sheffield UK, <http://www.e-i-s.org.uk>.
- [2] Gilmore RB, Shaw SJ. The effect of Temperature and humidity on the fatigue behavior of composite bonded joints. *Composite Bonding*, ASTM STP 1227, 1974.
- [3] Ashcroft IA, Hughes DJ, Shaw SJ. Adhesive bonding of fibre reinforced polymer composite materials. *Assembly Autom* 2000; 20(2):150-161.
- [4] Ashcroft IA, Hughes DJ, Shaw SJ, Wahab MA, Crocombe A. Effect of temperature on the quasi-static strength and fatigue resistance of bonded composite double lap joints. *J Adhes* 2001;75:61-68.
- [5] Ferreira JAM, Reis PN, Costa JDM, Richardson MOW. Fatigue behaviour of composite adhesive lap joints. *Compos Sci Technol* 2002;62(10-11):1373-1379.
- [6] Gregory JR, Spearing SM. Constituent and composite quasi-static and fatigue fracture experiments. *Compos Part A-Appl S* 2005;36(5):665-674.
- [7] Liechti KM, Arzoumanidis GA, Park SJ. Fatigue fracture of fully saturated bonded joints. *J Adhes* 2002;78(5):383-411.
- [8] Zhang Y, Vassilopoulos AP, Keller T. Temperature-dependent behavior of adhesively-bonded FRP joints under quasi-static tensile loading. 2008, submitted for publication.
- [9] De Castro, J, Keller, T. Ductile double-lap joints from brittle GFRP laminates and ductile adhesives. Part I: Experimental investigation. *Compos Part B-Eng* 2008; 29(2), 271-281.

-
- [10] Crocombe AD, Ong CY, Chan CM, Abdel Wahab MM, Ashcroft IA. Investigating fatigue damage evolution in adhesively bonded structures using backface strain measurement. *J Adhes* 2002; 78(9): 745-776.
- [11] Keller T, Vallée T. Adhesively bonded lap joints from pultruded GFRP profiles, Part I: Stress-strain analysis and failure modes. *Compos Part B-Eng* 2005; 36(4): 331-340.
- [12] Hart-Smith LJ. The key to designing durable adhesively bonded joints. *Compos* 1994; 25(9): 895-898.
- [13] Sendeckyj GP. Fitting models to composite materials. Test methods and design allowables for fibrous composites, ASTM STP 734, C. C. Chamis Ed., American Society for Testing and Materials, 1981, 245-260.
- [14] Keller T, Tirelli T, Zhou A. Tensile fatigue performance of pultruded glass fiber reinforced polymer profiles, *Comp Struct* 2005;68:235-245.

3 SUMMARY

3.1 Summary of results

In this PhD thesis, the mechanical and fracture behavior of adhesively-bonded joints composed of pultruded GFRP laminates and an epoxy adhesive was experimentally investigated and numerically modeled under both quasi-static and fatigue loadings. The environmental effects on both the short- and long-term performances of structural joints were evaluated and modeled based on experimental results.

Under quasi-static loading, the dominant failure mode of all four types of joints, i.e. DCBs, ELSs, DLJs and SLJs, was a fiber-tear failure, which occurred in the mat layers of the GFRP laminates. The final failure of DLJs and SLJs was very sudden and brittle. DLJs showed an almost linear behavior up to failure, while SLJs exhibited two stages of failure: adhesive failure in the small gaps and failure of the whole joint. The gap failure changed the SLJ configuration from stepped-lap to single-lap with a corresponding decrease in joint stiffness. As to fracture behavior, the applicability of the LEFM approach was validated for both fracture and structural joints (Section 2.1 and 2.2) by addressing two main problems: 1) the crack length measurement techniques and 2) methods for calculating the strain energy release rate. For fracture joints, the visual observation and video extensometer were successfully employed to record crack development in fracture joints. Different methods, including the Simple Beam Theory (SBT), Corrected Beam Theory (CBT), Experimental Compliance Method (ECM), Modified Compliance Calibration (MCC) and Virtual Crack Closure Technique (VCCT), were used to calculate the SERR. Good agreement was observed between different methods while SBT always provided an underestimation. For structural joints, crack propagation gages were used to identify crack initiation and propagation while the use of back-face strain gages was considered an efficient alternative for crack initiation detection. SERR values were calculated using ECM and VCCT. Good agreements were found for SLJs

whereas deviations were observed for DLJs due to small stiffness changes. For both fracture and structural joints, R-curves were formed and the critical strain energy release rates corresponding to crack initiation and propagation were determined. The fracture mode mixity of structural joints, (DLJs and SLJs), which changed with increasing crack length, was calculated using VCCT (Section 2.3). Based on the results obtained for both fracture and structural joints, a mixed mode fracture criterion was established for crack initiation and propagation, which exhibited a non-convex form.

The fatigue behavior of adhesively-bonded structural joints (DLJs and SLJs) was experimentally investigated and numerically modeled using both stiffness-based and fracture mechanics approaches (Section 2.5 and 2.6). During fatigue, DLJs exhibited an almost linear stiffness degradation and the residual stiffness was well represented by a linear model. For SLJs, a higher stiffness degradation rate was observed at the beginning, after failure of the small adhesive gaps, and at the end, close to fatigue failure, and a non-linear sigmoid model was therefore employed. The fatigue lives at failure and corresponding to allowable stiffness degradation were predicted. During fatigue cycles, crack propagation gages were used to measure the crack length and ECM to calculate the SERR based on LEFM. The crack propagation rate was calculated using the 5-point incremental polynomial method. For DLJs the crack propagation rate remained almost constant during fatigue, while for SLJs it was initially high but decreased until very close to failure when the rate increased again. FCG curves were formed for both joint types. The obtained fracture parameters were found to be very dependent on joint type - in other words fracture mode mixity - and thus they cannot be considered as material constants. The fatigue lives at failure and corresponding to allowable crack length were predicted.

The environmental effects on the mechanical and fracture behavior of structural joints were experimentally evaluated (Section 2.4 and 2.7). The change in environmental conditions was found to have an immediate influence on the failure modes of joints. With either the increasing temperature at glass transition or the presence of high humidity, the dominant failure modes changed from fiber-tear to adhesive failure. Under quasi-static loading, the change in the strength and stiffness of the joint followed the trend of the thermomechanical behavior of the adhesive, which remained unaffected in the operational range of -35°C to 40°C , below the glass transition temperature (T_g) of the adhesive and significantly decreased at temperatures above glass transition. The temperature-dependent joint stiffness can be

predicted based on the thermomechanical properties of the constituent materials using a simplified finite element model. As to fracture behavior under quasi-static loading, the increase in temperature led to a lower crack propagation rate, longer failure crack length and higher critical strain energy release rate. Under fatigue loading, increased temperatures seemed to shorten fatigue lifetime and cause higher stiffness degradation. This phenomenon was more pronounced in the presence of high humidity levels. An increase in temperature was also found to result in longer failure crack lengths while the presence of high humidity reversed this effect. A relationship between the equivalent static strength under different environmental conditions and cyclic loads and fatigue life was established using an empirical wear-out model.

3.2 Original contributions

Some attempts have been made to investigate the fracture behavior of adhesively-bonded structural joints, i.e. DLJs and SLJs, using the LEFM approach but only focusing on aerospace/automotive applications. However, the structural joints used in civil engineering structures, which are composed of pultruded GFRP laminates, present certain essential differences, e.g. the large component dimension on a full-scale level and asymmetric geometric configurations due to crack propagation. Based on experimental and numerical investigations, this thesis has validated the applicability of LEFM to adhesively-bonded pultruded GFRP joints and filled the knowledge gap regarding joint fracture behavior.

With the increasing use of pultruded GFRP composites in civil engineering applications, some results obtained for adhesively-bonded joints have recently been published, mainly concerning short-term performance however. Based on the investigations concerning fatigue behavior under the different environmental conditions to which a real structure may be subjected, this thesis provides original knowledge about the long-term performance of adhesively-bonded pultruded GFRP joints.

The detailed original contributions made by this PhD thesis concerning the applicability of the fracture mechanics approach, the fatigue behavior and environmental effects are presented in Section 3.2.1-3.2.3 respectively.

3.2.1 Applicability of fracture mechanics approach

The applicability of LEFM to adhesively-bonded fracture and structural joints composed of pultruded GFRP laminates has been validated in this PhD thesis by addressing two major problems: 1) the crack measurement technique and 2) the method for calculating the SERR.

For fracture joints, an alternative crack measurement technique, the video extensometer, was employed for the first time (Section 2.1). This technique can provide more accurate results, especially for Mode II fracture in which it is difficult to identify the crack tip, and it also eliminates observer error. The applicability of existing standards and protocols (ASTM D5528-01, 2007; ISO 15024:2000(E), 2000; ESIS(TC4), 2006) for interpretation of the fracture mechanics data obtained from experiments was validated.

For structural joints, the existing crack measurement technique commonly used for fracture joints proved unfeasible for structural joints. Neither visual observation nor compliance-based back-calculation (CBTE method presented in Section 2.2) can be applied due to the uncontrollable crack initiation, rapid crack propagation and the missing analytical solutions for the compliance. The crack propagation gages were selected and validated for structural joints under both quasi-static (Section 2.2) and fatigue loading (Section 2.6). The applicability of crack gages was also validated under different environmental conditions (Section 2.4 and 2.7). Similarly to the crack measurement techniques, three main categories of calculation methods (analytical, experimental and numerical) for the SERR were initially designated for standardized fracture joints (see Section 2.2) while their applicability to structural joints needs to be validated. In this research, the applicability of the experimental method (ECM) and the numerical method (VCCT) was examined for two types of structural joints (DLJs and SLJs) in Section 2.3. Comparing their results, excellent agreement was obtained for SLJs while deviations were observed for DLJs due to low stiffness degradation. The ECM proved very sensitive to the small stiffness loss that occurred for DLJs and the accuracy of VCCT was affected by the inability of the linear-elastic FE modeling to accurately model behavior before visual crack initiation. Both ECM and VCCT were validated for calculation of the SERR, although potential errors might exist under special conditions. In addition, it is worth mentioning that structural joints are normally multi-cracked, in other words more than one crack exists. The employment of the total crack length, a_{tot} , as proposed in this thesis proved to be a practical solution to establish the relationship between crack

development and the changing compliance for structural joints with a multi-cracking condition.

Beyond the knowledge of the total strain energy release rate (G_{tot}), this thesis extends to the separation of Mode I and II components for structural joints. The determination of the fracture mode mixity of DLJs and SLJs using VCCT accentuates the advantage of the numerical method (FEA) in dealing with complex structural joints. Furthermore, the possibility of establishing a mixed mode fracture criterion based on results of Mode I and II fracture and mixed mode structural joints was confirmed.

3.2.2 Characterization of fatigue behavior

In addition to the $F-N$ curves, the fatigue behavior of structural joints was successfully modeled by using the stiffness-based and fracture mechanics approaches. The residual stiffness of joints proved to be a sensitive damage matrix for the characterization of fatigue lifetime and since the stiffness degradation of DLJs and SLJs exhibited different behaviors a linear and a sigmoid non-linear model were correspondingly established. With regard to the fracture mechanics approach, the fatigue lifetime was modeled by Fatigue Crack Growth (FCG) curves, in which the crack propagation rate (da/dN) was represented as a function of the maximum SERR (G_{max}) during cyclic loading. The empirical fracture parameters of the FCG curves for DLJs and SLJs were found to be not identical, but dependent on joint type. The current evidence indicates that the FCG curve and its fracture parameters cannot be considered material constants but as being very dependent on fracture mode mixity. The idea presented in previous studies (Hadavinia et al., 2003; Abdel Waha et al., 2004) of using the fracture parameter obtained from pure Mode I and II fracture joints to predict the fatigue life of structural joints is disputed. It is worth mentioning that both stiffness-based and fracture mechanics approaches can provide the fatigue life prediction corresponding to specific allowables according to design codes, which is the critical stiffness degradation in the former approach (see Section 2.5) and critical crack length in the latter (see Section 2.6).

3.2.3 Characterization of environmental effects

The environmental effects on the mechanical and fracture behavior of structural joints (DLJs)

under quasi-static and fatigue loading were experimentally evaluated. Under quasi-static loading, the thermomechanical behavior of the adhesive, rather than that of the adherends, proved to be the prime factor influencing the mechanical and fracture behavior of joints. Temperatures below the T_g range (40°C-50°C) of the adhesive, even if they were very low (-35°C), influenced neither the mechanical nor fracture behavior of the joint, including the failure mode, joint strength and stiffness, linear load-elongation response, and load and elongation at crack initiation. In the glass transition temperature range (40°C-50°C), the adhesive became softer, leading to a decrease in joint stiffness. In contrast to stiffness, the maximum joint strength was observed at 40°C due to the combined effects of stress peaks with a statistical size effect described in (Vallée et al., 2006). When the T_g exceeded (40°C-60°C), both joint stiffness and strength significantly decreased following the trend of the thermomechanical properties of the adhesive. The high temperature also weakened the adhesive-adherend interface and changed the failure mode from fiber-tear to adhesive failure. Thanks to the fracture mechanics approach, the environmental effects on the fracture behavior of structural joints composed of pultruded GFRP laminates were evaluated for the first time. Under quasi-static loading, an increasing temperature resulted in the delay of crack initiation, longer failure crack length, the deceleration of crack propagation and higher critical strain energy release rates. The former two effects were also observed for structural joints composed of the same material and with the same geometric configurations under fatigue loading.

New knowledge regarding the effects of high humidity on adhesively-bonded structural joints composed of pultruded GFRP has been acquired through experimental investigation. The presence of high humidity led to the change of failure mode from fiber-tear to adherend-adhesive interface failure, shorter fatigue lifetime, more stiffness degradation and shorter failure crack length.

In this thesis, the modeling of environmental effects on pultruded GFRP structural joints is also carried out. Under quasi-static loading, a simplified finite element model was developed to predict the temperature-dependent joint stiffness based on the thermomechanical properties of the constituent materials.

3.3 Further investigations and future prospects

This section presents the limitations of the present research results and the investigations that should be carried out in the future. It concerns the application of the fracture mechanics approach, the prediction of fatigue behavior and the quantification of environmental effects, discussed in Section 3.3.1-3.3.3 respectively.

3.3.1 Fracture mechanics approach

Based on the results obtained for fracture and structural joints composed of pultruded GFRP laminates, the LEFM approach has proved a practical and efficient method for modeling fracture behavior. Like every approach, however, it has certain limitations and requires more investigation.

In Section 2.4, a mixed mode fracture criterion for pultruded composite joints was established based on the results obtained for four joint types (DCB, ELS, DLJ and SLJ), which constitutes a relatively small database, indicating that more confirmations are necessary. Although two types of structural joints (DLJs and SLJs) were employed to provide representative results for mixed mode fracture, neither has an ideal R-curve with a clear plateau and the fracture mode mixity changed with crack development. The former characteristic may result in underestimation of the critical strain energy release rate, G_c , corresponding to crack propagation. As to the latter one, more investigations using fracture joints with a fixed and known mode mixity, e.g. Mixed-Mode-Bending (MMB) specimens, should be performed to provide additional knowledge for mixed mode fracture. Based on the yet-to-be confirmed mixed mode fracture criterion, the predictions of the load-elongation response and strength of general structural joints can be developed.

3.3.2 Fatigue life prediction for general joints

A stiffness-based (Section 2.5) and a fracture-mechanics-based (Section 2.6) model have been established for structural joints (DLJs and SLJs) to characterize fatigue behavior, although both proved to be significantly dependent on the specific joint type. The stiffness degradation of DLJs and SLJs exhibited different trends, linear or sigmoid non-linear, and different failure

criteria were observed. Due to the dissimilar fracture mode mixity between DLJs and SLJs, distinct values of fracture parameters were obtained from FCG curves. This contradicts the previously held very popular opinion that fracture parameters can be considered material constants.

Given the variety of structural joints used in civil engineering structures, the generalization of existing fatigue life prediction models is an important consideration. By introducing a new equivalent formulation of the SERR, G_{eqv} , the fracture-mechanics-based model can be generalized (Quaresimin and Ricotta, 2006). This new parameter should be able to incorporate the contributions of both Mode I and II components of the SERR. Its ability to explicitly take into account the variation of fracture mode mixity during crack development, in other words during fatigue lifetime, is considered a promising feature. By using the equivalent strain energy release rate, a group of FCG curves obtained from different types of joints can be merged into a single dominant FCG curve, in which case the fracture parameters can be considered material constants. In order to complete this generalization procedure, more experimental investigations under fatigue loading should be performed for Mode I and II fracture joints (DCB and ELS) as well as for specimens with fixed fracture mode mixity (e.g. MBB).

Although in recent works a certain mathematical formulation of G_{eqv} has been suggested (Quaresimin and Ricotta, 2006), no clear physical background was provided. Thus a well-adapted formulation for G_{eqv} has to be mathematically originated, which at the same time involves a clear physical meaning.

3.3.3 Quantification of environmental effects

In the present research, the environmental effects on the mechanical and fracture behavior of structural joints (DLJs) under quasi-static and fatigue loadings are experimentally evaluated. Concerning the design of real structures, current knowledge concerning the effect on the trend of the mechanical and fracture behavior of joints is, however, insufficient for civil engineers and further quantification of the environmental effect is necessary. Some attempts have been made in this research to analytically or numerically quantify environmental effects, including a finite element model to predict the temperature-dependent stiffness of joints (see

Section 2.4) and a wear-out model to link cyclic stress and corresponding fatigue life to the temperature-dependent joint strength (see Section 2.7). Nevertheless, many more investigations have to be carried out concerning both the mechanical and fracture behavior of joints.

The temperature-dependent strength of joints composed of a certain type of composite laminate is believed to exhibit the same degradation trend as the stiffness (Feih et al., 2007), but this presumption needs to be validated for complex structural joints. As to the fracture behavior, no information concerning environmental effects on Mode I and II fracture joints has been provided here, although this nevertheless merits investigation. Following the standard testing procedure and validated calculation methods in Section 2.1, the R-curves and critical strain energy release rate (G_{Ic} and G_{IIc}) under different environmental conditions can be obtained for Mode I and II fracture specimens. Combining these with the corresponding results obtained for structural joints currently presented in Section 2.4, a universal mixed fracture criterion could be established for pultruded GFRP joints, which is designated as a function of the temperature and humidity. Similarly, but under fatigue loading, a more generalized FCG curve might be established based on the prospective results obtained for Mode I and II specimens together with the current results for structural joints presented in Sections 2.6 and 2.7. This universal FCG curve could not only incorporate the Mode I and II components of the SERR but also couple the temperature and humidity effects. It could therefore be used to make the fatigue life prediction, taking environmental effects into account, for any joint type composed of the same pultruded GFRP laminates.

References

- Abdel Wahab, M.M., Ashcroft I.A., Crocombe A.D., and Smith P.A., 2004. Finite element prediction of fatigue crack propagation lifetime in composite bonded joints. *Composites Part A: Applied Science and Manufacturing* 35(2), 213-222.
- ASTM D5528-01, 2007. Standard Test Method for Mode I Interlaminar Fracture Toughness of Unidirectional Fiber-Reinforced Polymer Matrix Composites. Annual book of ASTM standards: adhesive section 15.03.
- ESIS(TC4), 2006. Determination of the Mode II Delamination Resistance (Critical Energy Release Rate G_{IIc}) of Unidirectional Fiber-Reinforced Polymer Laminates Using the End-Loaded-Split Specimen (ELS). ESIS(TC4) Protocol, 2006.
- Feih, S., Mathys, Z., Gibson, A.G., and Mouritz, A.P., 2007. Modelling the tension and compression strengths of polymer laminates in fire. *Composites science and technology* 67(3-4), 551-564.
- Hadavinia, H., Kinloch, A.J., Little, M.S.G., and Taylor, A.C., 2003. The prediction of crack growth in bonded joints under cyclic-fatigue loading II analytical and finite element studies. *International journal of adhesion and adhesives* 23(6), 463-471.
- Irwin, G.R., 1957. Analysis of stresses and strains near the end of a crack traversing a plate. *Journal of Applied Mechanics* 24, 361-364.
- ISO 15024:2000(E), 2000. Standard test method for the mode I interlaminar fracture toughness, G_{Ic} , of unidirectional fibre-reinforced polymer matrix composites.
- Quaresimin, M., and Ricotta, M., 2006. Life prediction of bonded joints in composite materials. *International Journal of Fatigue* 28(10), 1166-1176.
- Vallée, T., Correia, JR., and Keller, T., 2006. Probabilistic strength prediction for double lap joints composed of pultruded GFRP profiles part I: Experimental and numerical investigations. *Composite Science and Technology* 66(13), 1903-1914.

CURRICULUM VITAE

Ye Zhang

ye.zhang@epfl.ch / ye_zhang@live.com

Date of birth: February 20th, 1979 in Beijing / P. R. China

Nationality: Chinese

Education

- | | |
|-----------|---|
| 2004-2010 | School of Architecture, Civil and Environmental Engineering, École Polytechnique Fédérale de Lausanne, (EPFL), Switzerland. PhD candidate at EPFL-CCLab (Composite Construction Laboratory) |
| 2002-2004 | Department of Civil and Environmental Engineering, Chalmers University of Technology, Göteborg, Sweden. Master of Civil Engineering |
| 1997-2002 | Department of Architecture, Tsinghua University, Beijing, China. Bachelor of Architecture |

Work Experience

- | | |
|-----------|---|
| 2004-2010 | Composite Construction Laboratory, EPFL
Research Assistant |
|-----------|---|

Publications

Journal papers

- [1] Zhang Y, Vassilopoulos AP and Keller T. Fracture of adhesively-bonded pultruded GFRP joints under constant amplitude fatigue loading. *International Journal of Fatigue* 2010; 32(7):979-987.
- [2] Zhang Y, Vassilopoulos AP and Keller T. Effects of low and high temperatures on tensile behavior of adhesively-bonded GFRP joints. *Composite Structures* 2010;92(7):1631-1639.
- [3] Zhang Y, Vassilopoulos AP and Keller T. Mode I and II fracture behavior of

-
- adhesively-bonded pultruded composite joints. *Engineering Fracture Mechanics* 2010; 77(1):128-143.
- [4] Zhang Y, Vassilopoulos AP and Keller T. Environmental effects on fatigue behavior of adhesively-bonded pultruded structural joints. *Composite Science and Technology* 2009; 69(7-8):1022-1028.
- [5] Zhang Y, Vassilopoulos AP and Keller T. Stiffness degradation and fatigue life prediction of adhesively-bonded joints for fiber-reinforced polymer composites. *International Journal of Fatigue* 2008;30:1813-1820.
- [6] Zhang Y, Keller T. Progressive failure process of adhesively bonded joints composed of pultruded GFRP. *Composite Science and Technology* 2008; 68(2):461-470.
- [7] Zhang Y, Keller T. Mixed-mode fracture of adhesively-bonded pultruded composite lap joints. *Engineering Fracture Mechanics*, submitted.

Conference papers

- [1] Zhang Y, Vassilopoulos AP and Keller T. Fatigue failure of adhesively-bonded structural joints for FRP composites. The 4th *International Conference on FRP Composites in Civil Engineering (CICE 2008)*, July 22-24, 2008, Zurich, Switzerland.
- [2] Zhang Y, Vassilopoulos AP and Keller T. Stiffness degradation and life prediction of adhesively-bonded joints for FRP composites. The 4th *International Conference on FRP Composites in Civil Engineering (CICE 2008)*, July 22-24, 2008, Zurich, Switzerland.
- [3] Zhang Y, Vassilopoulos AP and Keller T. Fatigue Behaviour of Adhesively Bonded Pultruded Gfrp. The 13th *International Conference on Experimental Mechanics*, July 1–6, 2007 Alexandroupolis, Greece.
- [4] Zhang Y, Keller T. Failure Process of Adhesively Bonded Joints from Pultruded GFRP Adherends. The 3rd *International Conference on Durability & Field Applications of FRP Composites for Construction (CDCC 2007)*, May 22-24, 2007, Quebec, Canada.
- [5] Zhang Y, Keller T. Failure Process of Adhesively Bonded Joints from Pultruded GFRP Adherends. The 3rd *International Conference on FRP Composites in Civil Engineering (CICE 2006)*, December 13-15, 2006, Miami, Florida, USA.
- [6] Zhang Y. Progressive failure process of adhesively bonded joints composed of pultruded GFRP. The 6th *International PhD Symposium in Civil Engineering*, August 23-26, 2006, Zurich, Switzerland.